BOEING

GPO PRICE $ _____

OTS PRICE(S) $ _____

Hard copy (HC) 5.00

Microfiche (MF) 1.25

N65-26083

(ACCESSION NUMBER) 183 (PAGES)

(THRU) 1 (CODE)

Cr 63371 (NASA CR OR TMX OR AD NUMBER)

09 (CATEGORY)

FACILITY FORM 602

SEATTLE, WASHINGTON

SPACE RADIATION TESTS ON REFLECTING SURFACES — FINAL REPORT

Submitted for

Jet Propulsion Laboratory Contract No. 950998

D2-36359-1

This work was performed for the Jet Propulsion Laboratory, California Institute of Technology, sponsored by the National Aeronautics and Space Administration under Contract NAS7-100.

The Boeing Company
Aero-Space Division

June 1965

ABSTRACT

SPACE RADIATION TESTS ON REFLECTIVE SURFACES

An experimental program was conducted to verify the stability of the Boeing-developed barrier-layer anodized aluminum reflecting surfaces in a simulated Earth-Mars charged particle radiation environment. This type of reflective surface is used to reflect sunlight onto solar cells in a light-concentrating solar cell panel design developed in earlier JPL contracts. Tests were also performed to determine the effects of charged particles on thermal properties of solar concentrator coatings including vapor deposited aluminum, chemically brightened aluminum, and high-emittance barrier-layer anodic coatings; and of spacecraft coatings including zinc oxide/potassium silicate, and zinc oxide/LTV-602 silicone coatings.

A 230-day Mars flight was chosen as a typical space mission. To evaluate the effects of the charged particle environment of this mission, specimens were bombarded with protons of energies 1 to 9 Kev and 2.5 Mev, and alpha particles of energies 2-16 Kev and 5.0 Mev. The barrier-layer anodized specimens were exposed to integrated particle flux (fluence) ranges for the various combinations of particles and energies as follows: Kev-energy protons, 9.5×10^{14} to 1.47×10^{17} protons/sq.cm.; Mev-energy protons, 7.1×10^{12} to 1.5×10^{15}; Kev-energy alpha particles, 5×10^{12} to 1×10^{16} alphas/sq.cm.; and Mev-energy alpha particles, 1.1×10^{13} to 4.4×10^{14}. The large integrated fluxes were chosen for Mev tests to obtain significant damage to samples for correlation studies.

The results of radiation tests and reflectance measurements on the barrier-layer anodic coatings proved them to be the most radiation-resistant of any six coatings tested. It was concluded that for an estimated Earth-Mars solar wind (protons and alpha particles) fluence of 8×10^{15} particles/sq.cm., a negligible change in solar absorptance will occur. No changes in emittance were observed in the anodic coatings. A fluence of Kev-energy particles on the order of 3×10^{16} protons/sq.cm. must be encountered before a significant change in solar absorptance occurs. A fluence of 9.25×10^{16} protons/sq.cm. was required to cause the solar absorptance to increase from 0.12 before irradiation to 0.23 after irradiation.

A calculation was made to determine the reduction in solar-cell short circuit current output in a concentrating panel, resulting from reflectance degradation of the anodized reflective surfaces. The reduction in current output due to reflectance changes will be negligible for an Earth-Mars mission. Fluences as high as 9.25×10^{16} protons/sq.cm. only reduced the calculated short circuit current output by 3.7 percent.

The zinc-oxide pigmented coatings were found to be much more radiation-sensitive than the barrier-layer anodized aluminum and other solar concentrator coatings. In Kev-energy proton tests a damage threshold of about 8×10^{14} protons/sq. cm. was observed for the zinc oxide/LTV-602(S-13) silicone coatings, whereas, the threshold for zinc oxide/potassium silicate (Z-93) coatings was found to be about 2×10^{14} protons/sq. cm. The estimated percentage changes in solar absorptances of the two paints due to an Earth-Mars mission solar wind fluence are 29 and 54 percent for S-13 and Z-93, respectively.

Both the vapor-deposited aluminum and chemically brightened aluminum blistered during irradiation with Kev-energy protons. The blisters, varying from 0.1 to 3 microns in diameter, caused an increase in the diffuse reflectance and a decrease in the total hemispherical reflectance. A proton fluence of 1×10^{16} protons/sq. cm. caused the total hemispherical reflectance to decrease by about 12 percent.

TABLE OF CONTENTS

	Page
ABSTRACT	
TABLE OF CONTENTS	
LIST OF TABLES	
LIST OF FIGURES	
1.0 INTRODUCTION	1
2.0 TECHNICAL DISCUSSION	3
2.1 Selection of Environment Test Conditions	3
2.2 Space Radiation Simulation Facilities	7
2.3 Test Samples	17
2.4 Test Procedures	22
2.5 Test Dosimetry	27
2.6 Analysis Procedures	41
2.7 Test Results	51
2.7.1 Reflectance Data and Thermal Property Analyses	51
2.7.2 Short Circuit Current Output of Solar Cell Concentrator Panel	94
3.0 CONCLUSIONS AND RECOMMENDATIONS	98
4.0 REFERENCES	99
5.0 APPENDICES	100
A. Study of the Radiation Environment for an Earth-Mars Mission	100
B. Calculations of Scattered Proton and Alpha Particle Flux Distributions	103
C. Reflectance Data	110
D. Detailed Data Table	168

LIST OF TABLES

Table		Page
1.	Table of Sample Reference Numbers	17
2.	Summary of Samples Tested	52
3.	Reflectance Measurement Summary	53
4.	Solar Absorptance Data	56
5.	Summary of Solar Cell Calculations	96

LIST OF FIGURES

Figure		Page
1	Summary of Space Radiation Integral Spectra	5
2	Average Proton Flux-Energy Curve for 230 Day Earth-Mars Mission	6
3	Proton Range, Ionization Loss, and Displacement Production	8
4	Test Setup For Solar Wind Simulator	9
5	Charged-Particle Source for Solar Wind Simulator	10
6	Sketch of Solar Wind Simulator	12
7	Experimental Setup for High-Energy Charged Particle Tests	14
8	Schematic of Dynamitron Test System	15
9	Schematic of Scattering Chamber	16
10	Section of Low-Emittance Anodic Coating	19
11	Section of High-Emittance Anodic Coating	21
12	Calibration of Solar Wind Simulator Particle Energy	23
13	Test Specimen Holder for Solar Wind Simulator	24
14a	Sample Configuration for 2.5 Mev Proton Test	26
14b	Sample Configuration for 5.0 Mev Alpha Particle Test	26
15a	Faraday Probe Trajectory	29
15b	Beam Profile as Measured by the Faraday Probe	29
16	Bucking-Voltage Energy Calibration Curve	30
17	Zero Probe Voltage Particle Energy Calibration Curve	31
18	Dosimetry Equipment Mounted on the Scattering Chamber	33
19	Schematic of Dynamitron Test Instrumentation	34
20	Positioning and Correction Curve for the Faraday Probe	36
21	2.5 Mev Scattered-Proton Flux	37
22	Scattering Chamber Specimen Holder	38
23	Particle Detection and Analysis	39
24	Particle Energy Resolution	40
25	Sample Calculation Sheet for Obtaining the Change in Solar Absorptance ($\Delta \alpha_s$)	45
26	Energy-Wavelength Plot for 22°C Black-Body Spectrum	47
27	Spectral Response of N on P Hoffman Solar Cell No. 132	48
28	Cross Section of V-Ridge Solar Cell Concentrator Panel	49
29	Effect of Kev-Energy Protons on Absolute Reflectance of Low Emittance Anodic Coatings	54
30	Reflectance of Unexposed Specimen No. 21 Measured at Various Angles of Incidence	57
31	Effect of 7.7 Kev Protons on Anodic Coated Aluminum	58
32	Effect of 7.7 Kev Protons on Anodic Coated Aluminum	59
33	Effect of 9 Kev Protons on Anodic Coated Aluminum	60
34	Effect of Low Energy Protons on Solar Absorptance of Low Emittance Anodic Coating	62

Figure		Page
35	Effect of Low Energy Protons on Diffuse Reflectance of Anodic Coated Aluminum	63
36	Barrier-Layer Anodic Coated Aluminum Before Irradiation	65
37	Barrier-Layer Anodic Coated Aluminum After Irradiation	66
38	Typical Large Spark Cavity on Anodic Coated Aluminum After Irradiation	67
39	Infrared Reflectance of Low-Emittance Anodic Coatings	68
40	Barrier-Layer Anodic Coated Aluminum After Alpha Particle Irradiation	70
41	Reflectance of Unexposed Specimen No. 161A Measured at Various Angles of Incidence	71
42	Effect of 8.7 Kev Protons on High-Emittance Anodic Coated Aluminum	72
43	Infrared Reflectance of High-Emittance Anodic Coatings	74
44	Effect of 8.2 Kev Protons on Chemically Brightened Aluminum	75
45	Effect of 8.2 Kev Protons on Chemically Brightened Aluminum	76
46	Chemically Brightened Aluminum Surface Before Irradiation	77
47	Proton Induced Blisters on Chemically Brightened Aluminum	78
48	Infrared Reflectance of Chemically Brightened Aluminum	79
49	Reflectance of Vapor Deposited Aluminum	80
50	Effect of 7.4 Kev Protons on Vapor Deposited Aluminum	82
51	Vapor Deposited Aluminum Surface Before Irradiation	83
52	Proton Induced Blisters on Vapor Deposited Aluminum Surface	84
53	Effect of 8 Kev Alpha Particles on Vapor Deposited Aluminum	86
54	Effect of 7.7 Kev Protons on ZnO-Potassium Silicate Thermal Coating	87
55	Change in Solar Absorptance of Zinc Oxide Potassium Silicate Thermal Coating	88
56	Infrared Reflectance of Zinc Oxide/Potassium Silicate Thermal Coating	90
57	Effect of 8.2 Kev Protons on ZnO/LTV-602	92
58	Change in Solar Absorptance of Zinc Oxide LTV-602	93
59	Infrared Reflectance of Zinc Oxide/LTV-602	95
A1	Integrated Proton Flux For A 230 Day Mars Mission	101
B1	Forward Gaussian Scattering of Protons	108
C1	Reflectance of Exposed Specimen No. 20 Measured at Various Angles of Incidence	111
C2	Reflectance of Exposed Specimen No. 29 Measured at Various Angles of Incidence	112
C3	Reflectance of Exposed Specimen No. 51 Measured at Various Angles of Incidence	113

Figure		Page
C4	Effect of 1.0 Kev Protons on Anodic Coated Aluminum	114
C5	Effect of 1 Kev Protons on Anodic Coated Aluminum	115
C6	Effect of 1.0 Kev Protons on Anodic Coated Aluminum	116
C7	Effect of 3.4 Kev Protons on Anodic Coated Aluminum	117
C8	Effect of 3.4 Kev Protons on Anodic Coated Aluminum	118
C9	Effect of 3.4 Kev Protons on Anodic Coated Aluminum	119
C10	Effect of 3.4 Kev Protons on Anodic Coated Aluminum	120
C11	Effect of 3.4 Kev Protons on Anodic Coated Aluminum	121
C12	Effect of 3.4 Kev Protons on Anodic Coated Aluminum	122
C13	Effect of 4.2 Kev Alpha Particles on Anodic Coated Aluminum	123
C14	Effect of 4.7 Kev Protons on Anodic Coated Aluminum	124
C15	Effect of 4.7 Kev Protons on Anodic Coated Aluminum	125
C16	Effect of 4.7 Kev Protons on Anodic Coated Aluminum	126
C17	Effect of 4.7 Kev Protons on Anodic Coated Aluminum	127
C18	Effect of 5 Kev Protons on Anodic Coated Aluminum	128
C19	Effect of 5 Kev Protons on Anodic Coated Aluminum	129
C20	Effect of 5.3 Kev Protons on Anodic Coated Aluminum	130
C21	Effect of 5.9 Kev Protons on Anodic Coated Aluminum	131
C22	Effect of 5.9 Kev Protons on Anodic Coated Aluminum	132
C23	Effect of 5.9 Kev Protons on Anodic Coated Aluminum	133
C24	Effect of 5.9 Kev Protons on Anodic Coated Aluminum	134
C25	Effect of 7.7 Kev Protons on Anodic Coated Aluminum	135
C26	Effect of 7.7 Kev Protons on Anodic Coated Aluminum	136
C27	Effect of 9.3 Kev Protons on Anodic Coated Aluminum	137
C28	Effect of 9.3 Kev Protons on Anodic Coated Aluminum	138
C29	Effect of 2.2 Kev Alpha Particles on Anodic Coated Aluminum	139
C30	Effect of 2.2 Kev Alpha Particles on Anodic Coated Aluminum	140
C31	Effect of 8 Kev Alpha Particles on Anodic Coated Aluminum	141
C32	Effect of 8 Kev Alpha Particles on Anodic Coated Aluminum	142
C33	Effect of 16 Kev Alpha Particles on Anodic Coated Aluminum	143
C34	Effect of 16 Kev Alpha Particles on Anodic Coated Aluminum	144
C35	Effect of 16 Kev Alpha Particles on Anodic Coated Aluminum	145
C36	Effect of 16 Kev Alpha Particles on Anodic Coated Aluminum	146
C37	Effect of 3.4 Kev Protons on High-Emittance Anodic Coated Aluminum	147

Figure		Page
C38	Effect of 9.3 Kev Protons on High-Emittance Anodic Coated Aluminum	148
C39	Effect of 2.5 Mev Protons on High-Emittance Anodic Coated Aluminum	149
C40	Effect of 2.5 Mev Protons on High-Emittance Anodic Coated Aluminum	150
C41	Effect of 8 Kev Alpha Particles on High-Emittance Anodic Coated Aluminum	151
C42	Effect of 5 Mev Alpha Particles on High-Emittance Anodic Coated Aluminum	152
C43	Effect of 8.2 Kev Protons on ZnO-Potassium Silicate Thermal Coating	153
C44	Effect of 2.5 Mev Protons on ZnO-Potassium Silicate Thermal Coating	154
C45	Effect of 2.5 Mev Protons on ZnO/Potassium Silicate Thermal Coating	155
C46	Effect of 5.5 Kev Alpha Particles on ZnO-Potassium Silicate Thermal Coating	156
C47	Effect of 8 Kev Alpha Particles on ZnO-Potassium Silicate Thermal Coating	157
C48	Effect of 5 Mev Alpha Particles on ZnO-Potassium Silicate Thermal Coating	158
C49	Effect of 5 Mev Alpha Particles on ZnO-Potassium Silicate Thermal Coating	159
C50	Effect of 8.2 Kev Protons on ZnO/LTV-602	160
C51	Effect of 2.5 Mev Protons on ZnO/LTV-602	161
C52	Effect of 2.5 Mev Protons on ZnO/LTV-602	162
C53	Effect of 2.5 Mev Protons on ZnO/LTV-602	163
C54	Effect of 8 Kev Alpha Particles on ZnO/LTV-602	164
C55	Effect of 8 Kev Alpha Particles on ZnO/LTV-602	165
C56	Effect of 5 Mev Alpha Particles on ZnO/LTV-602	166
C57	Effect of 5 Mev Alpha Particles on ZnO/LTV-602	167

1.0 INTRODUCTION

The experimental program described in this report was conducted to fulfill the requirements of Jet Propulsion Laboratory (JPL) Contract 950998 entitled, "Space Radiation Tests on Reflecting Surfaces." Submission of this final report to JPL completes contract commitments. The program was initiated on September 1, 1964, and was scheduled for completion on March 2, 1965. However, test equipment operation problems necessitated extending the contract performance period to June 2, 1965. The problems encountered were primarily due to troubleshooting the new test equipment and would not be expected in future testing. All test samples were satisfactorily irradiated after the equipment problems were eliminated.

This program was a follow-on to earlier contract programs (JPL Contracts 950270 and 950122) in which a light-concentrating solar cell panel was developed (References 1 and 2). One of the prime requirements for a solar cell concentrating panel or solar concentrators in general, is stability of the reflective surfaces in the pre-launch and space environments. It was found in these earlier programs that a high-purity aluminum surface which was anodized by a barrier-layer process, was highly stable in pre-launch and space environments. Abrasion, salt spray, humidity, temperature, and vacuum ultraviolet tests were conducted to prove-out the stability of the barrier-layer anodized aluminum. A limited number of cobalt-60 gamma radiation and 1.8 Mev proton tests (References 3 and 4) were conducted in a Boeing research program which indicated adequate stability of the barrier-layer coated aluminum in radiation environments which produce ionization and atomic displacements.

Subsequent to these tests, the solar cell concentrator panels have been studied as a candidate solar panel for Earth-Mars missions. Since the environment of an interplanetary space mission includes a large dose of solar protons and alpha particles, it was desired to evaluate the stability of solar panel reflective surfaces in charged particle tests. A study of the interplanetary environment was conducted which showed that the 1 to 4 Kev energy protons and alpha particles would probably produce the most damage to the reflective surfaces. This conclusion was based on the fact that particles of this energy range (solar wind particles) were much more numerous than higher energy particles (solar cosmic ray particles), and the assumption that the low energy particles would be capable of producing more displacement, ionization, and sputtering damage to surfaces than high energy particles.

To simulate the Earth-Mars environment, a program was planned in which low energy (1-16 Kev) proton and alpha particle experiments received maximum emphasis. However, to obtain experimental data for studies of dependence of

damage on energy, tests with 2.5 Mev proton and 5.0 Mev alpha particles were included in the program. The specific tests recommended at the outset of the program were: 1, 2, 4 and 8 Kev protons, fluences of 10^{14}, 10^{15}, and 10^{16} protons/sq.cm.; 2, 4, 8, and 16 Kev alphas, 10^{13}, 10^{14}, and 10^{15} alphas/sq.cm.; 2.5 Mev protons, 10^{14}, 10^{15}, and 10^{16}; 5.0 Mev alphas, 10^{13}, 10^{14}, and 10^{15}. It will be noted in this report that the proposed ranges of energies and fluences were covered except for minor deviations. These deviations were mutually agreed to by JPL and Boeing except for those dictated by available beam current in the high energy tests. The anticipated maximum fluence levels in the high energy tests were not achieved, however, the fluences obtained were well above the expected Earth-Mars mission dose.

The results of this research program point out the need for further experiments on some of the materials tested. The thermal properties of the barrier-layer anodized reflective surface have been clearly shown to be stable for an Earth-Mars mission, in fact, more stable than unprotected aluminum surfaces.

2.0 TECHNICAL DISCUSSION

The work accomplished in this program is described in the following seven subsections including: selection of environment test conditions, a description of test facilities, test samples, test procedures, test dosimetry, analysis procedures, and a discussion of test results.

2.1 SELECTION OF ENVIRONMENT TEST CONDITIONS

During an actual Mariner mission, surface materials will be exposed to an interplanetary environment that includes ultrahigh-vacuum, varying temperatures, solar electromagnetic radiation, and complex spectra of proton and alpha particle energies. Although desirable, complete combined environmental tests were not within the scope of the present study. After consideration of the present environmental effects knowledge and the significance of each component of the environment, the following conditions were selected:

2.1.1 Vacuum

Vacuum in the range of 10^{-6} to 10^{-7} torr was considered acceptable for these tests in order to eliminate the influence of oxygen and simulate sample outgassing. It is not yet known whether damage is a significant function of vacuum within this range. Gettering-type ion pumps have been found to provide an extremely clean vacuum, however, because of their slow pump-down speed they were undesirable in this program where many samples had to be tested. Oil-diffusion pumps can provide a clean environment if proper use is made of baffles and cold traps and can provide rapid pump down speeds. Therefore, silicone oil diffusion pumps were selected for this program.

Samples were irradiated in vacuum but then exposed to air for reflectance measurements. Typical time delays between irradiation and reflectance measurements were 20 to 40 hours. Future studies of degradation in situ would be desirable since damage may be modified by exposure to oxygen. Also, some annealing of damage may take place before measurements can be made. Limited annealing studies performed in the program and the results are given in Section 2.7.1.

2.1.2 Temperature

Temperature during and after irradiation can have a significant effect on accumulated permanent damage. Because the introduction of defects is affected by temperature at the time of damage, it is necessary to specify and control that temperature. Room temperature was selected as the condition for these tests. The most important temperature problem, however, was to avoid radiation induced sample heating during the test. Exposure rates in these tests were, in general, kept below those calculated to be of concern for sample heating.

In addition, samples were firmly clamped with retainer rings onto a large heat dissipating mount. Temperature was checked by the use of thermocouples after irradiation at the highest fluxes used.

2.1.3 Solar Electromagnetic Radiation

Illumination of optical materials by visible light may produce bleaching of color centers, however, irradiation-induced defects are not removed by this illumination, and color centers reappear upon further irradiation. Because of the fading phenomenon and the light sensitivity of solid-state particle detectors used in Mev-energy experiments, excessive light was avoided and irradiation exposures were performed either in the dark or semidarkness. Samples were also shielded from strong light after irradiation until final measurement.

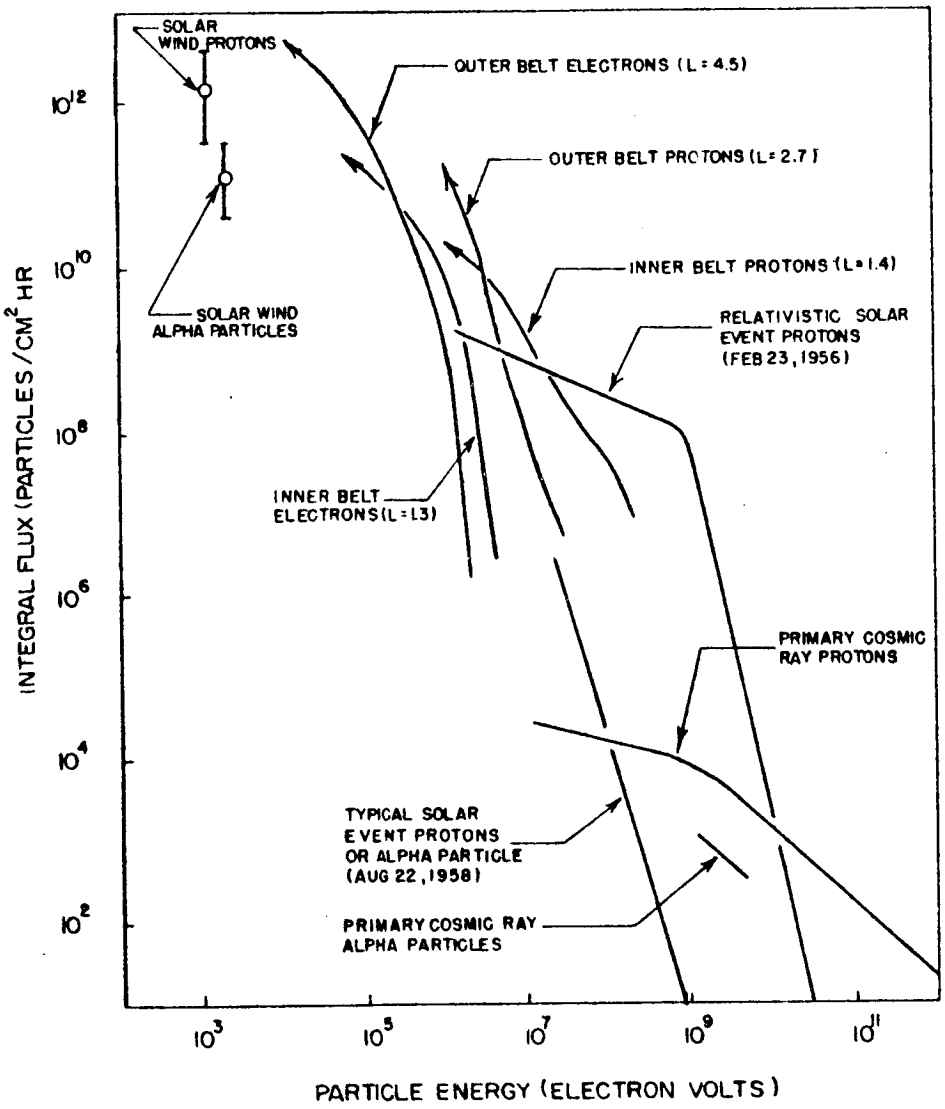
Ultraviolet radiation has already been shown to cause serious degradation to many reflecting materials and its influence has been studied extensively. Ultraviolet irradiation was not performed in this study due to the volume of existing UV data from References 1 and 2 and the lack of charged particle data.

2.1.4 Charged Particles

Solar concentrator and thermal control surfaces on Mariner missions will be subjected to both high energy protons and alpha particles streaming away from the sun during solar events, as well as very low energy protons and alpha particles in the solar wind. Characteristics of these types of radiation are known well enough now to allow a reasonable determination of the energy-dependent particle flux encountered in interplanetary space. Computer programs developed at Boeing aided in establishing the radiation criteria for the Mariner vulnerability studies. The significant values of integral flux of protons and alpha particles used in planning the experiments are shown in Figures 1 and 2. Values of integral flux shown are for the integral portion of the spectrum above the energy specified (>E).

During the program, the integral flux estimates were revised to incorporate data from the latest space environment measurements. A detailed description of the Earth-Mars radiation environment showing the latest integral fluxes is given in Appendix A. In general, the energy/flux spectrum of space radiation decreases rapidly with increasing energy.

Very-low-energy solar wind protons or alpha particles (1 to 10 Kev) interacting with a material can sputter off surface atoms. Their extremely short range results in a sudden transfer of energy and momentum to the surface layer of the target material. Material layers a few angstroms thick can be eroded away leaving the surface pitted, thus increasing diffuse reflectance. Protons or alpha particles that stop in the surface can also form into hydrogen molecules or helium atoms, respectively. Gas pockets have been observed in this program which produce blisters with a resulting increase in diffuse reflectance.



SUMMARY OF SPACE RADIATION INTEGRAL SPECTRA

FIGURE 1

USE FOR TYPEWRITTEN MATERIAL ONLY

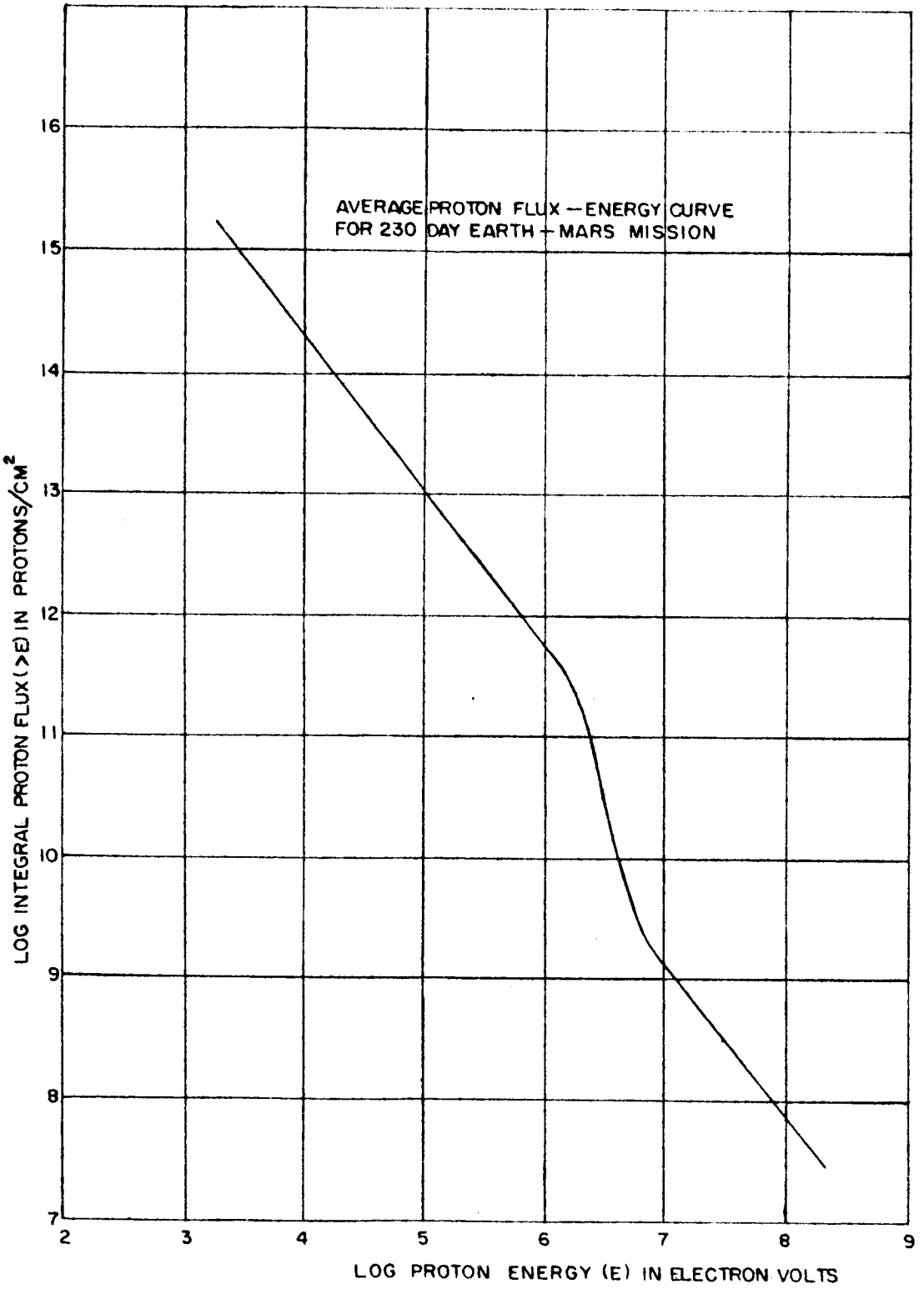


FIGURE 2

USE FOR TYPEWRITTEN MATERIAL ONLY

These extremely range-limited particles can also cause heavy surface ionization and displacements. Ionization can result in increased solar absorption in the coatings by providing electrons, which may be trapped at inherent or induced color centers, making these centers effective visible-light photon absorption sites.

The relative importance of surface versus bulk ionization depends on the energy of the charged particle. To investigate damage as a function of depth of penetration, protons of 1 to 8 Kev and alpha particles of 2 to 16 Kev were selected for the tests. Alpha particles of twice the proton energy have approximately the same range. Proton fluences from 1×10^{14} to 1×10^{16} p/cm^2 were selected to investigate effects over a wide exposure range below and above the estimated value of an Earth-Mars mission. Values of alpha particle fluence selected were of an order of magnitude less than the proton values in order to represent their relative intensity in the solar wind.

Higher energy protons and alpha particles (1-5 Mev), as well as particles of lower energies, are very plentiful in solar particle events. Protons of 2.5 Mev and alpha particles of 5 Mev were chosen for these tests. Tests at these energies were selected to check the relative importance of ionization versus displacement effects for comparison with the low energy tests. The study of high energy particle effects provides information on bulk ionization and displacements in thin surface coatings. A proton range-energy curve for aluminum is shown in Figure 3. Also shown in the figure are a $\frac{dE}{dX}$ ionization energy loss curve and a curve showing the displacement cross section of protons in silicon.

Selected fluence values for the high energy particle exposures ranged from approximately 1×10^{13} to 1×10^{16} particles/cm^2. Higher fluence values than those expected in space were selected to provide significant damage and to check the validity of predicting damage observed at one energy with that observed at another energy. The displacement cross section (D) is expected to decrease with increasing particle energy (E) by the relation $D \sim E^{-2}$.

2.2 SPACE RADIATION SIMULATION FACILITIES

2.2.1 Solar Wind Simulator

Both 1-9 Kev protons and 2-16 Kev alpha particles were generated by the solar wind simulator. A photograph of this low energy accelerator is shown in Figure 4.

Hydrogen and helium (commercial ultrapure laboratory grade gases) were used to produce protons and alpha particles, respectively. Gas from the pressure bottles (100-1,000 p.s.i.) was fed through a pressure regulator valve and gauge into the plasma chamber. The selected gas was ionized in an Oak Ridge Technical Enterprizes Company (ORTEC) ion source by an 80-Mc RF oscillator. A photograph of the ion source and its oscillator is shown in Figure 5. An ionized plasma of

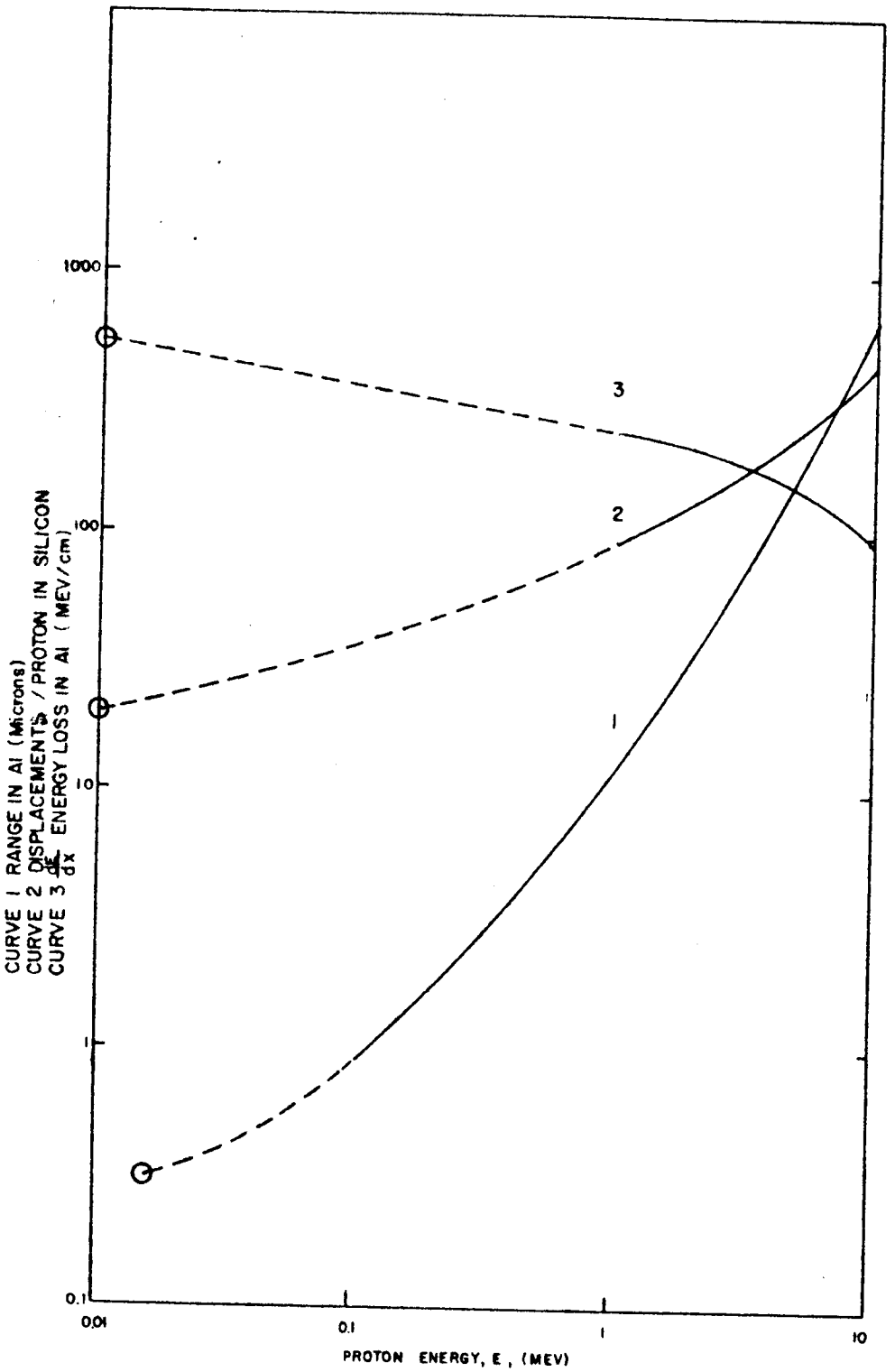
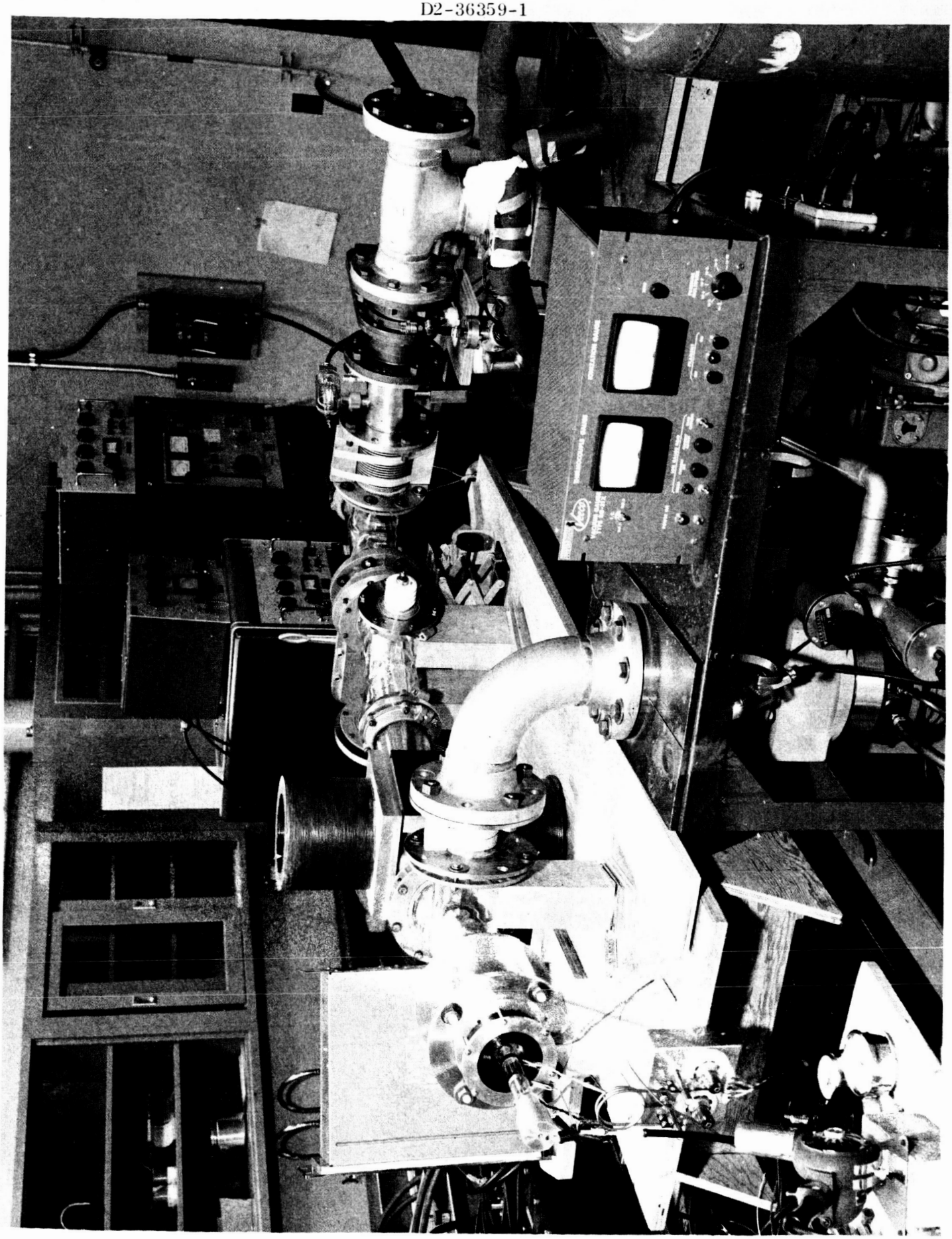
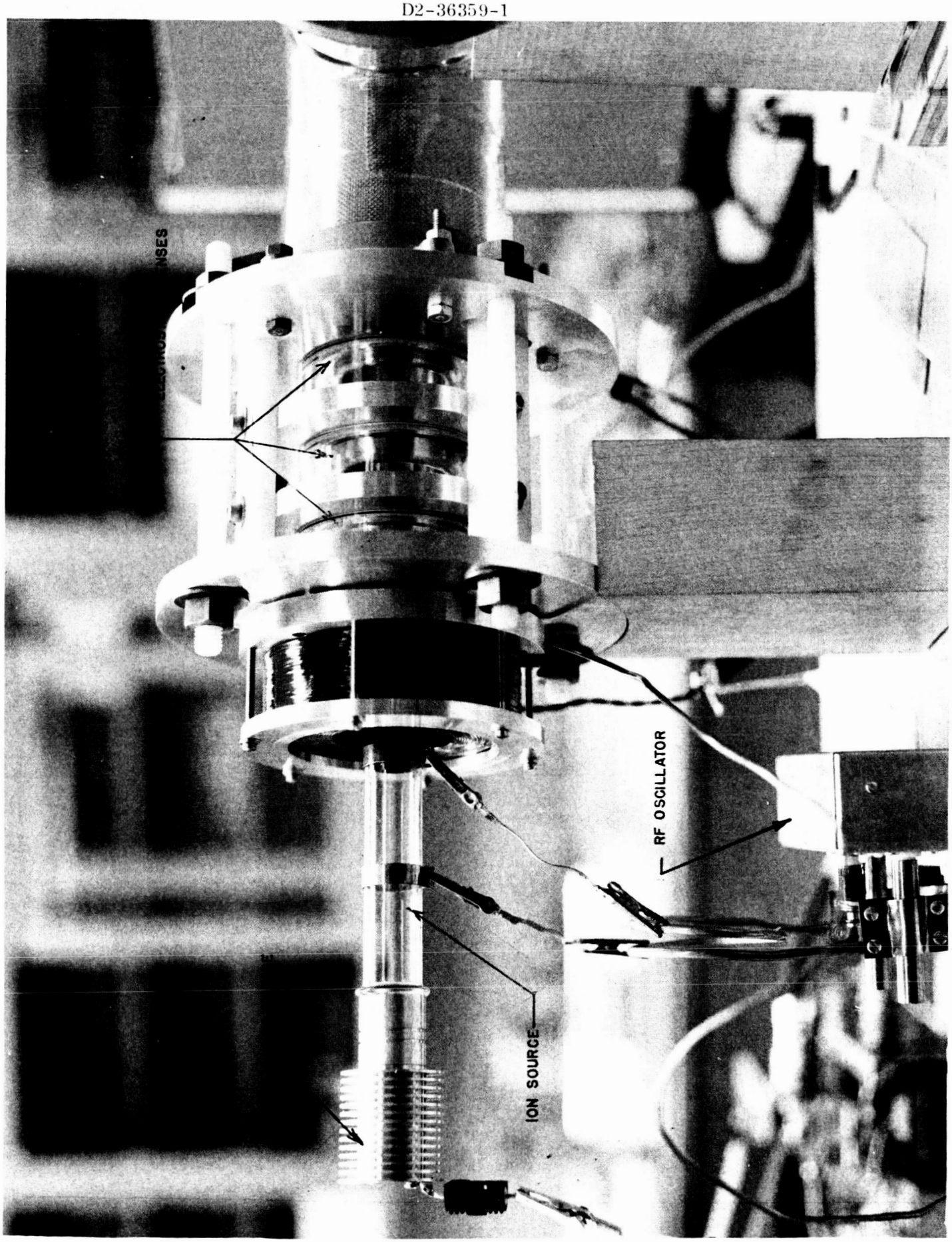


FIGURE 3 PROTON RANGE, IONIZATION LOSS, & DISPLACEMENT PRODUCTION

USE FOR TYPEWRITTEN MATERIAL ONLY



TEST SET-UP FOR SOLAR WIND SIMULATOR FIGURE 4



CHARGED - PARTICLE SOURCE FOR SOLAR WIND SIMULATOR

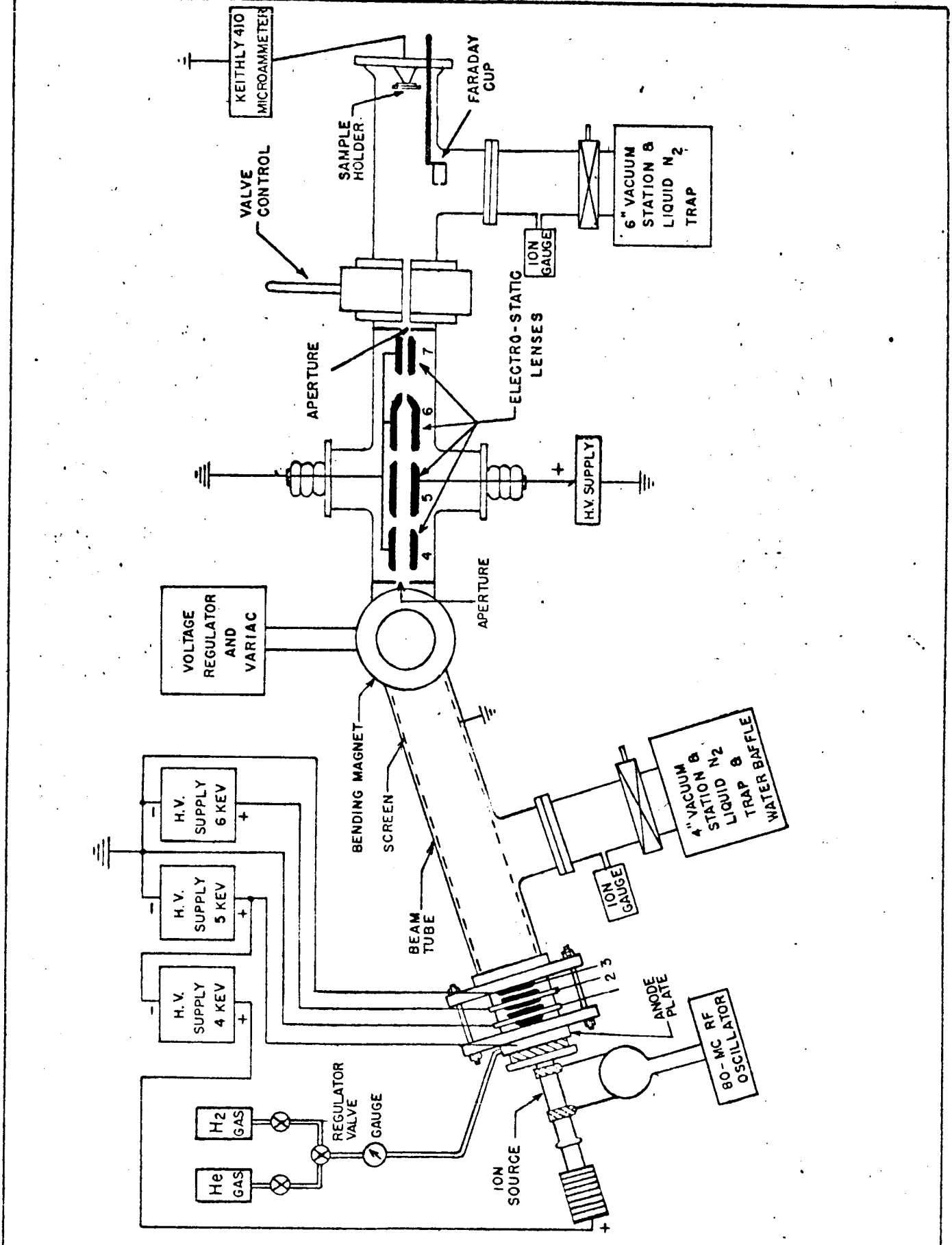
FIGURE 5

H^+, H_2^+, and H_2 - H^+ (95 percent mass 1 and 2 with some mass 3 particles) is formed from the hydrogen gas; or a plasma of He^+, He^{++} (singly and doubly ionized) is formed from the helium gas. Also seen in Figure 5, is the high voltage probe with its cooling fin jacket. Electrons stripped off of the neutral gas during the ionization process bombard and heat the probe during tests.

A schematic of the solar wind simulation facility is shown in Figure 6. Positive ions are electrostatically accelerated to the desired Kev energy by applying appropriate potentials to accelerating electrodes and focusing lenses. The electrostatic lens system is numbered from 1 through 7 in Figure 6 and typical values of high voltage (for 9-Kev protons) are shown. For the case shown, hydrogen plasma ionized in the chamber would "see" a potential difference of 4 Kv between the probe and the anode plate and another 5 Kv between the anode and the extractor (lens 1). Resulting protons of 9 Kev were focused without further acceleration by first passing through a retarding potential of 6 Kv between the anode and focusing lens 2, and then an accelerating potential of 6 Kv between lenses 2 and 3.

Mass, energy, and charge separation of the ions were accomplished by the use of a solenoid bending field and two limiting apertures of 3/4-inch diameter. The radius of curvature used for particle selection was 8 inches. This corresponded to a 25-degree bend angle in the beam tube. The solenoid field (about 300 gauss) was varied by a power driven Variac and controlled by a 3-phase filter supply. After bending, the particles passed through a second lens system. This system provides a capability for de-acceleration, further acceleration, and focusing of particles. The lens system was placed after the bending field so that the facility would not be limited by energy restrictions of the bending radius. Lens 5 was occasionally used to shape the beam spot. This scheme resulted in a uniform (± 5 percent variation) charged particle exposure of the samples. The beam spot size on the sample was about 0.9-inch diameter. A Keithly Micro Micro Ammeter was used to monitor sample and Faraday probe currents. (The Faraday probe will be described in Section 2.4.1). Proton and alpha particle currents from 0.01 to 10 microamps were used in the tests. The maximum attainable beam currents varied as a function of particle acceleration voltage. A maximum beam current of approximately 1 microamp was attainable with 1 Kev protons, whereas, 10 microamps was attainable with 9 Kev protons.

A vacuum of 2×10^{-6} torr was maintained during testing by the use of two vacuum stations. The first station was located near the ion source and consisted of a 4-inch oil diffusion pump with liquid nitrogen-cooled and water-cooled chevron baffles. The second station was located near the sample holder and consisted of a 6-inch oil diffusion pump with a liquid nitrogen-cooled chevron baffle. All O-ring seals were made of Viton-A and were concealed from radiation and direct exposure to the inside of the chamber. A minimum of Apiezon "L" grease was used on the rings to minimize the probability of contamination on sample surfaces.



CALC	RG/CB	3-29-5	REVISED	DATE
CHECK				
APR				
APR				

SKETCH OF
SOLAR WIND SIMULATOR

FIGURE 6

THE BOEING COMPANY

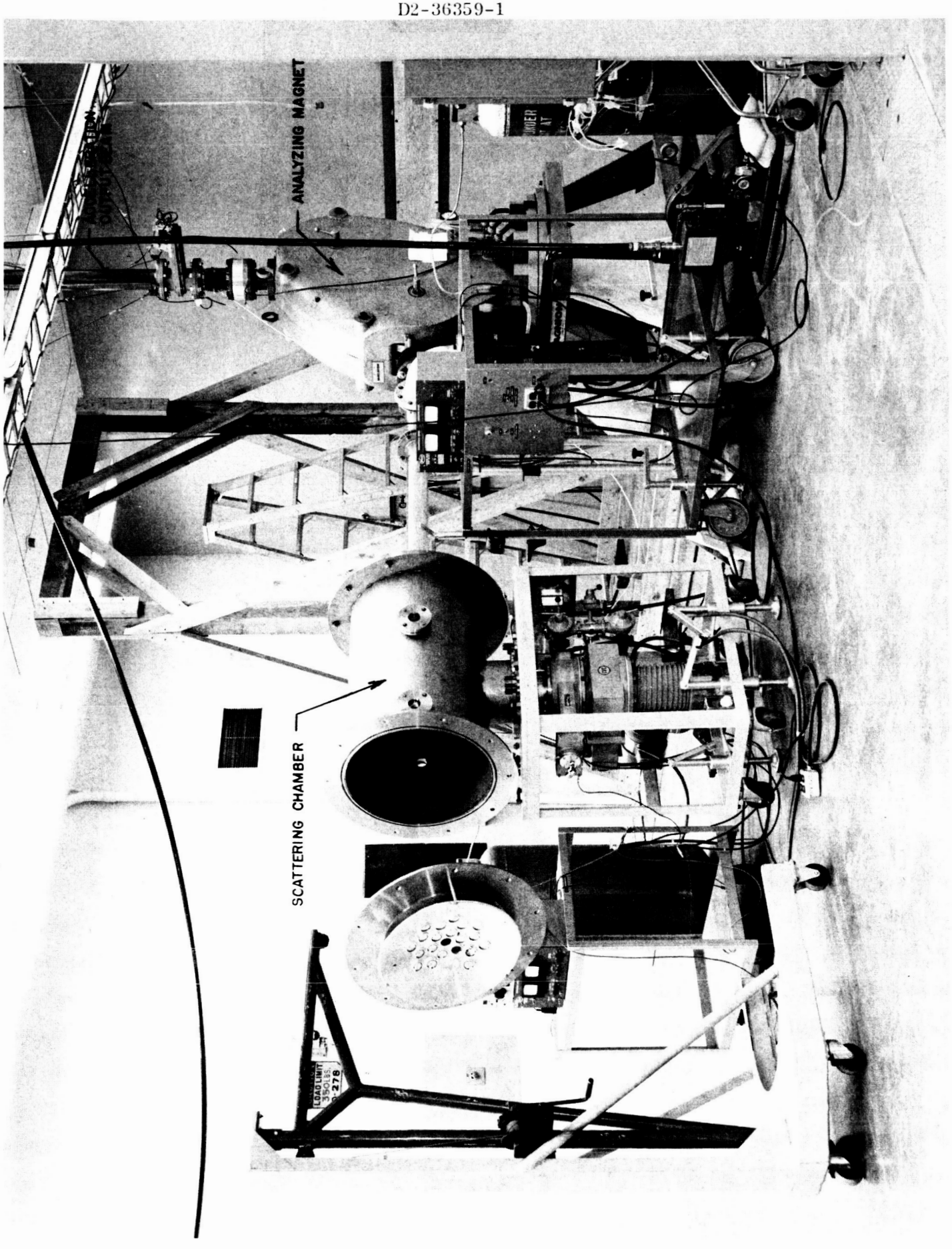
2.2.2 Dynamitron Charged-Particle Scattering Facility

Protons of 2.5 Mev and alpha particles of 5 Mev energy were obtained using the Dynamitron accelerator. In the Dynamitron, charged particles are produced from an ionized plasma of hydrogen or helium. These charged particles are extracted into the accelerator beam tube section in a similar manner to that described in Section 2.2.1. Maximum beam currents are obtained by adjusting the gas pressure and the voltage of the extractor electrode. The desired accelerating voltage is maintained by a stack of high voltage rectifiers. Stable currents can be obtained for voltages between approximately 0.5 and 5.0 Megavolts (Mv). For these tests, the accelerating potential chosen was 2.5 Mv. The resulting particle energies were 2.5 Mev for the singly-ionized, mass-one protons and 5.0 Mev for the doubly-ionized alpha particles.

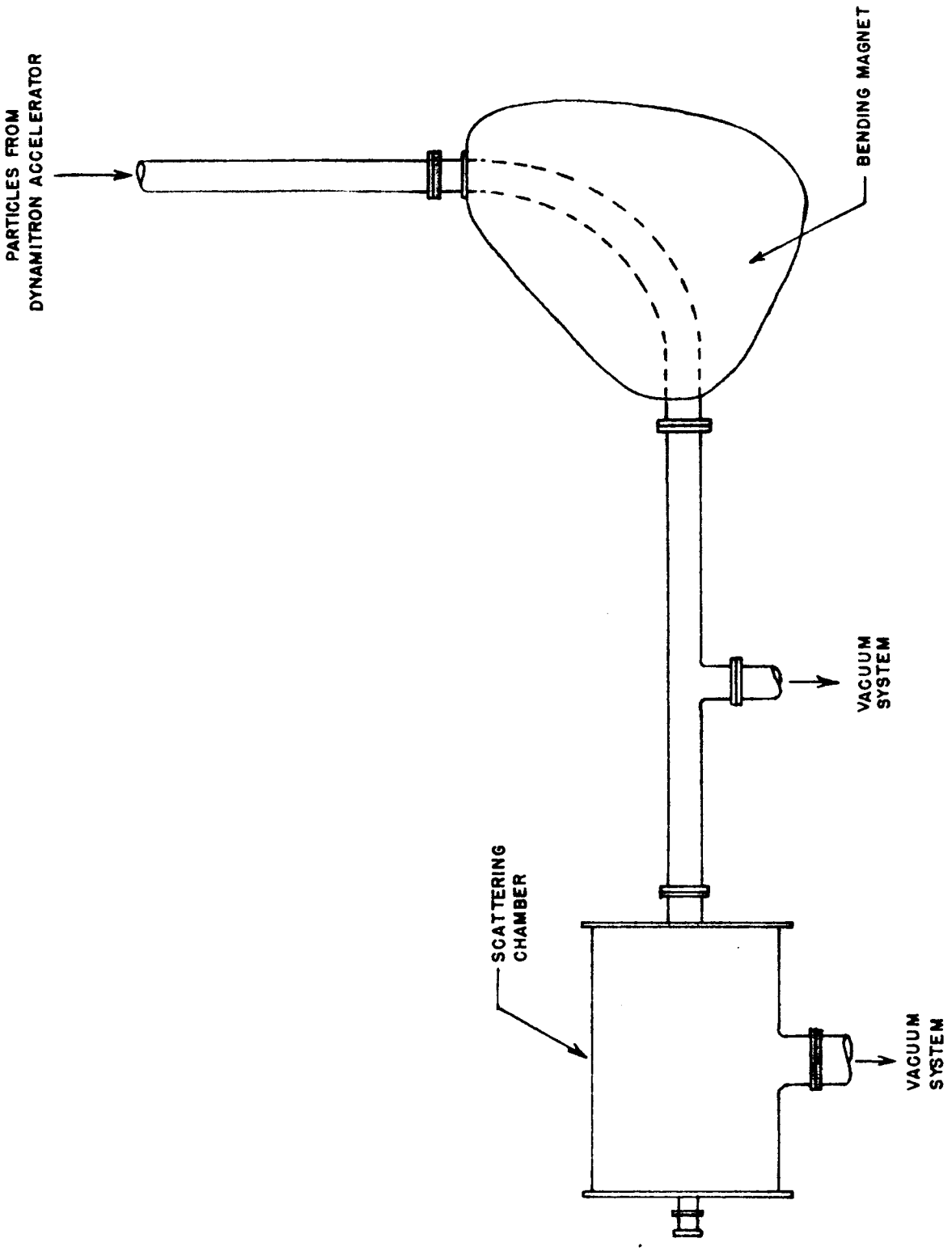
Figure 7 shows the 90 degree, mass-energy-product-16 analyzing magnet attached to the Dynamitron vertical beam port. The scattering chamber is connected to the magnet by a bellows and a four-inch diameter glass pipe. Control of current in the analyzing magnet provides the means of selecting proton or alpha particle energy as well as separating hydrogen ions into masses 1, 2, and 3 (H^+, H_2^+, $H_2 - H^+$) or helium into singly or doubly charged ions (He^+, He^{++}). The magnet current was set to select protons (H^+) of 2.5 Mev energy and alpha particles (He^{++}) of 5.0 Mev energy for the proton and alpha particle tests, respectively. A schematic of the Dynamitron scattering setup is shown in Figure 8. The resulting analyzed particle beam is then collimated by a 5/8-inch limiting aperture at the entrance to the scattering chamber. The collimated beam is then viewed by its fluorescence on the quartz window in the fixed Faraday cup. By insertion of a gold scattering foil in the beam path, large uniform exposure areas were obtained for both alpha particle and proton irradiation tests (see Section 2.5 and Appendix B).

High positive voltages (up to 2 Kv) were applied to the scattering foil to aid in suppressing the forward scattering of secondary electrons generated in the foil. In addition, a set of bending coils was placed in the back of the foil and in front of a baffle (see Figure 9). The magnetic field of the coils was used to bend the secondary electrons out of the forward scattering direction and into the grounded baffle plate. The field produced by the bending coils was measured by a gauss meter and calculations of the necessary coil currents were made. A high voltage (up to 500 volts) was applied to the shield of the movable Faraday probe (Figure 9) when it was not used for field mapping. This positive voltage aided in capturing secondary electrons.

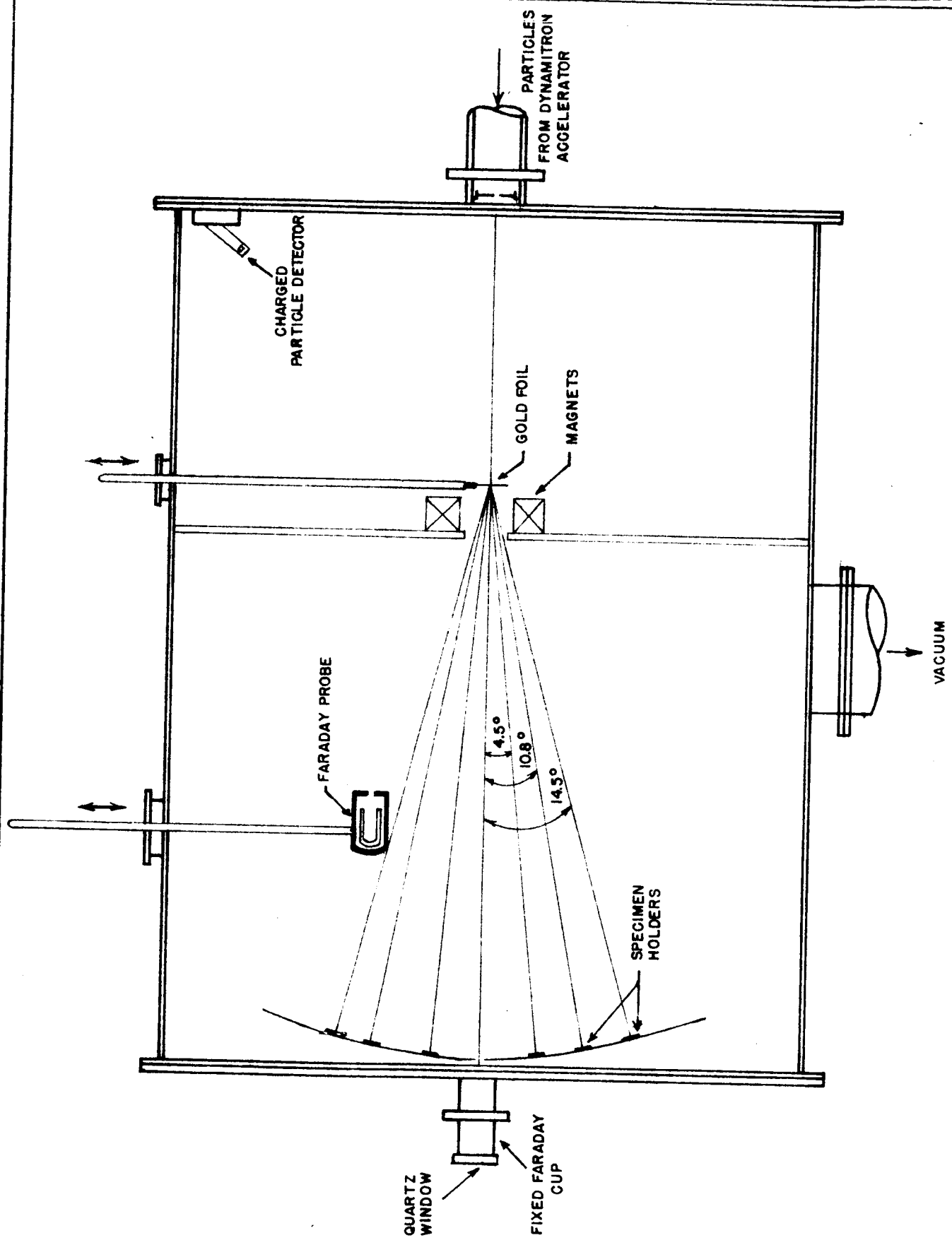
A vacuum of 10^{-6} torr was maintained by the use of two vacuum stations. The first station is connected to the beam pipe glass tee (Figure 8) and consisted of a 4-inch silicone oil diffusion pump with a liquid nitrogen cooled chevron baffle. The second station was mounted directly under the scattering chamber. It consisted of a 6-inch silicone oil diffusion pump with a liquid nitrogen cooled baffle. Temperature on the samples was checked by thermocouples after a high flux run. Induced electric fields prevented thermocouple measurements during a run.



EXPERIMENTAL SETUP FOR HIGH-ENERGY CHARGED PARTICLE TESTS FIGURE 7



CALC	RG/CB	4-8-5	REVISED	DATE	SCHEMATIC OF DYNAMITRON TEST SYSTEM	FIGURE 8
CHECK						
APR						
APR					THE BOEING COMPANY	PAGE 15



CALC	RG/GB	4-8-5	REVISED	DATE	SCHEMATIC OF SCATTERING CHAMBER	FIGURE 9
CHECK						
APR						
APR					THE BOEING COMPANY	PAGE 16

2.3 TEST SAMPLES

The test samples for this contract included five basic types: (1) barrier-layer anodic coated aluminum in both thin and thick sections (low and high emittance); (2) vapor deposited aluminum on an aluminum substrate; (3) chemically brightened aluminum; (4) zinc oxide/LTV-602 paint; and (5) zinc oxide/potassium silicate paint. The primary emphasis of the contract was to evaluate the stability of the low-emittance barrier-layer anodic coated aluminum under charged particle irradiation typical of an Earth-Mars flight environment. Therefore, the bulk of the test samples was the thin anodic coatings. A relatively small number of the other test samples was evaluated. A list of the types of test samples versus their assigned reference numbers is given in Table 1.

TABLE 1: TABLE OF SAMPLE REFERENCE NUMBERS

Type of Coating	Reference Numbers
Low-emittance anodic coatings	1 to 133
High-emittance anodic coatings	161A & B to 167A & B
Vapor deposited aluminum coatings	174 to 186
Chemically brightened aluminum coatings	187 to 199
Zinc oxide/LTV-602 coatings	211 to 224
Zinc oxide/potassium silicate coatings	225 to 239

A detailed physical description of the various types of samples follows:

2.3.1 Low-Emittance Anodic Coated Samples

The low-emittance anodic coated samples were prepared using the same process that was used to prepare the aluminum for solar cell concentrator panels in a previous JPL contract (Reference 1). Thus, any charged particle radiation damage measured on these samples should be representative of what may occur in an actual concentrator panel operating in interplanetary space.

The aluminum sheets were procured from Alcoa as 1199, H-18, 10-mil foil. The general process used to prepare and anodize the aluminum sheets is as follows:

1) The sheets (2 ft x 3 ft) were mechanically polished with a 20-inch diameter (cylindrical) Tanton flannel buffer. The buffing compound used was Learock 302C (Vdylite). Kerosence was used on the sheets during and after buffing. After buffing, the sheets were cleaned with naptha and cheese cloth, and dipped in a degreasing solution (Turco 4142).

2) The sheets were cleaned using a dilute sodium hydroxide solution. This bath was followed by a rinse in a nitric acid solution. The sheets were then chemically brightened in an Alcoa R-5 brightening bath. After brightening they were rinsed with water and a nitric acid solution.

3) The sheets were then electropolished in a fluoboric acid solution followed by a water rinse.

4) Finally, the sheets were anodized in an ammonium tartrate solution at a voltage of 300 volts. The anodization process was followed by rinses in a phosphoric acid solution and water.

One hundred thirty-three test samples of 1-1/2 inches diameter were punched from two sheets. Sample numbers 1 through 63 were taken from one sheet and the remainder from a second sheet. This size was selected for all samples because it was required for the specimen holder on the IR-4 reflectometer. The samples were numbered consecutively as they were taken from the sheets, and arrows were scratched on their back indicating the direction of roll marks.

Reflectance measurements on one of every four samples showed that the reflectance at various positions on a given sheet varied only by ±1 percent at given wavelengths in the 0.4 to 2.6 micron region. Variations of about ±2 percent were obtained in the ultraviolet wavelength region (0.25 to 0.4 microns). The reflectances of specimens taken from the two different sheets agreed within the above tolerances in their respective wavelength regions. The variation in coating thickness on these samples was estimated to be less than ±30 Angstroms (0.003 microns) based on the shift in wavelength of reflectance minima and maxima.

The thickness of the low-emittance anodic coatings is estimated to be about 0.39 microns, assuming a thickness of 13 Angstroms/volt of anodization voltage (Reference 5). As an independent check on thickness, a photomicrograph was made of a cross section of a typical low-emittance sample (Figure 10). This measurement showed a thickness of 0.35 to 0.7 microns which is in fair agreement with the above estimates. An exact thickness cannot be determined from the photomicrograph because of the thickness of the dark strip caused by buildup of the germanium during the vapor deposition shadowing process.

2.3.2 High-Emittance Anodic Coated Samples

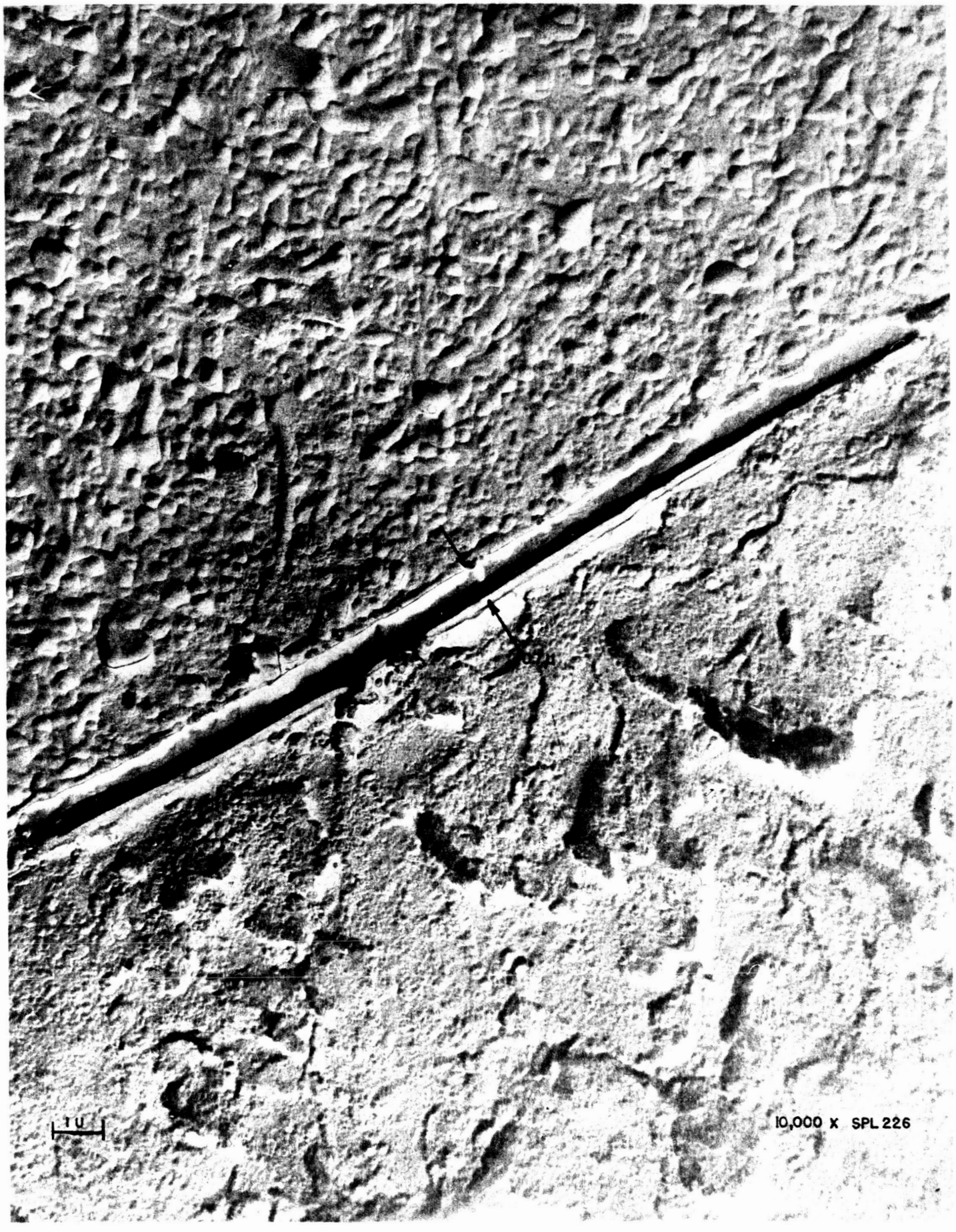
Twelve, high-emittance (ϵ = 0.25 to 0.28) barrier-layer anodic coated samples were prepared for inclusion in the test program. These thicker anodic coatings were chosen because of their applicability to solar cell panels and spacecraft for certain space missions, and because optical property changes such as color center formation in their anodic film should be more readily measured.

The high-emittance barrier-layer coatings were prepared using the process described in Section 2.3.1 with the following exceptions:

1) No mechanical polishing was done.

2) The size of the sheets was 2 x 5 inches.

3) The ammonium tartrate anodizing solution was modified to allow voltages as high as 1250 volts to be used.



SECTION OF LOW-EMITTANCE ANODIC COATING

FIGURE 10

The thickness of these anodic films, as estimated from a specific anodization thickness of 13 Angstroms/volt, is 1.6 microns. A thickness measurement with a photo-micrograph (Figure 11) showed the high-emittance anodic film to be 1.6 to 1.7 microns thick. It was noted that the variation in mean reflectance in the ultraviolet wavelength region between high-emittance anodic coated control samples varied by as much as ±15 percent (at 0.3 microns). No significant variation in mean reflectance was observed at wavelengths longer than 0.4 microns. It is assumed that the variations in ultraviolet reflectance are caused by differences in the coefficient of absorption in the aluminum oxide film.

2.3.3 Vapor Deposited Aluminum Samples

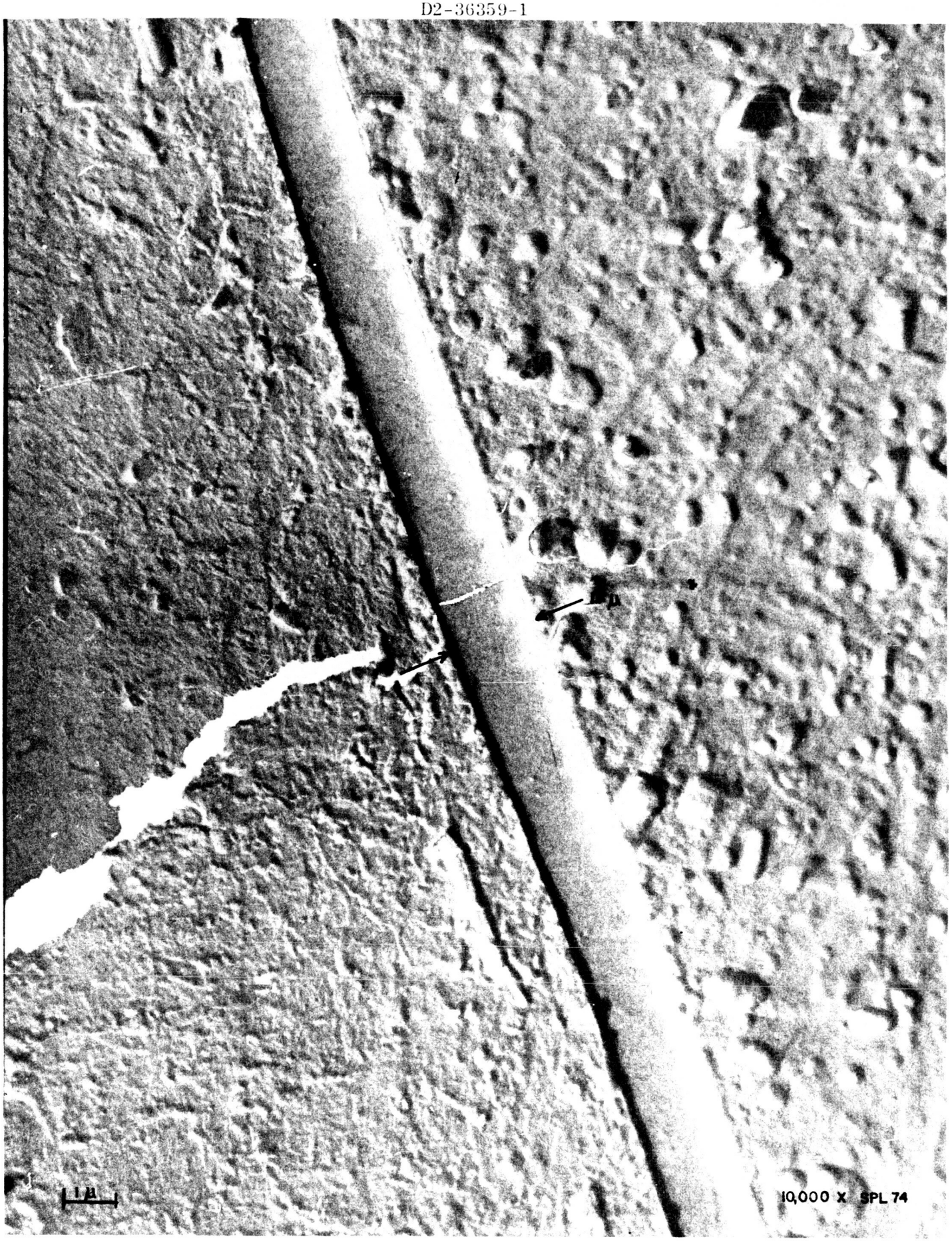
Thirteen, vapor-deposited aluminum samples were prepared for the test program. Vapor deposited aluminum was selected as a test coating because of its importance as a solar concentrator and spacecraft coating, and its uniqueness among the coatings to be evaluated. The aluminum coating was applied to the same chemically-brightened aluminum substrate used for the anodic samples. To assure uniformity of the samples, they were all coated at the same time. Since film thickness could not be measured during the coating process, deposition was continued until complete visual opaqueness was obtained on a transparent plastic film. A glass microscope slide was coated along with the aluminum samples. An attempt to section the glass slide and measure the film thickness by electron microscopy failed. Later in the program, one of the aluminum samples was sectioned and the film thickness was measured to be 1.0 micron by similar techniques.

2.3.4 Chemically-Brightened Aluminum Samples

Thirteen, chemically-brightened aluminum samples were prepared for the test program as described in Steps 1 and 2 in Section 2.3.1. These samples were selected because they are typical of the anodic coating substrate. Thus, any optical changes observed in the anodic coated samples could either be attributed to substrate or anodic coating changes. Also, it was desired to determine the differences in effects between aluminum and vapor deposited aluminum surfaces.

2.3.5 Pigmented Spacecraft Coating Samples

Two types of white, pigmented spacecraft coatings were included in the program. These were zinc oxide in a potassium silicate binder (Z-93) and zinc oxide in an LTV-602 silicone binder (S-13). Both coatings were sprayed onto an aluminum substrate which was about 0.050 inches thick. These coatings were prepared by the Illinois Institute of Technology in accordance with procedures discussed in detail in Reference 6. A total of fourteen of each type of coating was utilized in the program.



SECTION OF HIGH-EMITTANCE ANODIC COATING FIGURE 11

2.4 TEST PROCEDURES

2.4.1 Low Energy Particle Tests

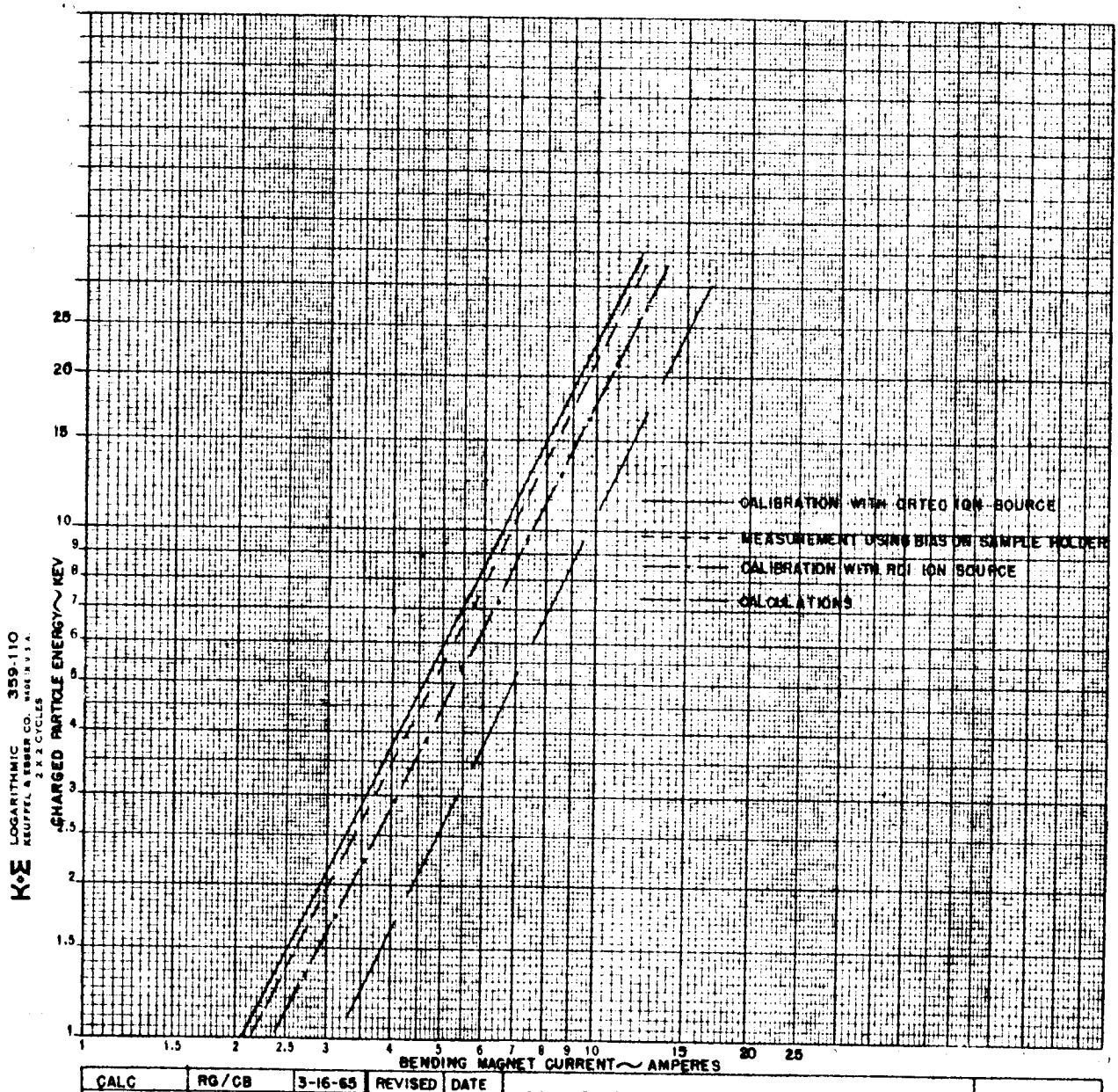
A descriptive sketch and a photograph of the test setup for the low energy proton and alpha particle tests are shown in Figures 4 and 6. Since similar procedures were used for both proton and alpha particle tests, the following discussion is applicable to both.

To begin operation of the solar wind simulator, cold traps were filled with liquid nitrogen and the diffusion pumps were turned on. During periods of inoperation, the beam tube was isolated from the vacuum systems by closed gate valves. When the diffusion pumps became operative, the gate valves were opened and the beam tube was pumped down to a pressure of about 5×10^{-7} torr. The ion source power supply and the gas flow to the ionizing chamber were then turned on and allowed to stabilize for a period of 1 to 2 hours. Typical beam tube pressures with the ion source operating were in the range of 1×10^{-6} to 3×10^{-6} torr.

The desired particle energy was selected by establishing a given current in the bending magnet based on the energy versus current data shown in Figure 12 (solid line) and discussed in detail in Section 2.3.1. While maintaining the magnet current fixed, the beam was directed to the target area by varying the probe, anode, and extractor voltages. The beam was centered and focused by viewing the fluorescence of a quartz window placed at the end of the beam tube. Typical beam sizes at the specimen position varied from 0.7 to 0.9 inches in diameter. The size and intensity distribution of the beam was varied with focusing electrode Nos. 2 and 5 (Figure 6). The most satisfactory arrangement for most tests was to ground electrode No. 5 and do all focusing with No. 2. The size of the beam was scaled directly from the quartz window fluorescent image.

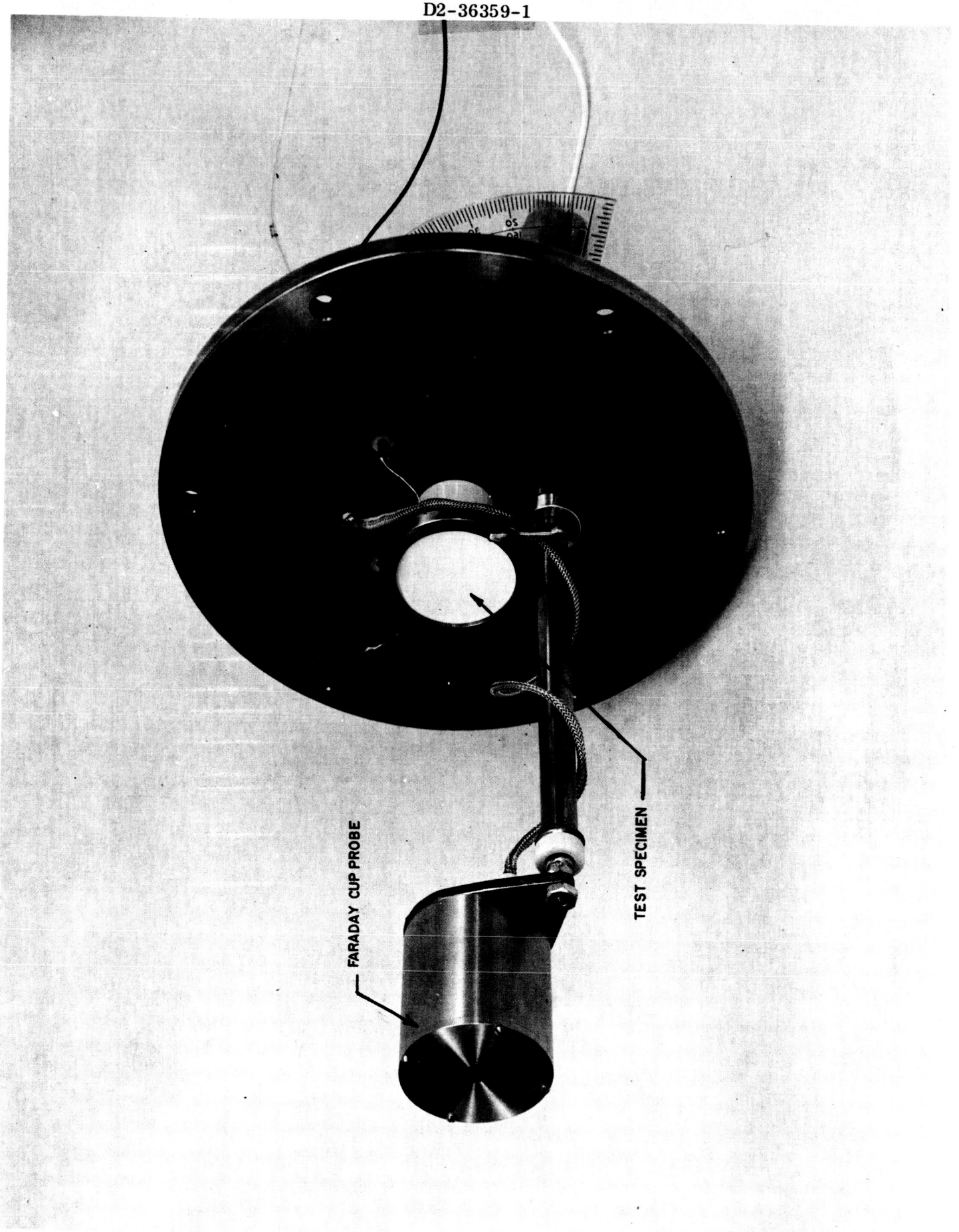
The quartz window was then removed and the specimen holding plate was installed. To accomplish this, the two gate valves were closed and dry nitrogen was bled into the test-end of the beam tube. Subsequent pump-down was done with a mechanical roughing pump and the 6-inch diffusion pump system.

Early in the test program, a movable Faraday cup with a 0.25-inch diameter aperture (Figure 13) was used to scan the beam at the beginning of each run. The purpose of these measurements was to obtain data on the current intensity distribution of the beam. Also, the Faraday cup readings were used to calculate the total beam current as described in Section 2.3.1. When Faraday cup readings were taken, sample current was measured immediately thereafter and the test run was begun. Faraday cup scans were not made in the latter portion of the program.



CALC	RG/CB	3-16-65	REVISED	DATE	CALIBRATION OF SOLAR WIND SIMULATOR PARTICLE ENERGY	FIGURE 12
CHECK						
APR					THE BOEING COMPANY	
APR						PAGE OF

USE FOR TYPEWRITTEN MATERIAL ONLY



TEST SPECIMEN HOLDER FOR SOLAR WIND SIMULATOR FIGURE 13

Throughout the tests, which varied from several minutes to 7 hours, depending on the fluence desired, current readings on the sample were measured with a Kiethley Model 410 Micro-Micro Ammeter. Considerable difficulty was encountered in measuring currents below about 0.5-microamperes due to RF pick-up from the 80-megacycle oscillator on the ion source. Care had to be taken by zeroing the microammeter before each reading. A zero reading was established by momentarily closing the beam-tube gate valve and thereby shutting off the beam. An effective RF shield is being built for the ion source and its power supply for future work with the solar wind simulator.

Test samples were mounted on the sample holder such that their reference arrows pointed vertically. Since many of the samples did not exhibit visible damage, alignment of the sample with the beam was important so that the reflectometer light beam could later be referenced to the irradiated area. This alignment was accomplished by noting the position of the beam on the quartz window and then subsequently locating the center of the specimen at the same position. The maximum displacement of the center of the beam from the center of the beam tube was about 3/16-inches. The position of the beam usually changed when the particle energy was changed.

At the end of a test the two gate valves adjacent to the specimen were closed, and that portion of the system was back-filled with dry nitrogen. The sample was then removed from the solar wind simulator and its reflectance was measured as described in Section 2.6.

2.4.2 High Energy Particle Tests

The sample mounting configurations for the 2.5 Mev proton test and the 5.0 Mev alpha particle test are shown in Figures 14a and 14b, respectively. The sample numbers of the specific samples are shown and correspond to types given in Table 1 of Section 2.3. The un-numbered sample holders did not contain test samples. The circle at the center of the array is the aperture of the fixed Faraday cup from which the direct particle beam was monitored (see Section 2.5.2). The samples were mounted in an array consisting of three circular rings about the beam axis. Charged particles were only scattered to the sample array when the gold scattering foil is inserted into the beam. All samples in a given ring were in angular symmetry with the beam axis and thus were all exposed to the same particle flux. The three rings at scattering angles 4.5, 10.8, and 14.5 degrees each received a different particle flux. Thus the samples in different rings received three different values of fluence covering a range of approximately two orders of magnitude.

To begin the irradiation test in the Dynamitron scattering chamber, the system was evacuated to approximately 1×10^{-6} torr. This vacuum was maintained throughout the test until the samples were removed for reflectance measurements in air. When the required vacuum was attained, the beam was turned on, aligned with the center of the fixed Faraday cup, and appropriate dosimetry measurements

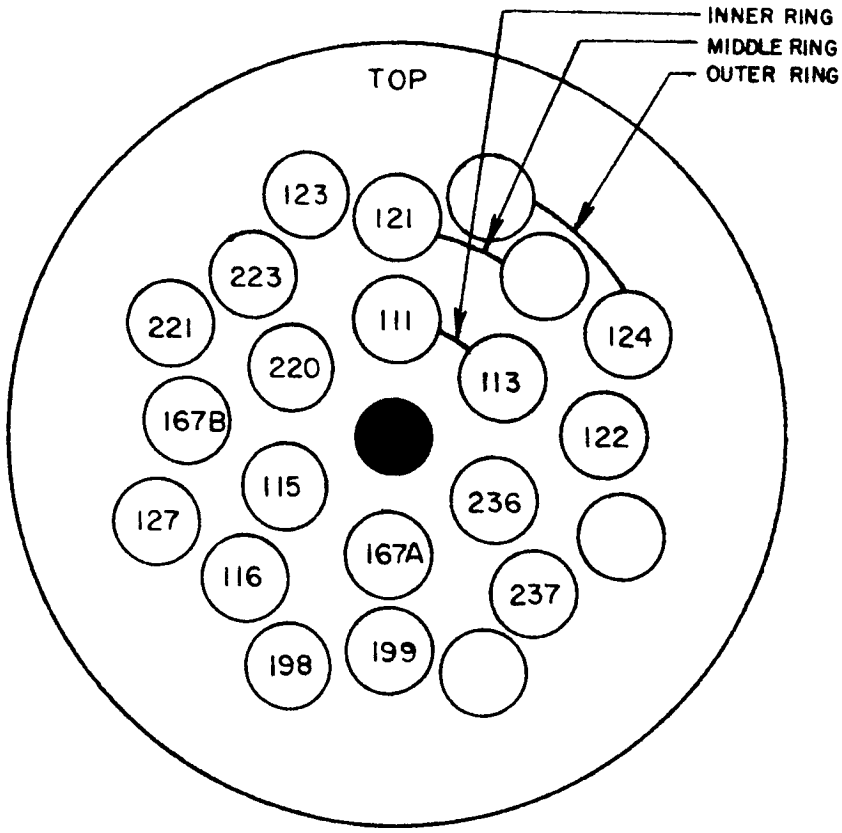


FIGURE 14 a SAMPLE CONFIGURATION FOR 2.5 MEV PROTON TEST

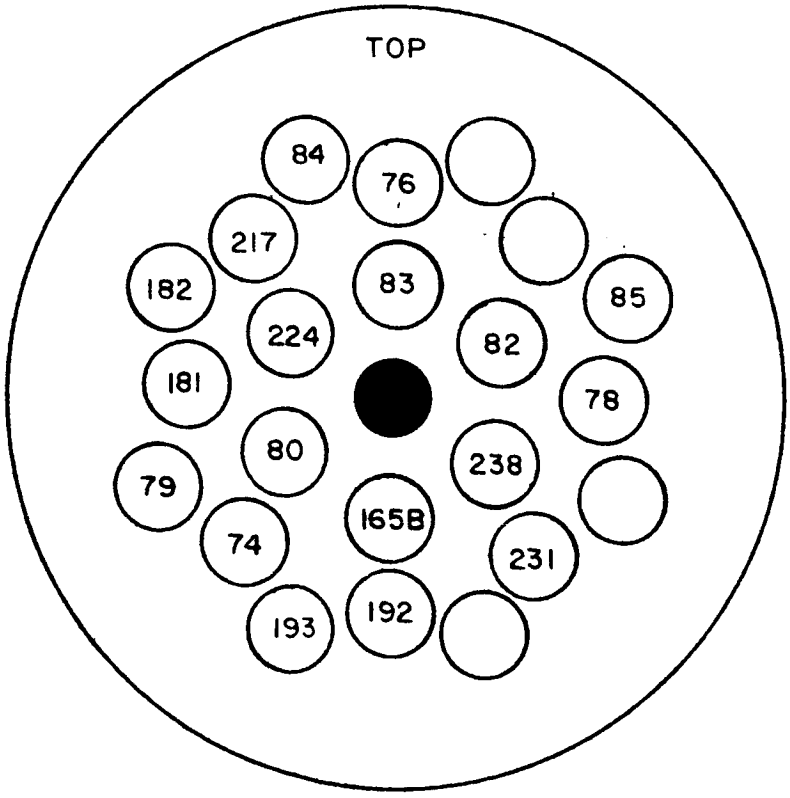


FIGURE 14 b SAMPLE CONFIGURATION FOR 5.0 MEV ALPHA PARTICLE TEST

were performed as described in Section 2.5.2. These preliminary measurements were made without the scattering foil being in the beam so that no sample exposure occurred. When a stable beam was attained, an appropriate magnet current (2-5 amps) was applied to the secondary electron bending coils and high voltage was applied to the gold foil to suppress secondary electrons. Then the scattering foil was inserted into the beam and integration of the portion of current collected in the fixed Faraday cup commenced. Other appropriate dosimetry data was taken from time to time during the test (Section 2.5.2).

The total accelerator operating times for the proton and alpha particle tests were approximately 24 hours each. The runs were continued until sufficient fluences in terms of sample damage thresholds (determined in preliminary pre-contract tests) and the Earth-Mars environment were obtained. Limitations in H^- and He^{++} beam currents prohibited testing to the maximum fluences planned at the beginning of the program.

At the termination of the tests, the chamber was back-filled with dry nitrogen and samples were removed. The samples were transported to the reflectance measuring apparatus (Section 2.6) in a light-protective container. Selected samples were stored in the dark until a later set of measurements, used to assess possible sample annealing, were conducted.

2.5 TEST DOSIMETRY

2.5.1 Low Energy Test Dosimetry

Dosimetry in low energy particle tests included beam spot size and shape measurements, sample current monitoring, exposure rate variations, and particle energy determination.

Beam spot size and shape were visually observed by the fluorescence on a quartz window which was put in place of the sample holder. The beam was centered by adjustment of the current in the bending coils; and the spot size was shaped by variation of the voltage on the focusing lenses 2 and 3 (Figure 6). Variations in spot size from circular to elliptical (±10 percent deviation from circular) were possible. The actual spot size, when properly adjusted, was measured directly off the quartz window. The area of the spot was used to determine the flux (protons/sq.cm.-sec), to verify that current monitored off of the sample was truly representative of exposure intensity, and to be sure that the sample was evenly irradiated.

Beam current for fluence determination was monitored continuously with a Kiethley 410 Micro-Micro Ammeter by direct current pickup off of the samples. A movable Faraday cup probe (Figure 13) of 0.292 sq.cm. aperture was used to check the validity of the direct sample current integration method as well as the beam uniformity. The Faraday probe was rotated across the sample position.

Measurements were made at various probe rotation angles as shown in Figure 15a. These angles were correlated with radial distance from the center of the beam spot. A typical 2-Kev proton beam profile as measured by this technique is shown in Figure 15b. The Faraday probe readings, in general, indicated a beam uniformity of ±5 percent across a 3/4-inch diameter circle (the maximum width of the reflectometer light beam). The current per sq. cm. (I_r) as a function of radial position was integrated over the beam spot radial position as follows, to obtain the total current:

$$I_{Tot} = 2 \int_{o}^{r} I_r r \, dr$$

The total current calculated was compared with that actually collected on the samples. From this method, correction values were obtained for the back-scattering of electrons off of the aluminum samples.

Exposure rates, in general, were kept at a low level to avoid radiation heating. Samples were irradiated to the same fluences (particles/sq.cm.) but at different fluxes. For the majority of the Kev-energy tests, charged particle exposure rates varied from 1×10^{11} to 5×10^{12} particles/sq.cm.-sec. Four tests were run at about 1×10^{13} protons/sq.cm.-sec. in which heating could have occurred (sample Nos. 39, 42, 161B and 162B).

The particle energy separation system was calibrated by measurement of bucking potentials. The bucking-voltage method consisted of applying a high positive potential to the sample holder to suppress the collection of positively charged particles. A typical curve representing collected beam current versus the voltage applied to the sample holder is shown in Figure 16. Curves such as this provided data on saturation voltages as a function of magnet current and resulted in the dashed curve of Figure 12.

A cross check for energy calibration consisted of measurements of the magnet current needed to bend particles for selected voltages on the ion probe and extractor electrodes. A family of extractor voltage curves was obtained as shown in Figure 17. For each extractor voltage a series of probe current values (using a 10-megohm resistor) were selected. The current through the bending solenoid was adjusted for each of the series of selected probe currents (down to 0.1 milliamp) so that the beam spot was always centered on the quartz viewing window. From the extrapolation of the data of Figure 17 to zero probe current, particle energy as a function of magnet current was obtained. The results of this method are also shown in Figure 12 for both the RF ion source and a Radiation Dynamics, Inc., (RDI) ion source. The results of this method are in quite good agreement with the bucking potential method. Calculation of particle energy versus bending current was also made from measurements of the magnetic field by a gauss meter. The data from calculations are also shown in Figure 12. The agreement with the more precise methods discussed is quite good considering the nonuniformity of the bending field. The solid curve was actually used for determination of particle energy in the tests.

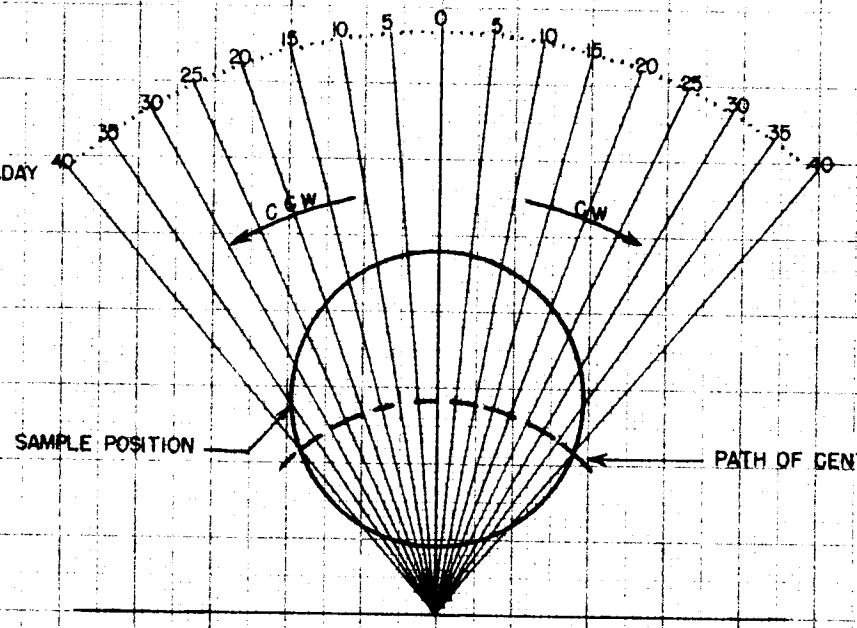


FIGURE 15a FARADAY PROBE TRAJECTORY

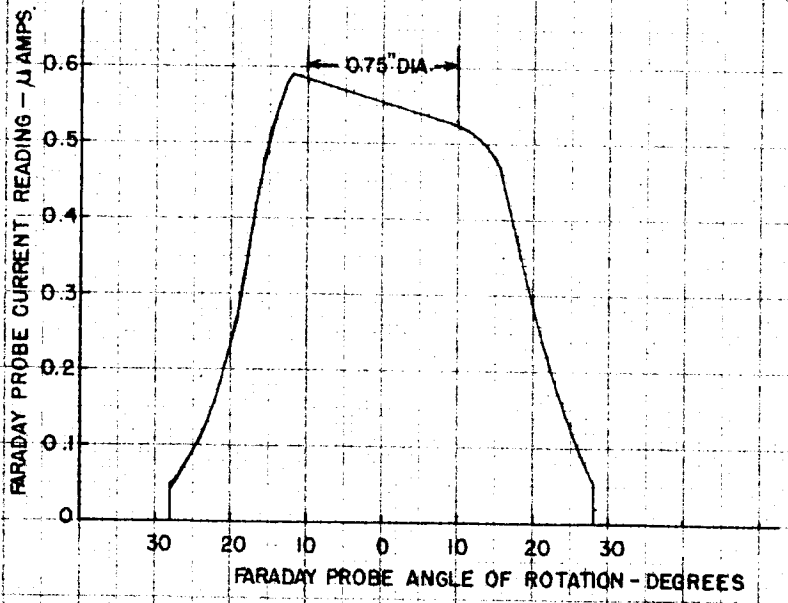


FIGURE 15b BEAM PROFILE AS MEASURED BY THE FARADAY PROBE

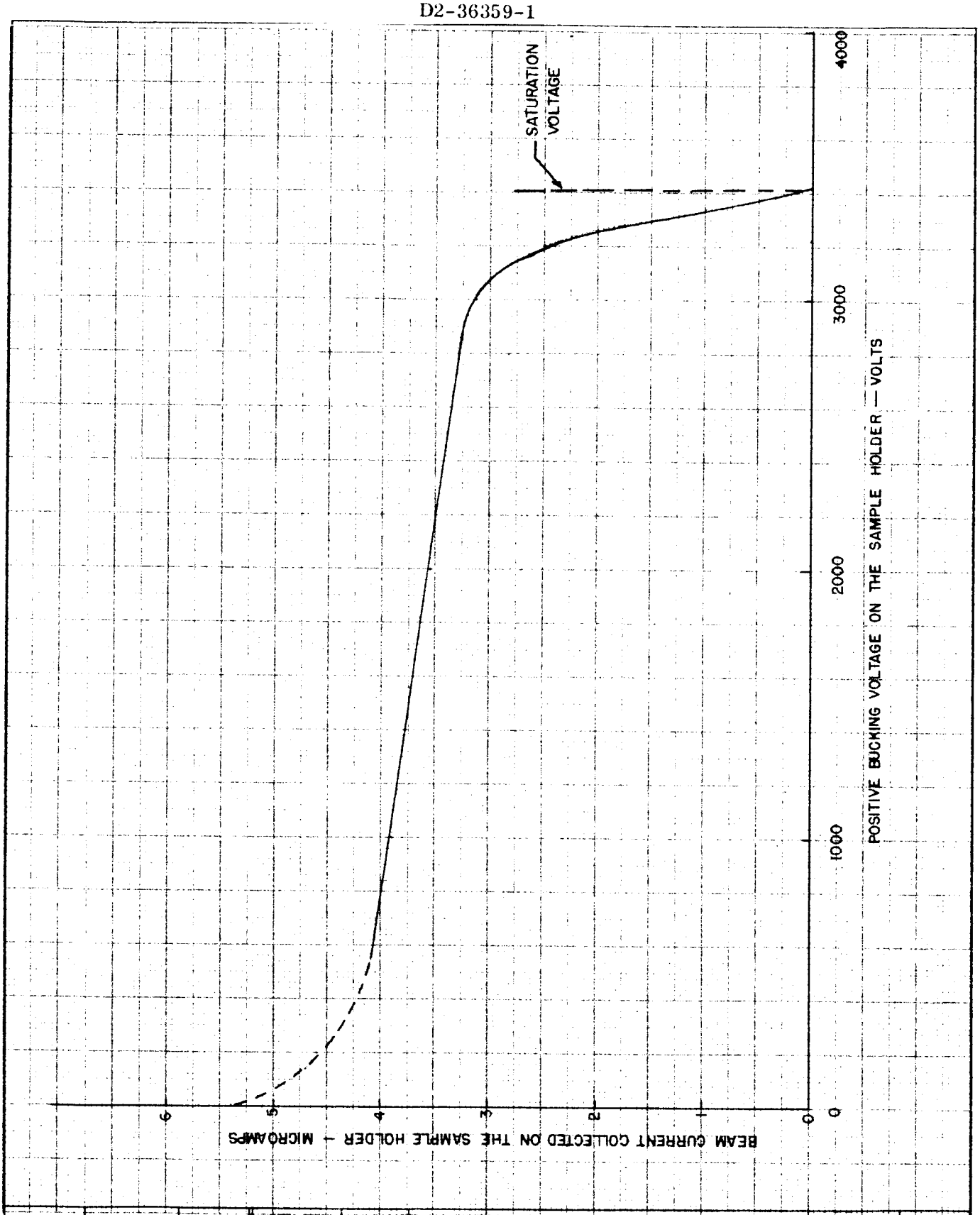
	INITIALS	DATE	REV BY INITIALS	DATE	TITLE	MODEL
CALC						
CHECK						
APPD.						
APPD.						

U3 4013 8000 REV. 12-64

REV LTR

BOEING NO 29

SH



	INITIALS	DATE	REV BY INITIALS	DATE	TITLE	MODEL
CALC	RB/CB	5-6-65			BUCKING-VOLTAGE ENERGY CALIBRATION CURVE	FIG. 16
CHECK						
APPD.						
APPD						

U3 4013 8000 REV. 12-64

REV LTR

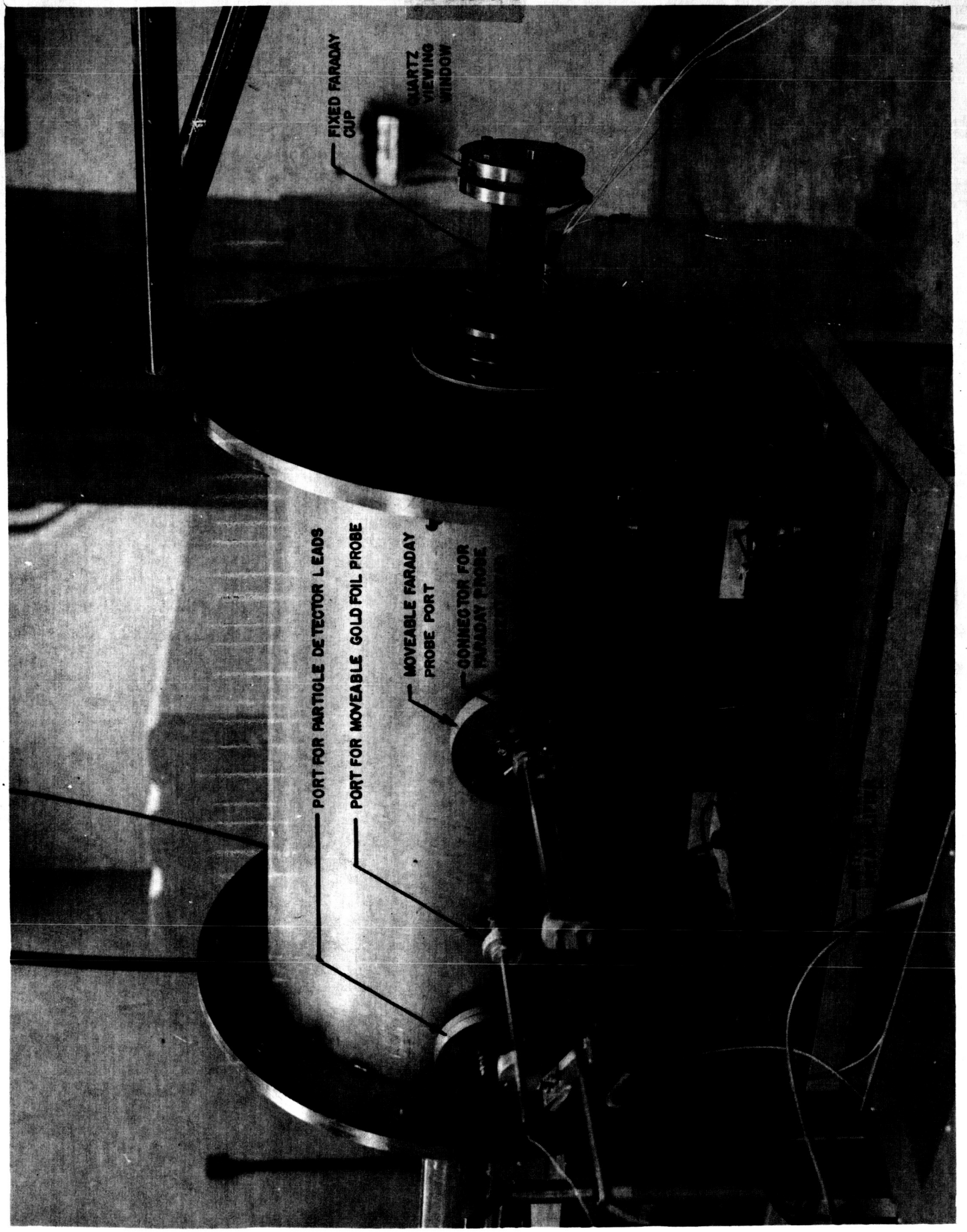
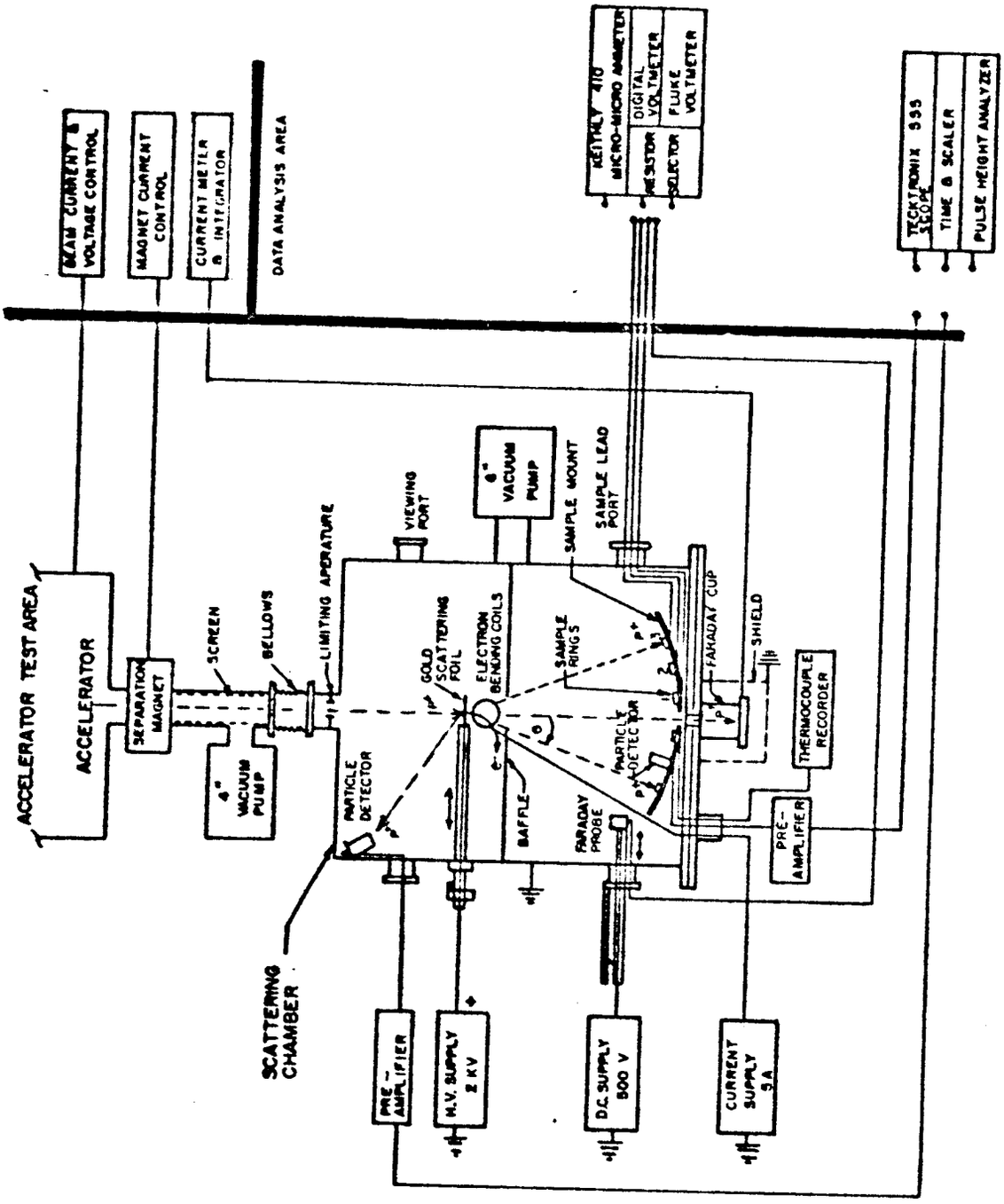


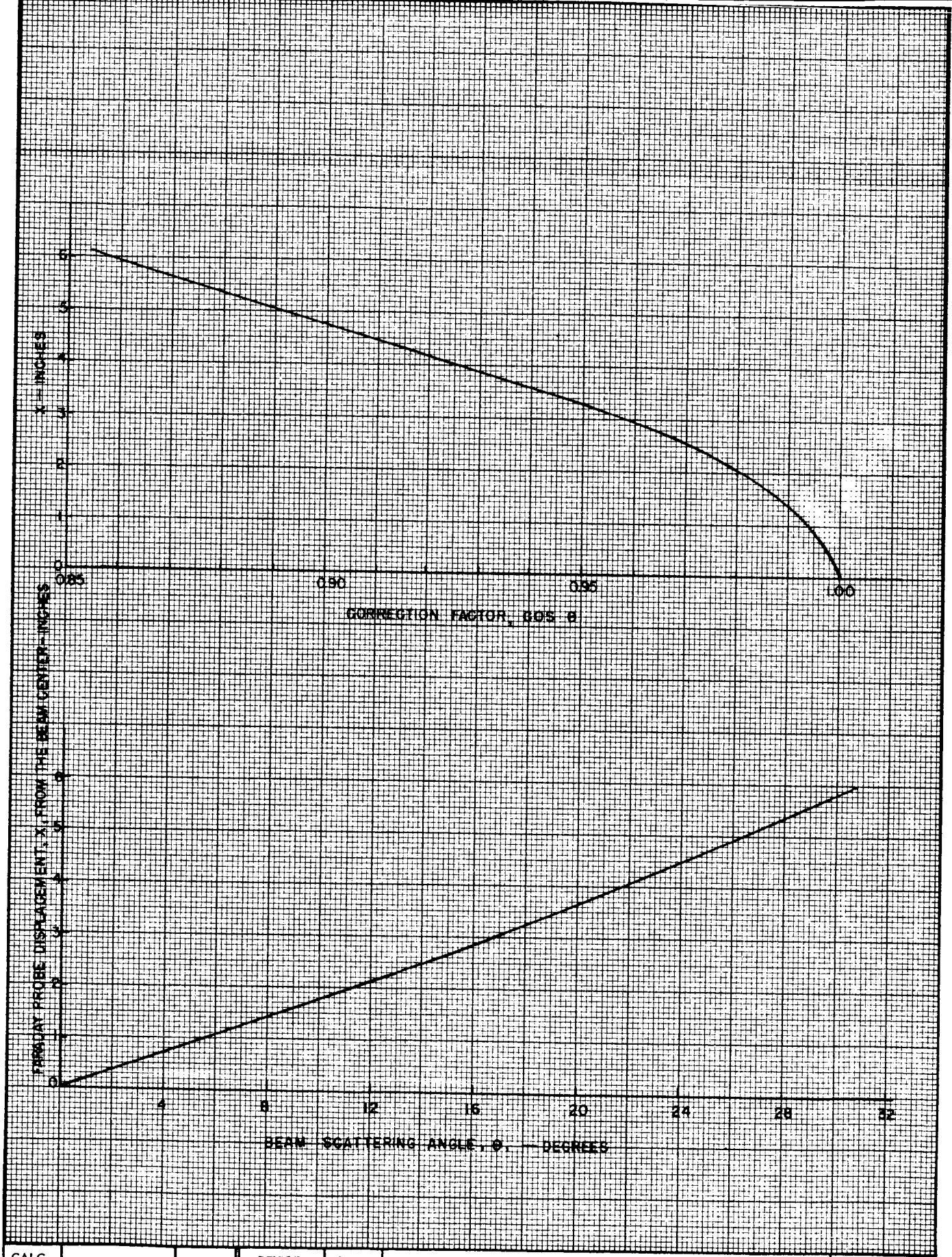
FIGURE 18

DOSIMETRY EQUIPMENT MOUNTED ON THE SCATTERING CHAMBER



SCHEMATIC OF DYNAMITRON TEST INSTRUMENTATION FIGURE 19

USE FOR TYPEWRITTEN MATERIAL ONLY



CALC			REVISED	DATE	POSITIONING AND CORRECTION CURVE FOR THE FARADAY PROBE
CHECK					
APR					FIG. 20
APR					
					THE BOEING COMPANY

PAGE 36

U3 4013 8000

K+E ALBANENE TRACING PAPER 703:7

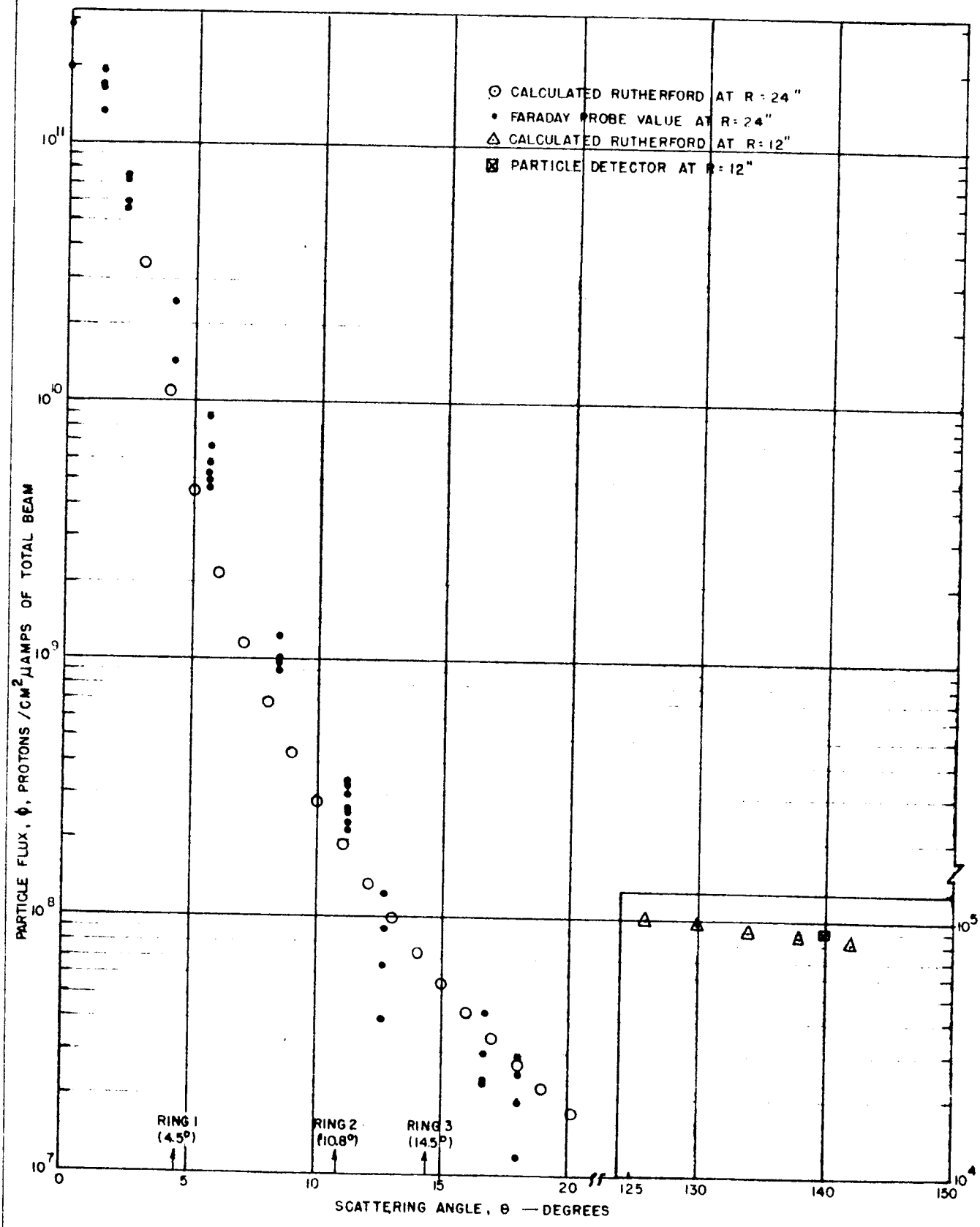
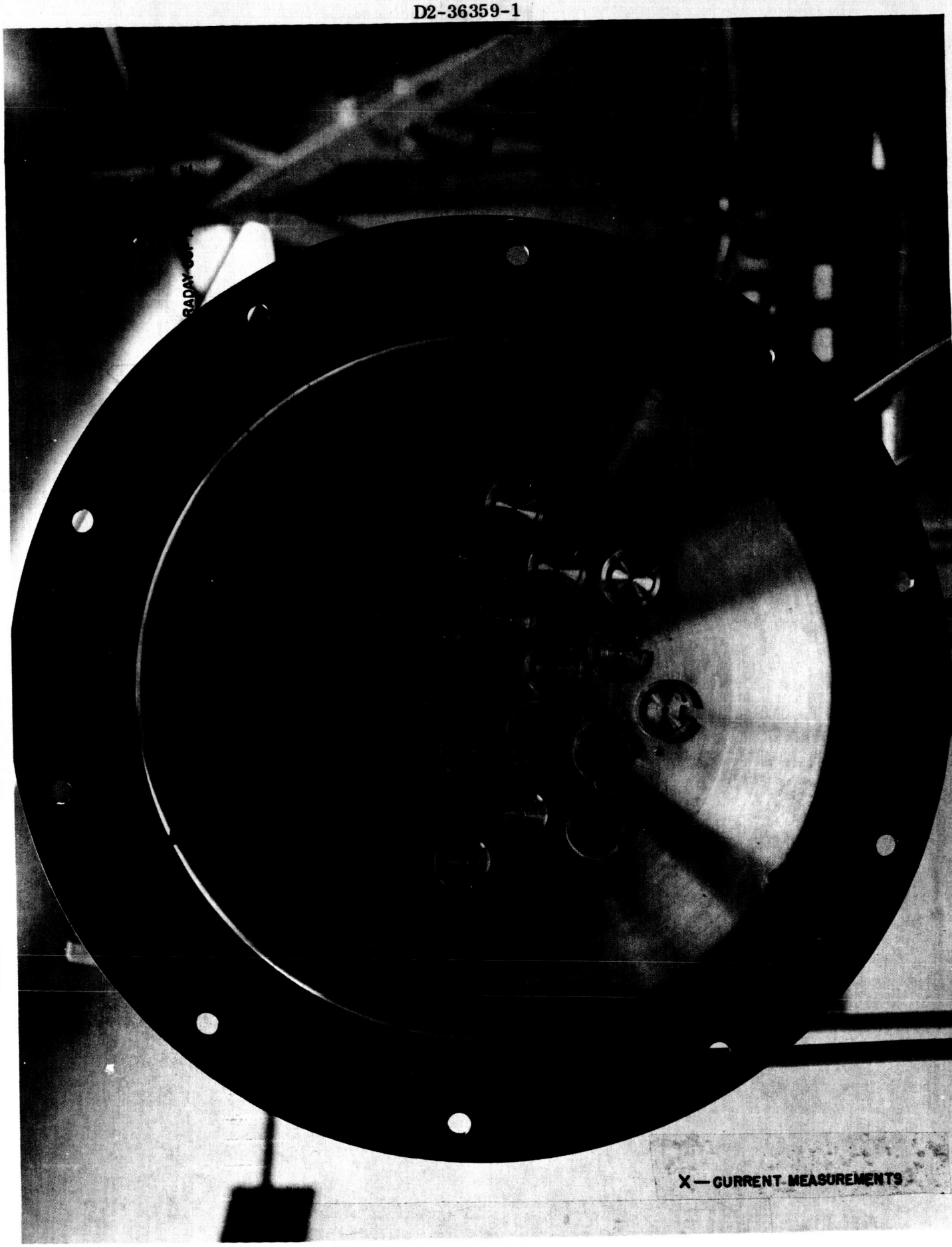


FIGURE 21 2.5 MEV SCATTERED— PROTON FLUX

USE FOR TYPEWRITTEN MATERIAL ONLY



SCATTERING CHAMBER SPECIMEN HOLDER

FIGURE 22

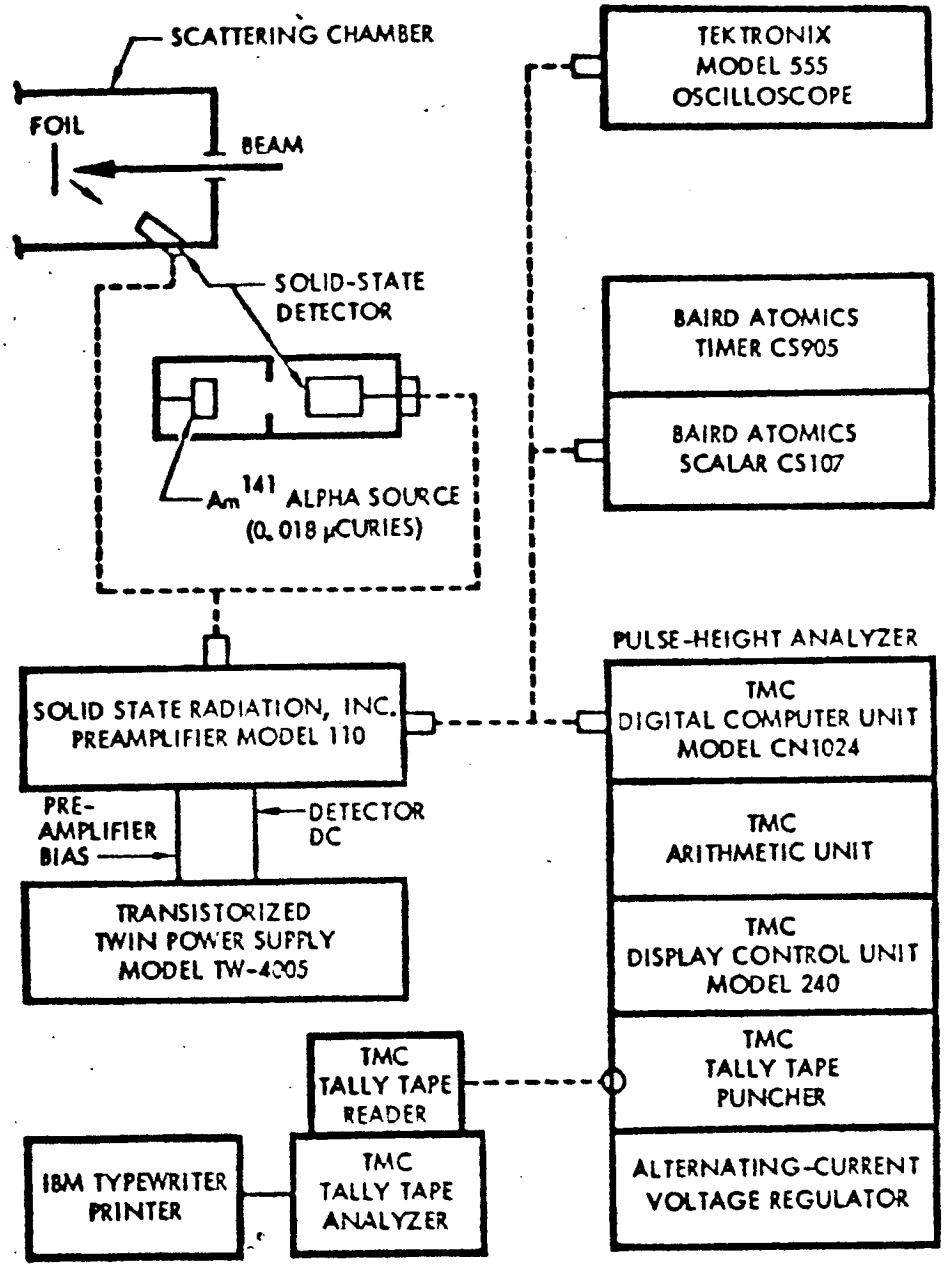
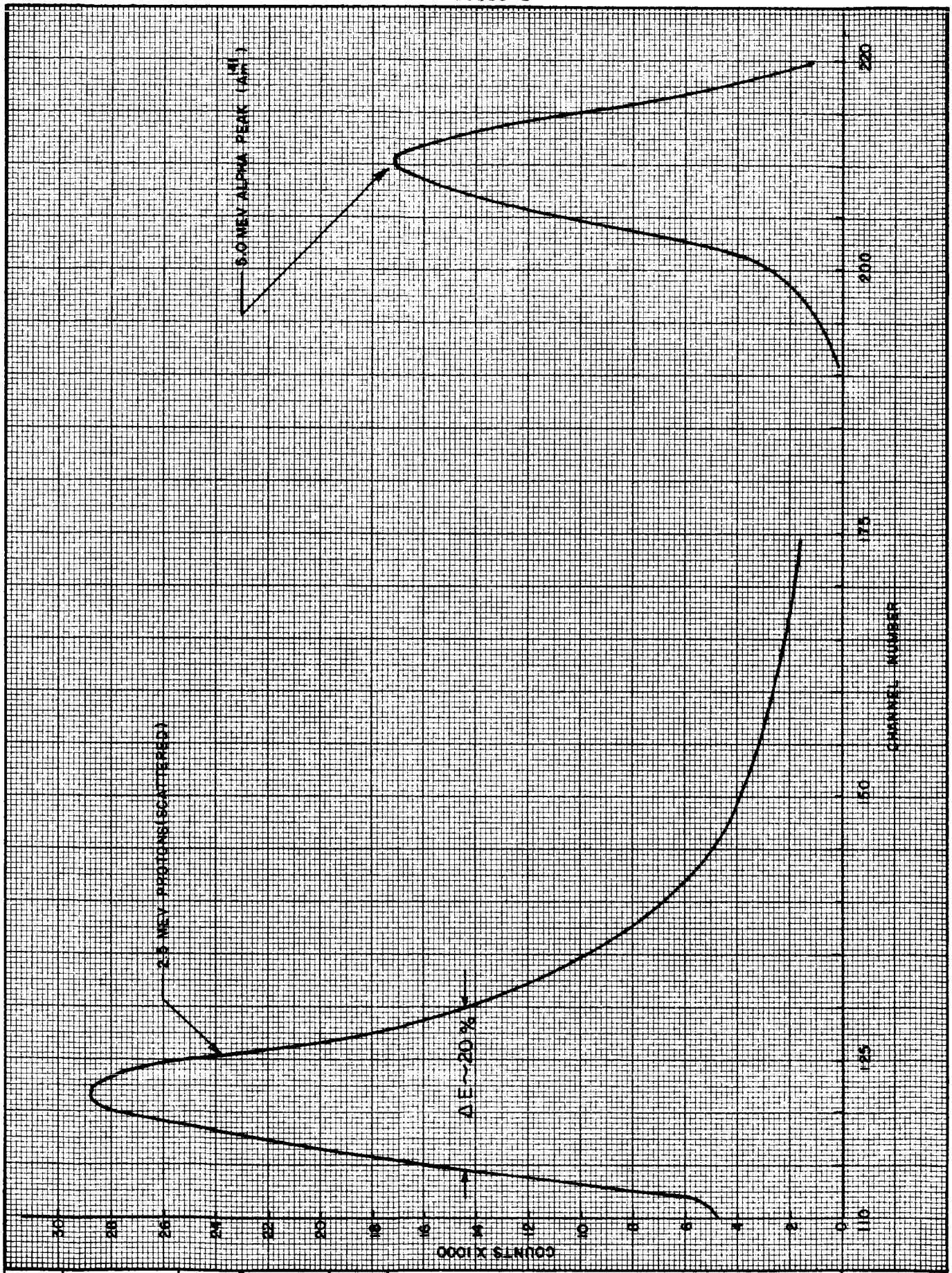


Figure 23- Particle Detection and Analysis

USE FOR TYPEWRITTEN MATERIAL ONLY



CALC			REVISED	DATE	PARTICLE ENERGY RESOLUTION	
CHECK						FIG. 24
APR						
APR					THE BOEING COMPANY	PAGE 40

K+E ALBANENE® TRACING PAPER 70317

2.6 ANALYSIS PROCEDURES

2.6.1 Reflectance Measurements

Three different instruments were used for reflectance measurements: (1) A Beckman DK-2A spectrophotometer utilizing an integrating sphere attachment for measurements in the 0.25 to 2.5 micron wavelength region; (2) a Perkin-Elmer Model 99 spectrophotometer utilizing a Gier-Dunkle integrating sphere attachment for measurements in the 0.3 to 2.0 micron region; and (3) a Beckman IR-4 spectrophotometer utilizing a heated hohlraum attachment for measurements in the 1 to 15 micron region. The majority of the measurements performed in the contract were made with the Beckman DK-2A reflectometer.

2.6.1.1 Specimen Orientation — It was recognized early in the program that oriented surface roughness such as roll marks on specularly reflecting samples, could cause erroneous reflectance readings in the DK-2A reflectometer. Therefore, an orientation arrow was scribed on the back side of each specimen. The direction of this arrow was made parallel to the direction of the roll marks. The orientation arrow was used both to locate the samples during irradiation and to orient them in the integrating sphere. During reflectance measurements, the samples were oriented such that the arrow pointed upward toward the detector. It was found that variations in reflectance of about ±2 percent could be obtained by rotating the sample in the port of the integrating sphere. This measurement justified the need for orienting all of the specularly reflecting samples in the same direction.

2.6.1.2 Pre-Irradiation Measurements — At the beginning of the program, the total-hemispherical, spectral reflectance of approximately one-fourth of all the different types of samples was measured with the DK-2A reflectometer. These data provided an indication of the variation in reflectance between similar samples, and was used for calculation of solar absorptances of the unirradiated samples. These measurements were made using a smoked, magnesium oxide coating as a reference surface. The reflectance of a National Bureau of Standards Vitrolite tile was recorded on each chart along with the data from the test samples. The Vitrolite tile data was required for calculation of solar absorptance. It should be pointed out that total hemispherical reflectance measurements in the DK-2A are made at an angle of 5 degrees from normal, and diffuse reflectances are measured normally. Specular reflectance can be calculated by subtracting the diffuse reflectance from the total hemispherical reflectance.

A study was made to determine whether day-to-day variations in spectral reflectance on a given sample would be greater than the variation from one sample to another. The answer to this question was of interest because it determined whether the reflectance of a sample should be measured before and after

irradiation (on different days) or could be measured relative to a similar control sample as will be discussed later. The spectral reflectance of sample No. 10 was measured on five different days using the same magnesium oxide reference. It was found that the measured spectral reflectance in the 0.4 to 2.6 micron wavelength region varied by about ±1 percent. The reflectance variation in the wavelength region from 0.25 to 0.4 microns was about ±0.5 percent. Comparing these variations to the reflectance deviations measured from one sample to another (given in Section 2.3.1), it can be seen that the variation in the long wavelength region is comparable. However, the variation in the short wavelength region is less when the same sample is measured from day to day. It was concluded from this study that the change in reflectance data would be more accurate if the reflectance of each sample was measured before and after irradiation. (This conclusion was not ultimately followed due to other considerations as will be discussed in Section 2.6.1.3.)

Pre-irradiation reflectance measurements were also performed with the Gier-Dunkle reflectometer on selected samples of low-emittance anodic coatings, high-emittance anodic coatings, and vapor deposited aluminum coatings. The total hemispherical spectral reflectances were measured at angles of 12, 22, and 62 degrees from normal. The primary purpose of these measurements was to obtain absolute reflectance data on specularly reflecting samples as a function of angle of incidence, particularly at 60 degrees from normal (the operating condition of the V-ridge solar cell concentrating panel). These data are later compared to post-irradiation reflectance values for irradiated samples. A secondary purpose for making the Gier-Dunkle reflectance measurements on the barrier layer coatings was to obtain more accurate values of their solar reflectance for solar cell panel design calculations.

Infrared reflectance measurements were made on selected test samples from each type of coating (except vapor deposited aluminum) with the IR-4 reflectometer. These measurements represent normal reflectance from a diffusely illuminated sample. A heated Hohlraum supplies the diffuse illumination to the sample. The purposes of the infrared reflectance measurements were to determine possible radiation effects on emittance and changes in molecular bonds.

2.6.1.3 Post-Irradiation Measurements — The majority of the post-irradiation reflectance measurements were made with the DK-2A reflectometer. Two different techniques were used for the DK-2A measurements. In the first technique, used on the low emittance anodic coatings, the vapor deposited aluminum coatings, and the chemically brightened aluminum coatings, the spectral reflectance of a given sample was measured relative to the reflectance of a control sample of the same material. Thus, the recorded reflectance data was a direct measurement of the percentage difference in reflectance between the irradiated and unirradiated samples. This method of recording the data was selected because the change in reflectance as a function of wavelength could be recorded directly on the DK-2A reflectometer charts. This simplified

data reduction procedures, and allowed direct tracing of the DK-2A charts for use in the final report. It should be pointed out that this relative reflectance measurement technique could only be used under the following conditions: (1) batches of samples that had similar (within ±2 percent) spectral reflectance values; and (2) control samples having absolute spectral reflectances of about 40 percent or greater. The latter condition was established because the amount of reference energy available for the detector was too small at low reflectances.

A typical example of a change-in-reflectance (Δ R) plot is shown in Figure C6 in Appendix C. The solid curve represents the variation in reflectance between two control samples, in this case, No.'s 104 and 99 as shown in the title block. The nomenclature, "Control Sample No. 104 vs No. 99," means that sample No. 104 was placed in the measurement port of the integrating sphere, and No. 99 was placed in the reference port. Control sample curves are shown on a large number of the charts to indicate the statistical variation between unirradiated samples. Control samples numbers were chosen as close to the irradiated sample numbers as possible to get maximum similarity between the two. Reflectance changes noted for an irradiated sample must then be larger than the statistical deviation between control samples to be significant. The dashed curve represents the percent difference in reflectance between the irradiated sample No. 109 and control No. 99. To generate the dashed curve, sample No. 109 was placed in the measurement port of the integrating sphere and No. 99 was placed in the reference port.

In the second technique for measuring reflectance with the DK-2A reflectometer, used on the S-13, Z-93 and high-emittance barrier layer coatings, the spectral reflectance of each irradiated sample was measured relative to a magnesium oxide reference by conventional techniques. Included on the same DK-2A chart were plots of the spectral reflectance of an NBS-calibrated Vitrolite tile and a control sample. The Vitrolite tile data was used to calculate the absolute reflectance of the samples. The reflectances of both the irradiated and control samples were placed on the same chart so that the change in reflectance could be scaled directly from the curves without correcting each curve to absolute reflectance. A typical example of a reflectance data sheet for this technique is shown in Figure C37 in Appendix C. Note that the ordinate scale represents relative reflectance in percent. As discussed above, this reflectance is relative to the magnesium oxide reference specimen and thus can exceed 100 percent on the scale. To expedite data reduction and to present the best reproduction of the change in spectral reflectance, the curves shown in Figure C37 were traced directly from the DK-2A chart.

The post irradiation measurements performed with the Gier-Dunkle and IR-4 reflectometers were accomplished similarly to those discussed in the previous section on Pre-Irradiation Measurements.

2.6.2 Calculation of Solar Absorptance and Emittance

2.6.2.1 Solar Absorptance — The solar absorptances of selected control samples of each type of coating were calculated from the DK-2A and Gier-Dunkle spectral reflectance data. The analysis of DK-2A reflectance data is discussed first. Solar absorptances of white paint coatings were calculated from DK-2A reflectance data. Since DK-2A reflectance data were measured relative to a magnesium oxide reference, corrections had to be made for the absolute reflectance of magnesium oxide. The first step in the calculation of solar absorptance was to correct the measured spectral reflectance data for the actual reflectance of the magnesium oxide reference being used. The following equation was used for correcting the measured reflectance (R_m) to absolute reflectance (R):

$$R = \frac{(R_m)(R_2)(R_3)}{(R_1)} \qquad (1)$$

where R_m = measured spectral reflectance of sample

R_1 = measured spectral reflectance of NBS Vitrolite tile standard No. V6-B203

R_2 = published spectral reflectance of the NBS Vitrolite tile, relative to the reflectance of a freshly deposited magnesium oxide reference

R_3 = published spectral reflectance of a freshly deposited magnesium oxide surface.

The Vitrolite tile data is included in the equation to account for the difference in reflectance between the actual magnesium oxide surface used and a freshly deposited surface.

Absolute spectral reflectances were calculated from Equation 1, for thirty different wavelengths in the solar wavelength region. The wavelength intervals chosen represented equal energy increments for the solar spectrum in space (Johnson spectrum, Reference 7). The spectral reflectances calculated for the equal energy increments were then summed and divided by thirty to obtain an integrated solar reflectance (R_S). The solar absorptance (α_S) was obtained from the solar reflectance by the following relation:

$$\alpha_S = 1 - R_S$$

The bulk of the analyses with DK-2A reflectance data involved calculation of the change in solar absorptance. A simpler technique was used for the change-in-solar-absorptance ($\Delta\alpha_S$ or ΔR_S) calculations. The difference in spectral reflectance (ΔR) between a control sample and an irradiated sample was plotted on a graph such as the one shown in Figure 25. This technique, discussed in

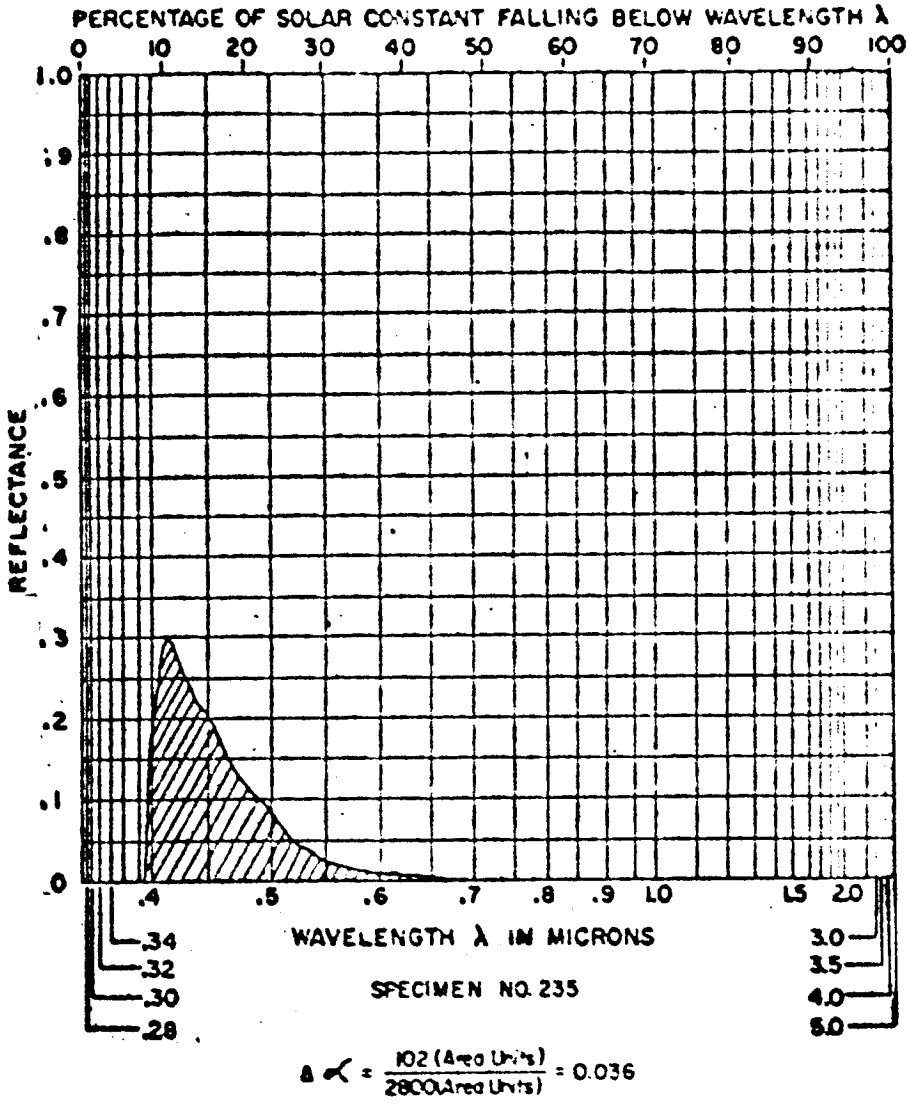


FIGURE 25 SAMPLE CALCULATION SHEET FOR OBTAINING THE CHANGE IN SOLAR ABSORPTANCE ($\Delta\alpha$)

USE FOR TYPEWRITTEN MATERIAL ONLY

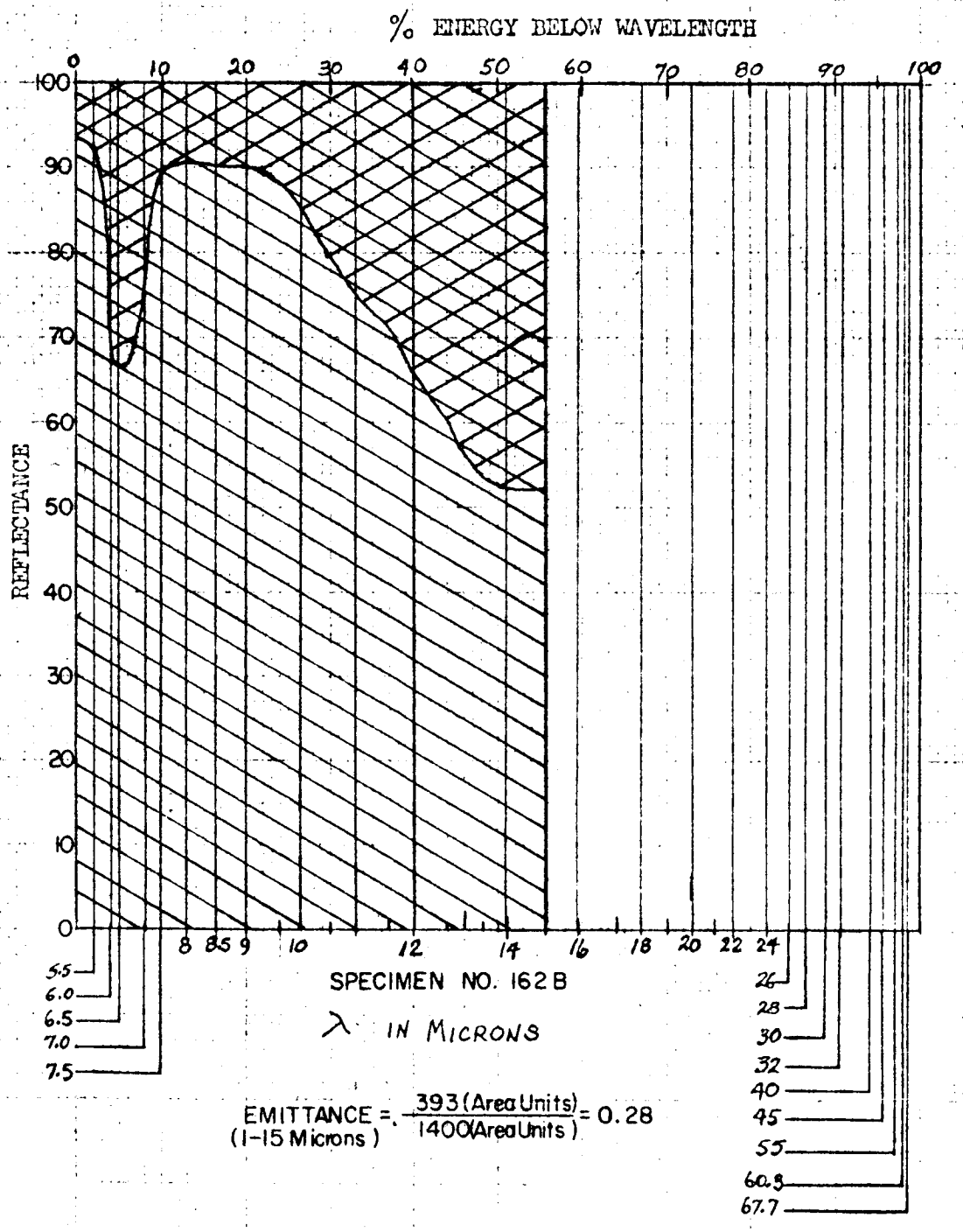
Reference 8, utilizes a plot of the Johnson solar spectrum on a distorted-wavelength/equal-energy-increment abscissa scale. The ordinate is divided into 100 divisions for plotting the reflectance (or change in reflectance) values as a function of wavelength. The change in solar absorptance or solar reflectance is determined by integrating the shaded area and dividing it by the total area of the graph. A planimeter was used for integration of the areas.

Solar absorptances were calculated from Gier-Dunkle reflectance data by plotting the absolute reflectance data on a graphical plot such as the one shown in Figure 25. The ratio of the integrated area above the reflectance curve to the total area of the graph represents the solar absorptance. Similarly, the ratio of the integrated area below the reflectance curve to the total area is solar reflectance.

2.6.2.2 Emittance — The emittances of samples were calculated from the IR-4 infrared reflectance data by a graphical integration technique similar to the one used for calculating solar absorptance from the Gier-Dunkle data. A graph of a 22°C black-body emission spectrum was prepared. A typical example of this graph and a sample emittance calculation for sample No. 162B are shown in Figure 26. The infrared reflectance data was plotted in the wavelength region of 1 to 15 microns. The ratio of the crosshatched area above the reflectance curve to the total area of the graph at wavelengths less than 15 microns represents the emittance of the sample. It should be pointed out that since the infrared reflectance was only measured out to 15 microns, and because about 45 percent of the energy in a 22°C black-body spectrum is at wavelengths longer than 15 microns, the emittances calculated only represent the emittance in the 1 to 15 micron region. Therefore, these calculated emittances do not represent the total thermal emittance of the surfaces. They do, however, provide a satisfactory method of showing radiation effects on emittance.

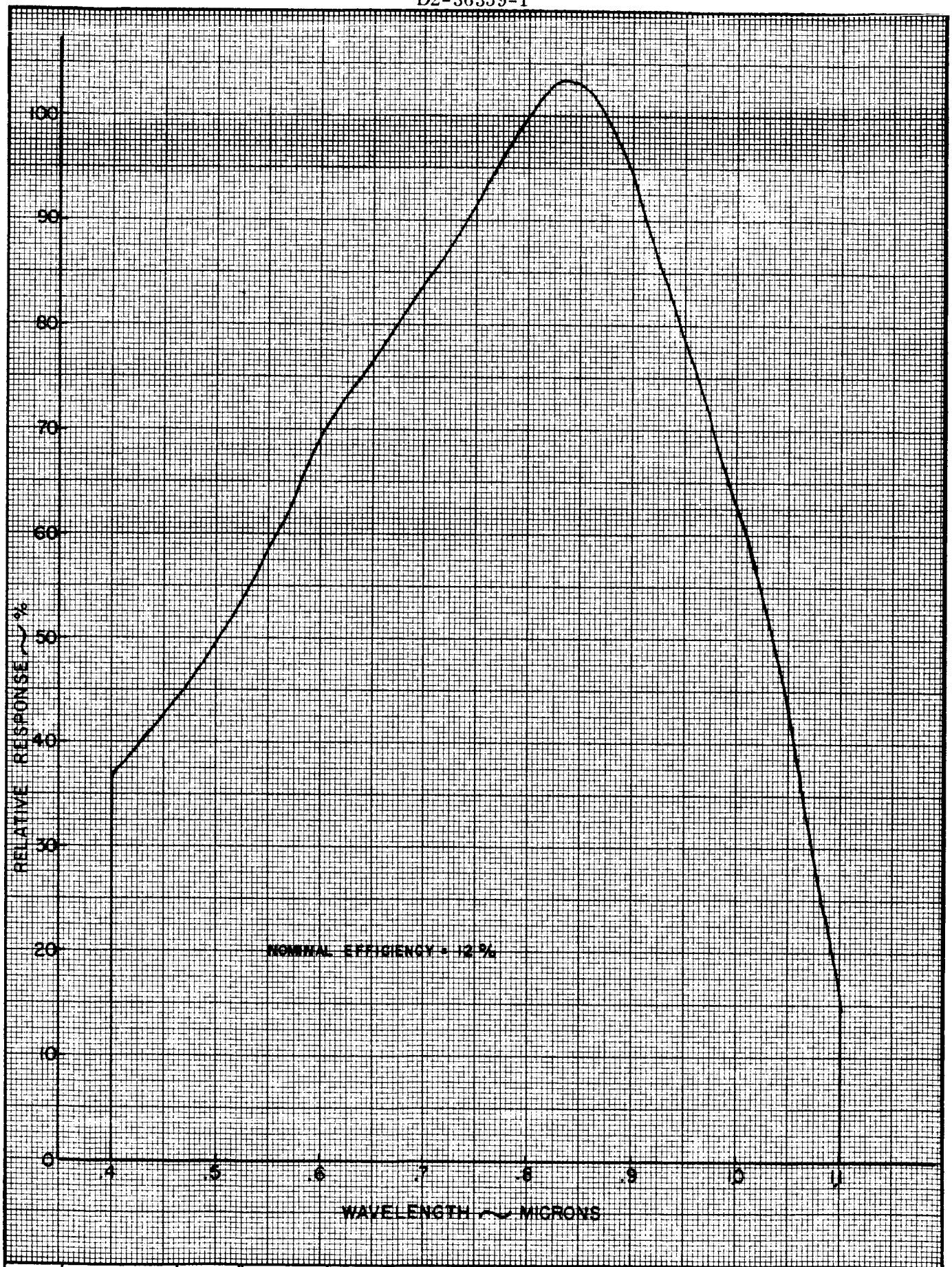
2.6.3 Calculation of Effect of Reflectance Changes on Solar Cell Panel Output

A calculation was made to estimate the percentage change in short-circuit current output of a concentrating solar cell panel due to radiation-effects changes in reflectance of the reflective surfaces. These calculations were performed assuming low-emittance barrier layer anodic coatings on the reflective surfaces. Reflectance data for various angles of light incidence on the reflectors, measured with both the DK-2A and Gier-Dunkle reflectometers, was used in the analysis. The type of solar cells assumed for the calculations was Hoffman n-on-p, 12 percent efficiency cells. This type of cell was chosen as a typical production solar cell being used on solar cell panels. The spectral response of special test cell No. 132 was used in the calculations. The spectral response, measured in the Boeing Solar Power Laboratory, is shown in Figure 27. A schematic drawing of a concentrating solar cell panel is shown in Figure 28.



$$\text{EMITTANCE } (1\text{-}15 \text{ Microns}) = \frac{393 \text{ (Area Units)}}{1400 \text{ (Area Units)}} = 0.28$$

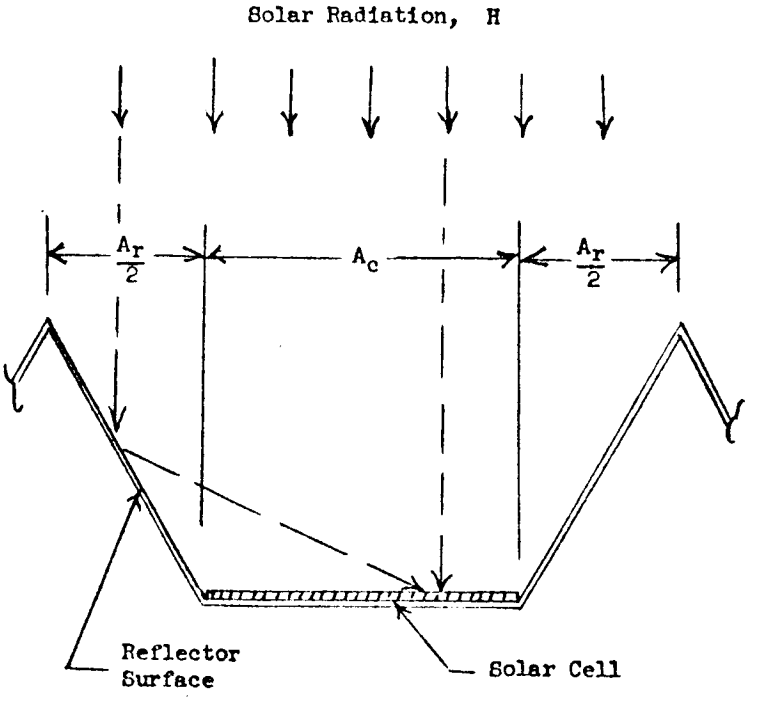
CALC			REVISED	DATE	ENERGY-WAVELENGTH PLOT FOR 22°C BLACK-BODY SPECTRUM	FIG. 26
CHECK						
APPD.						
APPD.					THE BOEING COMPANY SEATTLE 24, WASHINGTON	PAGE 47



CALC			REVISED	DATE	SPECTRAL RESPONSE OF N ON P HOFFMAN SOLAR CELL NO. 132	FIG. 27
CHECK						
APR						
APR					THE BOEING COMPANY	PAGE 48

US 4013 8000

K+E ALBANENE® TRACING PAPER 70737



CROSS SECTION OF V-RIDGE SOLAR CELL CONCENTRATOR PANEL

Fig. 28

USE FOR TYPEWRITTEN MATERIAL ONLY

The percentage change in short circuit current output (Δ I) of a concentrating panel was calculated by the following equation:

$$\Delta I = \frac{\text{(Change in current output)}}{\text{(Initial current output)}} \times 100$$

$$= \frac{\text{(Current change due to reflectance loss)}}{\left(\begin{matrix}\text{Current due to}\\ \text{reflected light}\end{matrix}\right) + \left(\begin{matrix}\text{Current due to direct}\\ \text{incidence sunlight}\end{matrix}\right)} \times 100$$

$$\Delta I = \frac{A_r \int_{.4}^{1.1} (H_\lambda)(\Delta R_\lambda)(I_\lambda)\, d\lambda}{A_r \int_{.4}^{1.1} (H_\lambda)(R_\lambda)(I_\lambda)\, d_\lambda + A_c \int_{.4}^{1.1} (H_\lambda)(I_\lambda)\, d_\lambda} \times 100 \quad (2)$$

where A_r = fraction of energy striking reflector surfaces (0.6)

A_c = fraction of energy striking solar cell surfaces (0.4)

λ = wavelength, microns

H_λ = spectral intensity of Johnson solar spectrum

R_λ = spectral reflectance of reflector surfaces

I_λ = spectral short circuit current response of solar cells

The limits of Equation 2 are established by the spectral response range of the silicon solar cell (0.4 to 1.1 microns). Graphical plots of the three integral functions versus wavelength were prepared and integrated with a planimeter. An example calculation using Equation 2 for reflectance data on sample No. 42 is given below.

$$\Delta I = \frac{(0.60)(413)}{(0.60)(2995) + (0.4)(3892)} \times 100$$

(Integral values shown are simply area units from planimeter readings.)

$$= \frac{248}{1798 + 1557} \times 100$$

$\Delta I = \underline{7.4}$ percent

2.7 TEST RESULTS

A summary of all tests conducted in the contract is given in Table 2. Particle type, particle energy, sample type, and the numbers of samples tested are shown in the table. A more detailed list of sample numbers, specific test conditions, and thermal property measurements is given in Appendix D. As shown in Table 2, low energy proton tests ranged in energy from 1.0 to 9.3 Kev and low energy alpha particle tests ranged from 2.2 to 16 Kev. The large variety of low energy proton energies used is primarily due to lack of calibration of particle energy early in the program. Subsequent corrections to particle energies were made when calibration data was obtained. The high energy particle tests consisted of 2.5 Mev protons and 5.0 Mev alpha particles. The original objective of the contract was essentially accomplished because it was originally planned to run proton energies of 1 to 8 Kev and 2.5 Mev, and alpha particle energies of 2 to 16 Kev and 5.0 Mev. The only significant deviations from the test plan were: (1) the fluences in the Mev experiments were not as large as planned; and (2) in low energy proton and alpha particle tests, low-emittance anodic coatings were exposed to fluences approximately one order of magnitude higher than originally planned. The reduction in Mev-particle fluences was due to beam current limitations in the Dynamitron. The change in Kev-particle fluences, as mutually agreed upon by JPL and Boeing, consisted of adding several test runs at 1×10^{17} protons/sq.cm. and at 1×10^{16} alphas/sq.cm., and eliminating all planned runs at 1×10^{14} protons/sq.cm. and 1×10^{13} alphas/sq.cm. This decision was made in an effort to get data on the barrier-layer anodic coatings that would show measurable degradation.

2.7.1 Reflectance Data and Thermal Property Analyses

As discussed in Section 2.6, reflectance measurements were made on control samples and irradiated samples with a Beckman DK-2A reflectometer, a Gier-Dunkle reflectometer, and a Beckman IR-4 reflectometer. A table showing the types of reflectance data measured and presented in this report for each type of sample is shown in Table 3. Because of the large number of reflectance data sheets, the bulk of them are included in Appendix C and merely referenced in the text. Selected data sheets from each type of sample are presented in the following text as required. For each type of sample and reflectance measurement, the data in Appendices C and D are arranged in order of increasing particle energy and fluence for protons and alpha particles, respectively.

2.7.1.1 Low-Emittance Anodic Coated Aluminum — A typical plot of absolute spectral reflectance of a low emittance anodic coating (No. 21) is shown in Figure 29. Also shown in the figure are absolute spectral reflectances for specimens (No.'s 20 and 51) which have been exposed to 1×10^{16} and 9.25×10^{16} protons/sq.cm. The charged particle irradiation typically resulted in an accentuation of the existing interference phenomena by decreasing the reflectance

Table 2: SUMMARY OF SAMPLES TESTED

Particle Type	Particle Energy	NUMBER OF SPECIMENS: Low-Emittance Anodic Coatings	High-Emittance Anodic Coatings	Chemically Brightened Aluminum	Vapor Deposited Aluminum	Zinc Oxide/ Potassium Silicate (Z-93)	Zinc Oxide/ LTV-602 (S-13)
Proton	1.0 Kev	3	--	--	--	--	--
Proton	3.4 Kev	7	--	--	--	--	--
Proton	4.7 Kev	6	--	--	--	--	--
Proton	5.0 Kev	2	--	--	--	--	--
Proton	5.3 Kev	1	--	--	--	--	--
Proton	6.0 Kev	6	--	--	--	--	--
Proton	7.4 Kev	1	--	--	1	--	--
Proton	7.7 Kev	5	--	--	--	1	--
Proton	8.0 Kev	--	--	--	1	--	--
Proton	8.2 Kev	--	--	2	--	1	2
Proton	8.7 Kev	--	1	--	--	--	--
Proton	9.0 Kev	1	--	--	--	--	--
Proton	9.3 Kev	2	1	--	--	--	--
Proton	2.5 Mev	9	2	2	--	2	3
Alpha	2.2 Kev	4	--	--	--	--	--
Alpha	4.2 Kev	3	--	--	--	--	--
Alpha	4.5 Kev	3	--	--	--	--	--
Alpha	5.5 Kev	--	--	1	--	1	--
Alpha	8.0 Kev	9	1	1	2	1	2
Alpha	16.0 Kev	8	--	--	--	--	--
Alpha	5.0 Mev	9	1	2	2	2	2

Table 3: REFLECTANCE MEASUREMENT SUMMARY

	0.25 to 2.5 Microns		0.3 to 2.0 Microns	1-15 Microns
	DK-2A REFLECTOMETER		Gier-Dunkle Reflectom-eter	IR-4 Reflectom-eter
	Reflectance Relative to Magnesium Oxide	Reflectance Relative to Control Specimen	Absolute Reflectance	Absolute Reflectance
Low-Emittance Anodic Coatings	0**	X*	X	X
High-Emittance Anodic Coatings	X,0			X
Chemically Brightened Aluminum	0	X		X
Vapor Deposited Aluminum	0	X		
Zinc Oxide/ Potassium Silicate	X, 0			X
Zinc Oxide/ LTV-602	X, 0			X

*X - denotes measurements made, from which graphs were prepared for final report

**0 - denotes measurements made, from which no graphs were prepared for final report. These were "quality control" type measurements made early in the program.

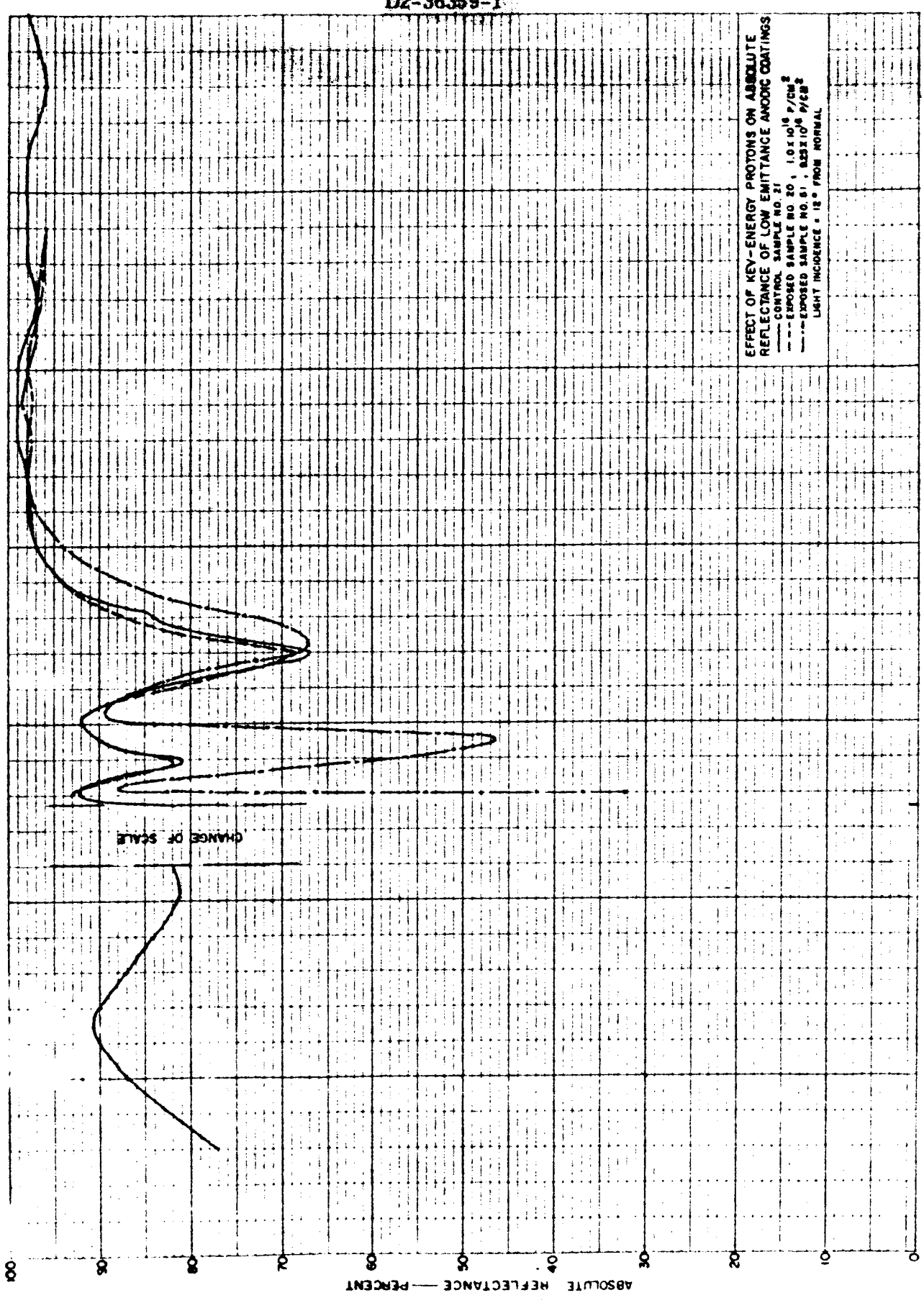

EFFECT OF KEV-ENERGY PROTONS ON ABSOLUTE REFLECTANCE OF LOW EMITTANCE ANODIC COATINGS
—— CONTROL SAMPLE NO. 21
– – – EXPOSED SAMPLE NO. 20 , 1.0 x 10^16 P/CM^2
—·— EXPOSED SAMPLE NO. 61 , 8.25 x 10^16 P/CM^2
LIGHT INCIDENCE = 12° FROM NORMAL
CHANGE OF SCALE
ABSOLUTE REFLECTANCE —— PERCENT
WAVELENGTH — MICRONS
100
90
80
70
60
50
40
30
20
10
0
.25 μ
.30
.35
.36
.6
1.1
1.6
2.1
2.6

FIGURE 29

at minima, shifting the maxima and minima to longer wavelengths, and reducing the reflectance of maxima at high fluences. The corresponding solar absorptances for the three curves shown in Figure 29 are 0.12, 0.12, and 0.23, indicating no change at 1×10^{16} protons/sq.cm. and a change of $\Delta \alpha_s = 0.11$ at 9.25×10^{16} protons/sq.cm. This corresponds to a percentage increase in absorptance of about 92 percent assuming an initial absorptance of 0.12 (Table 4).

The effect of angle of incidence of the reflectometer light beam on the reflectance of low emittance anodic coatings is shown typically in Figure 30. The three curves represent the reflectance of control sample No. 21 for angles of incidence of 12, 22, and 62 degrees from normal. As the sample is rotated from 0 to 62 degrees the wavelengths of maxima and minima shift to shorter values as expected from interference theory. Similar shifting of the interference maxima and minima occurs for irradiated samples as shown in Figures C1, C2, and C3 in Appendix C. The solar absorptances at 12, 22, and 62 degrees for sample No. 21 are 0.120, 0.119, and 0.108, respectively, as shown in Table 4. Absorptances at comparable angles for sample No. 51, irradiated with a fluence of 9.25×10^{16} of 3.4 Kev energy protons, are 0.232, 0.303, and 0.301. It is interesting to note that the absorptance of an unirradiated sample decreases as the angle of incidence from normal is increased, whereas, the absorptance of No. 51 increases for the same angular change. It will be seen later that the solar cell short-circuit current output (calculated from sample No. 51 reflectance data) actually increases as the angle of incidence changes from 12 to 62 degrees. This inverse relationship between absorptance and solar cell output points out the need for carefully measuring the spectral reflectance of a surface when interference characteristics are present in the reflectance data. The reflectance in the wavelength region near the peak of the solar cell spectral response is particularly important.

As previously discussed, a large number of change-in-reflectance (ΔR) versus wavelength plots were prepared from DK-2A reflectometer data on the low-emittance anodic coatings. These curves were obtained by measuring the reflectance of an irradiated sample relative to a similar control sample. The majority of these ΔR plots for low-energy proton tests is given in Figures C4 through C28 in Appendix C; however, three typical graphs are shown in Figures 31, 32, and 33 in the text. The curves shown in Figures 31, 32, and 33 represent typical effects of proton fluences of about 1×10^{15}, 1×10^{16}, and 1×10^{17} protons/sq.cm. These charts very clearly indicate the large decrease in reflectance in narrow wavelength bands and the change in these bands as the fluence increases. By comparing these ΔR plots with the absolute reflectance plot (Figure 29) it can be seen that the maximum changes in reflectance occur at the wavelengths of characteristic interference reflectance minima. It can also be noted that the wavelengths of the interference minima shift to larger values as the fluence is increased. The type of reflectance changes observed may be explained

Table 4: SOLAR ABSORPTANCE DATA

Specimen No.	Integrated Flux, Protons/sq. cm.	Particle Energy, Kev	Solar Absorptance, α_s		
			12°	22°	62°
21	Control	Control	0.120	0.119	0.108
36	Control	Control	0.120	0.119	0.108
20	1×10^{16}	7.7	0.120	0.119	0.108
29	1×10^{16}	4.7	0.120	0.119	0.108
51	9.25×10^{16}	3.4	0.232	0.303	0.301
178**	1×10^{16}	7.4	0.088	0.088	0.108
180**	Control	Control	0.083	0.081	0.103
161A	Control	Control	0.107	0.101	0.114
162A	Control	Control	0.107	0.112	0.122
214	Control	Control	0.181*		
233	Control	Control	0.157*		

*Calculated from DK-2A reflectance data, measured at about 5 degrees from normal.

**Measured at 10°, 20°, and 60° from normal.

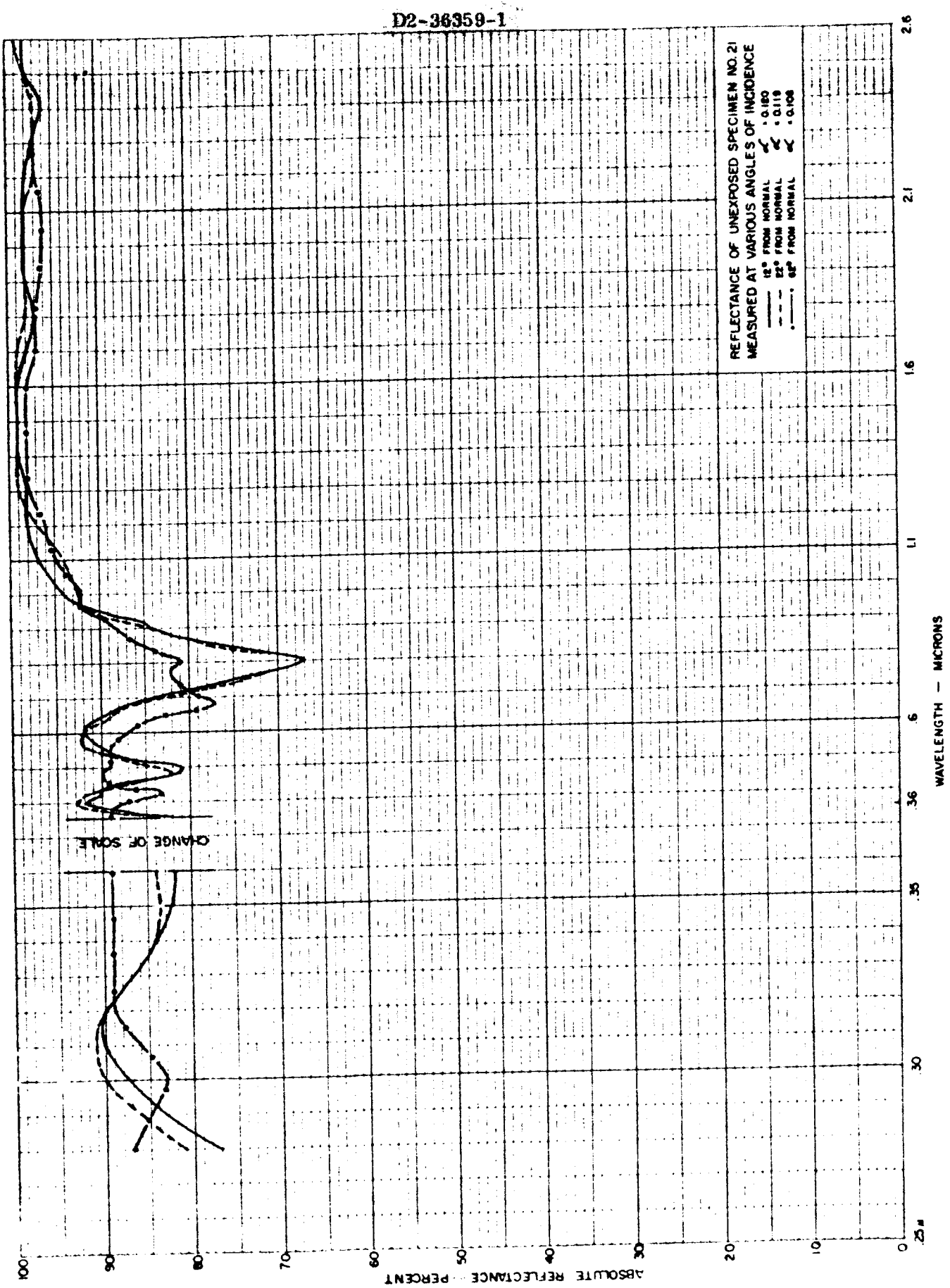

REFLECTANCE OF UNEXPOSED SPECIMEN NO. 21
MEASURED AT VARIOUS ANGLES OF INCIDENCE
12° FROM NORMAL
22° FROM NORMAL
62° FROM NORMAL
CHANGE OF SCALE
ABSOLUTE REFLECTANCE - PERCENT
WAVELENGTH - MICRONS

FIGURE 30

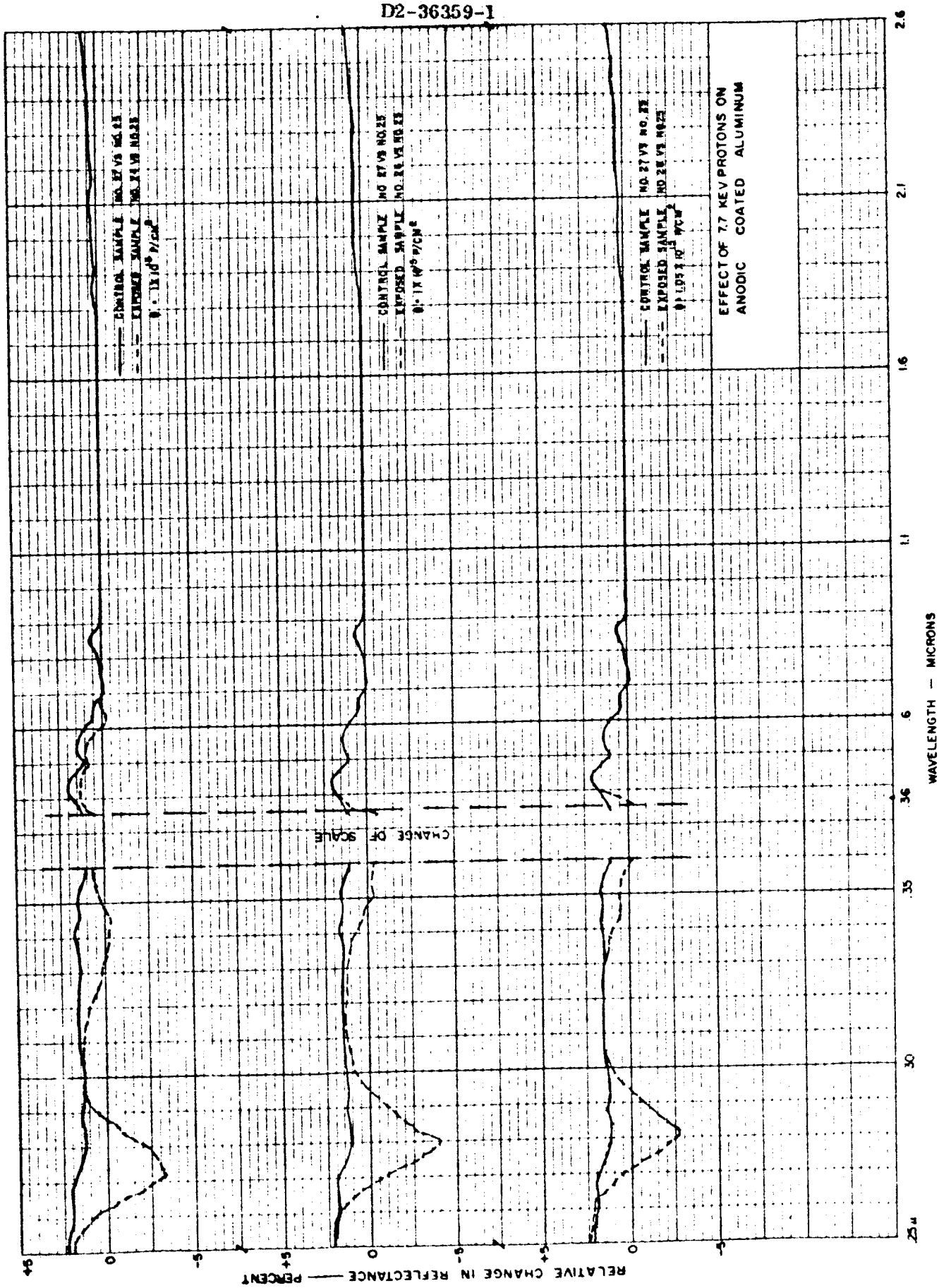

EFFECT OF 7.7 KEV PROTONS ON
ANODIC COATED ALUMINUM
CONTROL SAMPLE
EXPOSED SAMPLE
CHANGE OF SCALE
RELATIVE CHANGE IN REFLECTANCE — PERCENT
WAVELENGTH — MICRONS

FIGURE 31

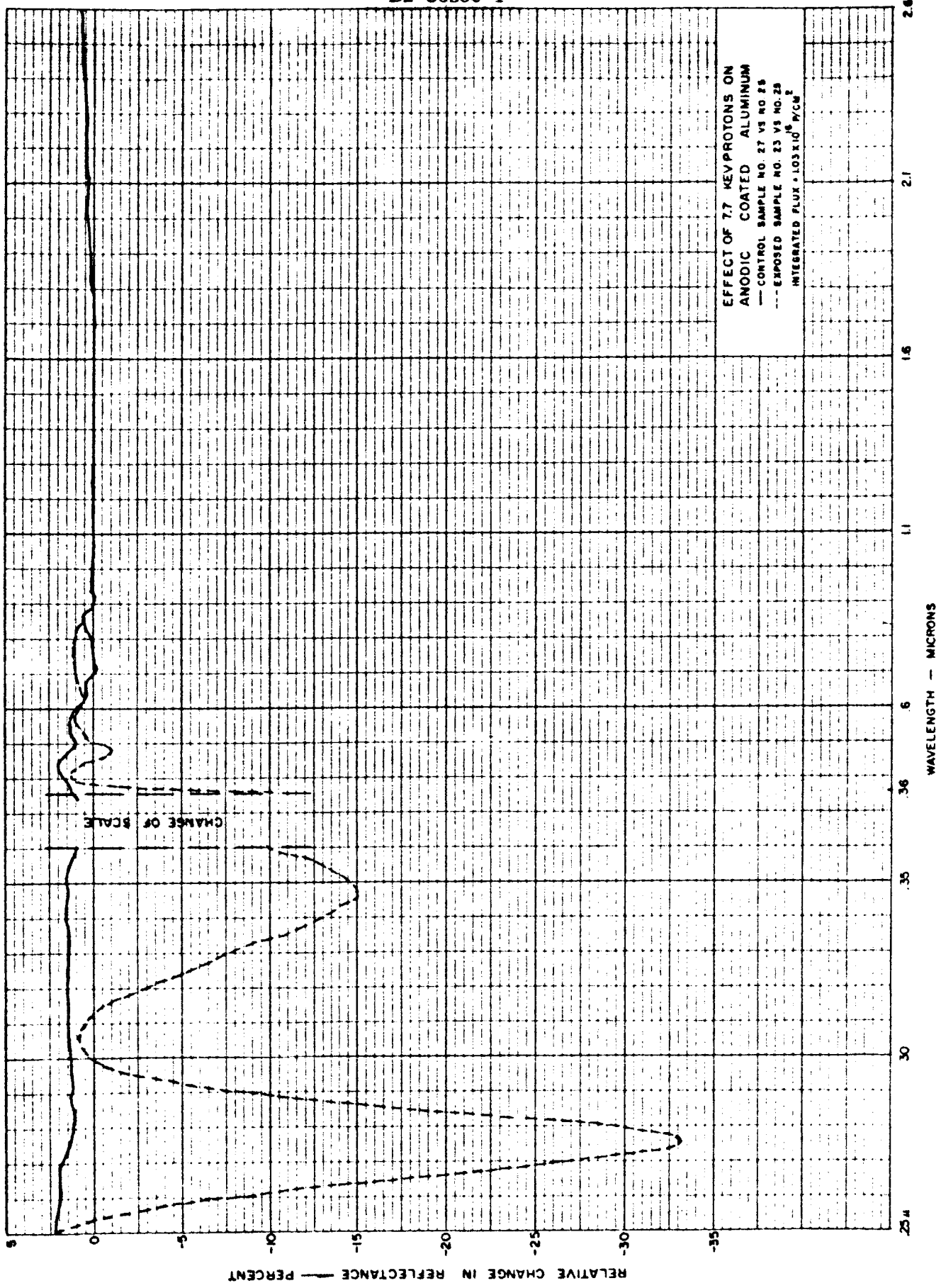

EFFECT OF 7.7 KEV PROTONS ON
ANODIC COATED ALUMINUM
— CONTROL SAMPLE NO. 27 VS NO 25
--- EXPOSED SAMPLE NO. 23 VS NO. 25
INTEGRATED FLUX = 1.03 X 10^16 P/CM^2
CHANGE OF SCALE
RELATIVE CHANGE IN REFLECTANCE —— PERCENT
WAVELENGTH — MICRONS

FIGURE 32

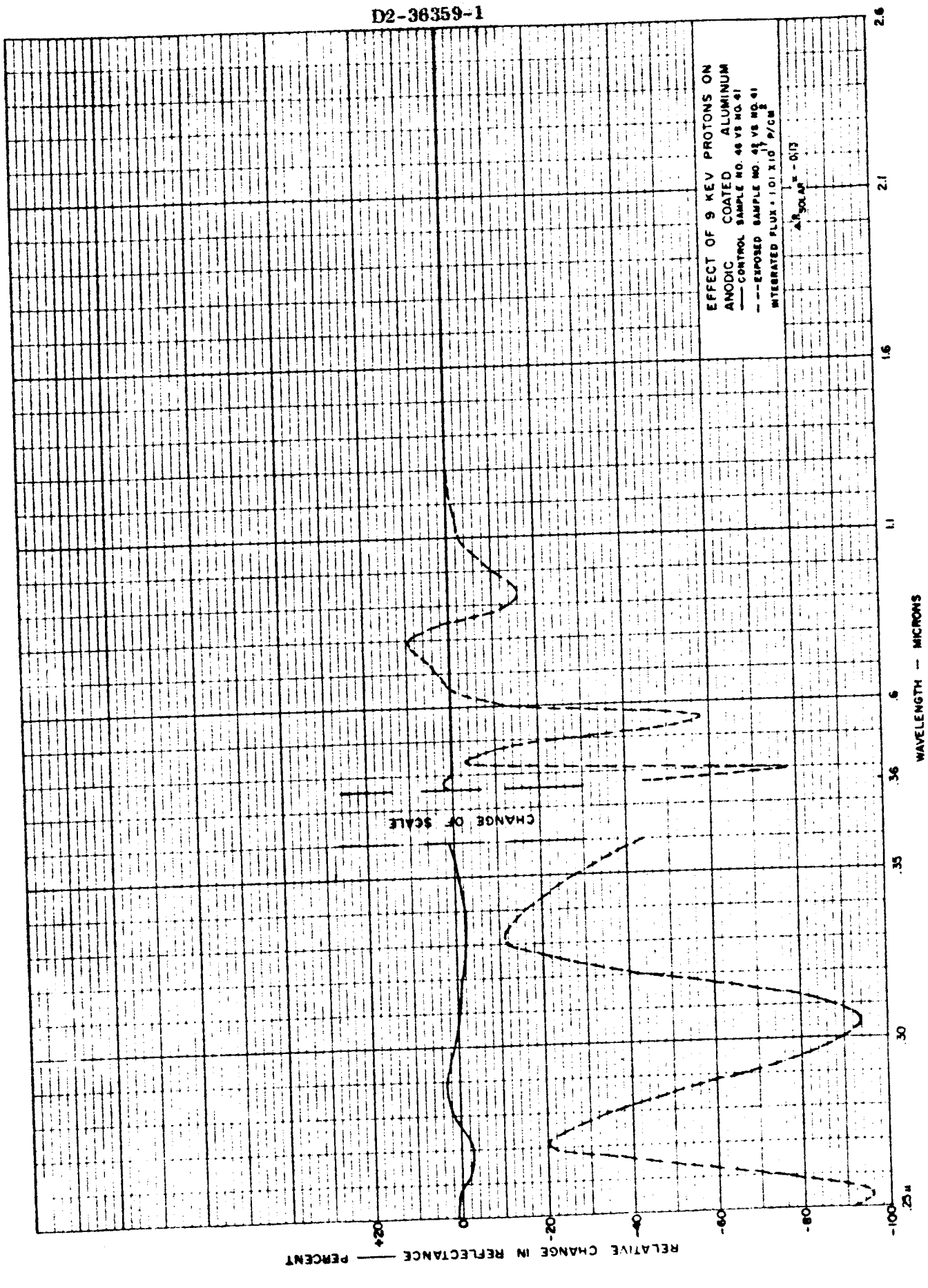

EFFECT OF 9 KEV PROTONS ON
ANODIC COATED ALUMINUM
—— CONTROL SAMPLE NO. 46 VS NO. 41
- - - EXPOSED SAMPLE NO. 45 VS NO. 41
INTEGRATED FLUX = 1.01 X 10^17 P/CM^2
Δα_SOLAR = .613
RELATIVE CHANGE IN REFLECTANCE —— PERCENT
+20
0
-20
-40
-60
-80
-100
CHANGE OF SCALE
.25 μ
.30
.35
.36
.6
1.1
1.6
2.1
2.6
WAVELENGTH — MICRONS

FIGURE 33

by either or all of the following three types of changes of the anodic film: (1) an increase in the refractive index; (2) an increase in film thickness; and (3) deposition of a thin reflective film onto the anodic film. Determination of specific radiation effects was beyond the scope of this program.

The changes in solar reflectance (ΔR_S) produced by Kev-energy protons was found to be negligible at integrated fluxes of 1×10^{15} protons sq.cm., less than $\Delta R_S = -0.01$ at 1×10^{16} protons/sq.cm., and $\Delta R_S = -0.13$ at 1×10^{17} protons/sq.cm. The foregoing ΔR_S values calculated from DK-2A reflectance data can be compared with similar values calculated from Gier-Dunkle reflectometer data (Table 4). For sample No. 51, the ΔR_S values for DK-2A and Gier-Dunkle data are 0.149 and 0.112, respectively. The difference between these two values is probably due to instrumentation errors or to the strong angular dependence of reflectance. The DK-2A data was measured at 3 degrees from normal and the Gier-Dunkle at 12 degrees. A plot of the change in solar reflectance (ΔR_S) measured on the DK-2A reflectometer versus integrated proton flux is shown in Figure 34. It can be seen from this curve that the threshold of measurable change ($\Delta R_S \cong 0.01$) in solar reflectance occurs at about 3×10^{16} protons/sq.cm. Although the points on this curve represent tests using proton energies varying from 3 to 9 Kev, it was assumed valid to draw a single curve through them. The effect of particle energy on solar reflectance could not be conclusively established for anodic coated samples.

The ΔR of sample Nos. 20 and 31 were measured at two different time intervals after irradiation to determine whether annealing effects were significant. The ΔR curves for sample No. 20 measured at 42 and 880 hours after irradiation showed considerable annealing as shown in Figure C25. However, sample No. 31 measured at 20 and 165 hours after irradiation (Figure C15) showed a very small annealing effect. Although annealing of reflectance of anodic coated aluminum was observed, no conclusions can be made because of the lack of data. Annealing studies were beyond the scope of this contract.

No ΔR_S curves were prepared for low-emittance anodic coatings irradiated with 2.5 Mev protons, because reflectance changes were negligible. Fluences in the 2.5 Mev proton tests ranged from 7.1×10^{12} in the center of the outer ring of samples to 2.95×10^{15} protons/sq.cm. at the inner edge of the inner ring.

An important objective of the contract was to determine whether the charged particles (particularly the Kev-energy particles) would increase the diffuse reflectance or decrease the specular reflectance of the specularly reflecting surfaces. The results of typical diffuse reflectance measurements on low-emittance anodic coatings are shown in Figure 35. It was concluded from these curves that the diffuse or specular reflectance of barrier-layer anodic coated aluminum does not change after fluences as high as 1×10^{17} protons sq.cm.

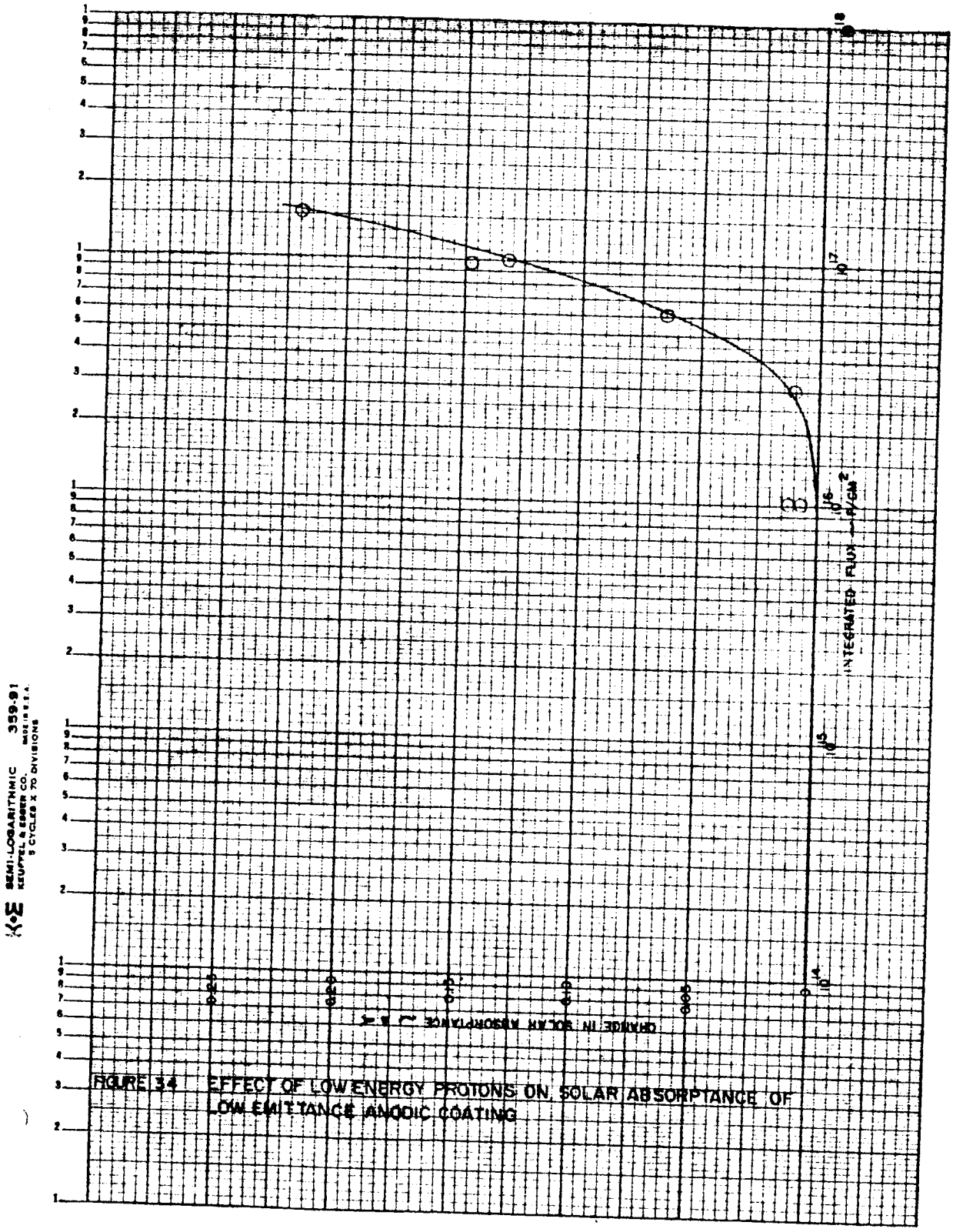


FIGURE 34 EFFECT OF LOW ENERGY PROTONS ON SOLAR ABSORPTANCE OF LOW EMITTANCE ANODIC COATING

USE FOR TYPEWRITTEN MATERIAL ONLY

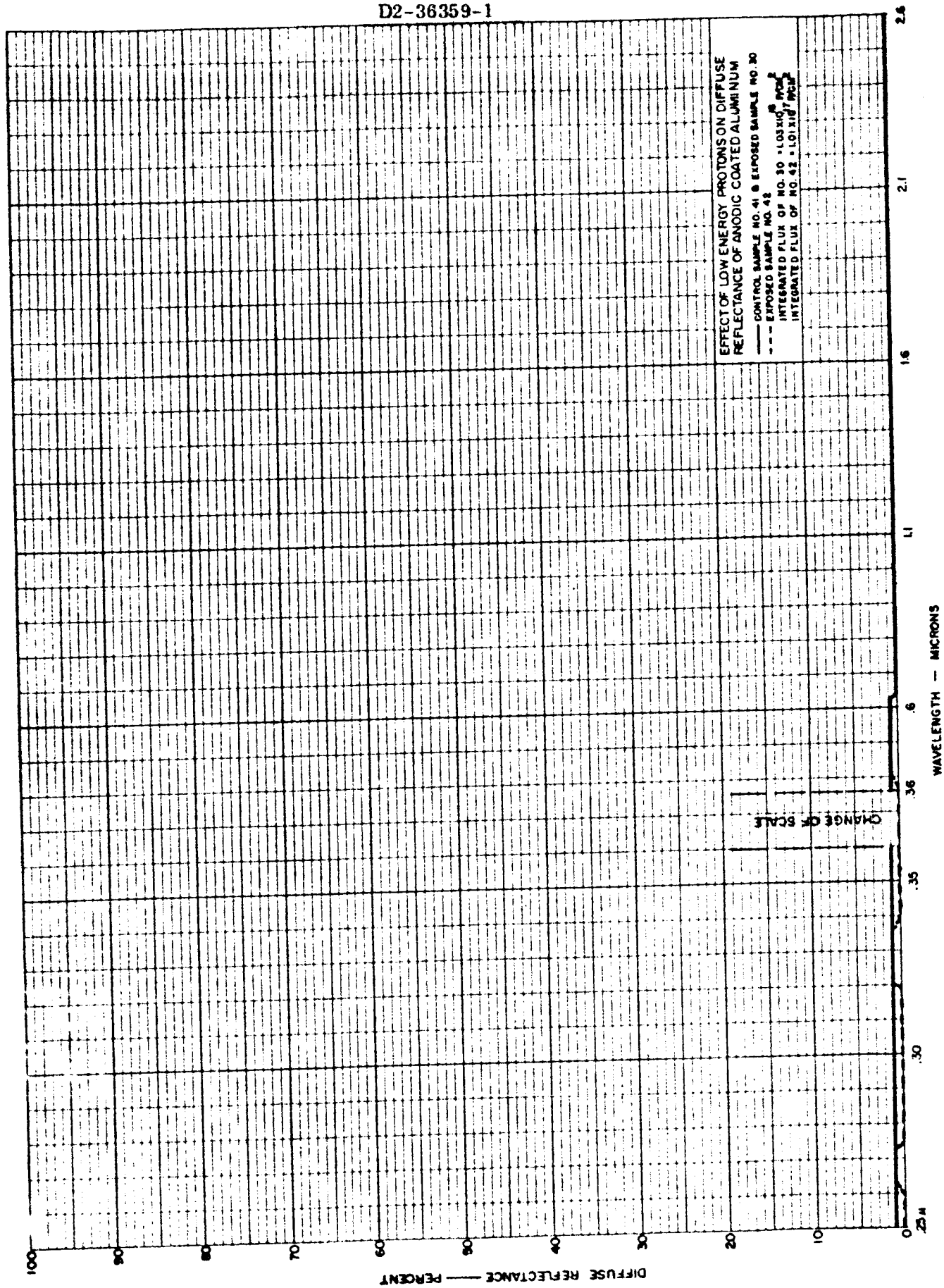

EFFECT OF LOW ENERGY PROTONS ON DIFFUSE REFLECTANCE OF ANODIC COATED ALUMINUM
—— CONTROL SAMPLE NO. 41 @ EXPOSED SAMPLE NO. 30
- - - EXPOSED SAMPLE NO. 42
INTEGRATED FLUX OF NO. 30 = 1.03 x 10^16 PROT/CM^2
INTEGRATED FLUX OF NO. 42 = 1.01 x 10^17 PROT/CM^2
CHANGE OF SCALE
DIFFUSE REFLECTANCE —— PERCENT
WAVELENGTH — MICRONS
100
90
80
70
60
50
40
30
20
10
0
.25μ
.30
.35
.36
.6
1.1
1.6
2.1
2.6

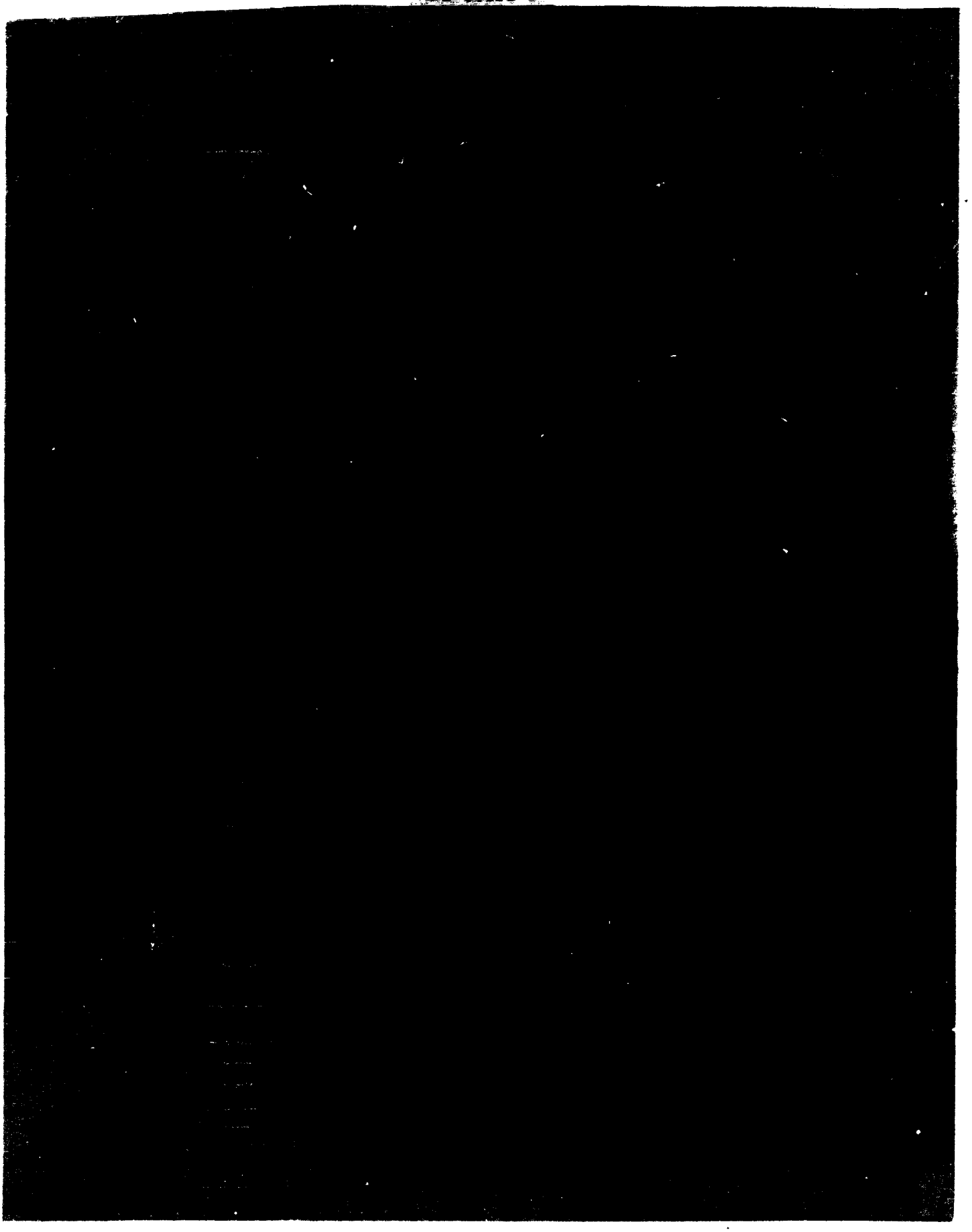
FIGURE 35

Numerous diffuse reflectance measurements were performed on anodic coatings but the data were not reproduced in this document because changes were no larger than those shown in Figure 35. The conclusion that diffuse reflectance does not change is substantiated by electron photomicrographs of surfaces of low emittance anodic coatings before and after irradiation (Figures 36 and 37). The photomicrographs, at 21,600x, indicate that the surface may have actually been smoothed by the irradiation. It is not known whether the dark blotches on the before-irradiation micrograph are cavities, protrusions, or residue on the anodic surface. Similar dark blotches have been observed on photomicrographs of Alzak anodic surfaces. The apparent blisters in Figure 37 are actually cavities in the anodic surface, not blisters. These cavities are only sparsely located and are blieved to be at locations where electrical breakdown across the anodic film occurred. A photomicrograph of a typical large "spark cavity" is shown in Figure 38. This cavity is about 14.5 microns in diameter and has 0.3 micron diameter pits in the cavity floor. Electrical breakdown across the anodic film was particularly prevalent in 1 to 4 Kev tests where charge-buildup occurred. Formation of spark cavities cannot be treated as a space radiation effects phenomenon because the charged particle fluxes in space are orders of magnitude lower than fluxes used in the tests, and the solar wind is believed to be a neutral plasma.

Infrared reflectance measurements were performed on about 18 samples to determine whether low energy protons have any effect on emittance or chemical bonds. Typical infrared reflectance curves for a control sample and for samples exposed to 1×10^{16} and 1×10^{17} protons/sq.cm. are shown in Figure 39. The emittances in the 1 to 15 micron wavelength region of all three of these samples were calculated to be 0.06. Emittances are tabulated in Appendix D. No conclusive changes in infrared reflectance were observed at fluences as high as 1×10^{17} protons/sq.cm. of low energy protons.

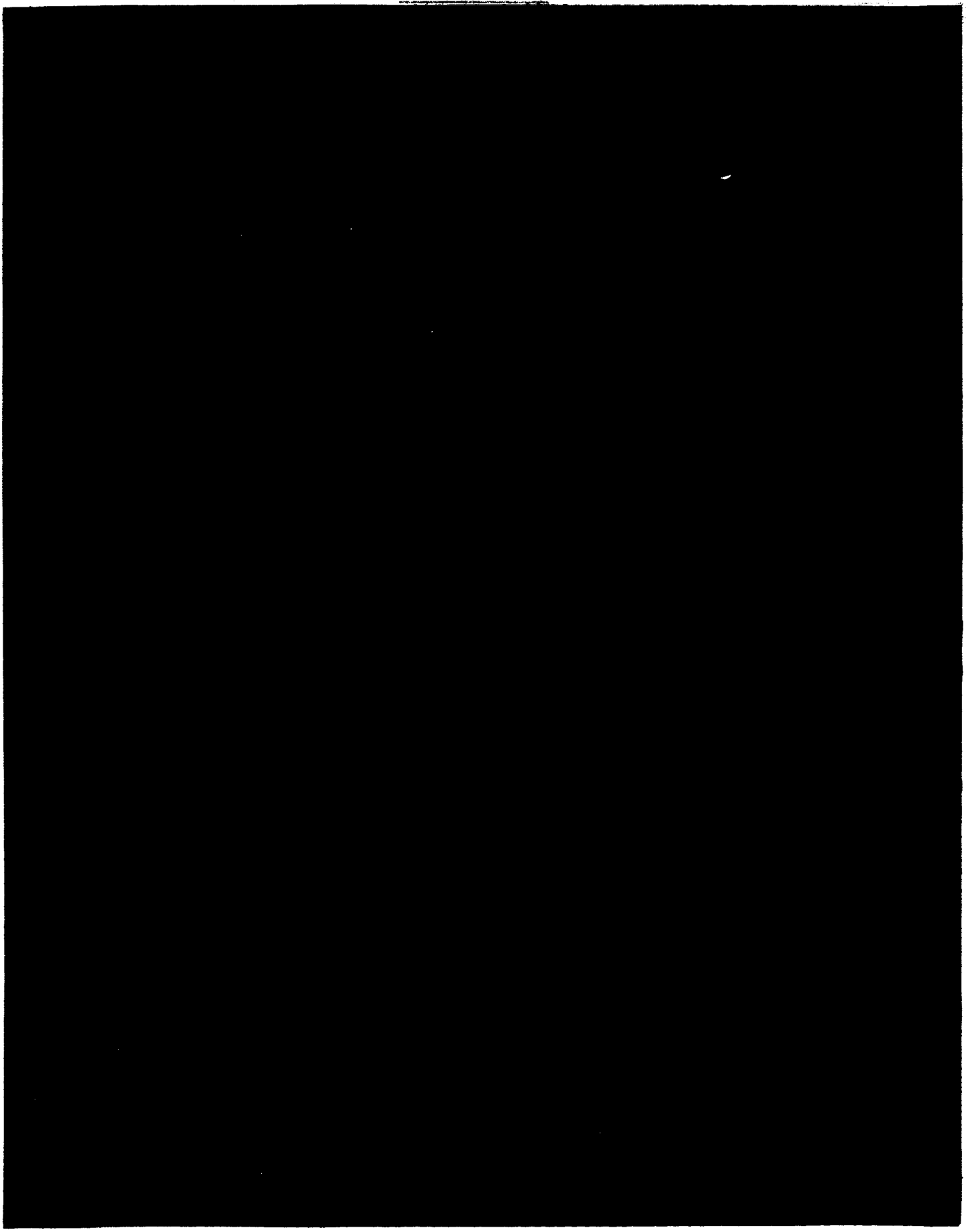
The effects of low-energy alpha particles on low-emittance anodic coatings can be observed in Figures C13 and C29 through C36 in Appendix C. Although 27 low emittance anodic coatings were exposed to Kev-energy-alpha particles, only 14 reflectance plots were prepared because insignificant reflectance changes occurred on the other samples. It was originally planned to expose samples to low-energy alpha particles in the energy range of 2 to 16 Kev and fluences of 1×10^{13}, 1×10^{14}, and 1×10^{15} alphas/sq.cm. However, because of the small reflectance changes observed at fluences of 1×10^{14} and 1×10^{15} alphas/sq.cm., it was decided to substitute several exposures at 1×10^{16} for the planned tests at 1×10^{13} alphas/sq.cm.

The type of reflectance change produced by low-energy alpha particles was found to be similar to that produced by low-energy protons. A fluence of 1×10^{16} alphas/sq.cm. produced a change in solar reflectance of $\Delta R_s = -0.031$. This change in absorptance is about three times the change produced by a comparable fluence of Kev-energy protons. No appreciable solar reflectance changes

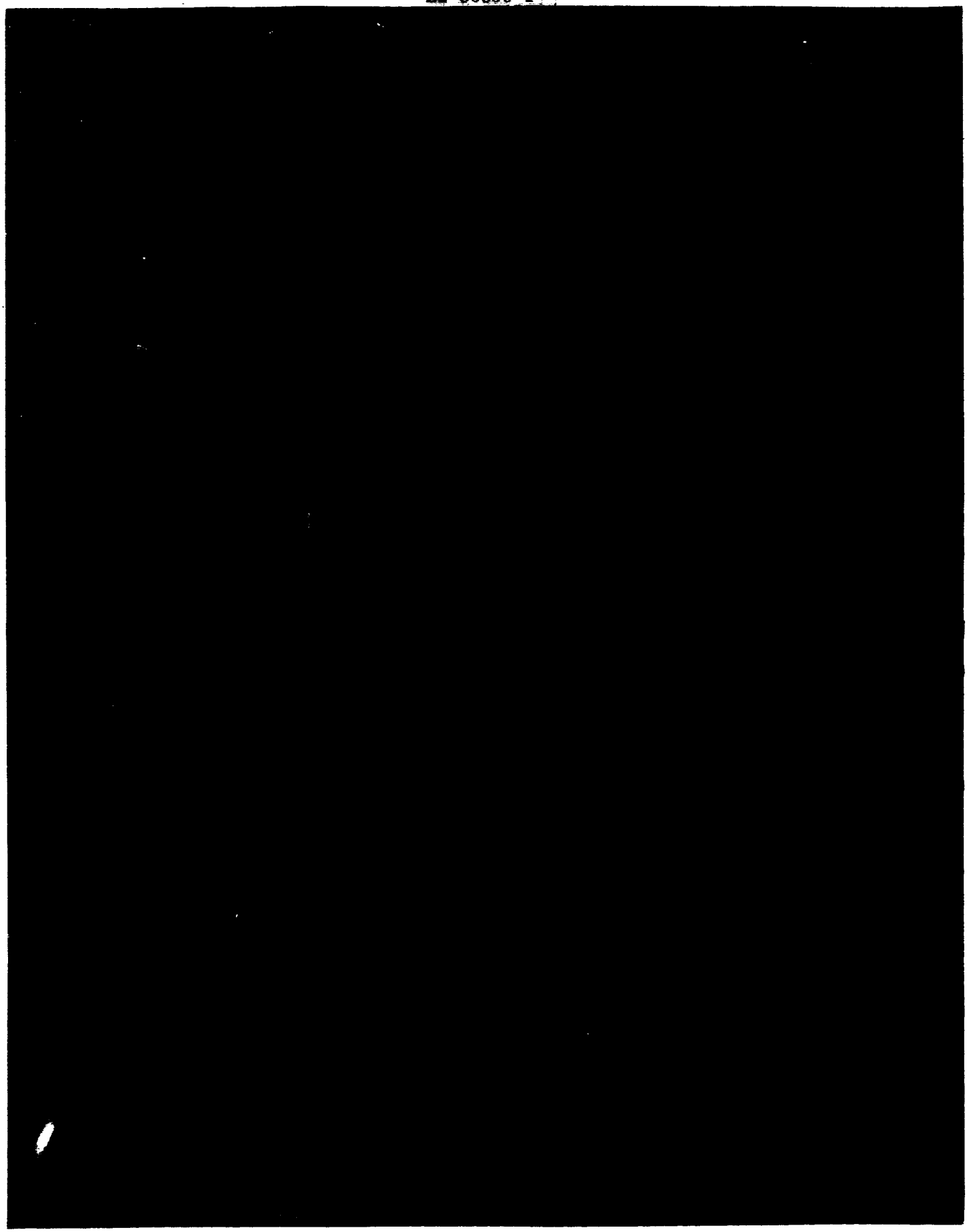


BARRIER-LAYER ANODIC COATED ALUMINUM BEFORE IRRADIATION

FIGURE 36



BARRIER-LAYER ANODIC COATED ALUMINUM AFTER IRRADIATION
9.3 KEV PROTONS - 1×10^{16} P/CM^2 FIGURE 37



TYPICAL LARGE SPARK CAVITY ON ANODIC COATED ALUMINUM AFTER IRRADIATION
9.3 KEV PROTONS – 1×10^{16} P/CM^2 FIGURE 38

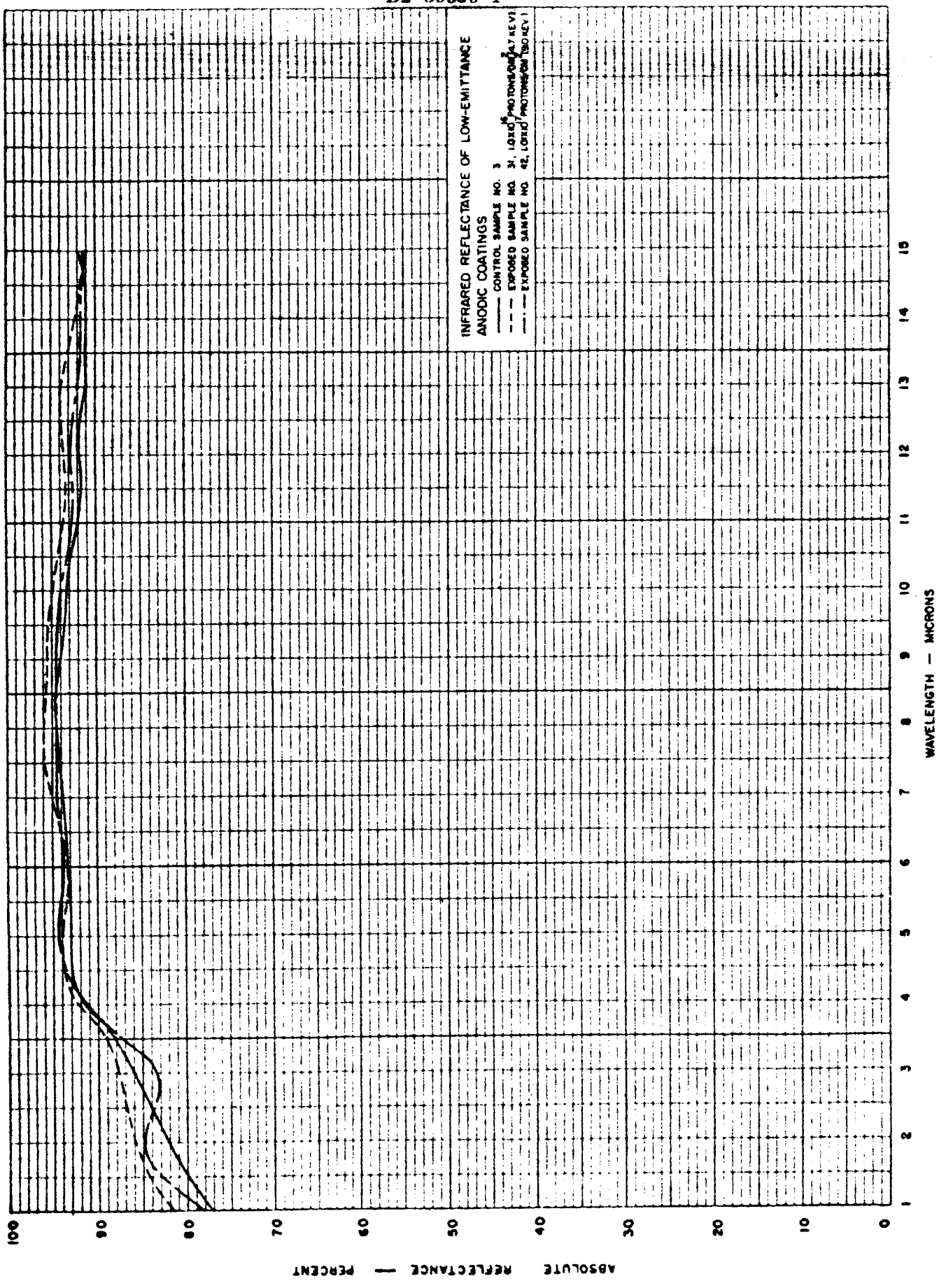

INFRARED REFLECTANCE OF LOW-EMITTANCE ANODIC COATINGS
CONTROL SAMPLE NO. 3
EXPOSED SAMPLE NO. 31, 1.0X10^16 PROTONS/CM^2 AT 7 KEV
EXPOSED SAMPLE NO. 42, 1.0X10^16 PROTONS/CM^2 AT 150 KEV
ABSOLUTE REFLECTANCE — PERCENT
100
90
80
70
60
50
40
30
20
10
0
1
2
3
4
5
6
7
8
9
10
11
12
13
14
15
WAVELENGTH — MICRONS

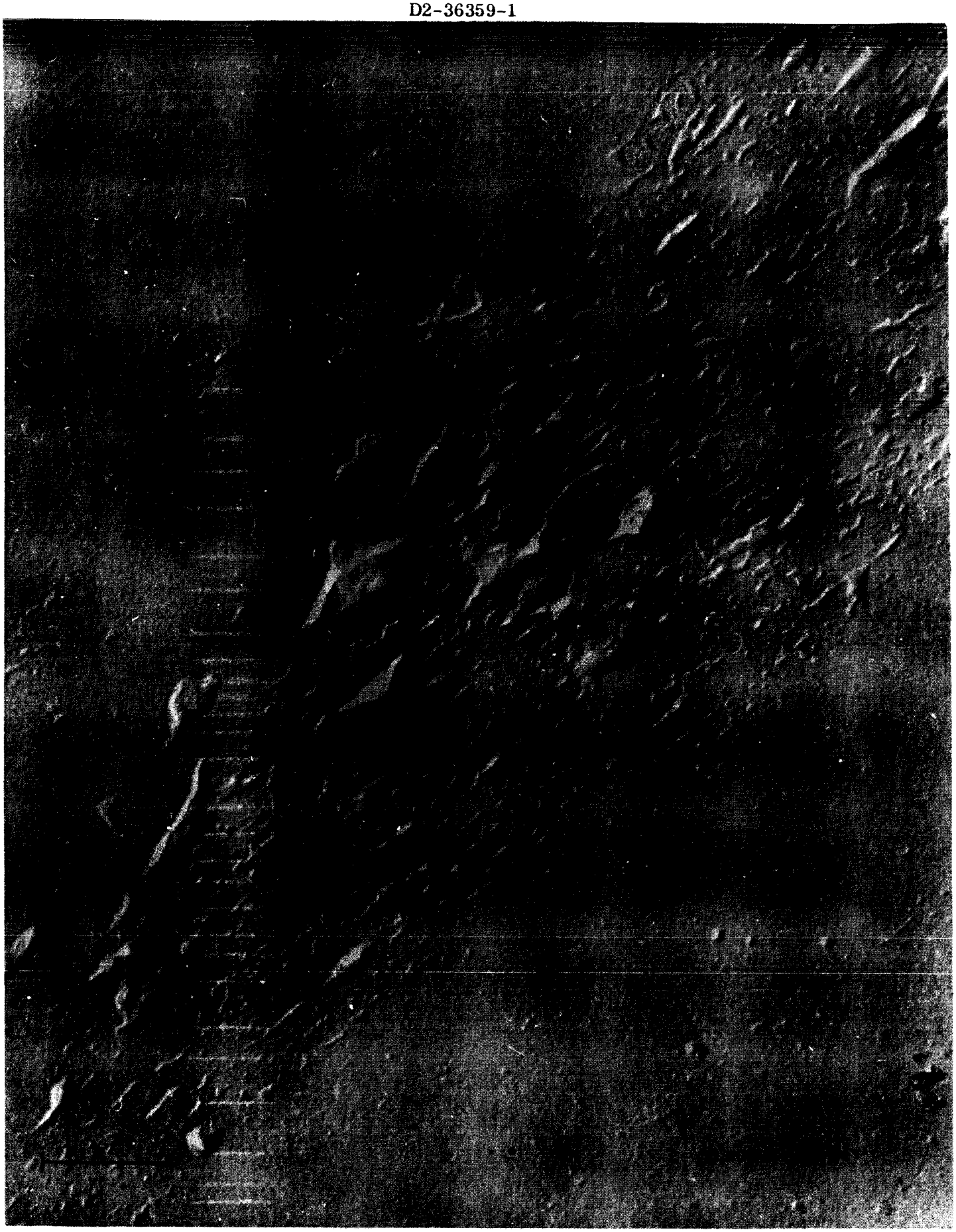
FIGURE 39

occurred at fluences below 1×10^{16} alphas/sq.cm. It is apparent from the ΔR versus wavelength plots (Figures C13 and C29 through C36) that the reflectance change at the 0.278 micron wavelength minimum varied considerably between samples exposed to the same fluence (for example, 1×10^{16}). Variations of this type and magnitude were not observed in Kev-energy proton experiments. This variation in reflectance could have been caused by either energy-dependent effects, errors in current measurement, or differences in fluxes.

Electron photomicrograph observations of a low-emittance anodic coated sample bombarded with 8 Kev alphas, revealed a smooth appearing surface similar to that observed on proton irradiated samples. However it was noted that a small portion of the surface was covered with irregular-shaped protrusions or cavities (Figure 40). These irregularities were located in a band about 12 microns wide as shown in the figure.

2.7.1.2 High-Emittance Anodic Coated Aluminum — A plot of the absolute reflectance of control sample No. 161A, measured at 12, 22, and 62 degrees from normal is shown in Figure 41. A similar plot for sample No.'s 162A and 162B, measured on the DK-2A reflectometer, is shown in Figure 42. Other relative reflectance curves which show the effects of low energy protons on the high-emittance anodic coatings are given in Appendix C (Figures C37 and C38). Figure 42 shows the reflectance of a control sample and a specimen irradiated with a fluence of 1×10^{16} protons/sq.cm. of 8 Kev protons. The nature of the spectral reflectance changes in the high-emittance anodic coatings is different from the changes observed in the low-emittance coatings. The reflectance of both the interference maxima and minima, in the thick coating reflectance curve, decrease after irradiation with 1×10^{16} protons/sq.cm. Note also, that the irradiated high-emittance anodic coating (No. 162B) has shorter wavelength maxima and minima than the control sample (No. 162A), whereas, the minima wavelengths of low-emittance anodic coatings shifted to longer wavelengths. The shift in wavelength of maxima and minima in the high-emittance coatings may be due to thickness variation of the anodic film between the two samples taken from the same sheet. This thickness variation may be the result of differential attack in the phosphoric acid bath following anodization (Section 2.3.1).

The solar absorptances of sample Nos. 161A and 162A measured at 12, 22, and 62 degrees are given in Table 4. The absorptances given in the table vary from 0.10 to 0.122. The change in solar absorptance or reflectance of sample No. 162B was found to be less than $\Delta R_s = -0.01$ (negligible) for a fluence of 1×10^{16} protons/sq.cm. of 8.7 Kev protons. Similarly, irradiation with smaller fluences of low and high energy alpha particles and high energy protons did not produce significant changes in solar reflectance. Since a degradation threshold ($\Delta R_s \geq 0.01$) was not reached, it can only be concluded that fluences



BARRIER—LAYER ANODIC COATED ALUMINUM AFTER ALPHA PARTICLE IRRADIATION FIGURE 40

8 KEV ALPHA PARTICLES 9.6×10^{14} α/CM^2 70

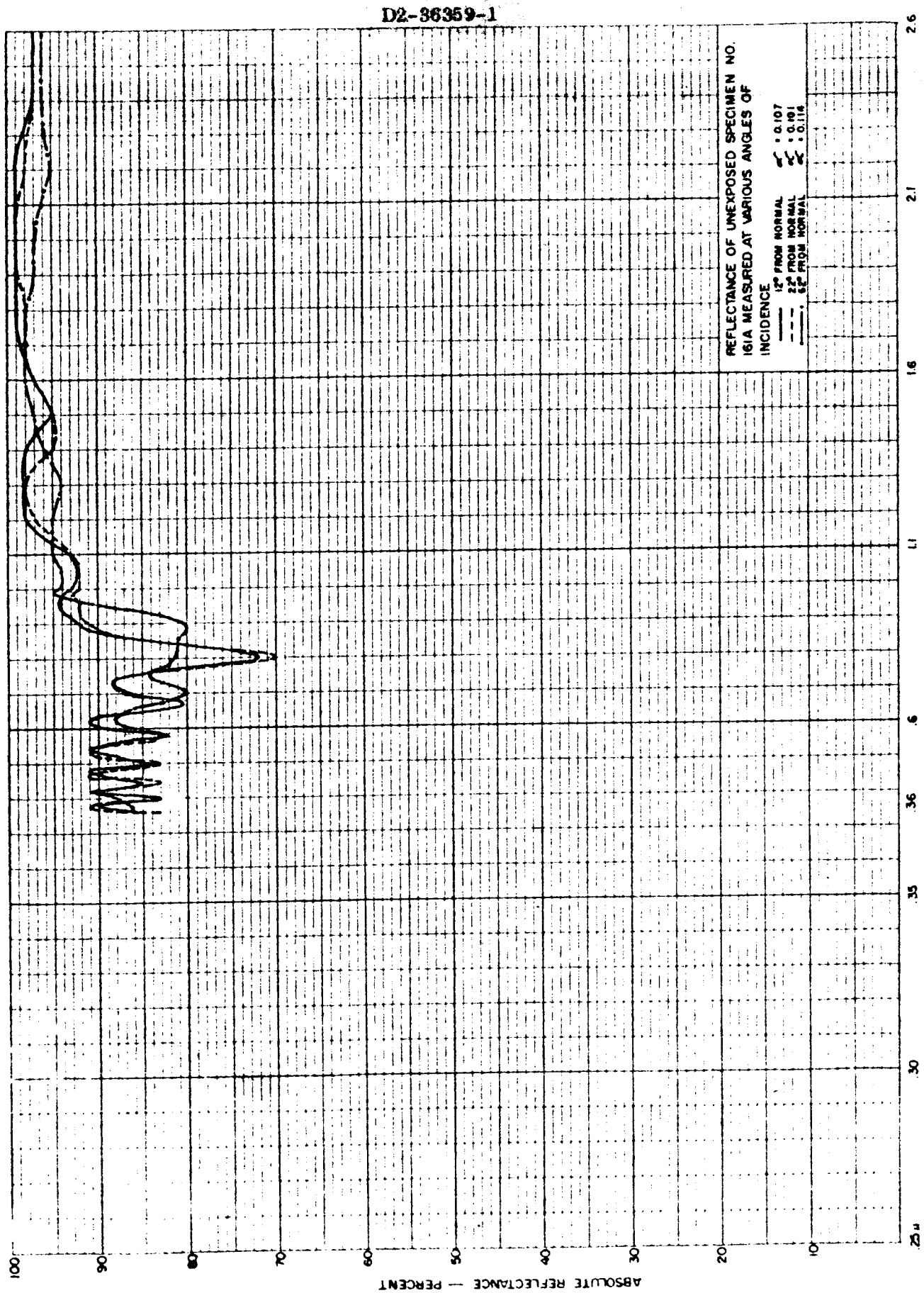

REFLECTANCE OF UNEXPOSED SPECIMEN NO. 161A MEASURED AT VARIOUS ANGLES OF INCIDENCE
12° FROM NORMAL ± 0.107
22° FROM NORMAL ± 0.101
62° FROM NORMAL ± 0.116
ABSOLUTE REFLECTANCE — PERCENT
100
90
80
70
60
50
40
30
20
10
0
.25 μ
.30
.35
.36
.6
1.1
1.6
2.1
2.6
WAVELENGTH — MICRONS

FIGURE 41

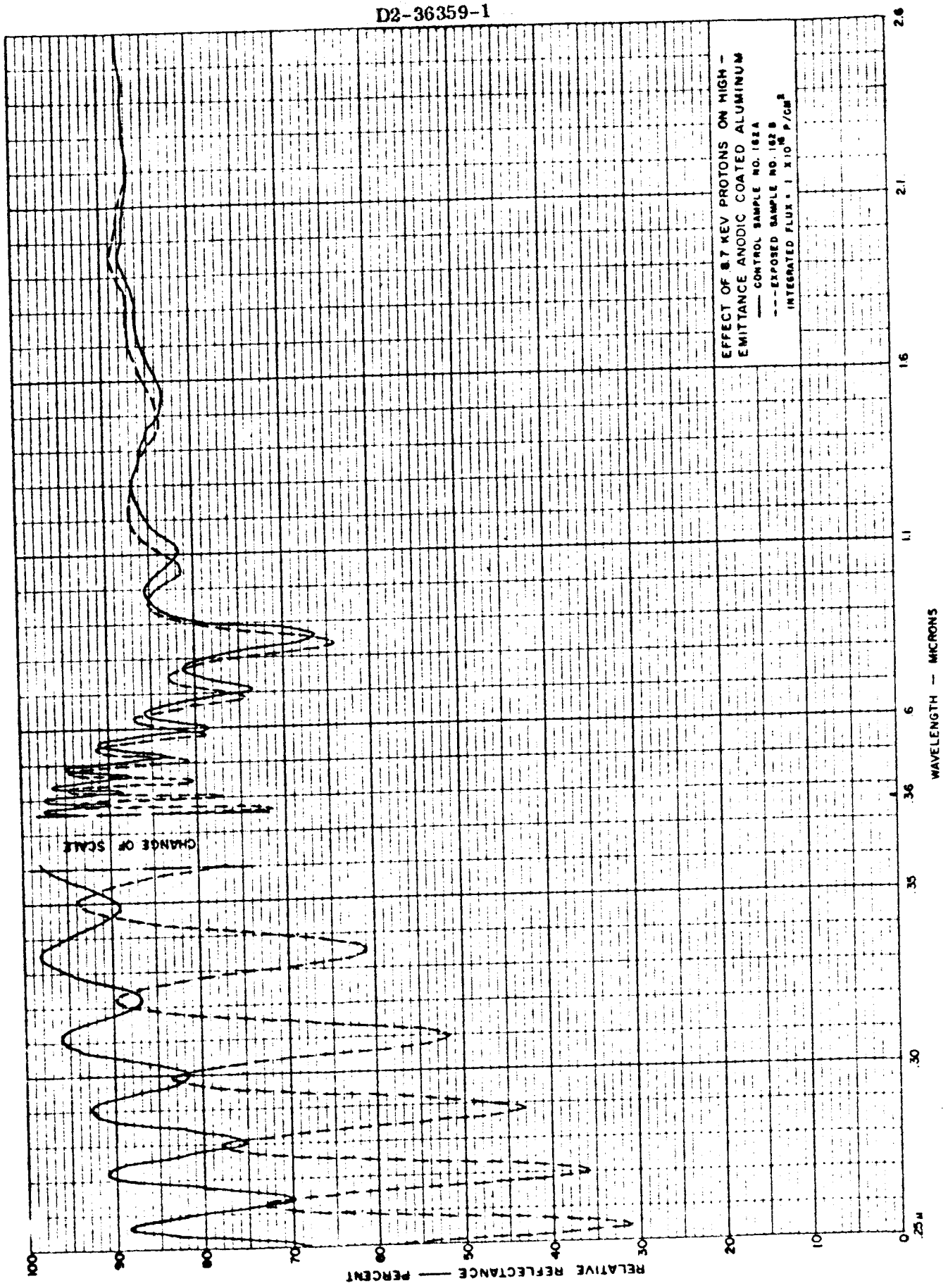

EFFECT OF 8.7 KEV PROTONS ON HIGH-EMITTANCE ANODIC COATED ALUMINUM
— CONTROL SAMPLE NO. 162A
---EXPOSED SAMPLE NO. 162B
INTEGRATED FLUX = 1 X 10^16 P/CM^2
CHANGE OF SCALE
RELATIVE REFLECTANCE — PERCENT
WAVELENGTH — MICRONS
100
90
80
70
60
50
40
30
20
10
0
.25μ
.36
.35
.30
.6
1.1
1.6
2.1
2.6

FIGURE 42

of greater than 1×10^{16} protons/sq.cm. of Kev-energy protons will be required to produce a significant decrease in solar reflectance. The infrared reflectance data on high emittance anodic coatings is shown in Figure 43. Typical emittances varied from 0.25 to 0.28 as shown in Appendix D, and were not affected by irradiation with low energy protons.

2.7.1.3 Chemically Brightened Aluminum — The change-in-reflectance (Δ R) plots for chemically brightened aluminum exposed to low energy protons are shown in Figures 44 and 45. Because the reduction in reflectance was small in the intense region of the solar spectrum, no measurable change in solar absorptance occurred at an integrated proton flux of 6.1×10^{15}. The shift in reflectance-change from the ultraviolet to visible wavelengths, noted in the two figures for different integrated fluxes, suggests that a decrease in solar reflectance will occur at a slightly higher integrated flux.

The nature of the reflectance change indicates that the degradation may have been caused by a roughening of the surface by either sputtering or blistering processes. Examination of the surfaces by electron photomicrographs revealed that the low energy protons caused blistering of the surface. Photomicrographs of chemically brightened aluminum before and after irradiation are shown in Figures 46 and 47. The photomicrograph of an unirradiated sample (No. 190) shows an extremely smooth surface except for what are believed to be oriented etch marks from the brightening bath (Section 2.3.1). The photomicrograph of sample No. 189 shows that the blisters have a definite pattern in their formation which is apparently not associated with surface etch marks. The size of the largest blisters in Figure 47 is about 0.3 microns. A study should be conducted to determine the process of formation of these blisters and their effect on solar concentrator performance.

The effect of low energy protons on the infrared reflectance of chemically brightened aluminum is shown in Figure 48. The reflectance of control sample No. 196 is compared to the reflectance of exposed sample No. 187 which was irradiated with 4.6×10^{15} protons/sq.cm. at 8.2 Kev. Although a small decrease in reflectance occurred, the calculated emittance for both curves in the 1 to 15 micron wavelength region is about 0.08. Thus, it was concluded that a fluence of 4.6×10^{15} protons/sq.cm. of 8.2 Kev protons has a negligible effect on emittance.

No Δ R reflectance curves are presented for samples irradiated with low energy alphas, high energy alphas, and high energy protons since negligible damage occurred in these tests.

2.7.1.4 Vapor Deposited Aluminum — A typical plot of the absolute spectral reflectance of a vapor deposited aluminum control sample (No. 180) and an exposed sample (No. 178) is shown in Figure 49. The reflectance data shown

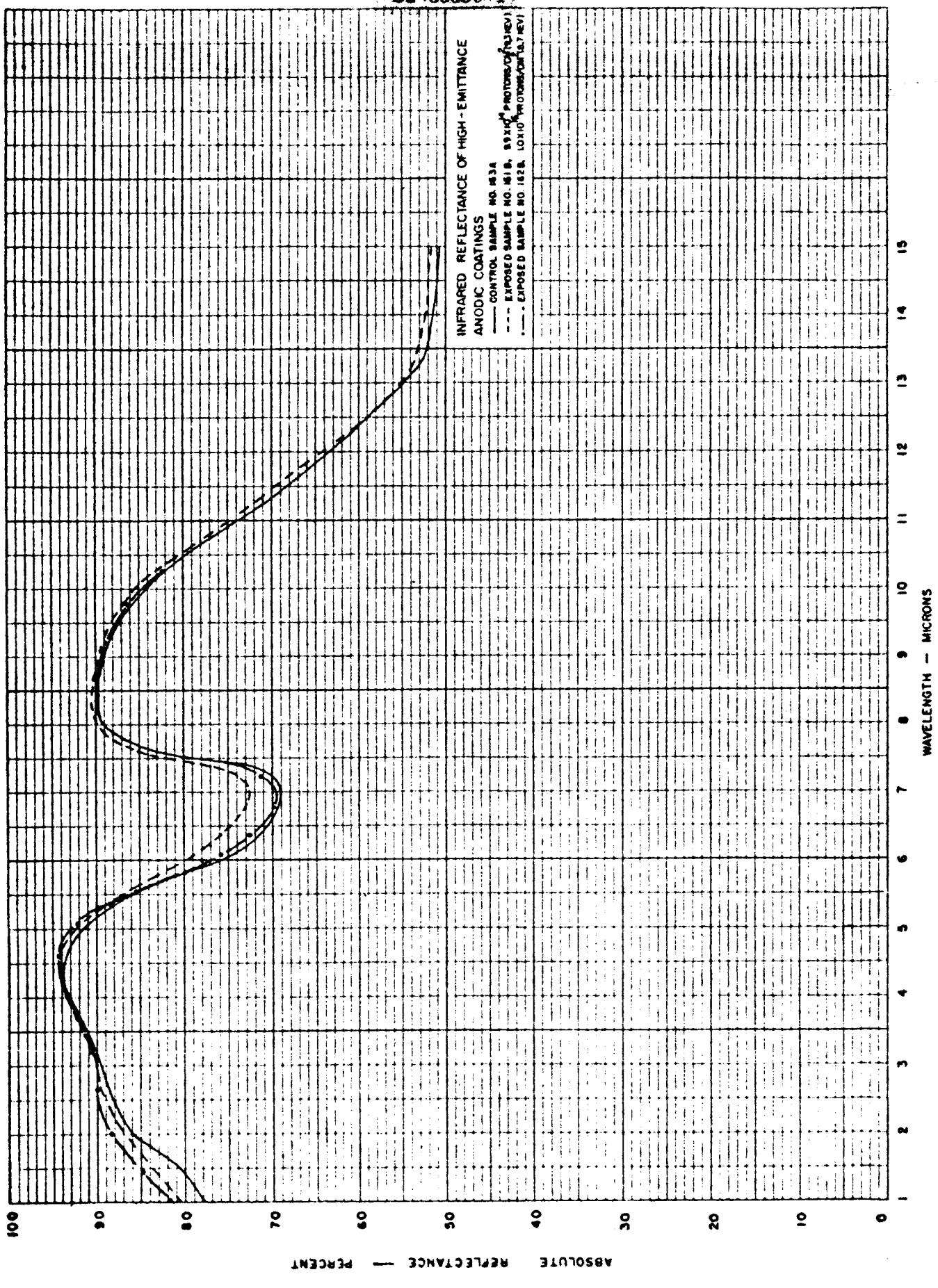

INFRARED REFLECTANCE OF HIGH-EMITTANCE ANODIC COATINGS
—— CONTROL SAMPLE NO. 163A
--- EXPOSED SAMPLE NO. 1618, 8.9x10^14 PROTONS/CM^2 (1 MEV)
·—· EXPOSED SAMPLE NO. 1628, 1.0x10^16 PROTONS/CM^2 (1 MEV)
ABSOLUTE REFLECTANCE — PERCENT
100
90
80
70
60
50
40
30
20
10
0
1
2
3
4
5
6
7
8
9
10
11
12
13
14
15
WAVELENGTH — MICRONS

FIGURE 43

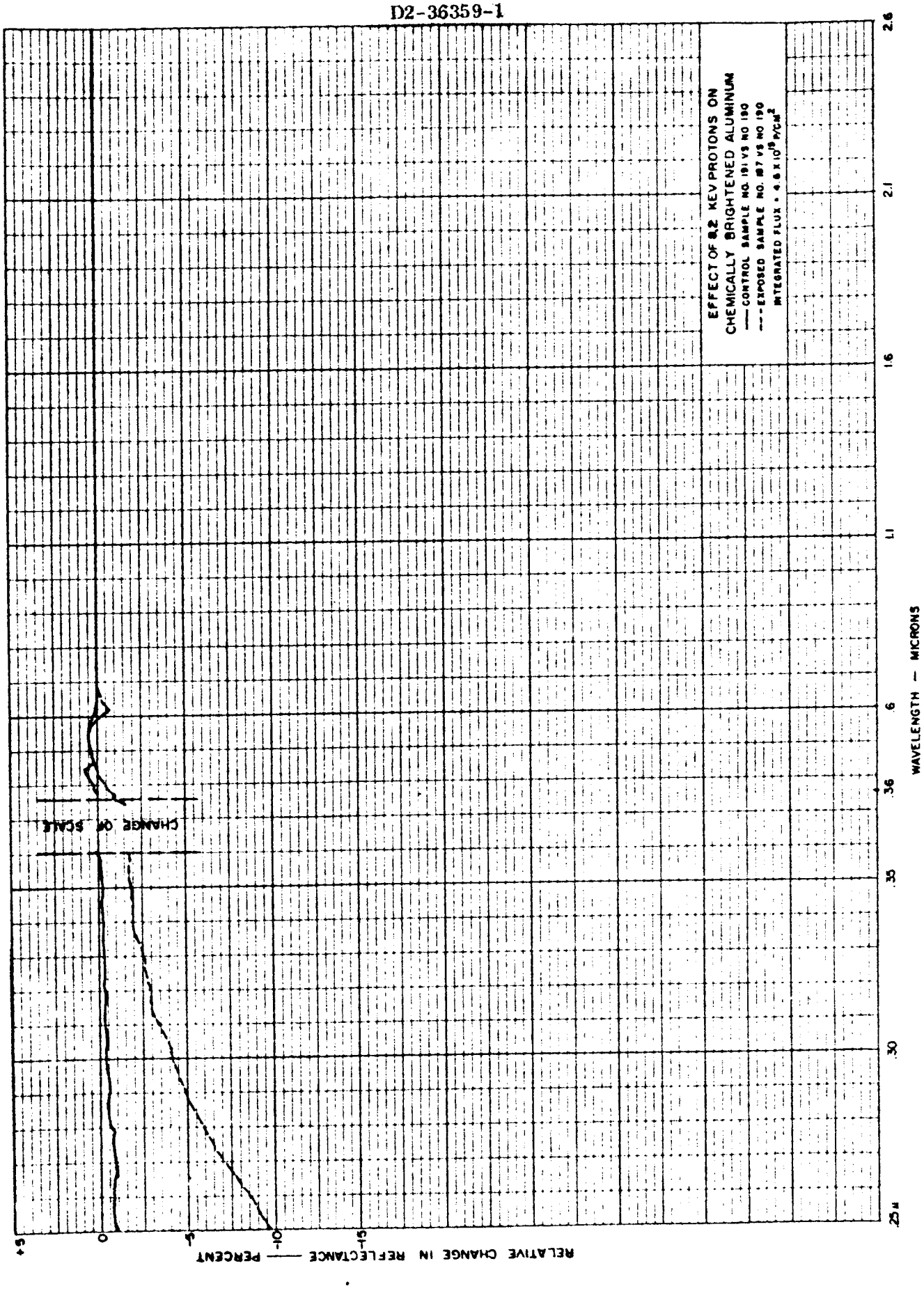

EFFECT OF 8.2 KEV PROTONS ON
CHEMICALLY BRIGHTENED ALUMINUM
—— CONTROL SAMPLE NO. 191 VS NO 190
– – – EXPOSED SAMPLE NO. 187 VS NO 190
INTEGRATED FLUX = 4.8 X 10^15 P/CM^2
CHANGE OF SCALE
+5
0
-5
-10
-15
RELATIVE CHANGE IN REFLECTANCE —— PERCENT
.25μ
.30
.35
.36
.6
1.1
1.6
2.1
2.6
WAVELENGTH — MICRONS

FIGURE 44

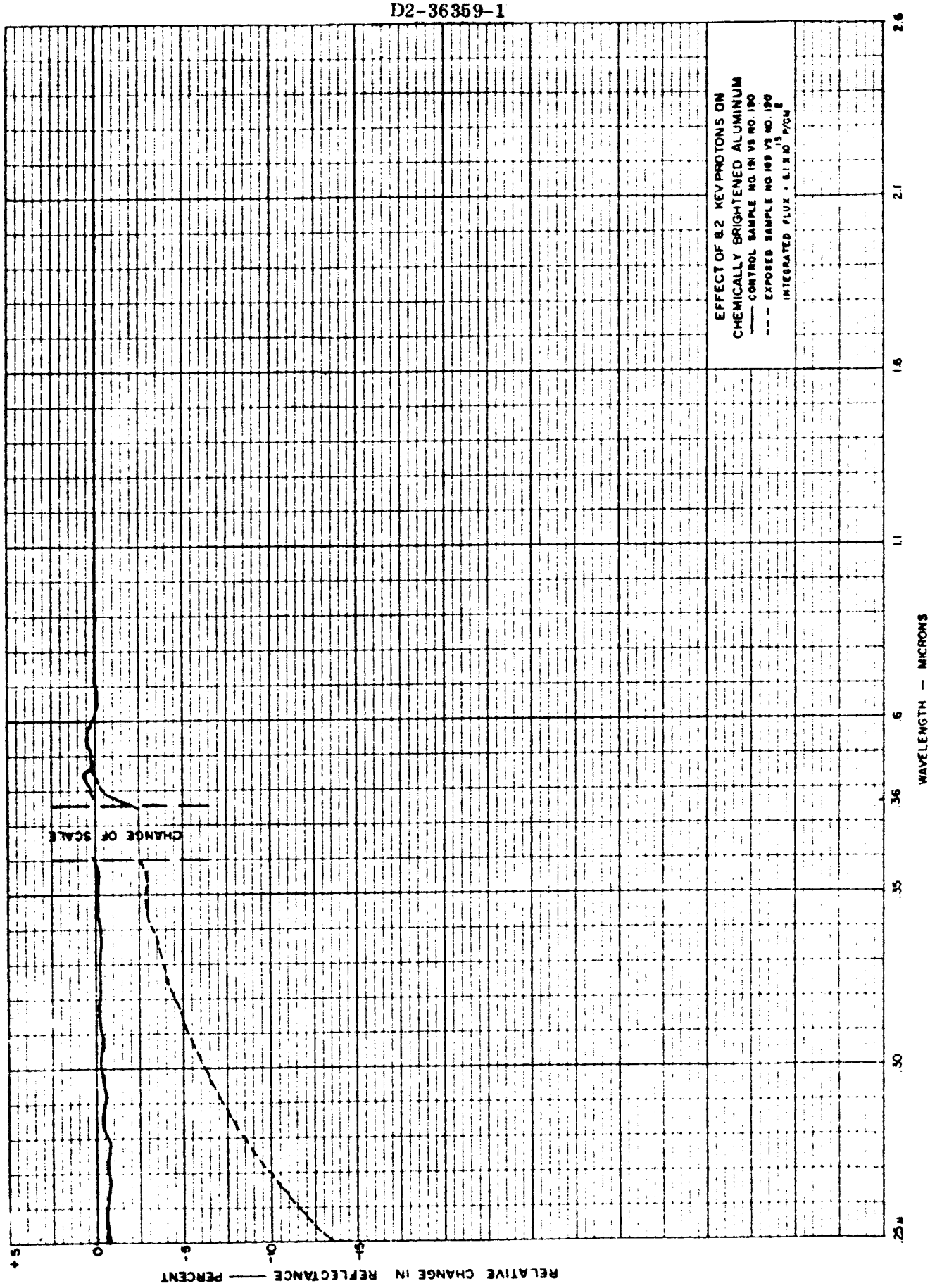
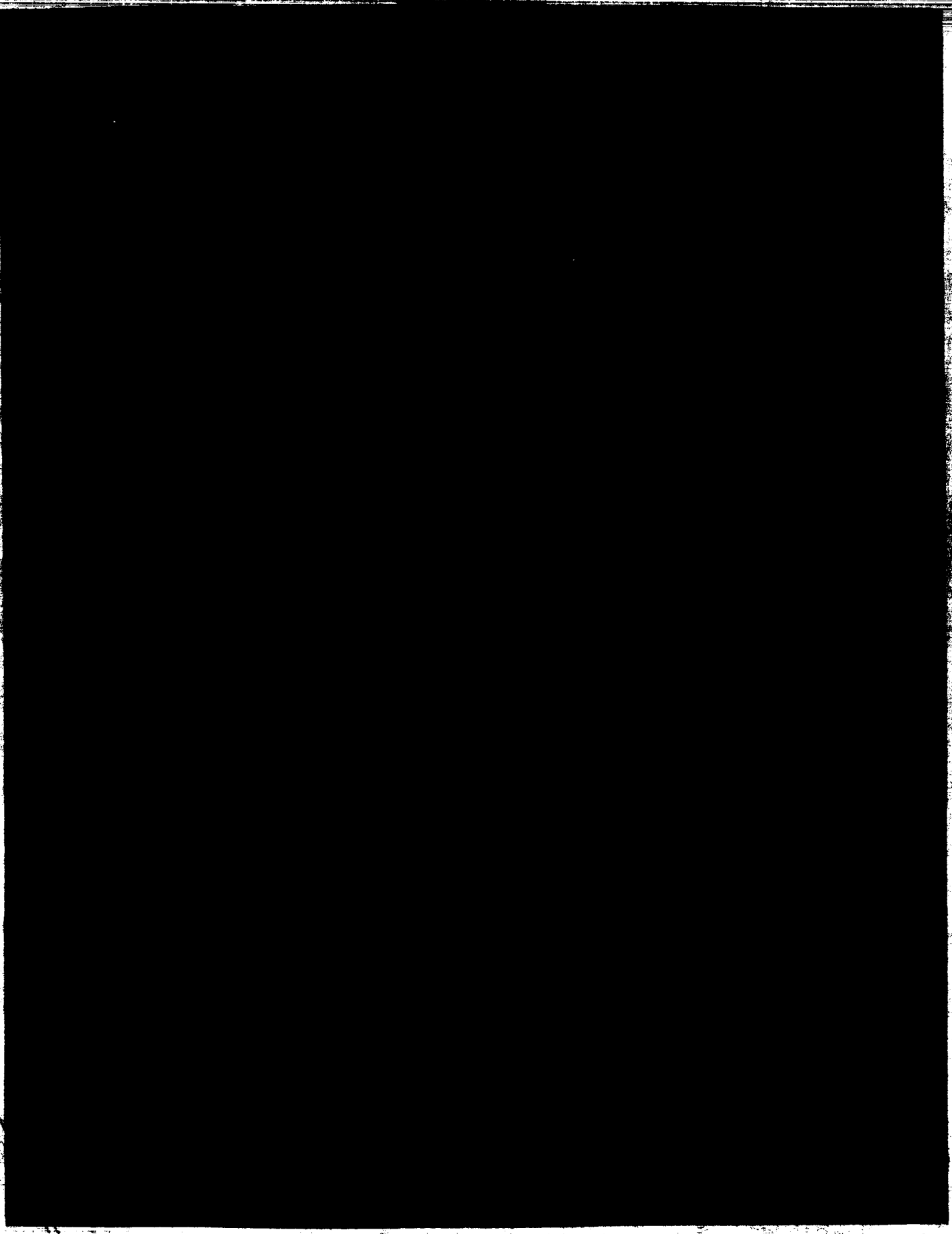
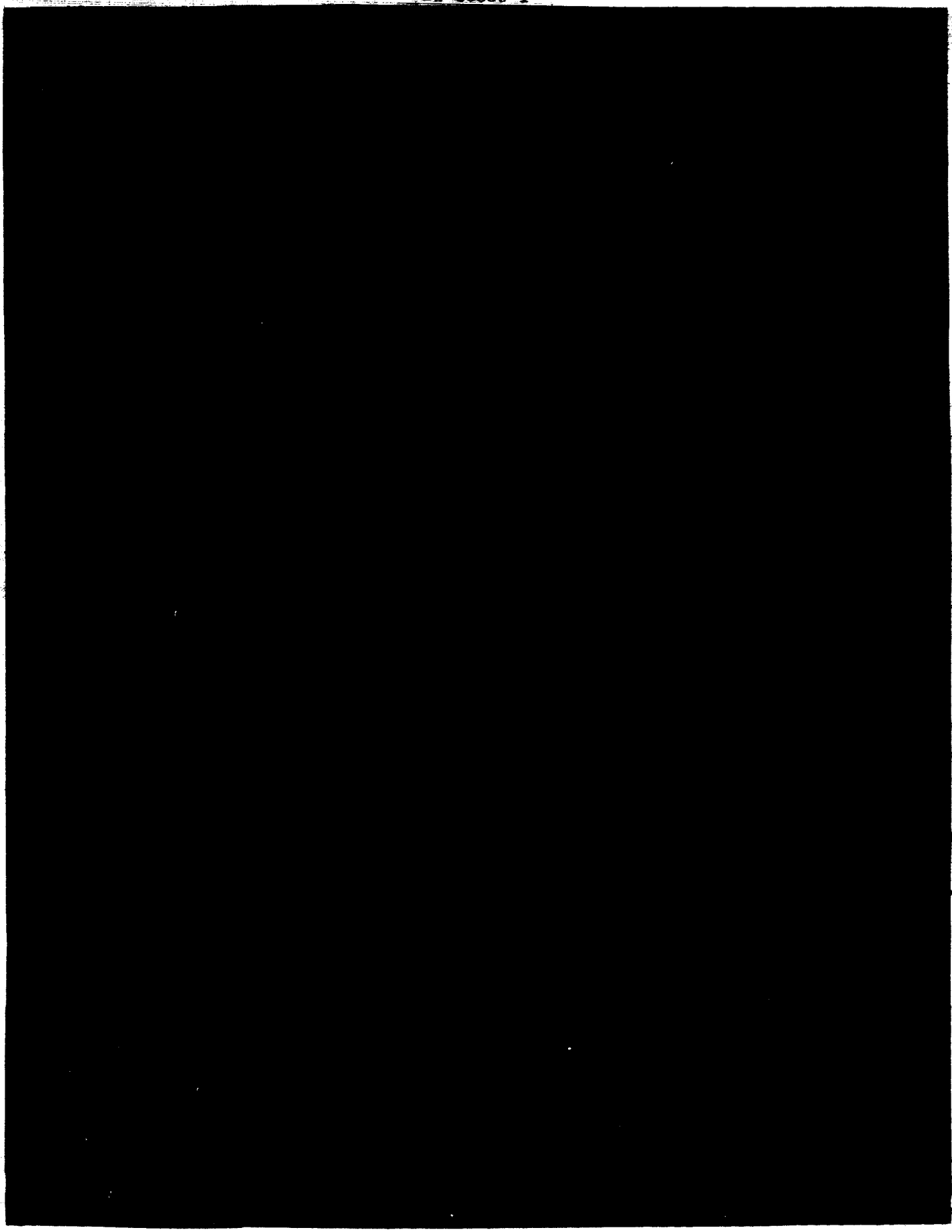

EFFECT OF 8.2 KEV PROTONS ON
CHEMICALLY BRIGHTENED ALUMINUM
—— CONTROL SAMPLE NO. 191 VS NO. 190
--- EXPOSED SAMPLE NO. 189 VS NO. 190
INTEGRATED FLUX = 6.1 X 10^15 P/CM^2
CHANGE OF SCALE
+5
0
-5
-10
-15
RELATIVE CHANGE IN REFLECTANCE —— PERCENT
.25μ
.30
.35
.36
.6
1.1
1.6
2.1
2.6
WAVELENGTH — MICRONS

FIGURE 45



CHEMICALLY BRIGHTENED ALUMINUM SURFACE BEFORE IRRADIATION

FIGURE 46



PROTON INDUCED BLISTERS ON CHEMICALLY BRIGHTENED ALUMINUM

8.2 KEV PROTONS — 6.1×10^{15} P/CM^2

FIGURE 4.7

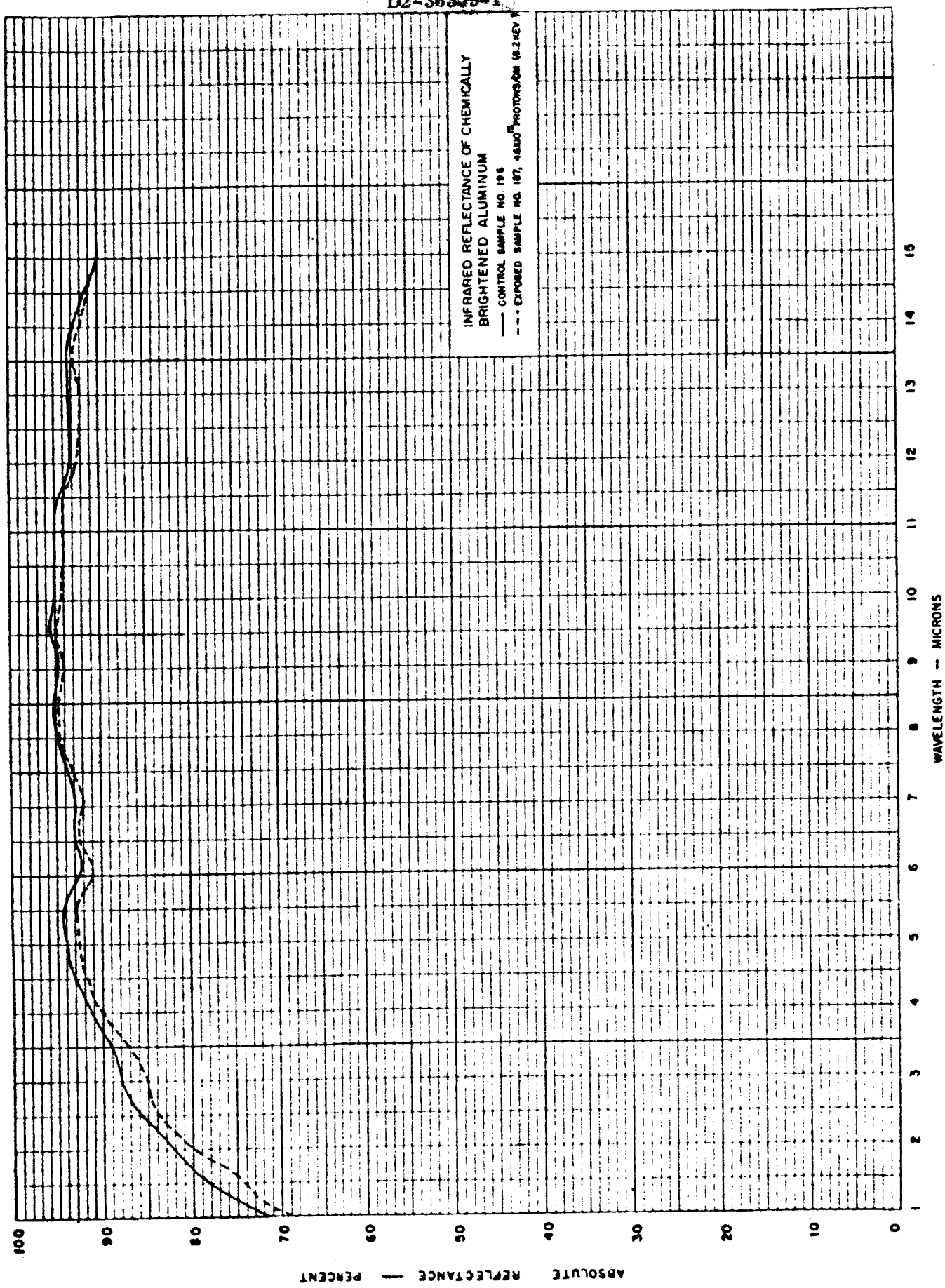

INFRARED REFLECTANCE OF CHEMICALLY BRIGHTENED ALUMINUM
—— CONTROL SAMPLE NO. 196
- - - EXPOSED SAMPLE NO. 187, 48X10^15 PROTONS/CM^2 (8.2 KEV)
ABSOLUTE REFLECTANCE — PERCENT
100
90
80
70
60
50
40
30
20
10
0
1
2
3
4
5
6
7
8
9
10
11
12
13
14
15
WAVELENGTH — MICRONS

FIGURE 48

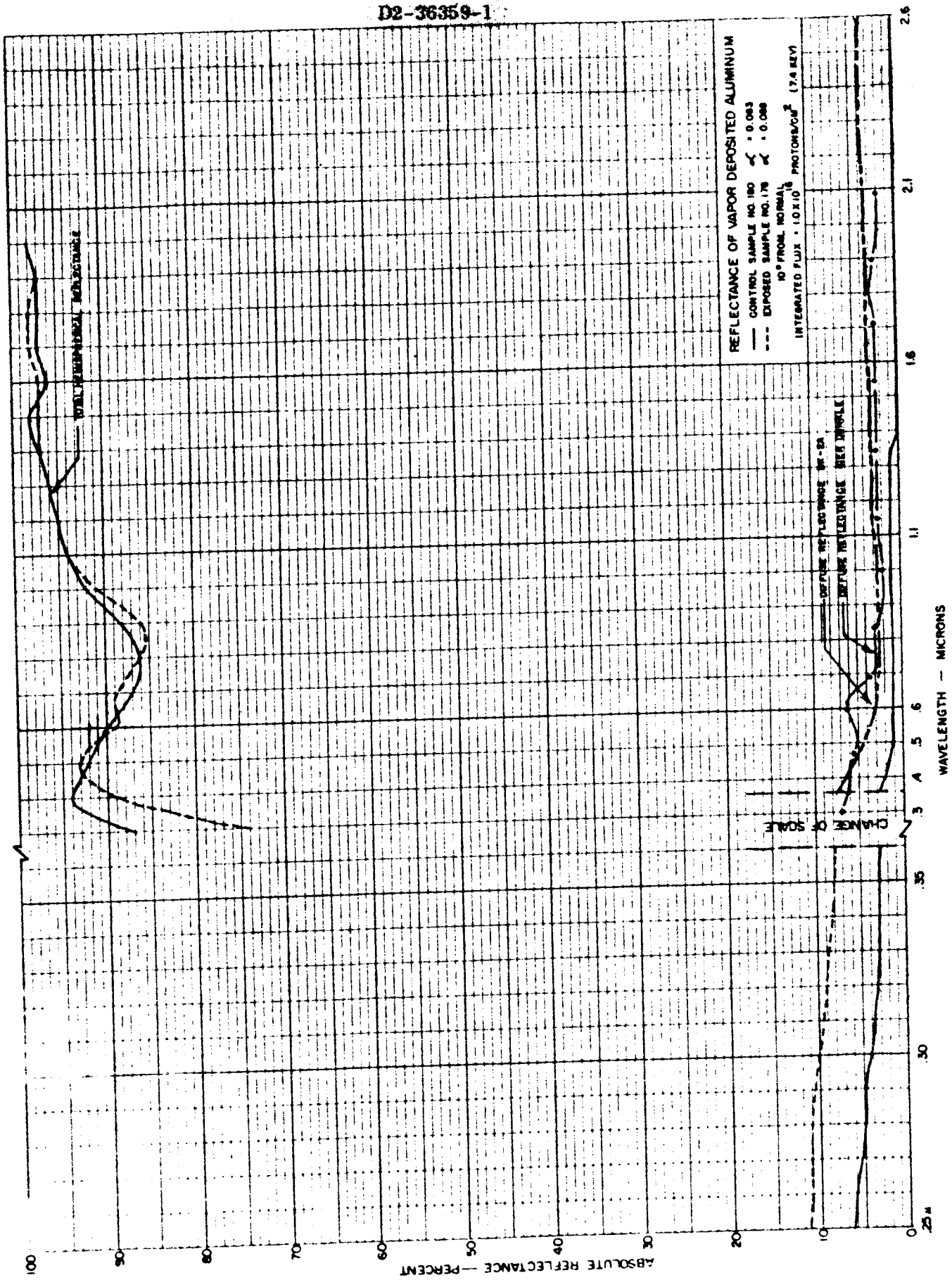

REFLECTANCE OF VAPOR DEPOSITED ALUMINUM
CONTROL SAMPLE NO. 180 α = 0.093
EXPOSED SAMPLE NO. 178 α = 0.088
10° FROM NORMAL
INTEGRATED FLUX = 1.0 X 10^16 PROTONS/CM^2 (7.4 KEV)
DIFFUSE REFLECTANCE (M-D)
DIFFUSE REFLECTANCE (BEAM ANGLE)
CHANGE OF SCALE
ABSOLUTE REFLECTANCE — PERCENT
WAVELENGTH — MICRONS

FIGURE 49

in Figure 49 were measured at a 10-degree angle from normal incidence using the Gier-Dunkle reflectometer. Calculated solar absorptances for angles of incidence of 10, 20, and 60 degrees for these two samples are shown in Table 4. The solar absorptances at 10 degrees of sample Nos. 180 and 178, respectively, are 0.083 and 0.088. This indicates a change in solar absorptance of only $\Delta \alpha_s = 0.005$ or a percentage change of 0.5 percent after irradiation with 1 x 10^{16} protons/sq.cm. with 7.4 Kev protons. Rotating the samples from 10 to 60 degrees caused the solar absorptance to increase by $\Delta \alpha_s = 0.02$.

For comparison purposes, it was found that the change in solar absorptance observed on sample No. 178 from DK-2A reflectance data (Figure 50) is $\Delta \alpha_s = 0.015$. The changes in absorptance derived from reflectance data from different reflectometers are not in agreement, however, the changes are small and are probably less than typical measurement errors or are due to the different angles of light incidence used in the two instruments. The change in spectral reflectance measured on the two instruments can be compared in Figures 49 and 50. A comparison at 0.3 microns shows a decrease in reflectance of about 16 percent and 11 percent for the Gier-Dunkle and DK-2A reflectometers, respectively.

At 0.5 microns the changes are -1.0 percent and -1.0 percent, respectively. Thus, the two sets of data are in fair agreement considering the differences in measurement techniques and the magnitude of the changes.

The decrease in total hemispherical reflectance of sample No. 178 is accompanied by an increase in diffuse reflectance as shown in Figure 49. The spectral change in diffuse reflectance measured with both types of reflectometers is shown in the figure. The comparison between data taken on the two instruments is in fair agreement.

A possible explanation for the increase in diffuse reflectance and decrease in total hemispherical reflectance (which becomes larger as wavelength becomes smaller) is an increase in surface roughness. Roughness on the surface could both scatter reflected light and cause increased light absorption due to multiple reflections. It was first suspected that the visual diffuseness observed on the irradiated samples was caused by sputtering. However, electron photomicrographs revealed a blistering phenomenon on the surface of the vapor deposited aluminum similar to that observed on the chemically brightened aluminum. Typical photomicrographs of vapor deposited aluminum surfaces before and after irradiation with 1 x 10^{16} protons/sq.cm. are shown in Figures 51 and 52. Note that the unirradiated vapor deposited aluminum surface is rougher than the chemically brightened aluminum surface shown in Figure 46. This surface roughening, caused by the vapor deposition process, reduces the reflectance of the surface. The etch marks on the chemically brightened aluminum surface are actually accentuated by the vapor deposition of additional aluminum.

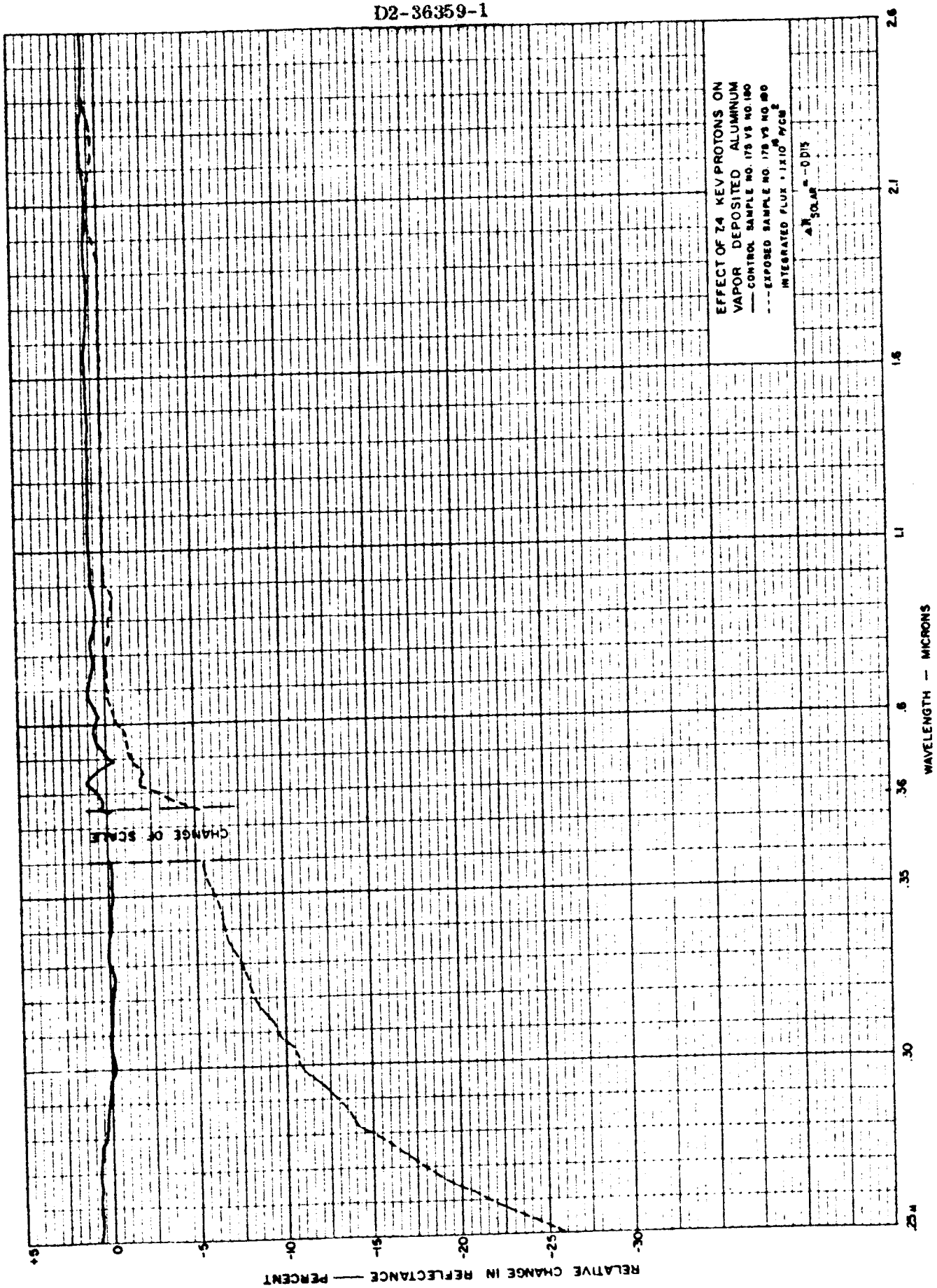
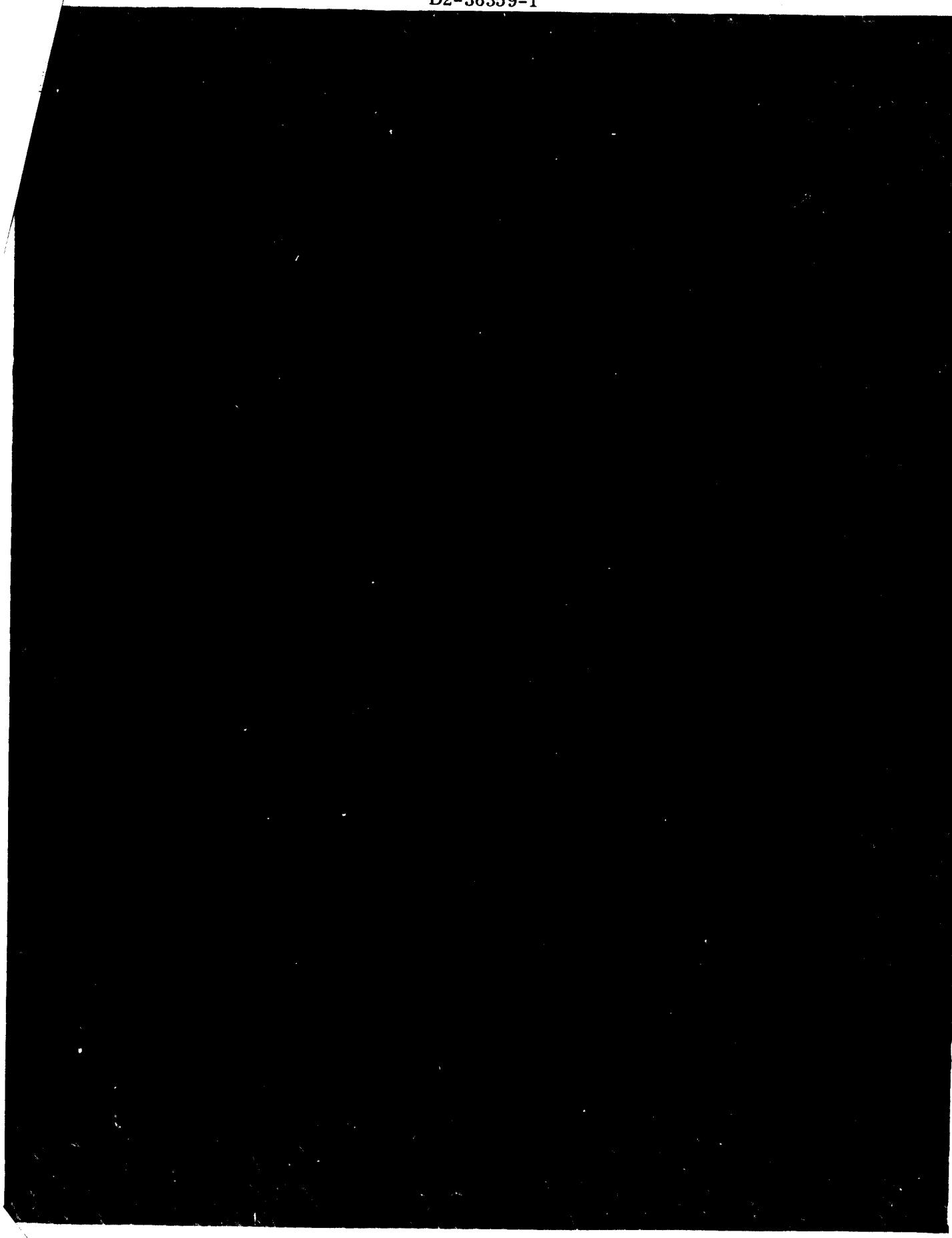
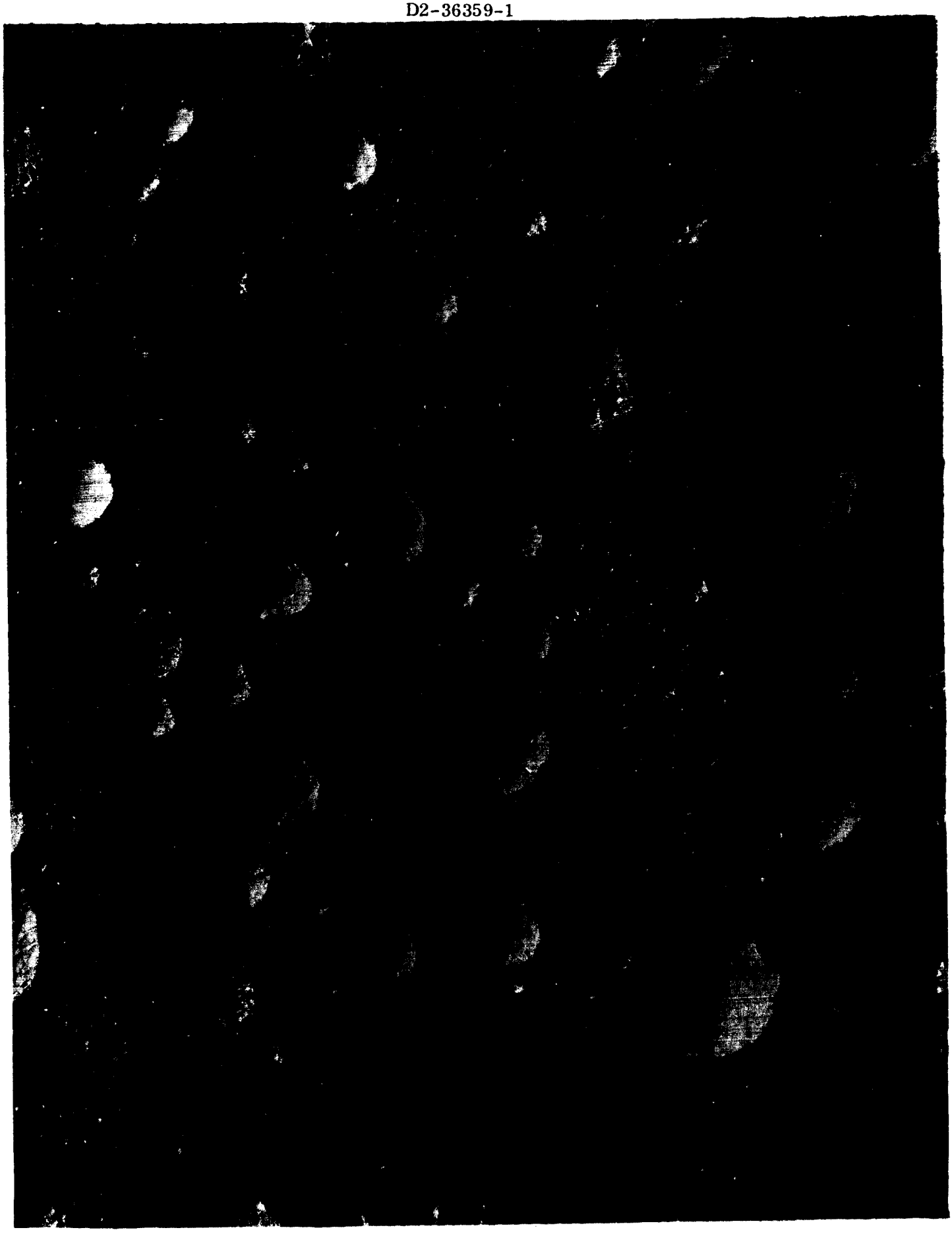

EFFECT OF 2.4 KEV PROTONS ON VAPOR DEPOSITED ALUMINUM
— CONTROL SAMPLE NO. 178 VS NO. 180
---EXPOSED SAMPLE NO. 178 VS NO. 80
INTEGRATED FLUX = 1.2 X 10^16 P/CM^2
Δα SOLAR = 0.015
CHANGE OF SCALE
RELATIVE CHANGE IN REFLECTANCE — PERCENT
+5
0
-5
-10
-15
-20
-25
-30
.25
.30
.35
.36
.6
1.1
1.6
2.1
2.6
WAVELENGTH — MICRONS

FIGURE 50



VAPOR DEPOSITED ALUMINUM SURFACE BEFORE IRRADIATION

FIGURE 51



PROTON INDUCED BLISTERS ON VAPOR DEPOSITED ALUMINUM SURFACE

FIGURE 52

After irradiation with Kev-energy protons, the aluminum surface becomes almost completely covered with small blisters (about 0.2 microns diameter) and large blisters (varying in size from 0.6 to 3.0 microns diameter). A rough calculation of the height of a 3-micron diameter blister indicated it to be 0.4 to 0.5 microns. It is interesting to note on the blistered photomicrograph that one blister (top left) has actually collapsed due to either internal gas pressure or the replication process. Small pinholes are evident at the periphery of other large blisters. As noted in Section 2.3.3, the thickness of the vapor deposited aluminum film was measured to be about one micron. The estimated range of penetration of the 7.4 Kev-energy protons is 0.2 microns. The question of whether the blisters (particularly the large ones) represent separation of the vapor deposited film from the substrate cannot yet be definitely answered. Electron micrographs of a cross section of a blistered surface, taken just prior to publication of this report, indicated that the range of 7.4 Kev protons is no larger than 0.2 microns and that the gas pockets form in the vapor deposited film. This conclusion is somewhat substantiated by the apparent thickness of the skin of the collapsed blister shown in Figure 52 which showed the skin thickness to be about 0.024 microns. Although the ranges of the protons as estimated by two different methods are not in good agreement, they indicate that the large blisters are not separation of the film from the substrate. Further analyses of blistered surfaces are recommended to resolve the unknowns of the blistering phenomena.

The effects of 8 Kev alpha particles on a vapor deposited aluminum surface are shown in Figure 53. The nature of the reflectance change produced is similar to changes produced by low energy protons.

The Mev-energy protons and alpha particles did not produce a significant damage and thus no ΔR plots are shown for them.

2.7.1.5 Zinc Oxide/Potassium Silicate Coatings — The effects of low energy protons on the reflectance of zinc oxide/potassium silicate (Z-93) thermal coatings are shown in Figure 54 and Figure C43 in Appendix C. The characteristic reflectance changes on these coatings consist of a shift of the ultraviolet cutoff wavelength and a general decrease or increase in reflectance in the infrared region. Solar absorptance changes resulting from low energy protons varied from less than $\Delta \alpha_s = 0.01$ at the threshold of 1.5×10^{14} protons/sq.cm., to $\Delta \alpha_s = 0.131$ at 1×10^{16} protons/sq.cm. A plot of the change in solar absorptance ($\Delta \alpha_s$) as a function of fluence is shown in Figure 55. Assuming that the proton fluence for an Earth-Mars mission will be about 4×10^{15} protons sq.cm. (Appendix A) of primarily low energy protons, the change in absorptance caused by these particles will be $\Delta \alpha_s$ 0.075. This represents a change of (0.075/0.157)100 47.8 percent based on an initial solar absorptance of 0.157 (Table 4).

The reflectance of sample No. 234 was measured at time intervals of 41 hours and 2300 hours after irradiation. No annealing of reflectance damage was observed over that time interval.

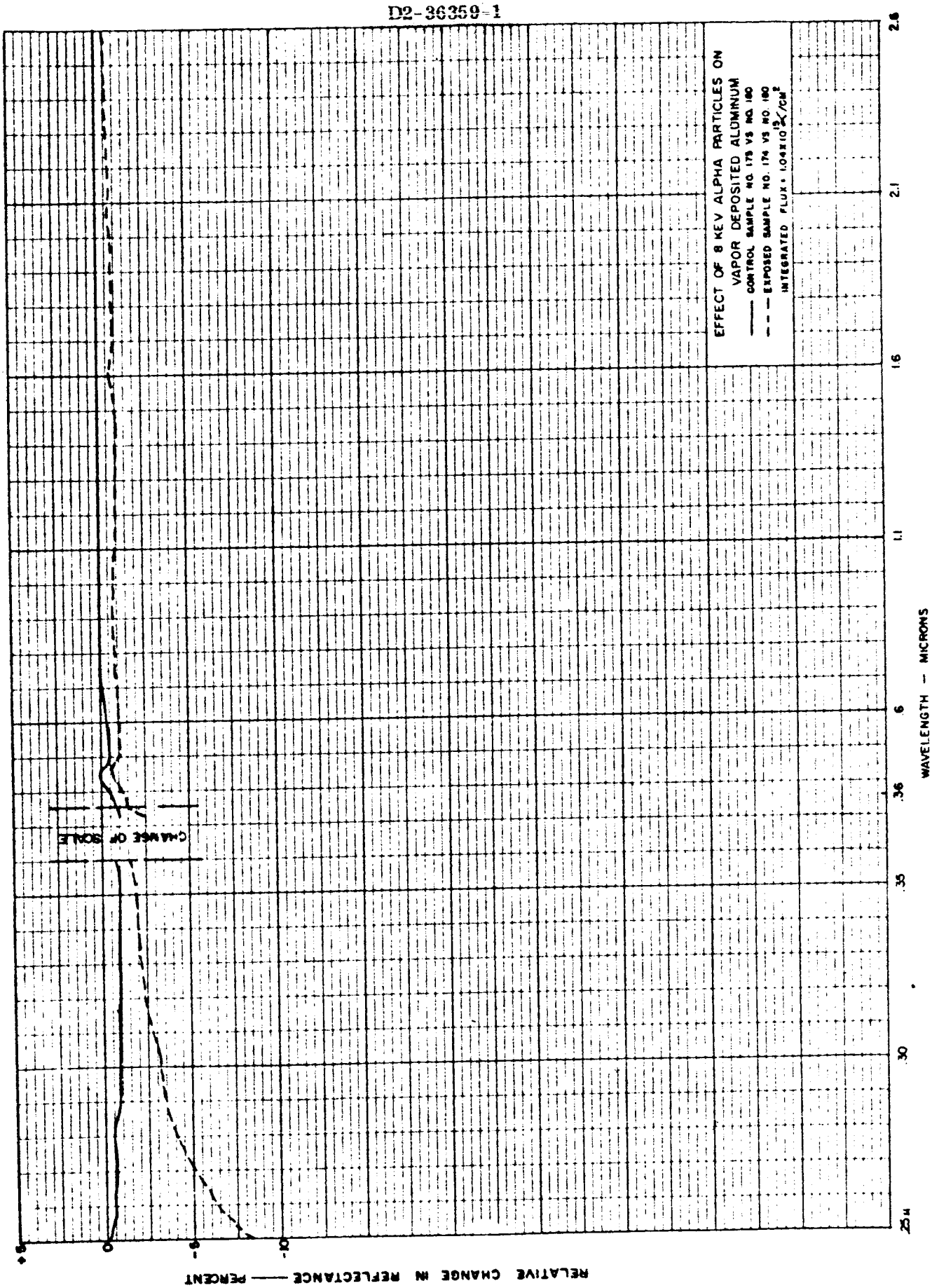

EFFECT OF 8 KEV ALPHA PARTICLES ON VAPOR DEPOSITED ALUMINUM
—— CONTROL SAMPLE NO. 173 VS NO. 180
- - - EXPOSED SAMPLE NO. 174 VS NO. 180
INTEGRATED FLUX = 1.04 X 10^12 P/CM^2
CHANGE OF SCALE
RELATIVE CHANGE IN REFLECTANCE —— PERCENT
WAVELENGTH — MICRONS
2.6
2.1
1.6
1.1
.6
.36
.35
.30
.25 M

FIGURE 53

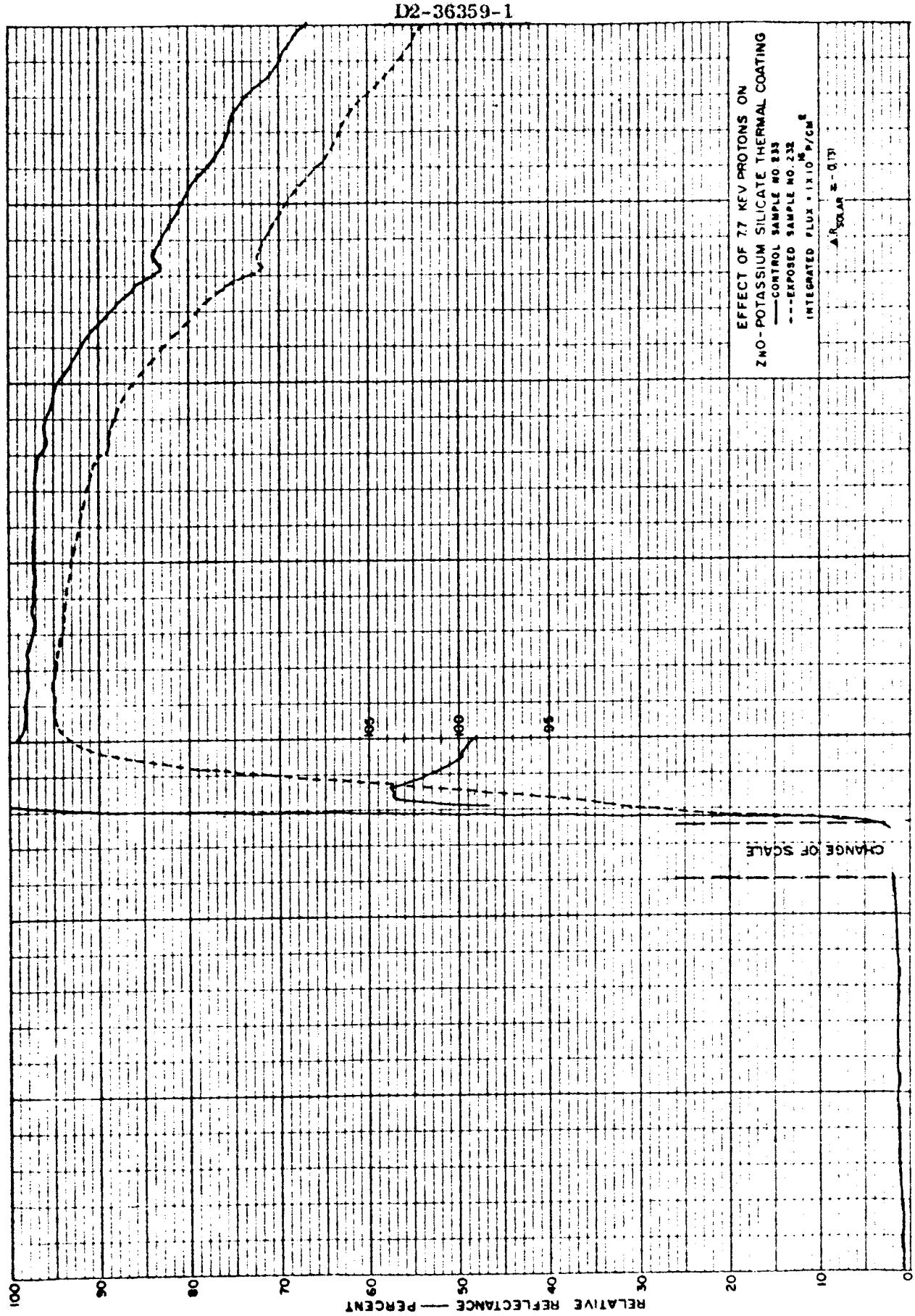

EFFECT OF 7.7 KEV PROTONS ON
ZnO-POTASSIUM SILICATE THERMAL COATING
——CONTROL SAMPLE NO 233
- - -EXPOSED SAMPLE NO. 232
INTEGRATED FLUX = 1 X 10^16 P/CM^2
ΔA_SOLAR = 0.131
CHANGE OF SCALE
RELATIVE REFLECTANCE —— PERCENT
WAVELENGTH — MICRONS

FIGURE 54

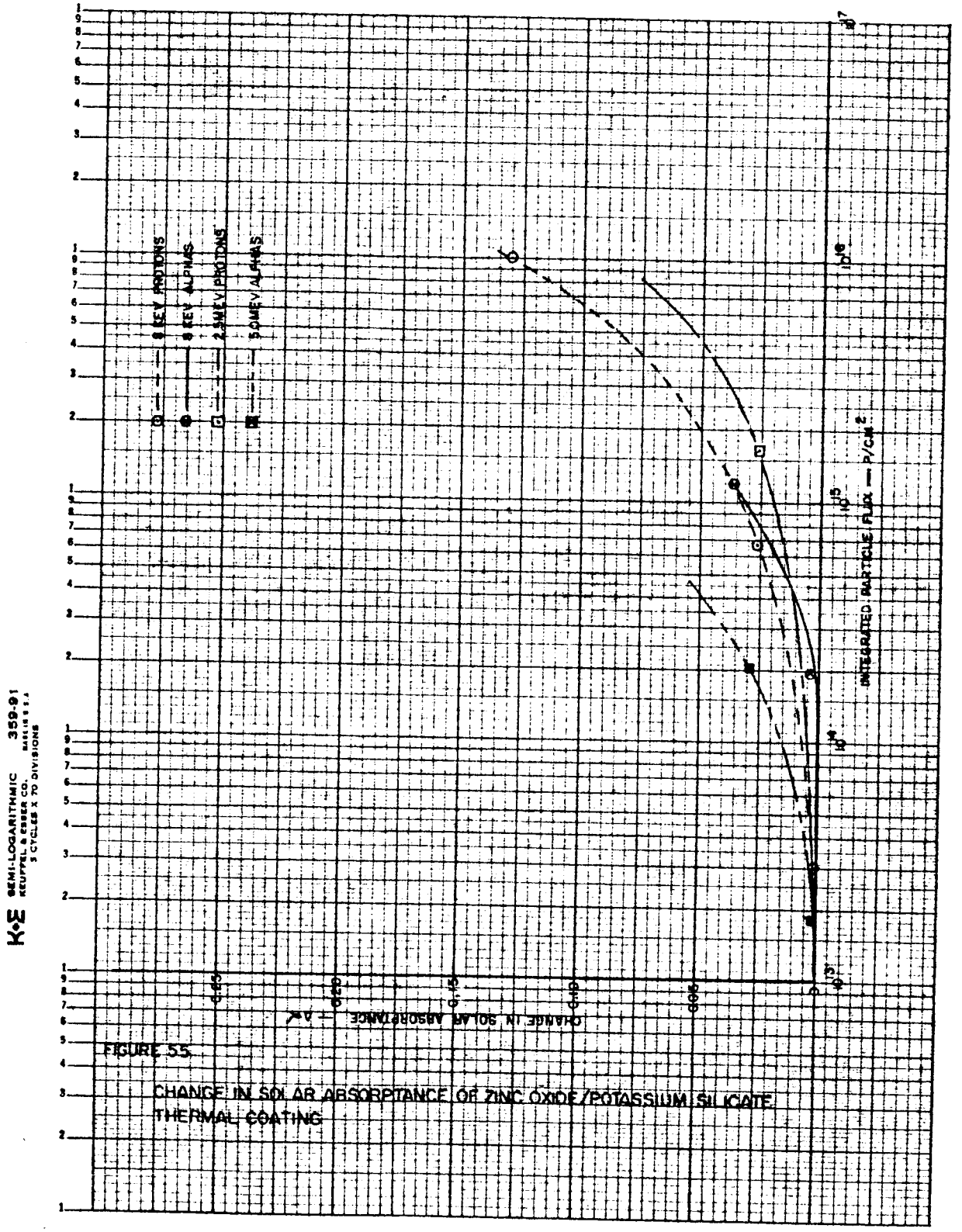


FIGURE 55.

CHANGE IN SOLAR ABSORPTANCE OF ZINC OXIDE/POTASSIUM SILICATE THERMAL COATING

USE FOR TYPEWRITTEN MATERIAL ONLY

The effects of 2.5 Mev protons on the reflectance of Z-93 coatings are shown in Figures C44 and C45 in Appendix C. Resulting solar absorptance changes are shown in Figure 55. Although only one data point was obtained where significant damage occurred, it is indicated that the 2.5 Mev protons are less damaging than Kev-energy protons. To produce equivalent damage of $\Delta \alpha_s = 0.025$, about 2.5 times more 2.5 Mev protons are required than Kev-energy protons. Since the integral proton flux of energies greater than 2.5 Mev expected for an Earth-Mars mission is only about 5×10^{10} protons/sq.cm., no reflectance changes are expected from the protons of energy greater than 2.5 Mev.

The reflectance data for low energy alpha particles is shown in Figures C46 and C47 in Appendix C. Solar absorptance changes produced by the low energy alpha particles are shown in Figure 55. The curve, drawn through the two data points shown, closely coincides with the low-energy proton curve. The fluence of primarily low energy alpha particles expected for an Earth-Mars mission is about 4×10^{14} alphas/sq.cm. Thus, a change in solar absorptance of $\Delta \alpha_s = 0.01$ is expected due to the low energy alpha particles. The percentage change in absorptance for the Earth-Mars mission due to low energy alpha particles is (0.01/0.157)100 = 6.4 percent.

The reflectance data for 5.0 Mev alpha particle tests on the Z-93 coatings is presented in Figures C48 and C49 in Appendix C. Solar absorptance changes produced by the high energy alphas are shown in Figure 55. It was found that the high-energy alphas are considerably more damaging than protons or alphas of other energies. To produce equivalent damage of $\Delta \alpha_s = 0.03$, about 80 times more 2.5 Mev protons are required than 5.0 Mev alpha particles. The estimated integral flux of alpha particles of energy greater than 5.0 Mev for an Earth-Mars mission is 5×10^{10} alphas/sq.cm. (Appendix A). Since this integral flux of high energy alpha particles is substantially below the damage threshold of about 7×10^{13} alphas/sq.cm., no damage is expected from these particles.

If the assumption is correct that effects of different particles are additive, the total change in solar absorptance expected on an Earth-Mars mission for the Z-93 coating is $\Delta \alpha_s = 0.075 + 0.01 = 0.085$. This would correspond to a percentage increase in absorptance of (0.085/0.157)100 = 54 percent.

Measurements of infrared reflectance were made on control sample No. 227 and exposed sample No. 232 to ascertain whether low energy protons would have any effect on emittance. The results of these measurements, shown in Figure 56, indicate that the reflectance degradation caused by an exposure to 1.0×10^{16} protons/sq.cm. of 7.7 Kev protons continues out to a wavelength of about 6.5 microns. The emittance of both specimens, however, was calculated to be 0.855 indicating no change in emittance. The reason that the reflectance changes without a corresponding change in emittance is that a 22°C black-body spectrum was assumed in the calculations and this spectrum has only about 7 percent of its energy at wavelengths shorter than 7 microns.

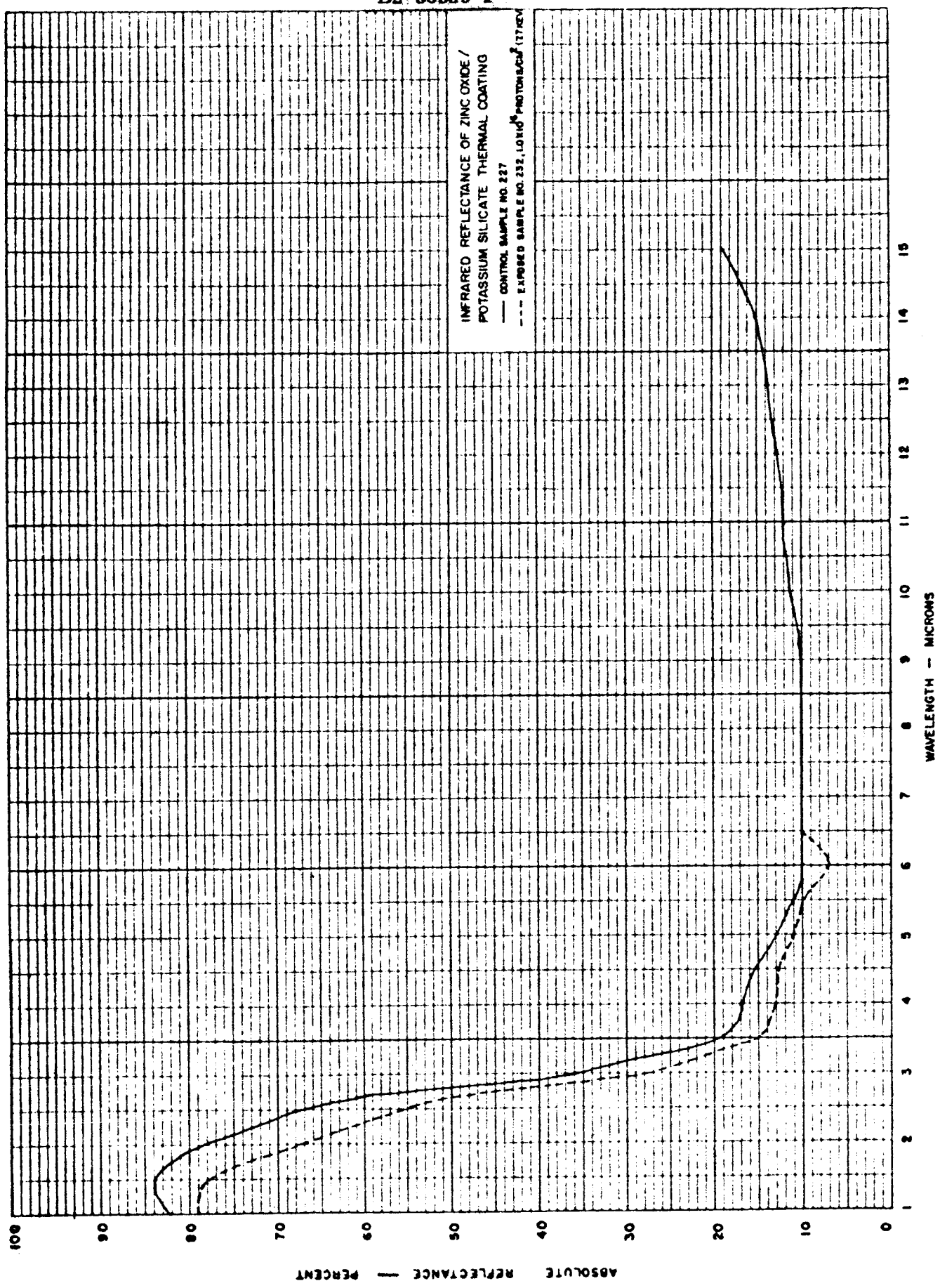

INFRARED REFLECTANCE OF ZINC OXIDE / POTASSIUM SILICATE THERMAL COATING
— CONTROL SAMPLE NO. 227
--- EXPOSED SAMPLE NO. 232, 1.0 X 10^15 PROTONS/CM^2 (17 KEV)
ABSOLUTE REFLECTANCE — PERCENT
100
90
80
70
60
50
40
30
20
10
0
1
2
3
4
5
6
7
8
9
10
11
12
13
14
15
WAVELENGTH — MICRONS

FIGURE 56

2.7.1.6 Zinc Oxide/LTV-602 Coatings — The effects of low energy protons on the reflectance of zinc oxide/LTV-602 (S-13) thermal coatings are shown in Figure 57 and Figure C50 in Appendix C. The characteristic reflectance changes in the S-13 coatings are a slight increase in reflectance in the ultraviolet region, a shift in the ultraviolet absorption cutoff, and a general decrease or increase in the infrared wavelength region. A plot of the change in solar absorptance ($\Delta \alpha_s$) as a function of fluence for the S-13 coatings is shown in Figure 58. For the approximate fluence of low energy protons expected for an Earth-Mars mission (4×10^{15} protons/sq.cm.), a change in solar absorptance of $\Delta \alpha_s = 0.048$ will occur. This represents a percentage increase in absorptance of (0.048/0.181)100 = 26.5 percent based on the initial solar absorptance of 0.181 given in Table 4. Note that this is lower than the change expected for the Z-93 coatings.

The reflectance of sample No. 216 was measured at time intervals of 14 hours and 2070 hours after irradiation. No annealing of reflectance damage was observed.

The effects of 2.5 Mev protons on reflectance of S-13 coatings are shown in Figures C51, C52, and C53 in Appendix C. Figure C53 shows the reflectance measured at 3 different positions on sample No. 220 which was located in the inner ring of the scattering chamber. Resulting solar absorptance changes are shown in Figure 58. Although only two of the three samples irradiated in this test showed measurable damage, the three reflectance measurements made on the heavily damaged sample provided additional data points. It was noted in this test that the heavily damaged S-13 coating exhibited cracking, however, the coating still adhered to the aluminum. It can be seen in Figure 58 that the high energy protons are more damaging to the S-13 coatings than the low energy protons. The reverse was true for Z-93 coatings. To produce equivalent damage of $\Delta \alpha_s = 0.085$, about 2 times more low energy protons than high energy protons are required. No solar absorptance changes due to high-energy protons are anticipated for an Earth-Mars mission.

The reflectance data for low-energy alpha particle tests are shown in Figures C54 and C55 in Appendix C. The maximum change in solar absorptance obtained in low energy alpha particle tests was $\Delta \alpha_s = 0.005$ at 1.49×10^{15} alphas/sq.cm. Therefore, no correlations can be made between this data and results of other tests. It can only be concluded that low energy alpha particles have less effect than low energy protons on S-13 coatings.

The reflectance data for high energy alpha particle tests is shown in Figures C56 and C57 in Appendix C. Figure C57 shows the reflectance measured at three different positions on sample No. 224 which was located in the inner ring of the scattering chamber. The resulting solar absorptance changes produced in the S-13 specimens are shown in Figure 58. It can be seen in the figure that

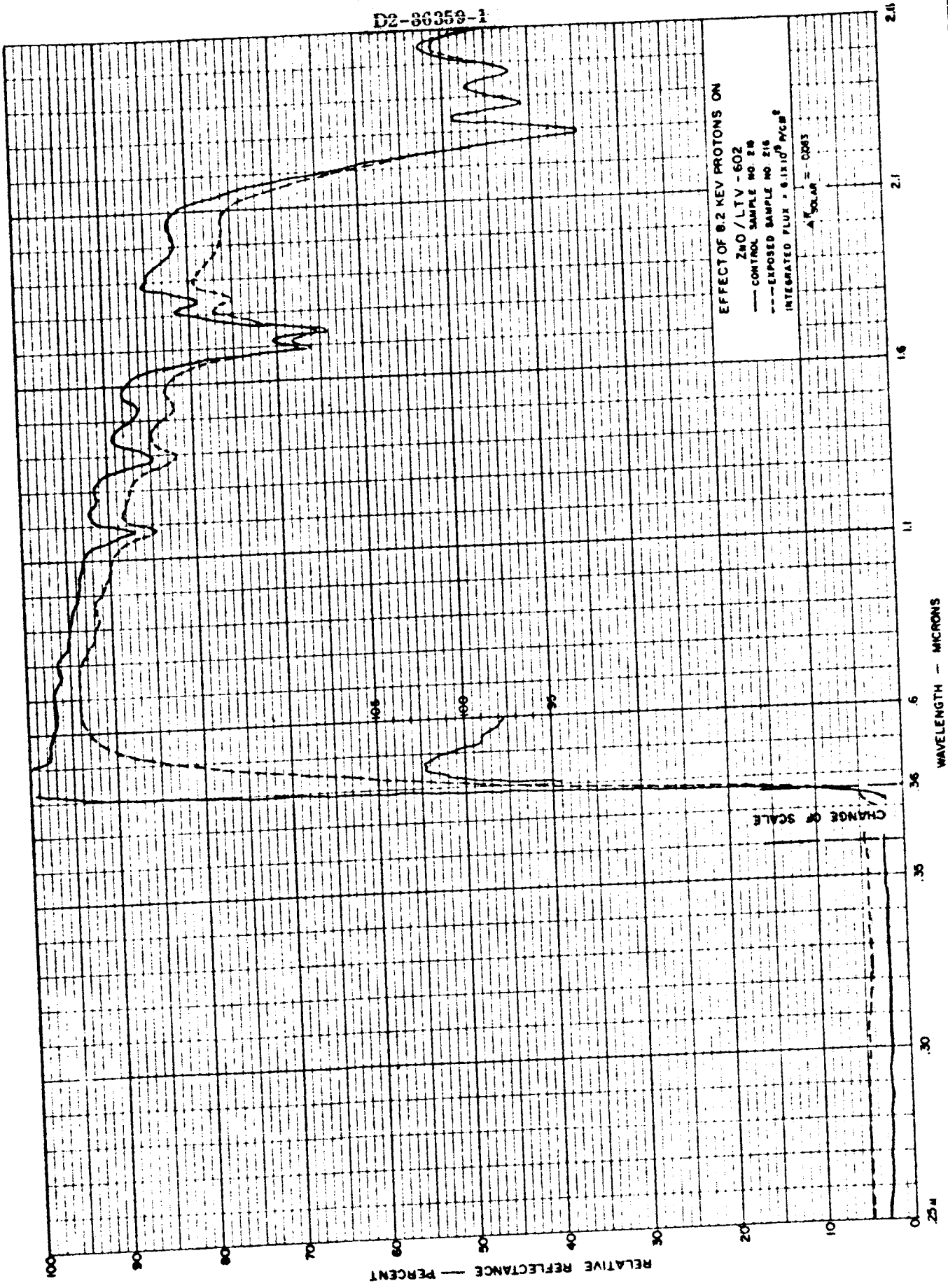

EFFECT OF 8.2 KEV PROTONS ON
ZnO / LTV - 602
—— CONTROL SAMPLE NO. 218
- - - EXPOSED SAMPLE NO. 216
INTEGRATED FLUX = 8.1X10^15 P/CM^2
Δα SOLAR = - 0.043
RELATIVE REFLECTANCE — PERCENT
WAVELENGTH — MICRONS
CHANGE OF SCALE
100
90
80
70
60
50
40
30
20
10
0
.25μ
.30
.36
.6
1.1
1.6
2.1
2.6

FIGURE 57

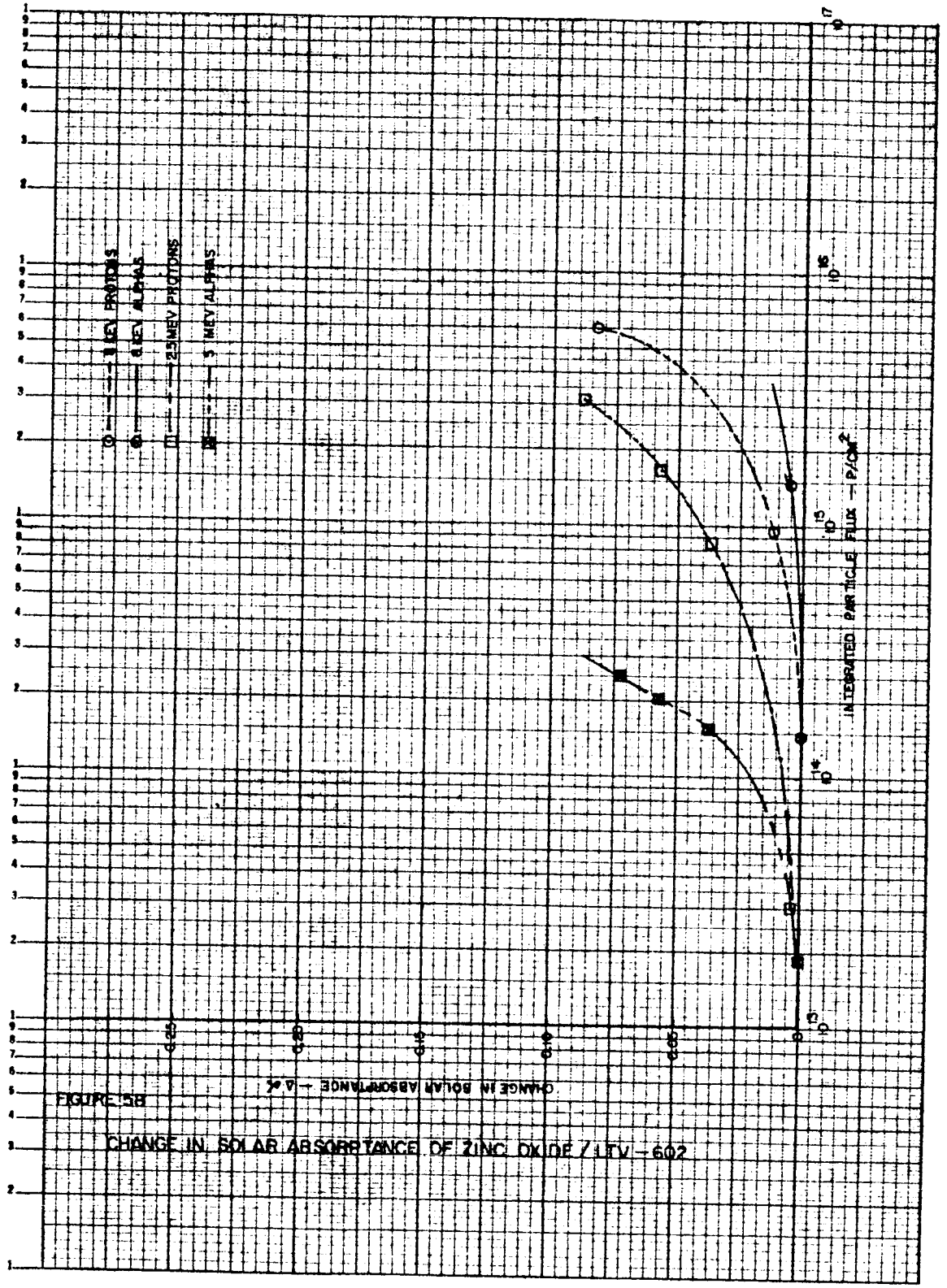


FIGURE 58

CHANGE IN SOLAR ABSORPTANCE OF ZINC OXIDE / LTV-602

USE FOR TYPEWRITTEN MATERIAL ONLY

the high energy alpha particles were far more damaging than protons or low energy alpha particles. To produce equivalent damage of $\Delta \alpha_s = 0.05$, a factor of about 74 more high energy protons than high energy alpha particles is required. The anticipated change in solar absorptance on an Earth-Mars mission due to high energy alpha particles will be negligible because of the low integral flux of the high energy alphas.

Summarizing the expected charged particle damage to the S-13 coating for an Earth-Mars mission, the total change in solar absorptance will be $\Delta \alpha_s = 0.048 + 0.005 = 0.053$. This represents a percentage increase in absorptance of $(0.053/0.181)100 = 29.3$ percent.

Measurements of infrared reflectance were made on control sample No. 214 and exposed sample No. 216 as shown in Figure 59. Contrary to results obtained with Z-93 coatings, the S-13 sample exposed to 6.1×10^{15} protons/sq.cm. of 8.2 Kev protons exhibited an increase in reflectance out as far as 15 microns (the measurement limit). As a result of this, the emittance of sample No. 216 changed from 0.89 before irradiation to 0.85 after irradiation.

2.7.2 Short Circuit Current Output of Solar Cell Concentrator Panel

The primary goal of this contract was to determine the effect of protons and alpha particles on the performance of V-ridge concentrating solar cell panels. A simulated Earth-Mars mission was of particular interest since panels of this type have been proposed for that mission. An estimate was made of the respective fluences of protons and alpha particles for an Earth-Mars mission (Appendix A). Since the estimates of fluences are subject to change as more space environment measurements are made, the short-circuit current output of the panel was calculated for a range of fluences. The short-circuit current was calculated rather than power output because it could be obtained directly from the spectral response data and is directly proportional to the power output. Details of the method of calculation were discussed in Section 2.6.3.

The results of solar cell current calculations are shown in Table 5. As noted in the table, calculations were made from DK-2A reflectance data on exposed sample No.'s 29, 38, and 42. Changes in short circuit current in these calculations were based on data from control sample No. 10. Calculations were also made using Gier-Dunkle reflectometer data on exposed sample No.'s 29 and 51. For the Gier-Dunkle data calculations, changes were based on the reflectance of control sample No. 21. On sample No.'s 29 and 51, the change in short-circuit current was calculated for angles of 12 degrees and 62 degrees from normal.

It was found that a fluence of 1×10^{16} protons sq.cm. will produce an insignificant change in output of the solar cells. The DK-2A data on sample No. 29, measured at 5 degrees from normal, showed a decrease of only 0.12 percent.

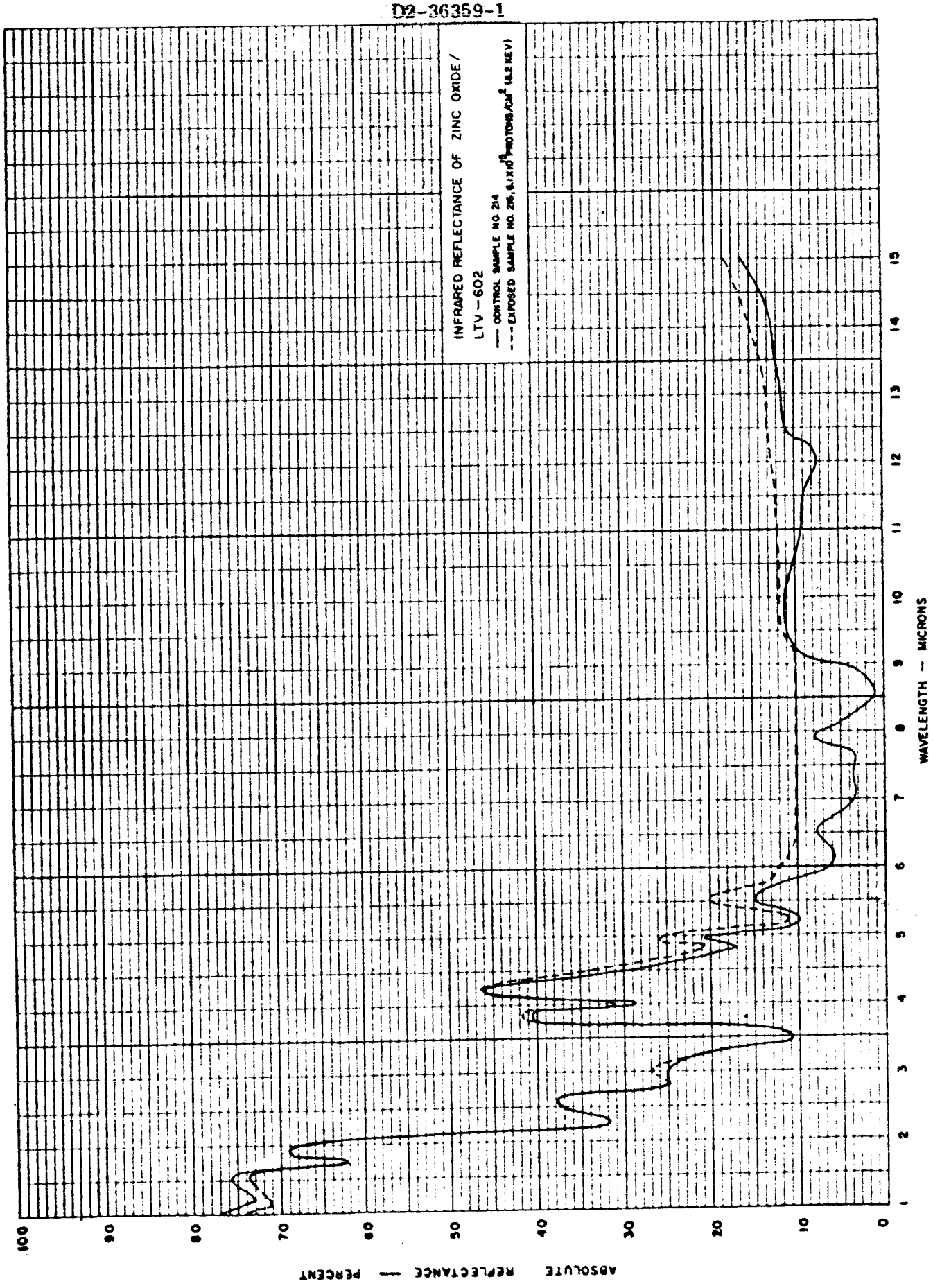

INFRARED REFLECTANCE OF ZINC OXIDE/
LTV-602
— CONTROL SAMPLE NO. 214
---EXPOSED SAMPLE NO. 216, 6.1 X 10^15 PROTONS/CM^2 (4.8 KEV)
ABSOLUTE REFLECTANCE — PERCENT
100
90
80
70
60
50
40
30
20
10
0
1
2
3
4
5
6
7
8
9
10
11
12
13
14
15
WAVELENGTH — MICRONS

FIGURE 59

Table 5: SUMMARY OF SOLAR CELL CALCULATIONS

Exposed Specimen No.	Control Specimen No.	Percent Change S.C. Current	Reflectometer Used	Angle of Incidence, Degrees	Integrated Flux, P/cm^2	Particle Type	Particle Energy Kev
29	10	-0.12	DK-2A	5	1×10^{16}	Protons	4.7
38	10	-32.2	DK-2A	5	1.47×10^{17}	Protons	5.3
42	10	-13.8	DK-2A	5	1.01×10^{17}	Protons	9.0
51	21	-5.7	Gier Dunkle	62	9.25×10^{16}	Protons	3.4
51	21	-7.8	Gier Dunkle	12	9.25×10^{16}	Protons	3.4
29	21	-1.13	Gier Dunkle	62	1×10^{16}	Protons	4.7
29	21	+0.07	Gier Dunkle	12	1×10^{16}	Protons	4.7

The Gier-Dunkle data on the same sample showed an increase in output of 0.07 and 1.13 percent for angles of 12 degrees and 62 degrees, respectively. In a concentrating solar cell panel the light is reflected at an angle of about 60 degrees from normal. Therefore, it can be concluded that a fluence of 1×10^{16} protons/sq.cm. of 4.7 Kev protons will produce a slight increase (1.13 percent) in solar panel output. The unexpected increase in reflectance is caused by the partial elimination of the characteristic aluminum absorption band at 0.83 microns when the surface is rotated to 60 degrees from normal as shown in Figure 30. At this particular angle of incidence, an interference maximum is located at about the same wavelength as the aluminum absorption minimum. The net result is a substantial increase in reflectance in the wavelength region near the peak of the solar cell spectral response (0.83 microns, Figure 27).

Significant reductions in solar cell output did occur for surfaces bombarded with fluences in the range of 1×10^{17} protons sq.cm. The calculations based on DK-2A data showed decreases in short circuit current of 13.8 and 32.2 percent for fluences of 1.01×10^{17} and 1.47×10^{17} protons/sq.cm., respectively. Calculations based on Gier-Dunkle reflectance data at 12 degrees from normal showed a decrease of 7.8 percent for a fluence of 9.25×10^{16} protons/sq.cm. The 6 percent difference between the results obtained by two different reflectance measuring techniques may be attributed to measurement errors, the 7 degree difference in viewing angle, or possibly the difference in proton energies and fluxes. The maximum decrease in short-circuit current noted was 32.2 percent for a fluence of 1.47×10^{17} protons/sq.cm.

In general, it was concluded from these calculations that the change in solar-cell short circuit current output for an Earth-Mars mission will be negligible. A similar conclusion can be made for solar wind alpha particles and solar cosmic ray protons and alpha particles based on their respective reflectance data.

3.0 CONCLUSIONS AND RECOMMENDATIONS

The following conclusions can be made as a result of the research conducted under JPL Contract 950998:

1) The solar reflectance or absorptance of the barrier-layer anodic coated aluminum reflective surfaces is not expected to change as a result of solar charged-particle irradiation on an Earth-Mars mission. Consequently, it was also concluded that the short-circuit current output of a solar cell concentrating panel will not change on the same mission because of the negligible reflectance change.

2) The solar absorptances of the zinc oxide/potassium silicate (Z-93) and zinc oxide/LTV-602 (S-13) spacecraft coatings will increase substantially due to solar charged-particle irradiation on an Earth-Mars mission.

3) Test procedures and facilities developed in this program proved to be satisfactory for irradiation of samples.

The following recommendations are presented:

1) Selected test samples which were bombarded with protons or alpha particles in this program, should be irradiated with an ultraviolet exposure typical of an Earth-Mars mission. Similar samples which have not previously been bombarded with charged particles, should also be exposed to ultraviolet in the same test. This follow-on type test is recommended because it is believed that coatings will degrade much more rapidly in ultraviolet tests when they have previously been irradiated with protons and alpha particles. A preliminary test in a Boeing research program has shown that barrier-layer anodized aluminum degrades a significant amount when exposed ultraviolet radiation after irradiation with protons. The ultraviolet follow-on tests should be seriously considered because they would provide additional valuable data, applicable to Voyager vehicle design, at a relatively low cost compared to the cost of sample irradiation with charged particles.

2) Both the S-13 and Z-93 white coatings should be subjected to additional Kev-energy proton and alpha particle tests. The purpose of these tests would be to more accurately establish the dependence of damage on particle energy and type, and to obtain more data on the change in solar absorptance versus fluence.

3) The blistering phenomena observed on aluminum surfaces should be studied in much more detail to determine the mechanism of formation, the effect on mechanical and chemical properties, and the effect on optical properties such as specular reflectance, and the effect of particle energy on blister formation.

4) A study of the range of 1 to 10 Kev-energy protons and alpha particles in solids should be conducted. Radiation effects analyses and energy loss (dE/dx) studies are of questionable accuracy since existing data in the 1 to 10 Kev range has been extrapolated from higher energies.

4.0 REFERENCES

1) "Photovoltaic Concentrator Development - Final Report," Boeing Document D2-90480, Prepared under JPL Contract 950270, by R. J. Tallent and others, October 1963.

2) "Concentrator Structure for a Solar Energy Photovoltaic Conversion System - Final Report," Boeing Document D2-90041-A, by R. J. Tallent and others, Prepared under JPL Contract 950122, November 1961.

3) "Radiation Degradation Studies of Specular Reflecting Surfaces," Boeing Document D2-20334-1, by R. B. Gillette, R. R. Brown, and D. D. Abbott, January 1964.

4) "Performance Characteristics of Barrier-Layer Anodic Coatings," Boeing Document D2-20423-1, by R. B. Gillette and D. R. Clarke, April 1964.

5) "On the Preparation of Hard Oxide Films with Precisely Controlled Thickness on Evaporated Aluminum Mirrors," by G. Hass, Journal of Optical Society of America, Vol. 39, No. 7, July 1949.

6) "Stable White Coatings," by G. A. Zerlaut and Y. Harada, research report prepared under JPL Contract No. 950111, November 1962.

7) "The Solar Constant," by F. S. Johnson, Journal of Meteorology, Vol. 11, No. 6, December 1954.

8) "Increasing the Far-Ultraviolet Reflectance of Silicon-Oxide-Protected Aluminum Mirrors by Ultraviolet Irradiation," by A. P. Bradford and G. Hass, Journal of the Optical Society of America, Vol. 53, No. 9, September 1963.

5.0 APPENDICES

APPENDIX A

STUDY OF THE RADIATION ENVIRONMENT FOR AN EARTH-MARS MISSION

The purpose of this study was to estimate the charged particle radiation environment for an Earth-Mars mission. The radiation environment of interest consists of protons and alpha particles emanating from the sun, the solar wind at low energies and solar cosmic rays at high energies. The solar wind is the continuous expansion of the solar corona and has been measured by satellites which went beyond the magnetosphere. Data from Explorer X[1], Lunik II and III[2] indicate that the solar wind, while continuous, has turbulent variation associated with magnetic irregularities in interplanetary space. Velocity variations range from 300 to 800 km/sec with occasional excursions to 1200 km/sec, and the particle density varies from 1 to 30 particles/cm^3 with an average of 5 particles/cm^3. Investigations currently being made by Mariner 4, IMP-I and OGO-I will give a better definition of the solar wind, and as these studies are continued over the next several years the solar cycle variation will be determined. An evaluation of the 230-day Mars mission indicates a proton fluence of 4×10^{15} protons/sq.cm. with an average energy of 1 Kev., and an integrated alpha particle flux of 4×10^{14} alphas/sq.cm. with an average energy of 2 Kev. from the direction of the sun.

The model environment for solar cosmic ray protons is shown in Figure A1. This evaluation derives from the work of Webber[4] and is based on 1959, the year of maximum solar cosmic ray activity of solar cycle 19. The values below 10 Mev are an extrapolation of the exponential rigidity spectrum, but have been enhanced to account for the "magnetic storm particles."[5,6] Very few measurements have been made of solar cosmic rays below 10 Mev and the available data are not in good agreement. Observations of polar glow aurora during polar cap absorption events[7] indicate few particles below 1 Mev, thus the integral spectrum below 1 Mev is expected to become flat. Measurements made at the same time with rocket-borne scintillation counters indicate a steeply rising spectrum below 1 Mev. Both of these measurements were made near the earth where the geomagnetic field can greatly affect impinging low energy particles. An adequate definition of the solar cosmic ray spectrum at low energies will be made by the current generation of satellites which have measurement capability at low energy and which probe beyond the magnetosphere. A model environment for a mission during a more average year than 1959 would show omnidirectional proton fluxes reduced by about one order of magnitude and a somewhat flatter spectrum.

A model environment for solar cosmic ray alpha particles, derived from Webber's values, is also shown in Figure A1. The evaluation is again based on the maximum year 1959. These values are more tenuous than those given for protons since the uncertainty in the alpha particle component of solar cosmic radiation is about

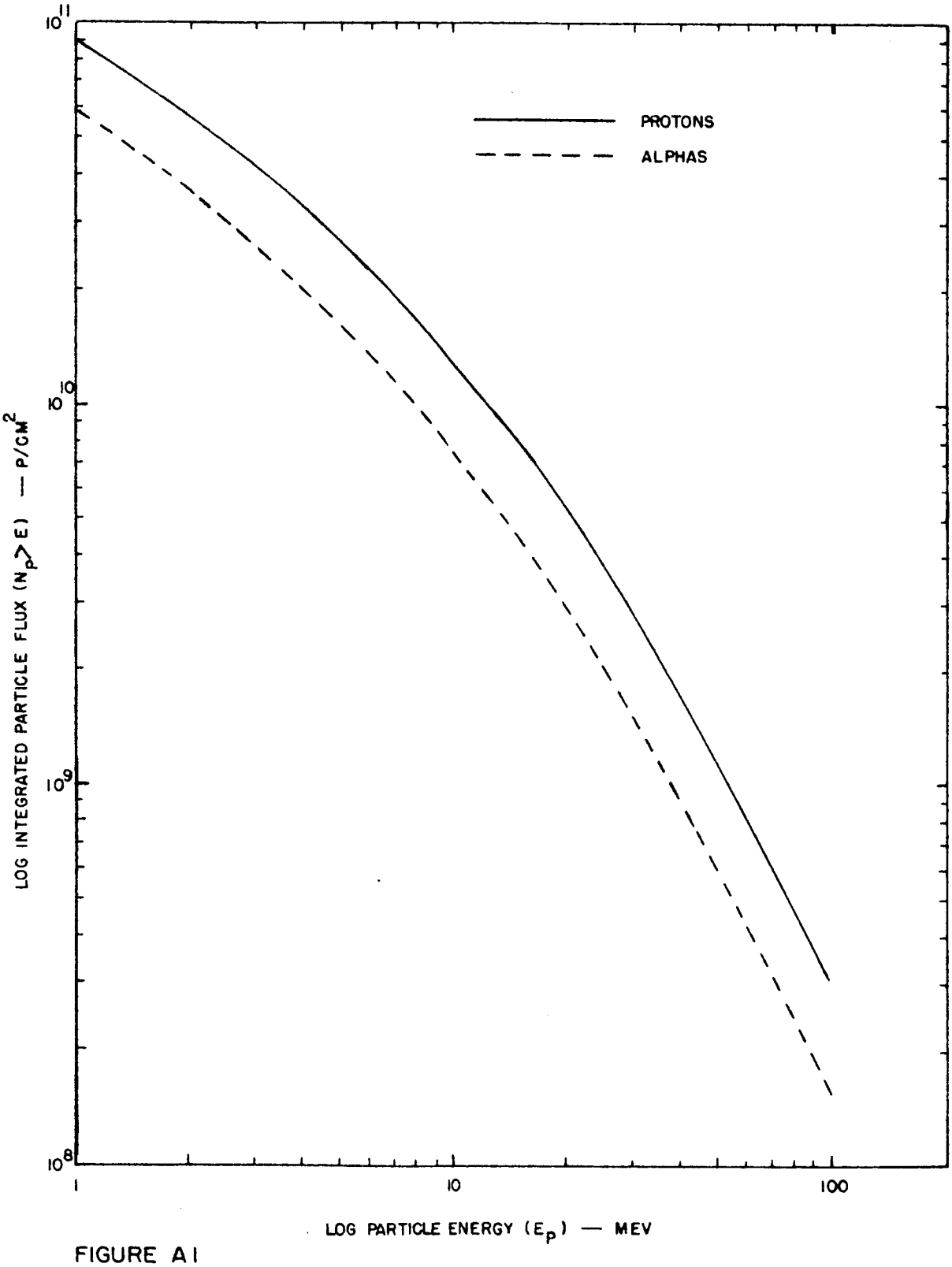


FIGURE A I

INTEGRATED PROTON FLUX FOR A 230 DAY MARS MISSION

50 percent, and because the low energy values are larger extrapolations in energy than for the protons. The fluence of solar cosmic ray alpha particles for a mission during a more average year would be about two orders of magnitude less, since 1959 was dominated by four alpha-rich solar particle events.

Appendix-A References

1) Bonetti, A., H. S. Bridge, A. J. Lazurnus, E. F. Lyon, B. Rossi and F. Scherb, "Explorer X Plasma Measurements," Space Research III, 540 (1963).

2) Rossi, Bruno, "Interplanetary Plasma," Space Research III, 529, (1963).

3) Snyder, Conway W. and Marcia Neugebauer, "Interplanetary Solar-Wind Measurements by Mariner II," Space Research IV, 89 (1964).

4) Webber, William R., "An Evaluation of the Radiation Hazard Due to Solar Particle Events," Boeing Document D2-90469 (1963).

5) Freier, Phyllis and William R. Webber, "Radiation Hazard in Space From Solar Particles," Science 142, 1587 (1963).

6) Davis, L. R. and K. W. Ogilvie, "Rocket Observations of Solar Protons During the November 1960 Events," Journal of Geophysical Research 67, 1711 (1962).

7) Sanford, B. P., "Optical Studies of Particle Bombardment in Polar Cap Absorption Events," Planetary and Space Science 10, 195 (1963) and "Polar-glow Aurora in Polar Cap Absorption Events," Journal of Atmospheric and Terrestrial Physics 24, 155 (1962).

APPENDIX B

CALCULATIONS OF SCATTERED PROTON AND ALPHA PARTICLE FLUX DISTRIBUTIONS

Calculations were made of the scattering of 2.5 Mev protons and 5.0 Mev alpha particles from a thin gold foil. The purpose of scattering was to provide high fluxes of charged particles for uniform exposure of large numbers of specimens. Scattering considerations included: (1) optimum scattering foil thickness, (2) elastic nuclear scattering (Rutherford-Coulomb) cross sections, (3) elastic electron scattering (Thompson-Gaussian) angular distribution. These three calculations will be discussed in respective order.

Calculation of Foil Thickness:

Criteria for determining the optimum scattering foil thickness include satisfactory compromises between: (1) minimum loss of charged particle energy resolutions; (2) maximum uniformity in scattered flux as a function of scattering angle from the straight-through beam; and (3) minimum heating of the scattering foil at maximum incident beam intensities. The energy loss per particle (ΔE) in the scattering foil can be calculated from the differential energy loss (dE/dx) of the particle, the foil density (ϱ), and foil thickness (d) as follows:

$$\Delta E = \int_0^d \frac{dE}{dX} \varrho \, dX \qquad (1)$$

For particles incident on a foil which is thin compared to the particle range, the rate of energy loss (dE/dx) during penetration is approximately constant, Thus,

$$\Delta E = \frac{dE}{dX} \varrho \, d \qquad (2)$$

For 2.5 Mev protons passing through gold[1] ($\varrho = 19.32$ gm cm^{-3}), $\frac{dE}{dx}$ is approximately 44 Mev cm^2 gm^{-1}. Thus,

$$\Delta E \cong 0.085 \, d \qquad (3)$$

where d is the foil thickness in microns and ΔE is the energy loss in Mev. Doubly ionized alpha particles of 5.0 Mev energy have about the same $\frac{dE}{dX}$ and thus, the same ΔE.

The power deposited in the scattering foil is determined by the particle energy loss in the foil and the incident particle flux (Θ) as follows:

$$P = \Theta \Delta E \qquad (4)$$

The particle flux is determined from measurements of the incident beam current, (I). For protons, which are singly ionized hydrogen, the particle flux is given by,

$$\theta_p = (6.24 \times 10^{12} \text{ protons sec}^{-1} \text{ micro amp}^{-1})\ (I) \tag{5}$$

where I is the incident beam current in units of microamps cm^{-2}. For alpha particles, which are doubly ionized helium, the particle flux is given by,

$$\theta_\alpha = (3.12 \times 10^{12} \text{ alpha particles sec}^{-1} \text{ microamp}^{-1})(I) \tag{6}$$

The power, in watts, deposited in a thin gold foil by 2.5 Mev protons can be calculated from Equations 3, 4, and 5 as follows:

$$P_p \cong 0.085\ I\ d \tag{7}$$

Similarly, the power deposited in a thin gold foil by 5.0 Mev alpha particles can be calculated from Equations 3, 4, and 6 as follows:

$$P_\alpha \cong 0.042\ I\ d \tag{8}$$

The temperature, (T), which the gold foil will attain during scattering is calculated by equating the energy deposition and energy radiation from the foil. Assuming negligible conduction of heat to the foil holder (valid for very thin foils of large diameter) and no convection, the equilibrium equation is

$$P \cong 2\ \varepsilon\ \sigma\ A\ (T^4 - T_w^4) \tag{9}$$

where ε is the emittance of the foil, A is the surface area of one side of the foil, σ is the Stefan-Boltzmann constant (5.67×10^{-12} watts cm^{-2} deg^{-4} K), and T_W is the temperature of the walls surrounding the foil. Solving for T gives,

$$T \cong \left[(P/2\ \varepsilon\ \sigma\ A) + T_w^4 \right]^{1/4} \tag{10}$$

The emittance of unoxidized gold is 0.02 at 100°C and 0.03 at 500°C. The wall temperature was assumed to be 300°K. The approximate equilibrium temperature of the gold foil during scattering can be calculated for 2.5 Mev protons from Equations 7 and 10 as follows:

$$T \cong \left[(3.0 \times 10^{11}\ I\ d/A) + 8.1 \times 10^{9} \right]^{1/4} \tag{11}$$

Similarly, the foil temperature for 5.0 Mev alpha particle scattering can be calculated using Equations 8 and 10 as follows:

$$T \cong \left[(1.5 \times 10^{11}\ I\ d/A) + 8.1 \times 10^{9}\right]^{1/4} \tag{12}$$

Solving Equation 9 to determine the maximum power (P_m) which the foil can foil withstand without melting ($T < 1063°C$) gives,

$$P_m \cong 1.08\ A \text{ watts} \tag{13}$$

where A is the surface area of the scattering foil which is approximately equal to the incident beam spot size.

The maximum foil thickness as determined from Equation 3 is calculated from the maximum tolerable energy loss, ΔE_m. For 2.5 Mev protons or 5.0 Mev alpha particles,

$$d_m \cong 11.8\ \Delta E_m \tag{14}$$

where d_m is given in microns.

The maximum incident beam current, I_m, is determined from Equation 13 and Equations 7 and 8, respectively, for 2.5 Mev protons and 5.0 Mev alpha particles. For 2.5 Mev protons

$$I_m \cong 12.7\ A/d \tag{15}$$

and for 5.0 Mev alpha particles

$$I_m \cong 25.4\ A/d \tag{16}$$

where I_m is in microamps, A is in cm^2, and d is in microns.

The actual values of foil thickness and beam current are determined from Equations 14, 15, and 16 and maximum uniform beam scattering with minimum loss of energy resolution. The area of the foil, A, is determined from a compromise between maximum uniform beam defocusing, the strength of the foil (sensitive to pressure differences during pump-down), and minimum deviation from a point source.

Calculations of Elastic Nuclear Scattering:

The fluence (Φ) (particles cm^{-2}) of charged particles from elastic nuclear scattering[2] can be calculated from the following equation:

$$\Phi(\theta) = n\,d\,I\,t\,R^{-2}\sigma_{\Omega}(\theta, E) \tag{17}$$

where n is the atomic density, d is the scatterer thickness, I is the incident beam current intensity, t is the exposure time, R is the radial distance from the scatterer, and $\sigma_{\Omega}(\theta, E)$ is the Rutherford scattering cross section. Elastic scattering dominates inelastic nuclear scattering at low energies (2.5 Mev protons and 5.0 Mev alpha particles) and even to fairly large scattering angles.

The atomic density, atoms cm^{-3}, is given by

$$n = \rho N_o A_t^{-1} \tag{18}$$

where ρ is the density of the scattering foil, N_O is Avogadros number (6.03×10^{23} atoms/at.wt.), and A_t is the atomic weight of the scatterer. The Rutherford cross section, $\sigma_{\Omega}(\theta, E)$ in units of cm^2 is given by

$$\sigma_{\Omega}(\theta, E) = e^4 Z^2 z^2 / 16 E^2 \sin^4(\theta/2) \tag{19}$$

where e is the electronic charge (4.8×10^{-10} e.s.u.), z is the atomic number of the incident particle, Z is the atomic number of the scattering foil, E is the energy of the particle, and θ is the angle of scattering in the center-of-mass coordinate system. Equation 19 is valid for laboratory scattering angles when $z << Z$. For a gold scattering foil,

$$\rho = 19.32 \text{ gm cm}^{-3}$$

$$A = 197.2 \text{ gm at wt.}^{-1}$$

$$Z = 79$$

Thus from Equation 18, $n = 5.9 \times 10^{22}$ atoms cm^{-3}. For 2.5 Mev protons,

$$I = 6.24 \times 10^{12} \text{ protons sec}^{-1} \text{ microamps}^{-1} \text{ (I)}$$

$$z = 1$$

$$E = 2.5 \text{ Mev} \times 1.6 \times 10^{-6} \text{ erg/Mev} = 4.0 \times 10^{-6} \text{ erg.}$$

Then from Equations 17, 18, and 19, the charged particle fluence for 2.5 Mev protons is,

$$\Phi(\theta) = 1.28 \times 10^4 \, I \, d \, t \, R^{-2} \sin^{-4}(\theta/2) \tag{20}$$

and for 5.0 Mev alpha particles

$$\Phi(\theta) = 6.4 \times 10^3 \, I \, d \, t \, R^{-2} \sin^{-4}(\theta/2) \tag{21}$$

Elastic Electron Scattering:

For charged particle forward angle scattering the contribution due to elastic electron scattering can also be calculated[3]. The probability function for forward scattering is given by

$$P(\theta) = (2/\theta^2)\ \theta\, e^{-\theta^2/\beta^2} \tag{22}$$

Thus the fraction of the beam scattered within an angle θ is

$$\int_0^{\theta_0} P(\theta)\, d\theta = 1 - e^{-\theta^2/\beta^2} \tag{23}$$

The scattering parameter, β^2, is given by

$$\beta^2 = 2\pi\, n\, d\, Z^2 z^2 e^4 \ln(a_o E/z Z^{4/3} e^2) \tag{24}$$

where a_o is the Bohr radius (5.29×10^{-9} cm) and the other symbols are defined already for Equations 17 and 19. The scattered fluence in particles cm^{-2} microamp^{-1} as a function of angle can be calculated from changes in the values of Equation 23 and changes in increments of area from solid angle considerations, $2\pi R^2 \Delta (1 - \cos\theta)$. For protons (singly ionized)

$$\Phi(\theta) = 6.2 \times 10^{12}\ \Delta\, (1 - e^{-\theta^2/\beta^2})/2\pi R^2 \Delta (1 - \cos\theta) \tag{25}$$

Figure B1 shows curves of $\Phi(\theta)$ as a function of scattering angle for applicable values of β^2 (typical of foil thicknesses and energies involved).

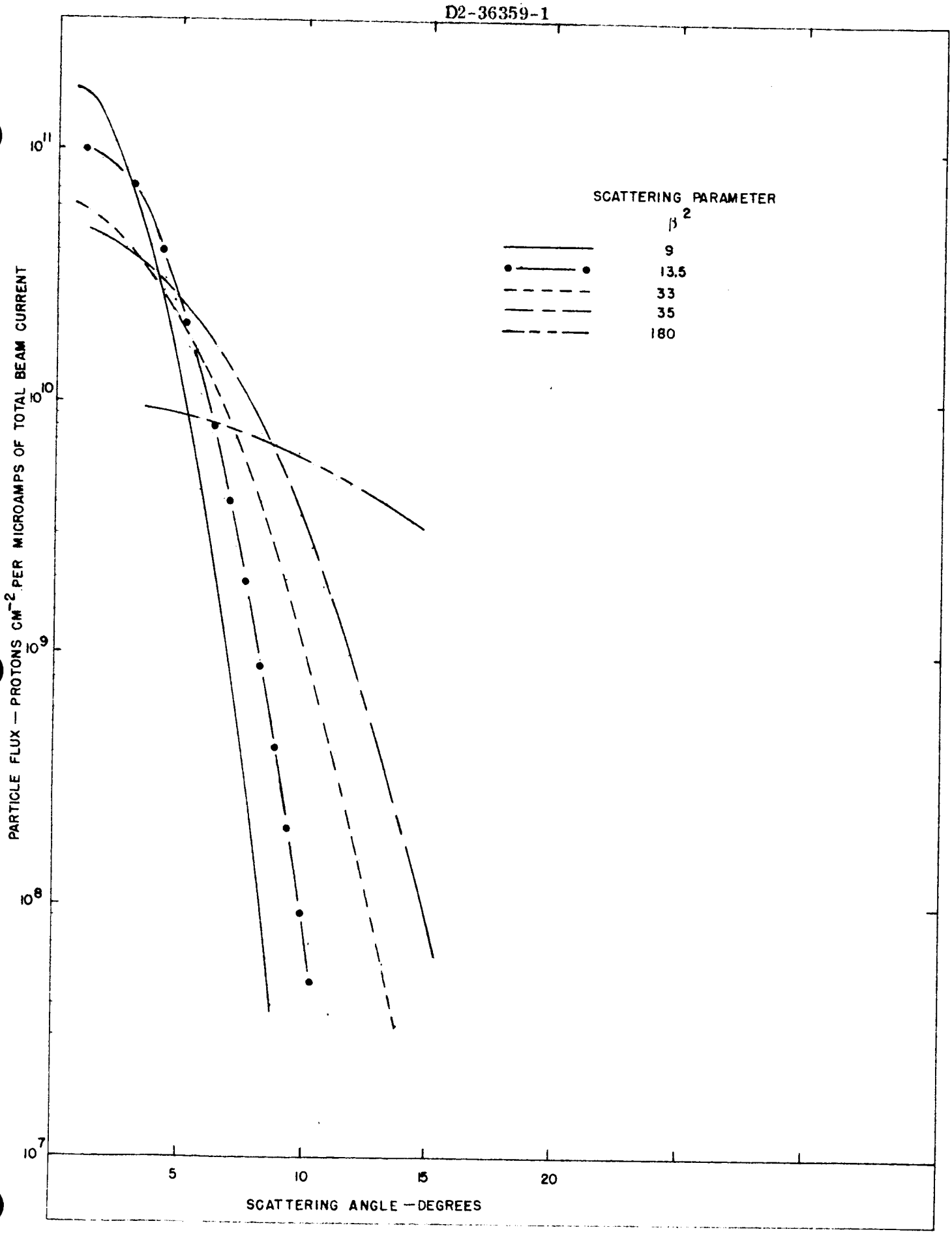


FIGURE B1 FORWARD GAUSSIAN SCATTERING OF PROTONS

APPENDIX B - REFERENCES

1) "Tables of Energy Losses and Ranges of Heavy Charged Particles," W. H. Barkas and M. J. Berger, NASA-SP-3013, 1964

2) "Atomic Nucleus," R. D. Evans, McGraw-Hill, 1955

3) "Nuclear Physics," E. Fermi, Univ. of Chicago Press, 1950

APPENDIX C - REFLECTANCE DATA

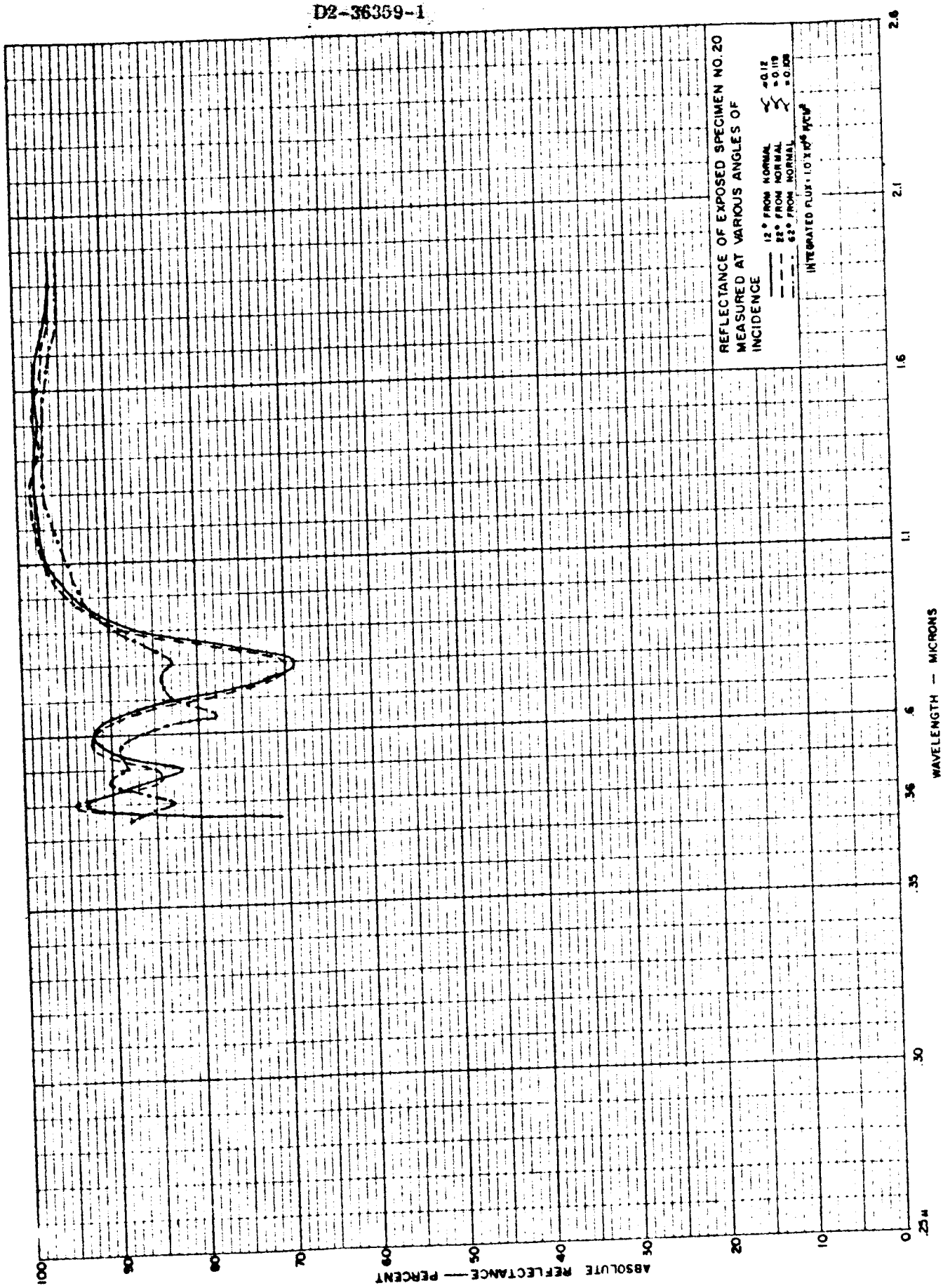

REFLECTANCE OF EXPOSED SPECIMEN NO.20
MEASURED AT VARIOUS ANGLES OF INCIDENCE
12° FROM NORMAL
22° FROM NORMAL
62° FROM NORMAL
ABSOLUTE REFLECTANCE — PERCENT
WAVELENGTH — MICRONS

FIGURE C1

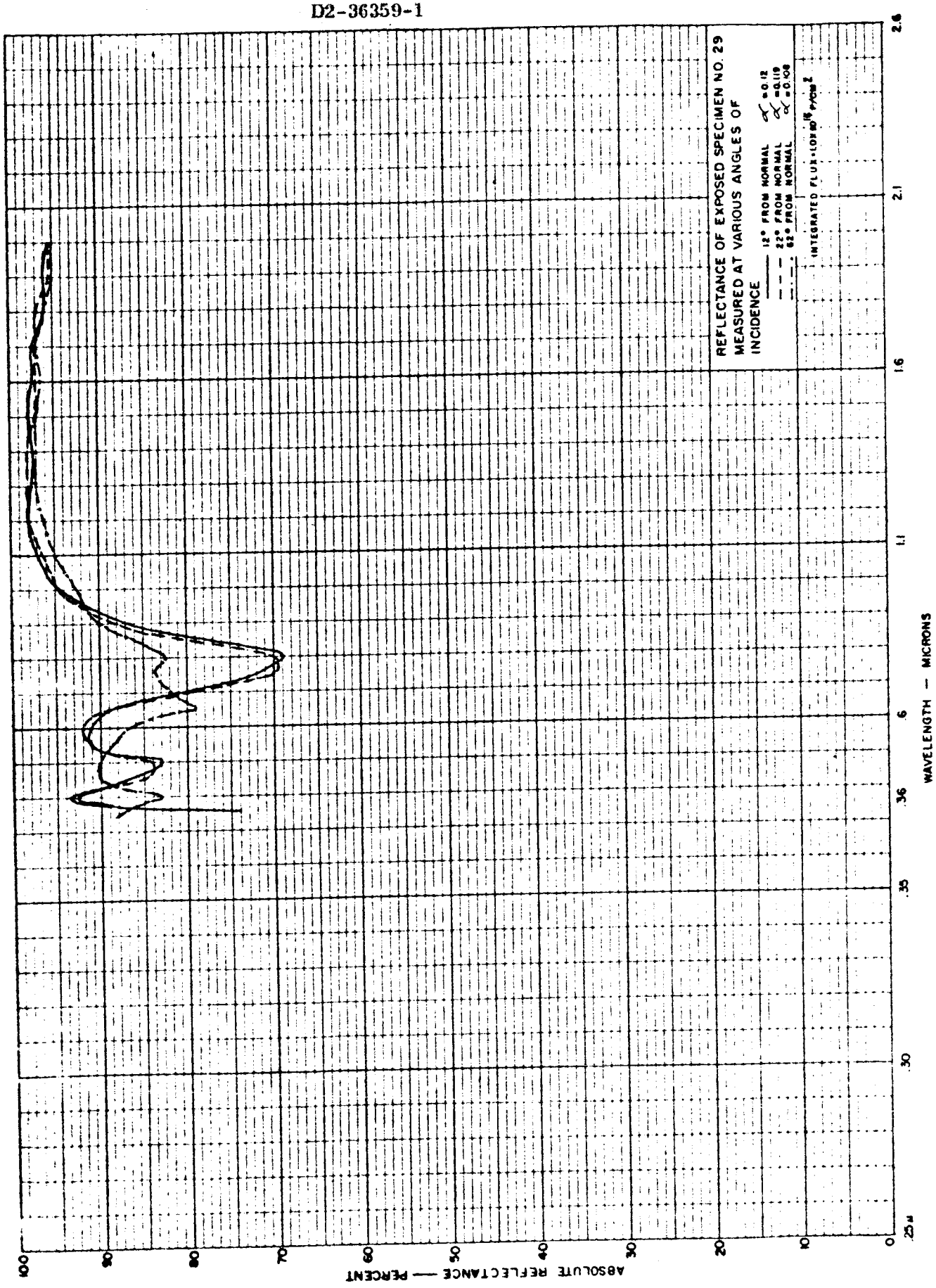

REFLECTANCE OF EXPOSED SPECIMEN NO. 29
MEASURED AT VARIOUS ANGLES OF INCIDENCE
12° FROM NORMAL α = 0.12
22° FROM NORMAL α = 0.119
62° FROM NORMAL α = 0.109
INTEGRATED FLUX-LOW
ABSOLUTE REFLECTANCE — PERCENT
WAVELENGTH — MICRONS

FIGURE C2

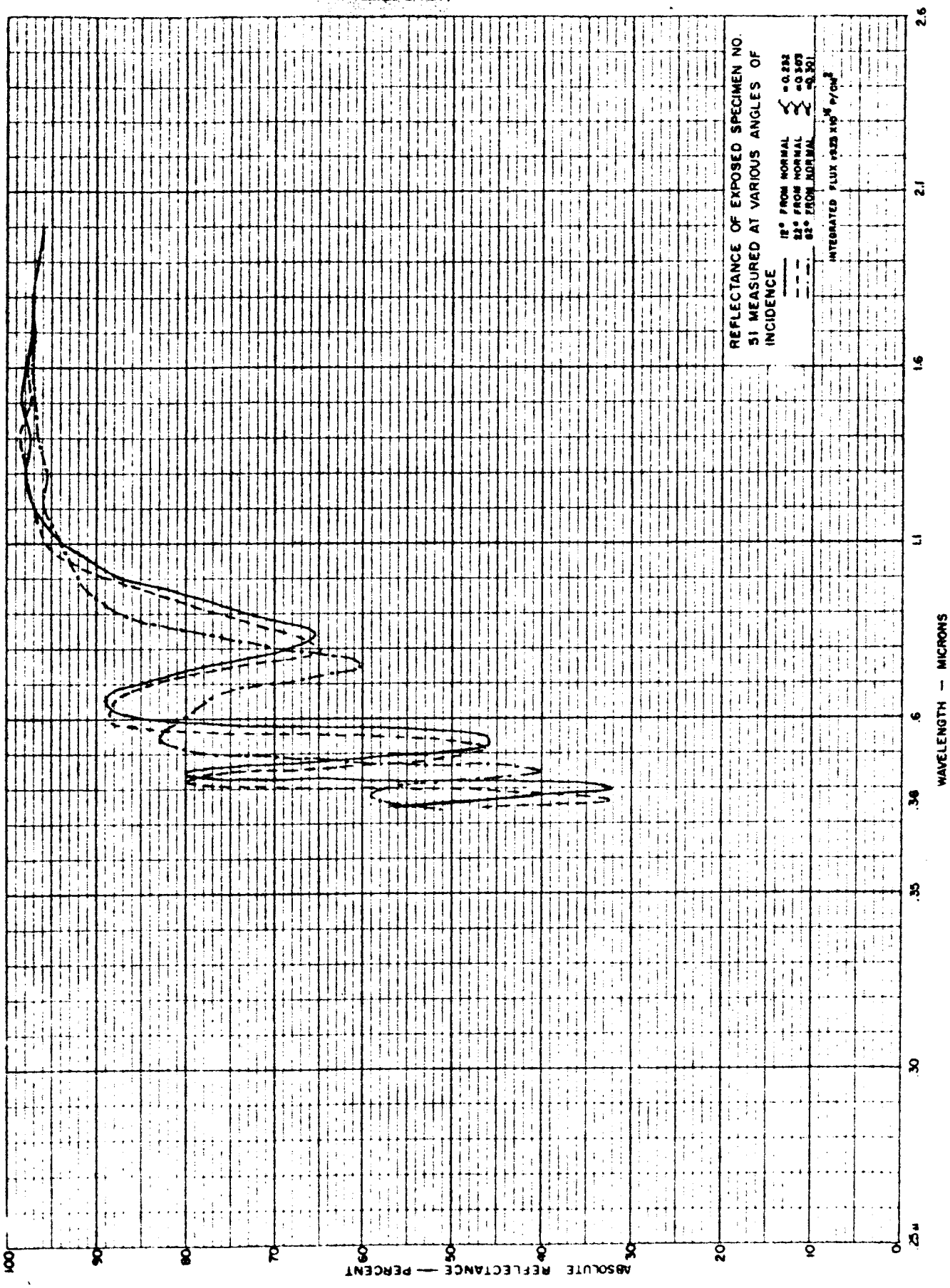

REFLECTANCE OF EXPOSED SPECIMEN NO. 51 MEASURED AT VARIOUS ANGLES OF INCIDENCE
12° FROM NORMAL
22° FROM NORMAL
62° FROM NORMAL
INTEGRATED FLUX
ABSOLUTE REFLECTANCE — PERCENT
WAVELENGTH — MICRONS

FIGURE C3

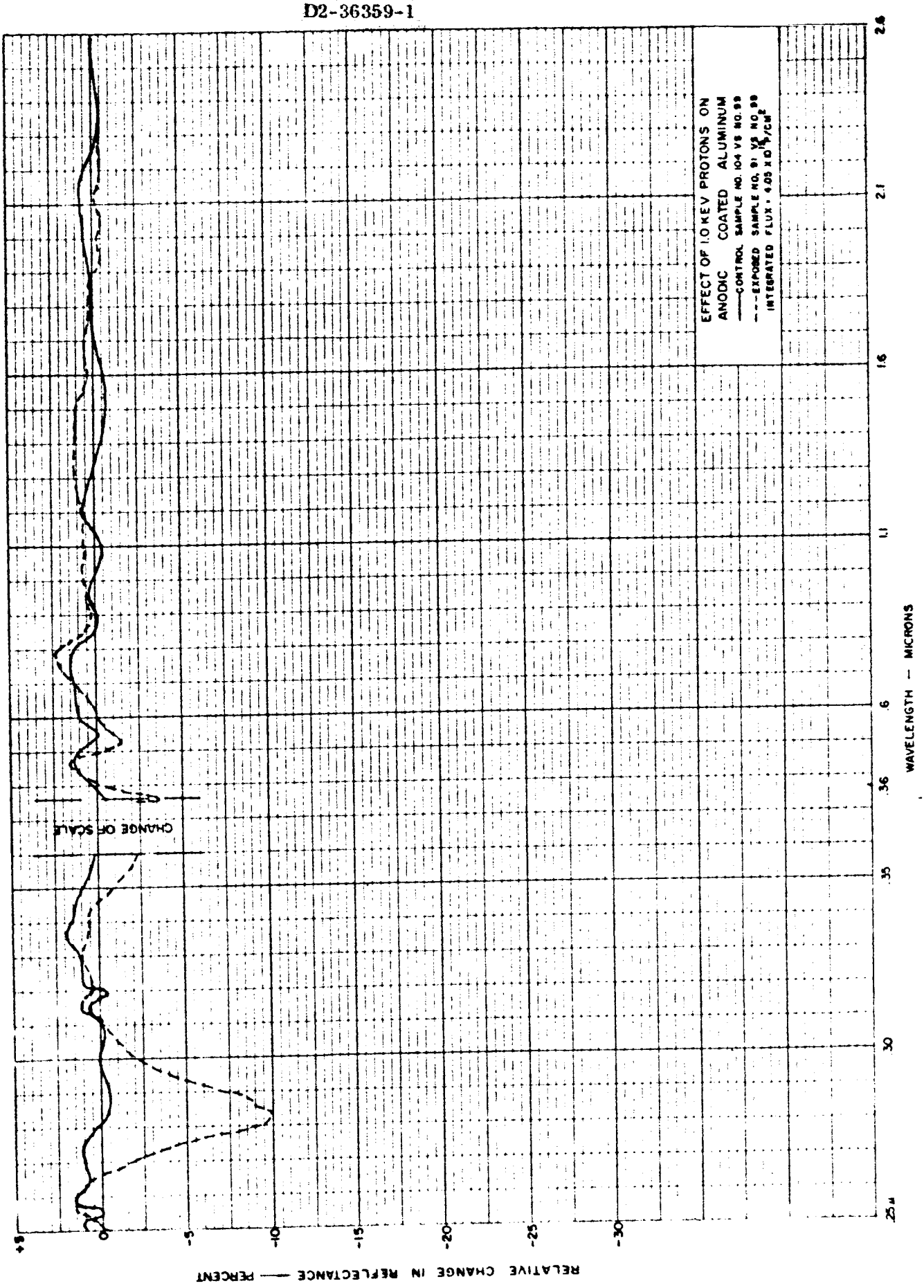

EFFECT OF 1.0 KEV PROTONS ON
ANODIC COATED ALUMINUM
——CONTROL SAMPLE NO. 104 VS NO. 99
- - - EXPOSED SAMPLE NO. 91 VS NO. 99
INTEGRATED FLUX = 4.05 X 10^15 P/CM^2
CHANGE OF SCALE
RELATIVE CHANGE IN REFLECTANCE —— PERCENT
+5
0
-5
-10
-15
-20
-25
-30
2.6
2.1
1.6
1.1
.6
.36
.35
.30
.25 μ
WAVELENGTH — MICRONS

FIGURE C4

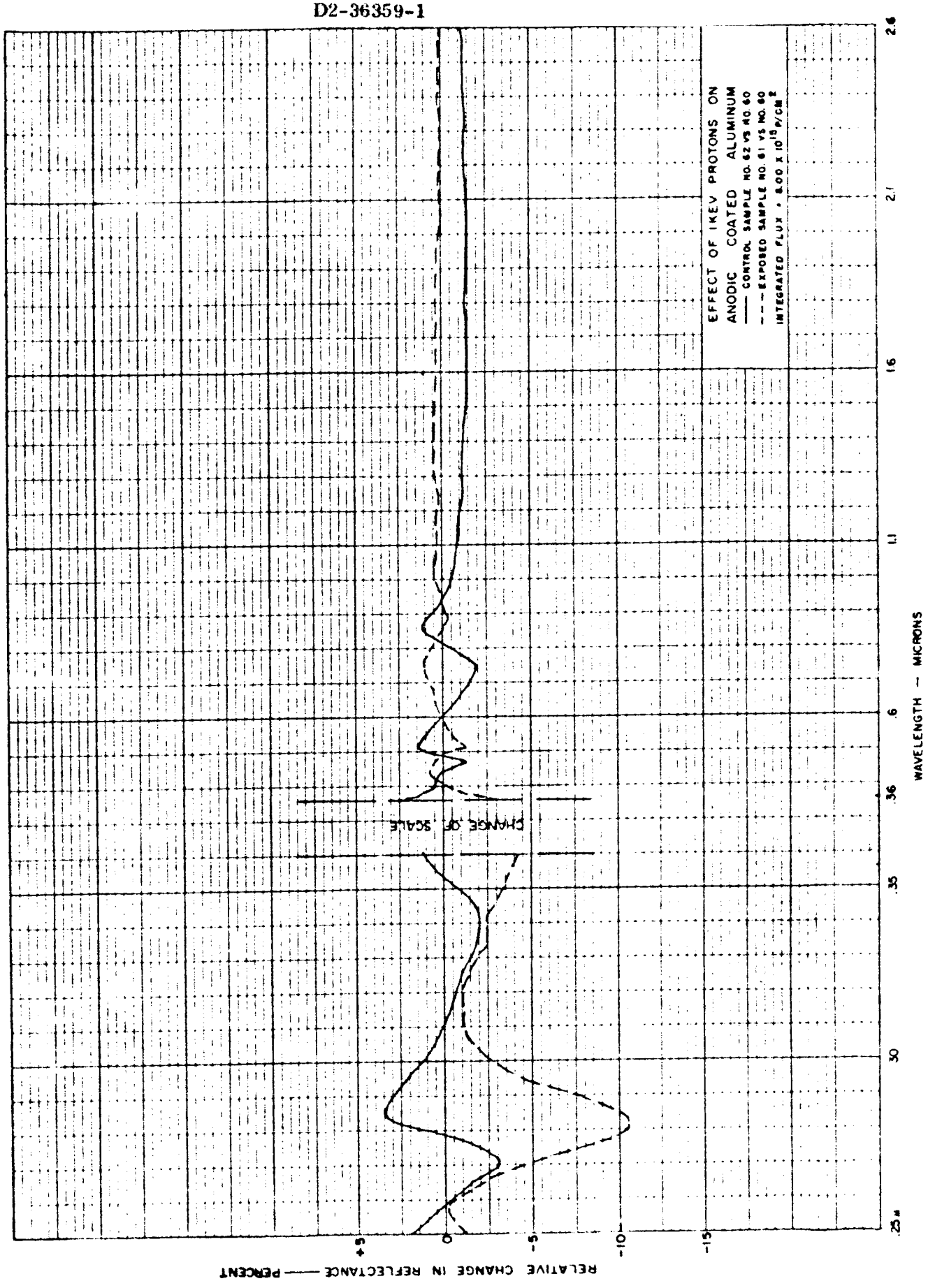

EFFECT OF 1KEV PROTONS ON
ANODIC COATED ALUMINUM
—— CONTROL SAMPLE NO. 62 VS NO. 60
– – – EXPOSED SAMPLE NO. 61 VS NO. 60
INTEGRATED FLUX = 8.00 X 10^15 P/CM^2
CHANGE OF SCALE
RELATIVE CHANGE IN REFLECTANCE —— PERCENT
+5
0
-5
-10
-15
.25μ
.30
.35
.36
.6
1.1
1.6
2.1
2.6
WAVELENGTH — MICRONS

FIGURE C5

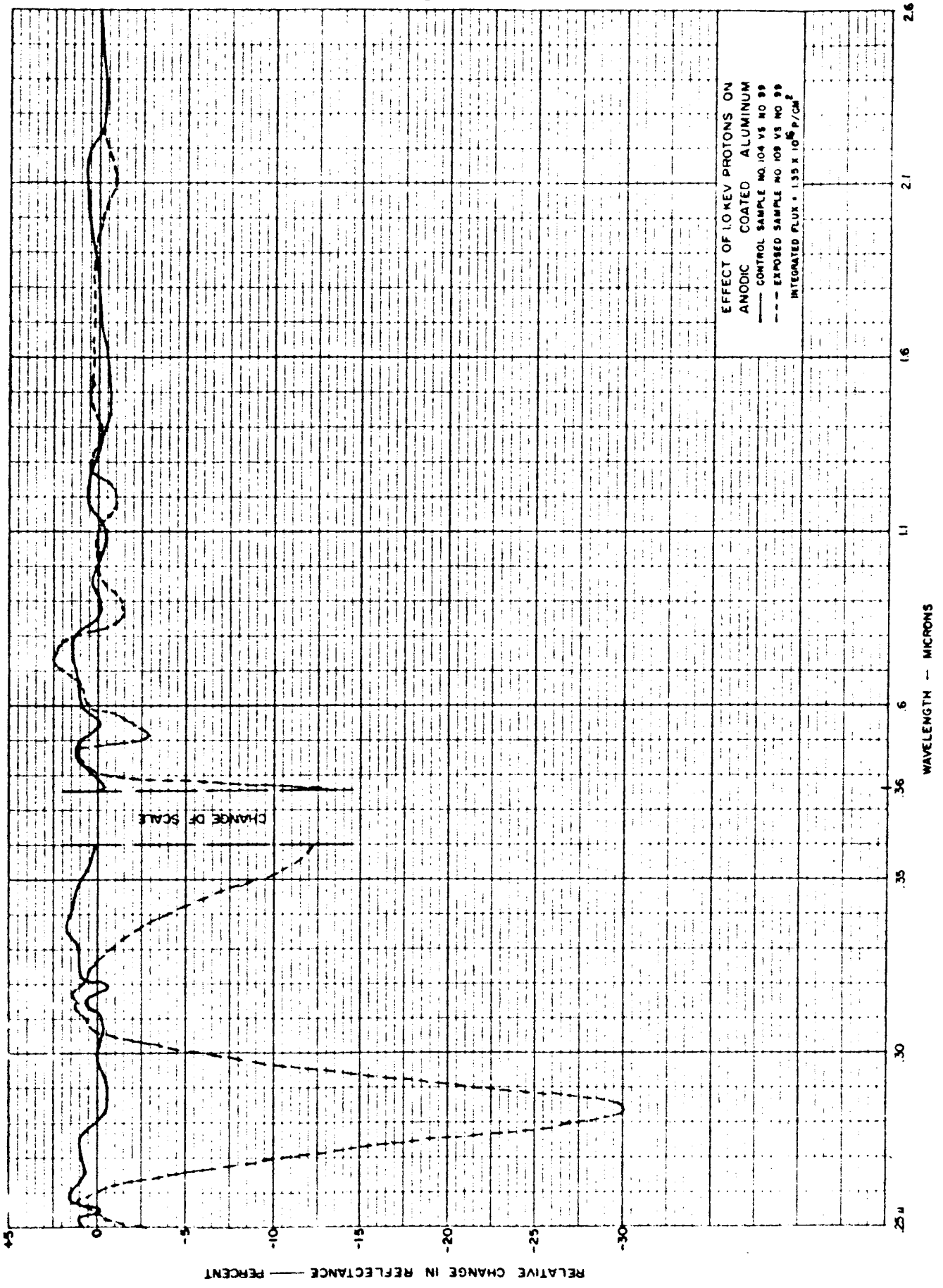

EFFECT OF 1.0 KEV PROTONS ON
ANODIC COATED ALUMINUM
—— CONTROL SAMPLE NO. 104 VS NO 99
- - - EXPOSED SAMPLE NO 109 VS NO 99
INTEGRATED FLUX = 1.35 X 10^16 P/CM^2
CHANGE OF SCALE
+5
0
-5
-10
-15
-20
-25
-30
RELATIVE CHANGE IN REFLECTANCE —— PERCENT
.25
.30
.35
.36
.6
1.1
1.6
2.1
2.6
WAVELENGTH — MICRONS

FIGURE C6

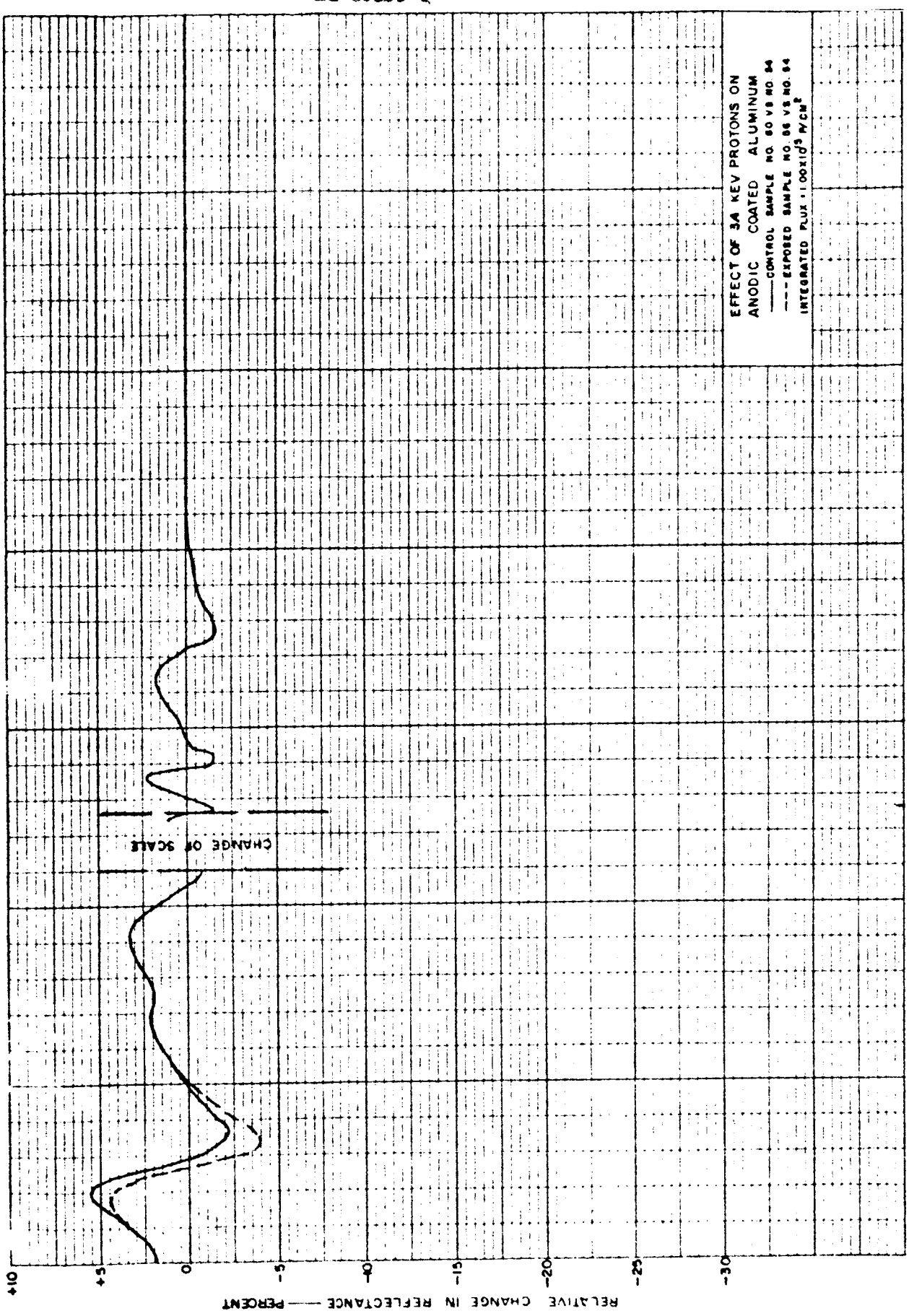

EFFECT OF 3A KEV PROTONS ON
ANODIC COATED ALUMINUM
——CONTROL SAMPLE NO. 60 VS NO. 84
---EXPOSED SAMPLE NO. 86 VS NO. 84
INTEGRATED FLUX 1.00X10^13 P/CM^2
CHANGE OF SCALE
+10
+5
0
-5
-10
-15
-20
-25
-30
RELATIVE CHANGE IN REFLECTANCE —— PERCENT
.25μ
.30
.35
.36
.6
1.1
1.6
2.1
2.6
WAVELENGTH — MICRONS

FIGURE C 7

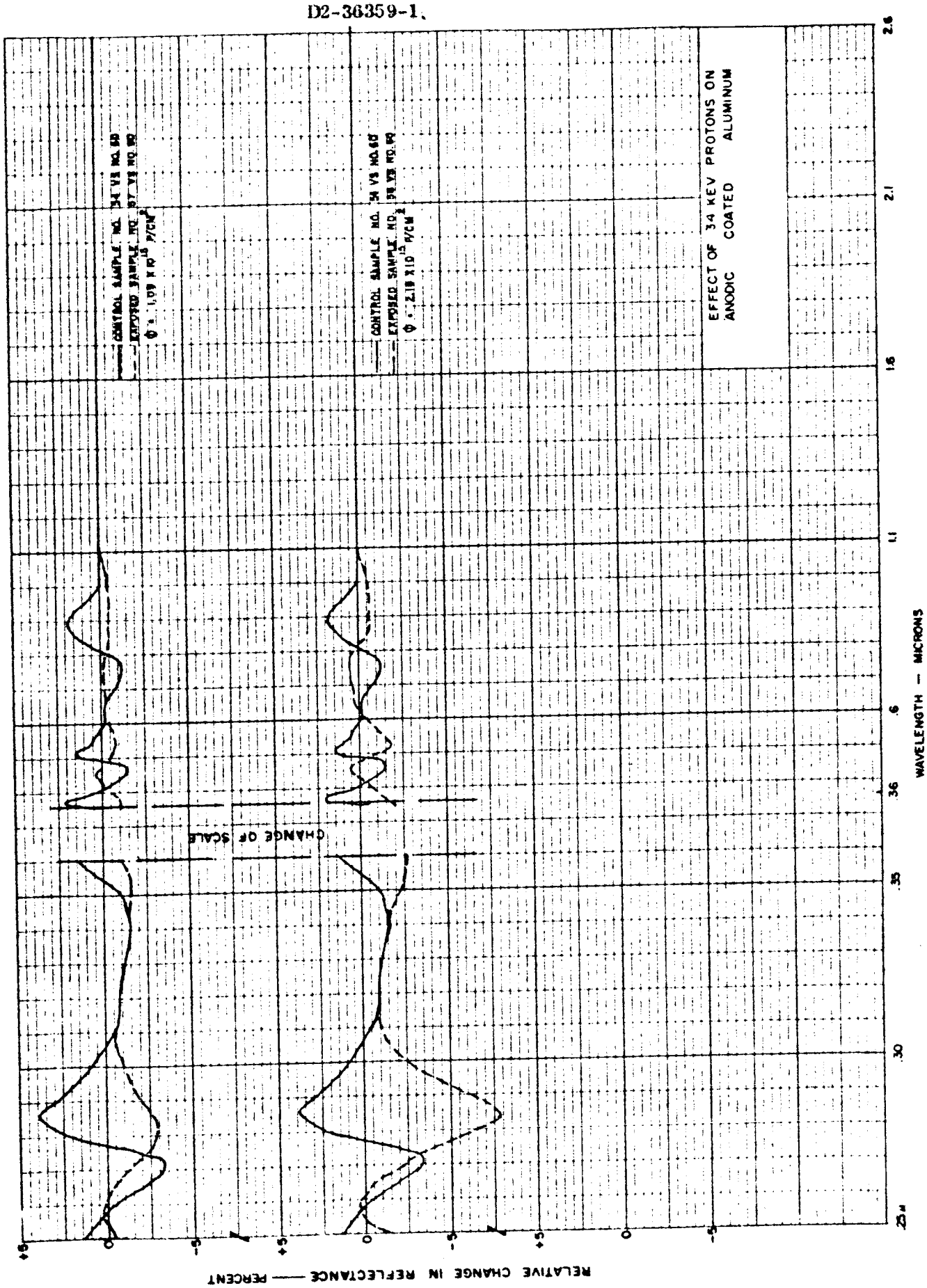

EFFECT OF 34 KEV PROTONS ON ANODIC COATED ALUMINUM
CONTROL SAMPLE NO. 34 VS NO. 68
EXPOSED SAMPLE NO. 67 VS NO. 69
Φ = 1.09 X 10^15 P/CM^2
CONTROL SAMPLE NO. 34 VS NO. 65
EXPOSED SAMPLE NO. 34 VS NO. 64
Φ = 2.18 X 10^15 P/CM^2
CHANGE OF SCALE
RELATIVE CHANGE IN REFLECTANCE — PERCENT
WAVELENGTH — MICRONS
+5
0
-5
.25μ
.30
.35
.36
.6
1.1
1.6
2.1
2.6

FIGURE C8

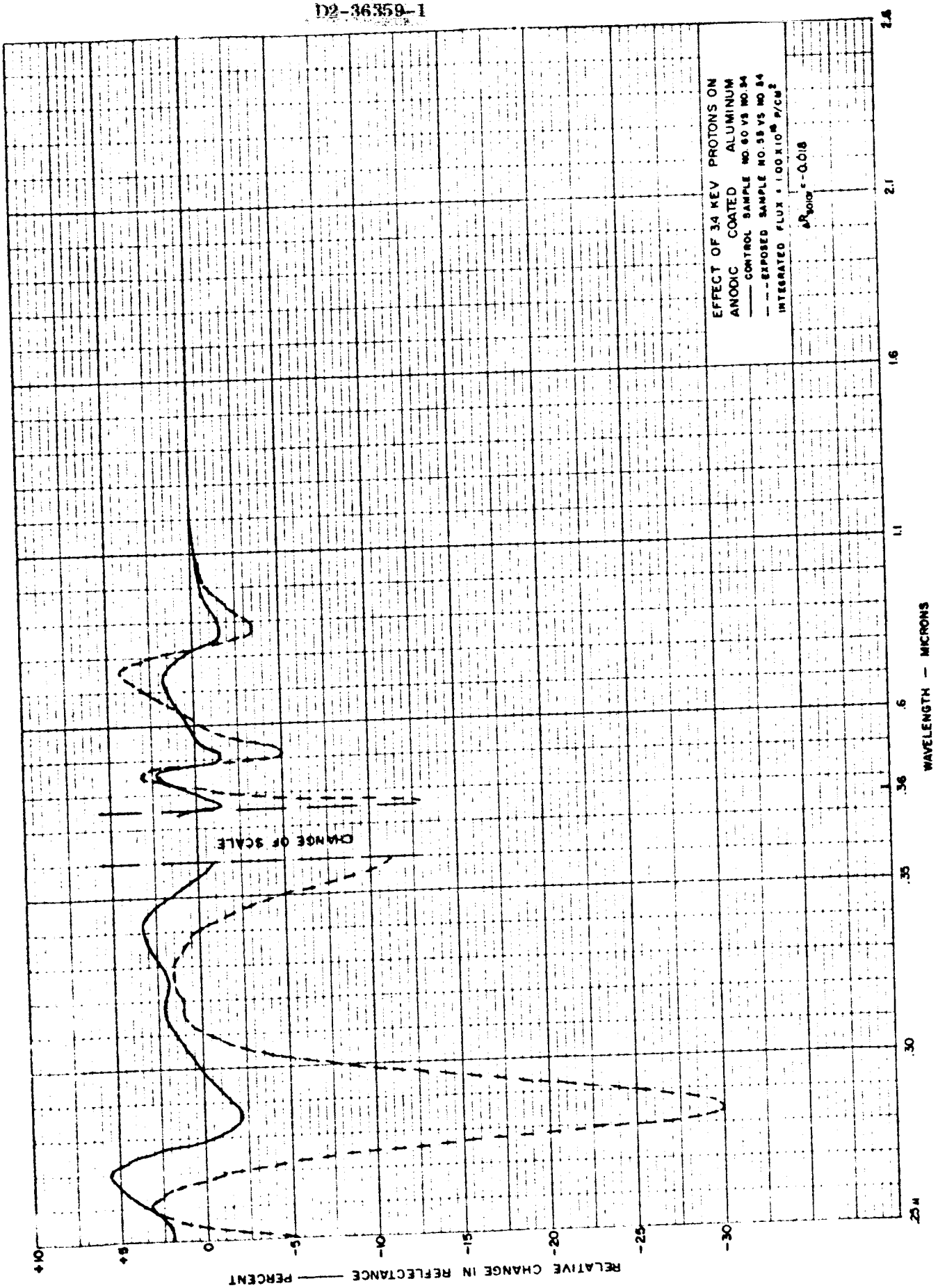

EFFECT OF 34 KEV PROTONS ON
ANODIC COATED ALUMINUM
—— CONTROL SAMPLE NO. 60 VS NO. 84
– – – EXPOSED SAMPLE NO. 58 VS NO. 84
INTEGRATED FLUX = 1.00 X 10^15 P/CM^2
ΔR 0.018
CHANGE OF SCALE
+10
+5
0
-5
-10
-15
-20
-25
-30
RELATIVE CHANGE IN REFLECTANCE —— PERCENT
2.4
2.1
1.6
1.1
.6
.36
.35
.30
25 μ
WAVELENGTH — MICRONS

FIGURE C 9

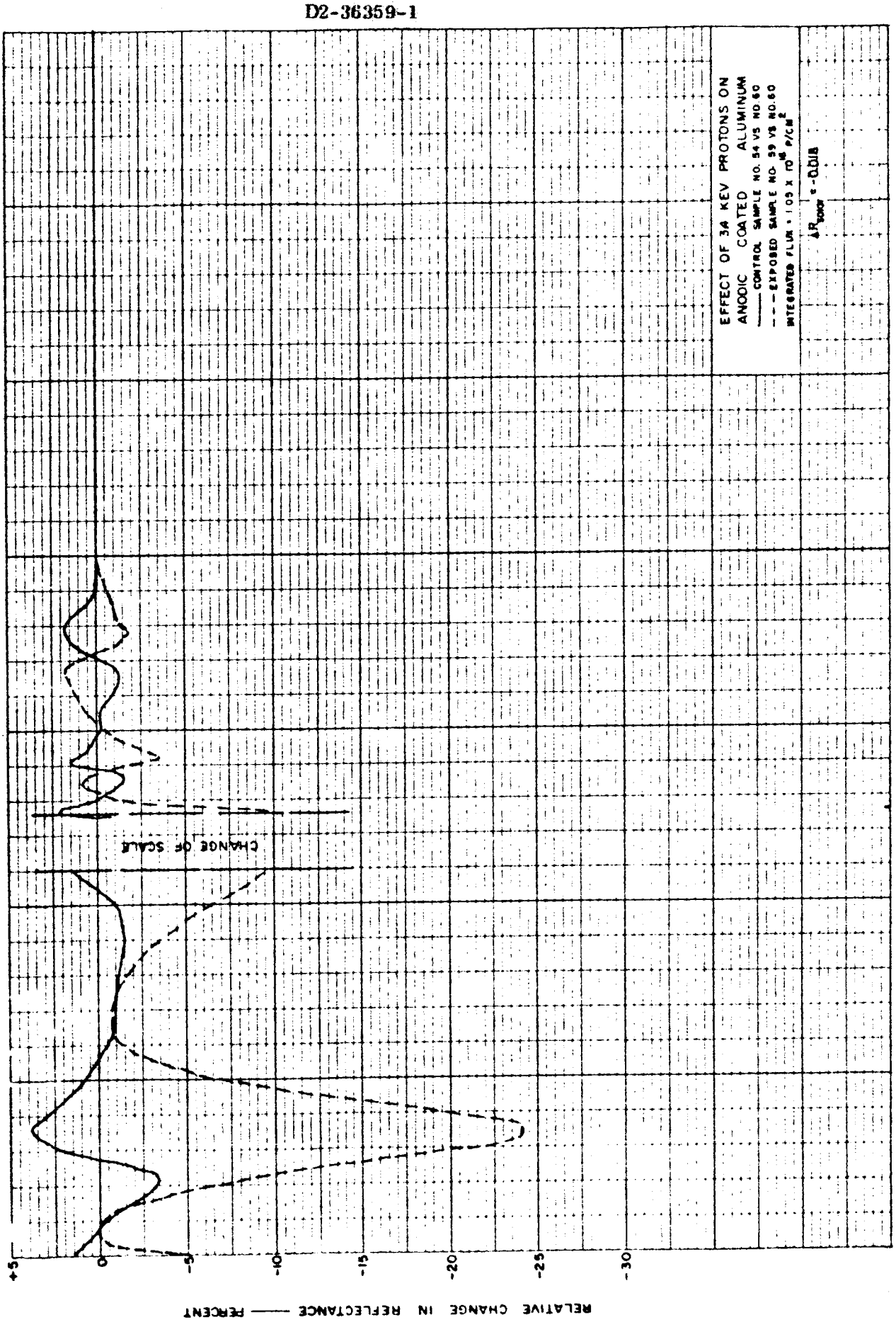

EFFECT OF 34 KEV PROTONS ON ANODIC COATED ALUMINUM
——— CONTROL SAMPLE NO. 54 VS NO. 60
– – – EXPOSED SAMPLE NO. 59 VS NO. 60
INTEGRATED FLUX = 1.05 X 10^16 P/CM^2
ΔR_SOLAR = -0.018
CHANGE OF SCALE
+5
0
-5
-10
-15
-20
-25
-30
.25μ
.30
.35
.36
.6
1.1
1.6
2.1
2.6
WAVELENGTH — MICRONS
RELATIVE CHANGE IN REFLECTANCE —— PERCENT

FIGURE G10

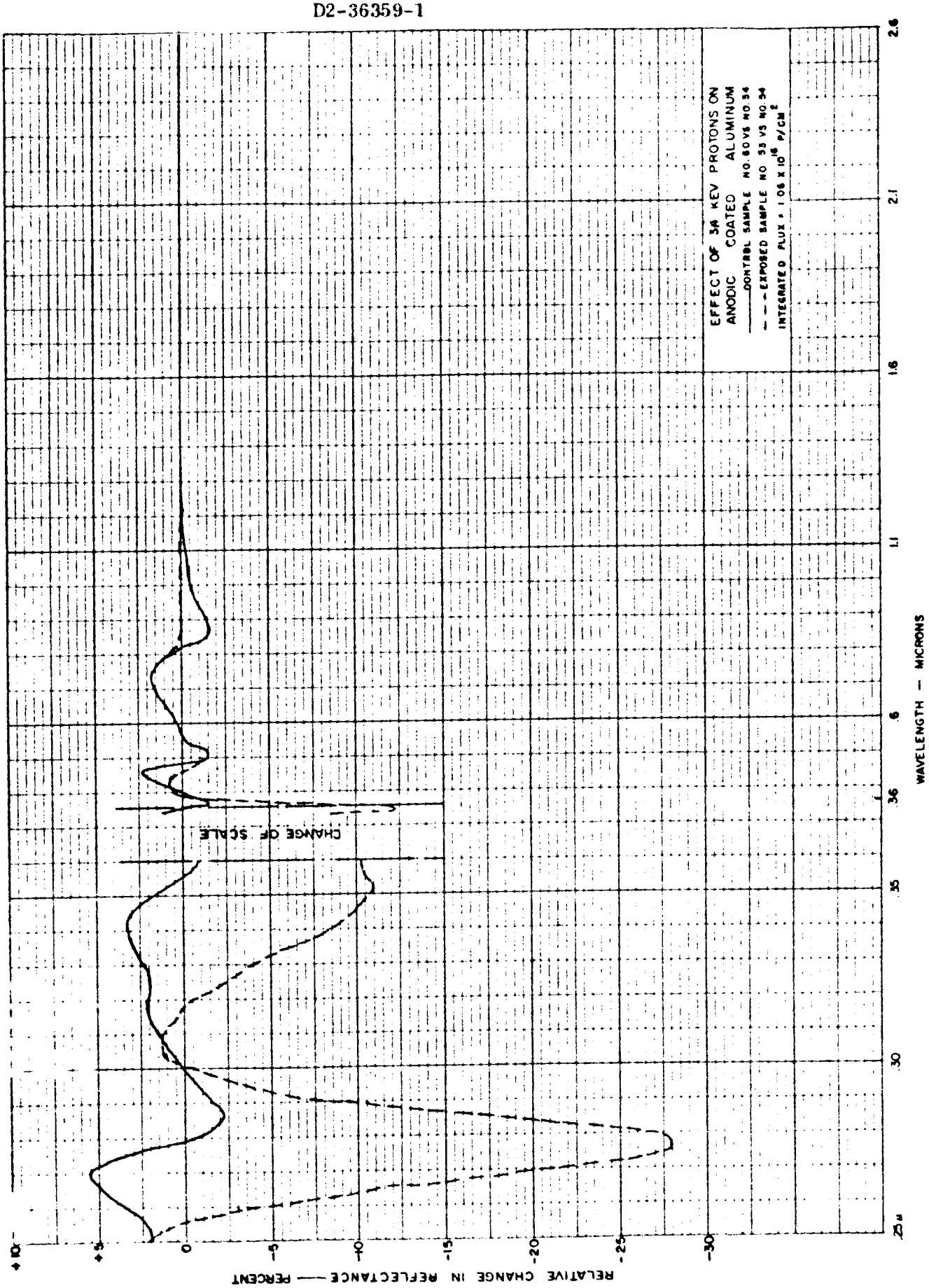

EFFECT OF 34 KEV PROTONS ON
ANODIC COATED ALUMINUM
——CONTROL SAMPLE NO. 60 VS NO. 54
– – – EXPOSED SAMPLE NO 53 VS NO. 54
INTEGRATED FLUX = 1.06 X 10^16 P/CM^2
CHANGE OF SCALE
+10
+5
0
-5
-10
-15
-20
-25
-30
RELATIVE CHANGE IN REFLECTANCE —— PERCENT
.25 μ
.30
.35
.36
.6
1.1
1.6
2.1
2.6
WAVELENGTH — MICRONS

FIGURE C11

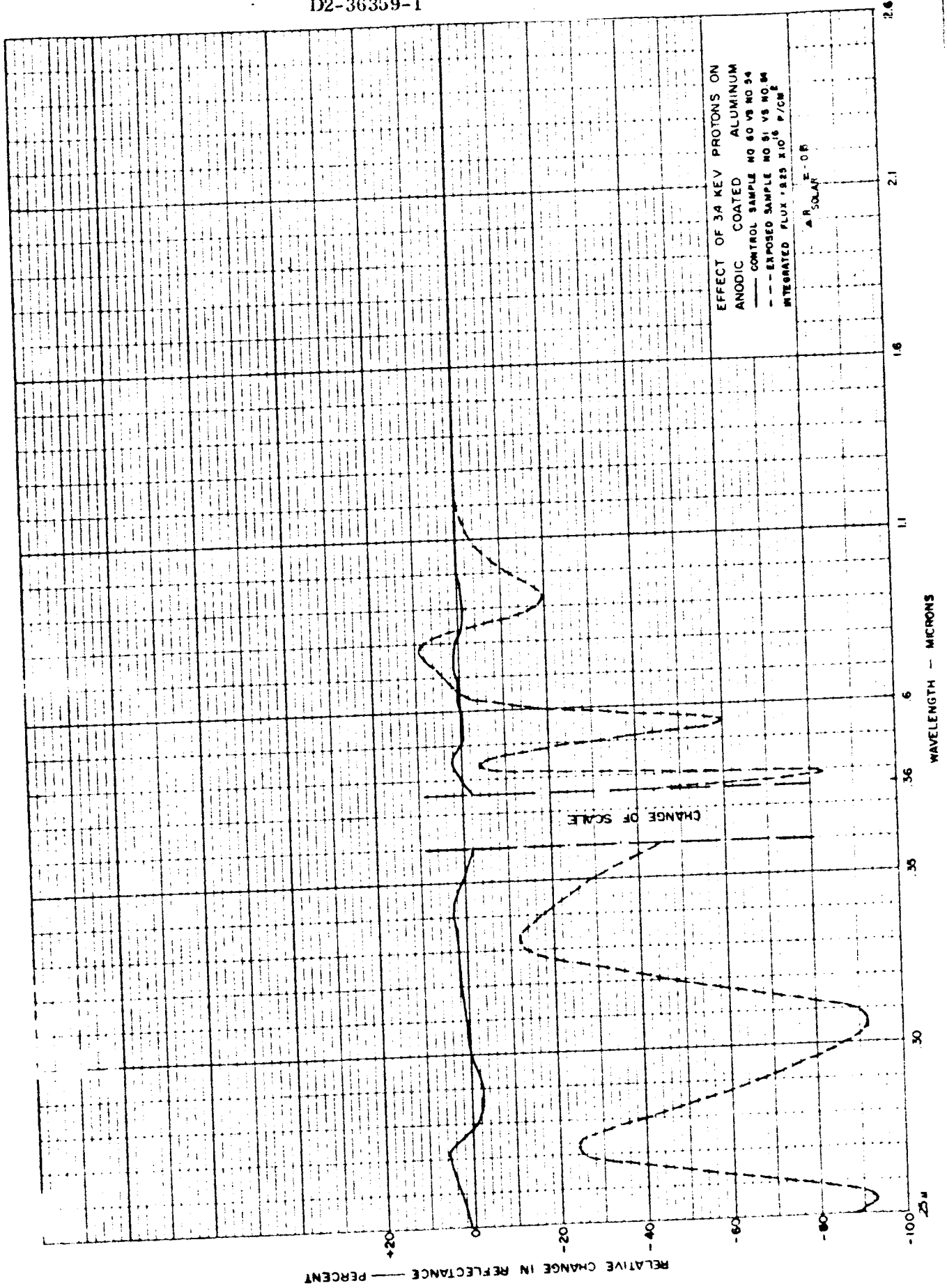

EFFECT OF 3.4 KEV PROTONS ON
ANODIC COATED ALUMINUM
—— CONTROL SAMPLE NO 60 VS NO 54
- - - EXPOSED SAMPLE NO 51 VS NO 54
INTEGRATED FLUX 1.825 X10^16 P/CM^2
ΔR_SOLAR E-0.5
CHANGE OF SCALE
RELATIVE CHANGE IN REFLECTANCE —— PERCENT
+20
0
-20
-40
-60
-80
-100
WAVELENGTH — MICRONS
.25
.35
.36
.6
1.1
1.6
2.1
2.6

FIGURE C12

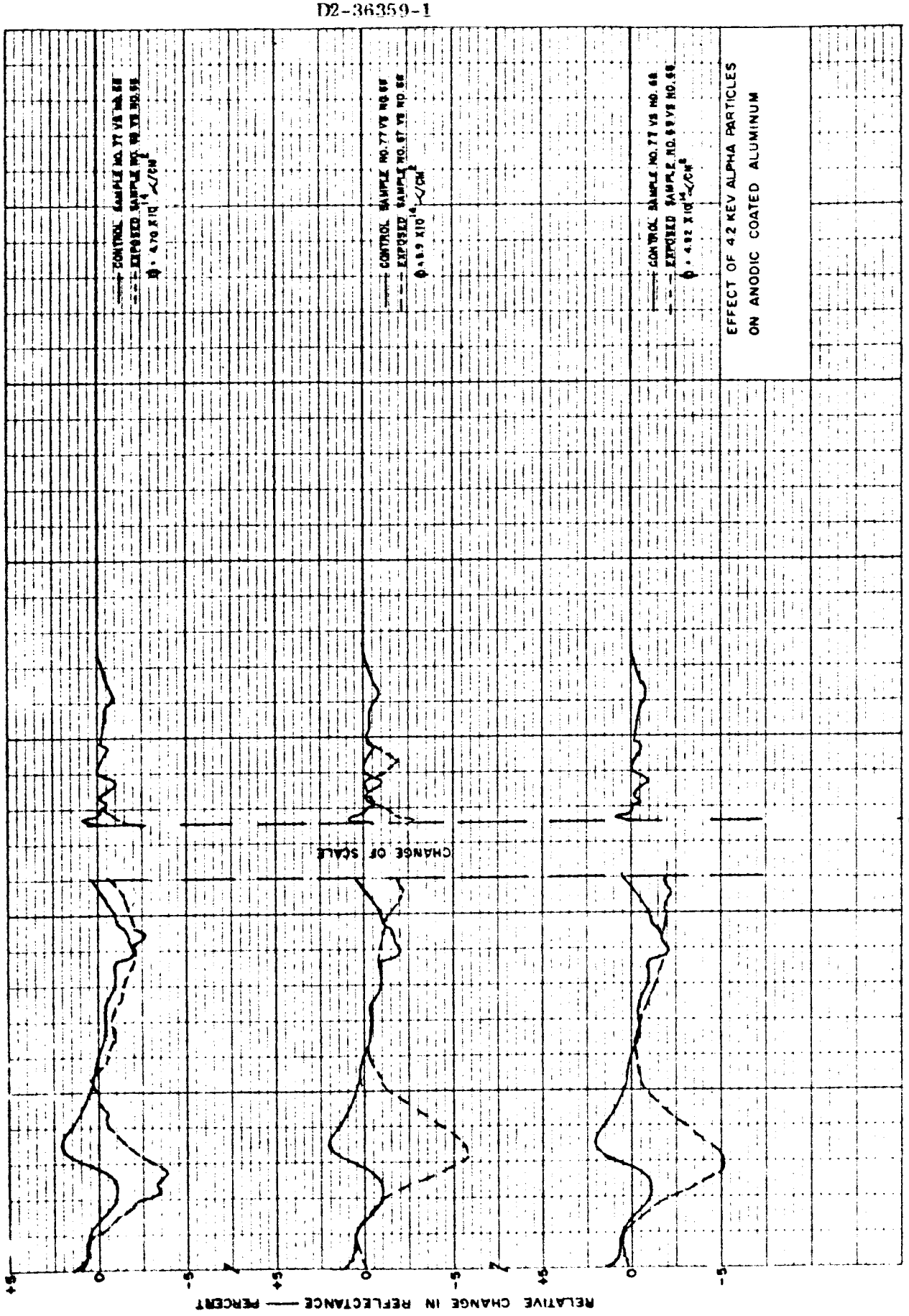

EFFECT OF 4.2 KEV ALPHA PARTICLES
ON ANODIC COATED ALUMINUM
CONTROL SAMPLE NO. 77 VS NO. 66
EXPOSED SAMPLE NO. 66 VS NO. 66
Φ = 4.92 X 10^14 P/CM^2
CONTROL SAMPLE NO. 77 VS NO. 68
EXPOSED SAMPLE NO. 67 VS NO. 68
Φ = 8.9 X 10^14 P/CM^2
CONTROL SAMPLE NO. 77 VS NO. 69
EXPOSED SAMPLE NO. 69 VS NO. 69
Φ = 4.70 X 10^14 P/CM^2
CHANGE OF SCALE
RELATIVE CHANGE IN REFLECTANCE — PERCENT
+5
0
-5
WAVELENGTH — MICRONS
2.6
2.1
1.6
1.1
.6
.36
.35
.30
.25 μ

FIGURE C13

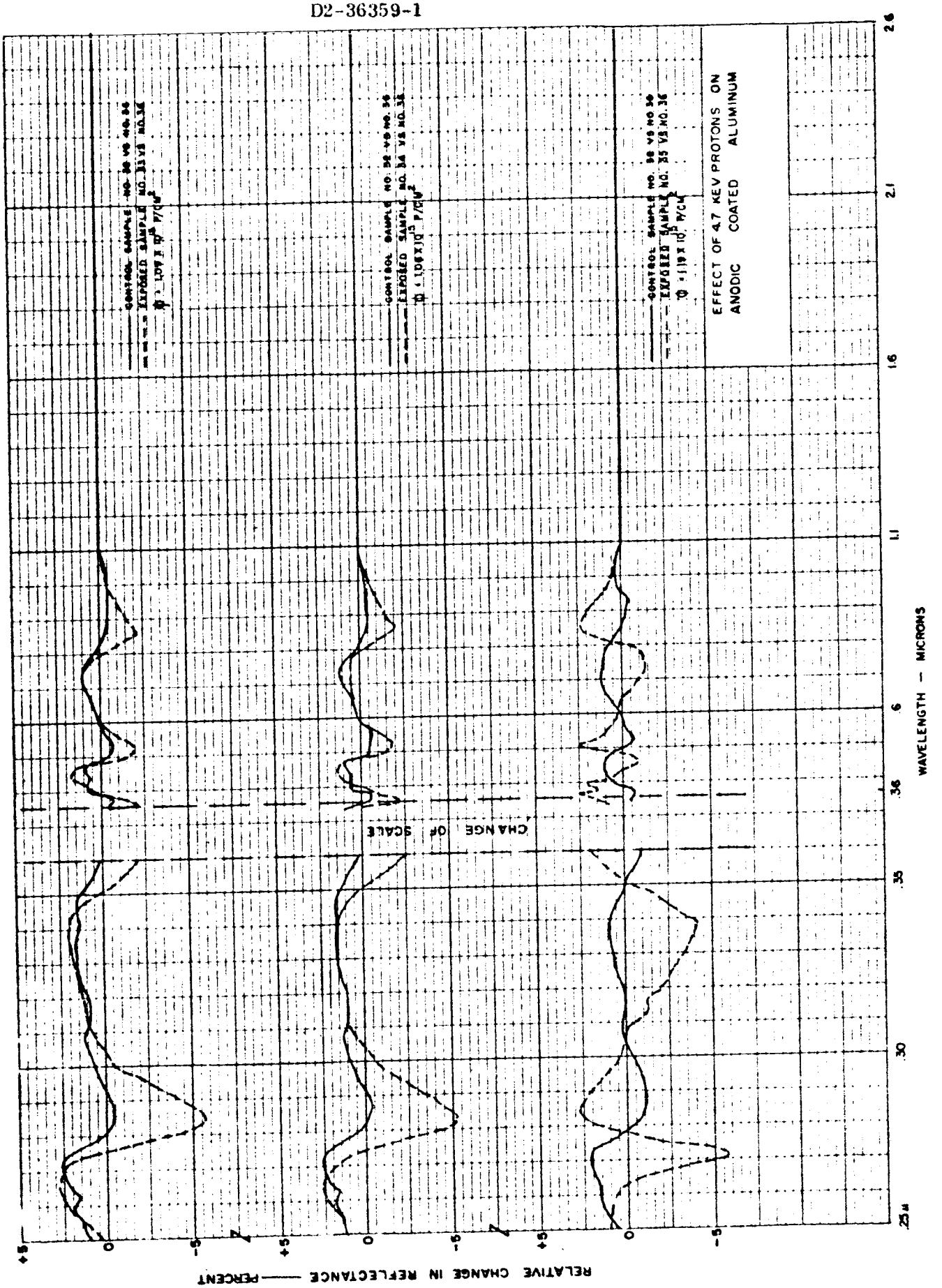

EFFECT OF 4.7 KEV PROTONS ON ANODIC COATED ALUMINUM
CONTROL SAMPLE NO. 36 VS NO. 34
EXPOSED SAMPLE NO. 36 VS NO. 34
Φ = 1.109 X 10^15 P/CM^2
CONTROL SAMPLE NO. 36 VS NO. 35
EXPOSED SAMPLE NO. 35 VS NO. 36
Φ = 1.119 X 10^15 P/CM^2
CHANGE OF SCALE
RELATIVE CHANGE IN REFLECTANCE —— PERCENT
WAVELENGTH — MICRONS
+5
0
-5
.26
.21
.16
.11
.06
.36
.35
.30
.25μ

FIGURE 6.14

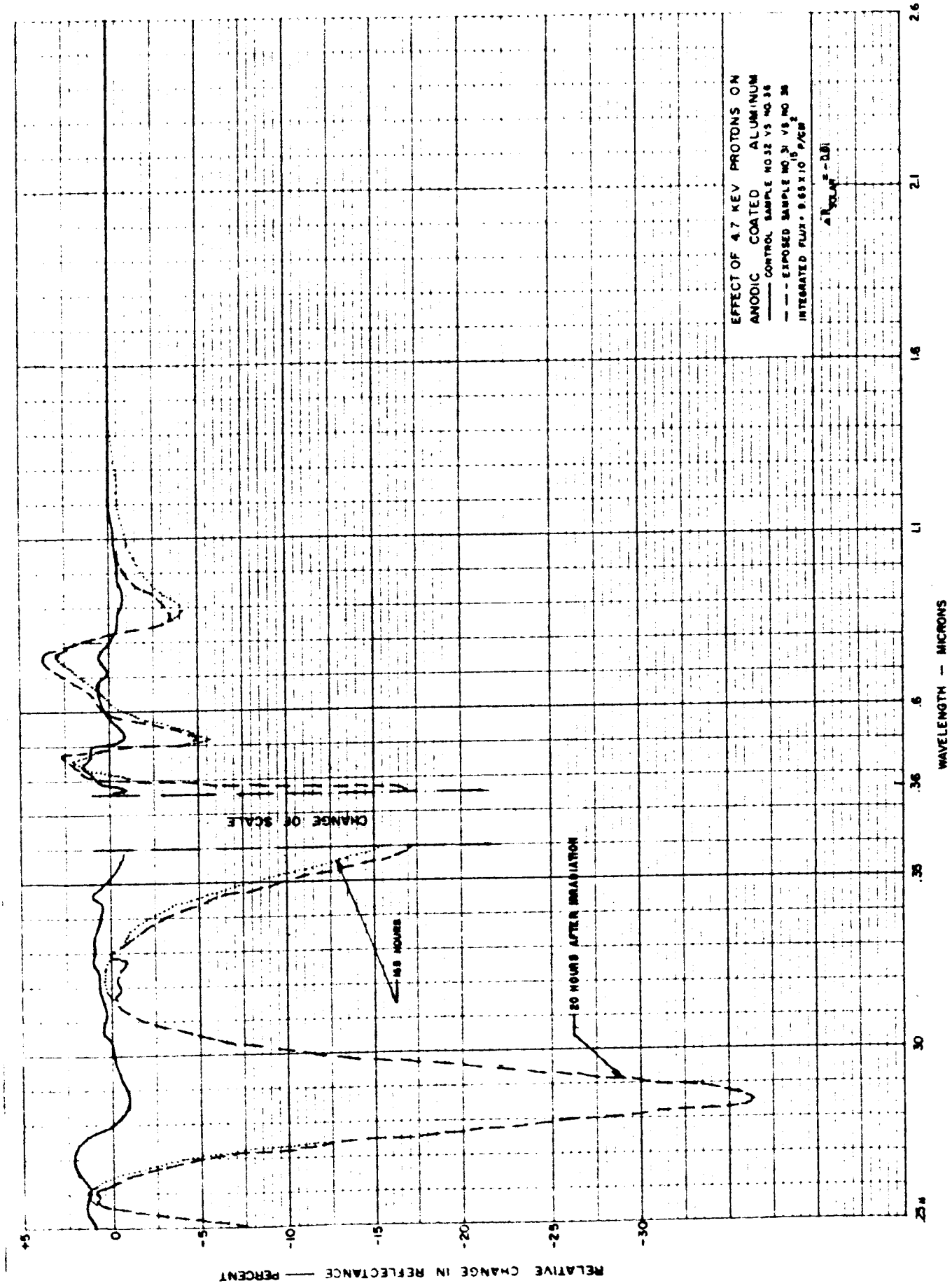

EFFECT OF 4.7 KEV PROTONS ON
ANODIC COATED ALUMINUM
—— CONTROL SAMPLE NO 32 VS NO 36
— — EXPOSED SAMPLE NO 31 VS NO 36
INTEGRATED FLUX = 9.65 X 10^15 P/CM^2
ΔE SOLAR = 0.81
CHANGE OF SCALE
168 HOURS
20 HOURS AFTER IRRADIATION
RELATIVE CHANGE IN REFLECTANCE —— PERCENT
+5
0
-5
-10
-15
-20
-25
-30
.25μ
.30
.35
.36
.6
1.1
1.8
2.1
2.6
WAVELENGTH — MICRONS

FIGURE C15

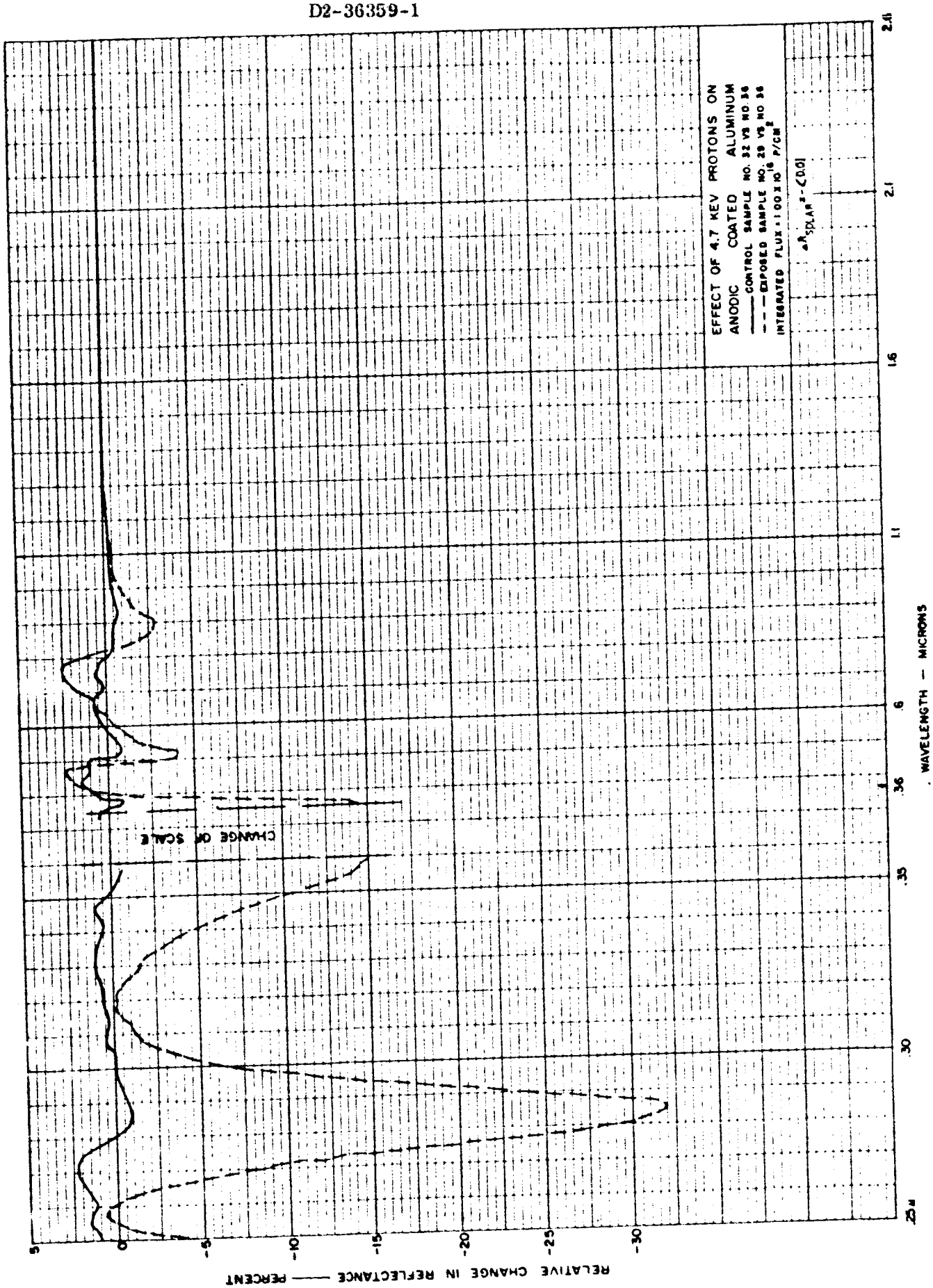

EFFECT OF 4.7 KEV PROTONS ON ANODIC COATED ALUMINUM
——CONTROL SAMPLE NO. 32 VS NO 36
- - -EXPOSED SAMPLE NO. 28 VS NO 36
INTEGRATED FLUX = 1.00 x 10^16 P/CM^2
ΔR_SOLAR = .0.01
CHANGE OF SCALE
RELATIVE CHANGE IN REFLECTANCE —— PERCENT
5
0
-5
-10
-15
-20
-25
-30
.25
.30
.35
.36
.6
1.1
1.6
2.1
2.6
WAVELENGTH — MICRONS

FIGURE C16

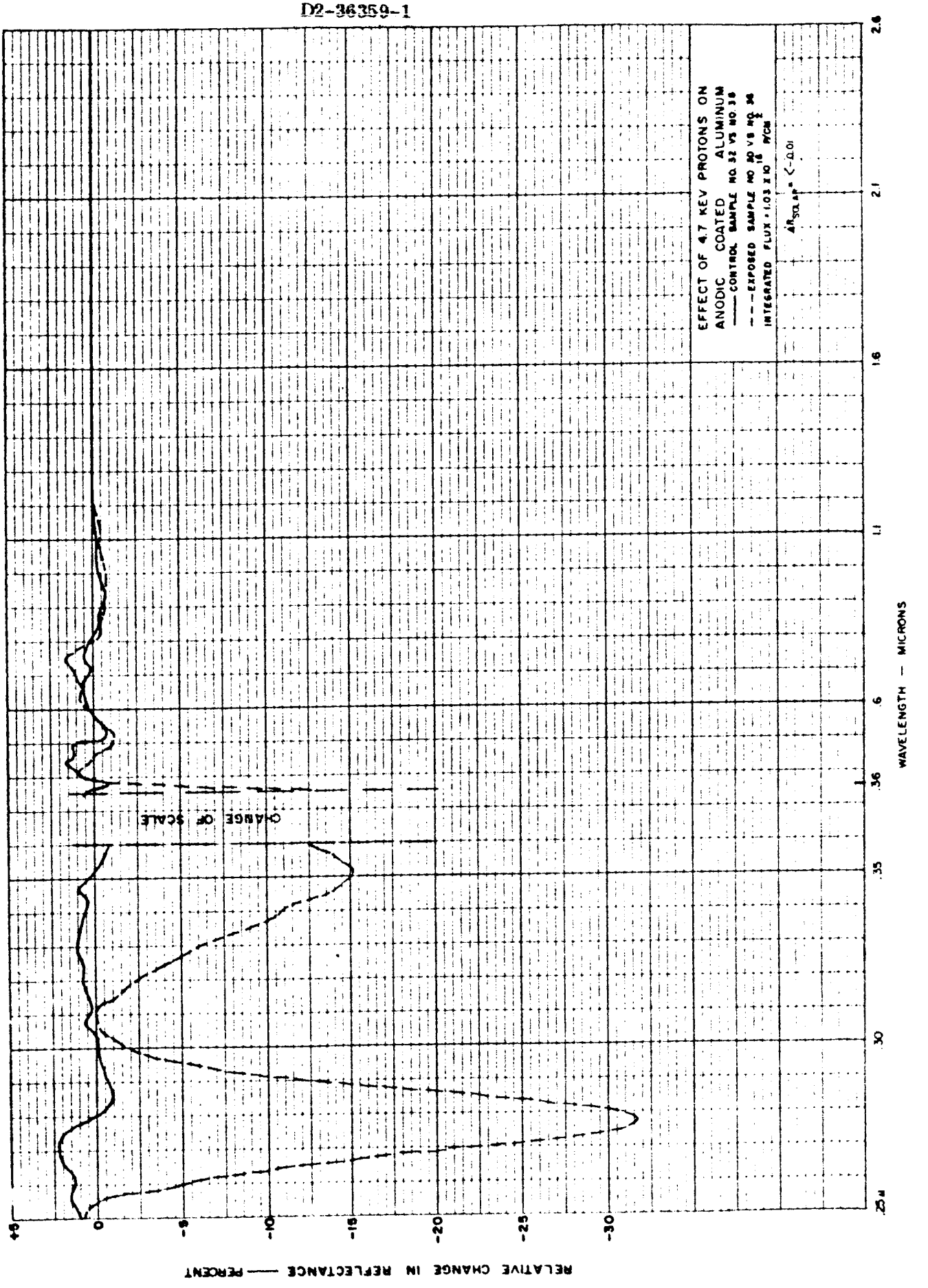

EFFECT OF 4.7 KEV PROTONS ON ANODIC COATED ALUMINUM
——CONTROL SAMPLE NO 32 VS NO 38
– – –EXPOSED SAMPLE NO 30 VS NO 36
INTEGRATED FLUX = 1.03 X 10^16 P/CM^2
ΔR_SOLAR < 0.01
CHANGE OF SCALE
RELATIVE CHANGE IN REFLECTANCE —— PERCENT
+5
0
-5
-10
-15
-20
-25
-30
.25μ
.30
.35
.36
.6
1.1
1.6
2.1
2.6
WAVELENGTH — MICRONS

FIGURE C17

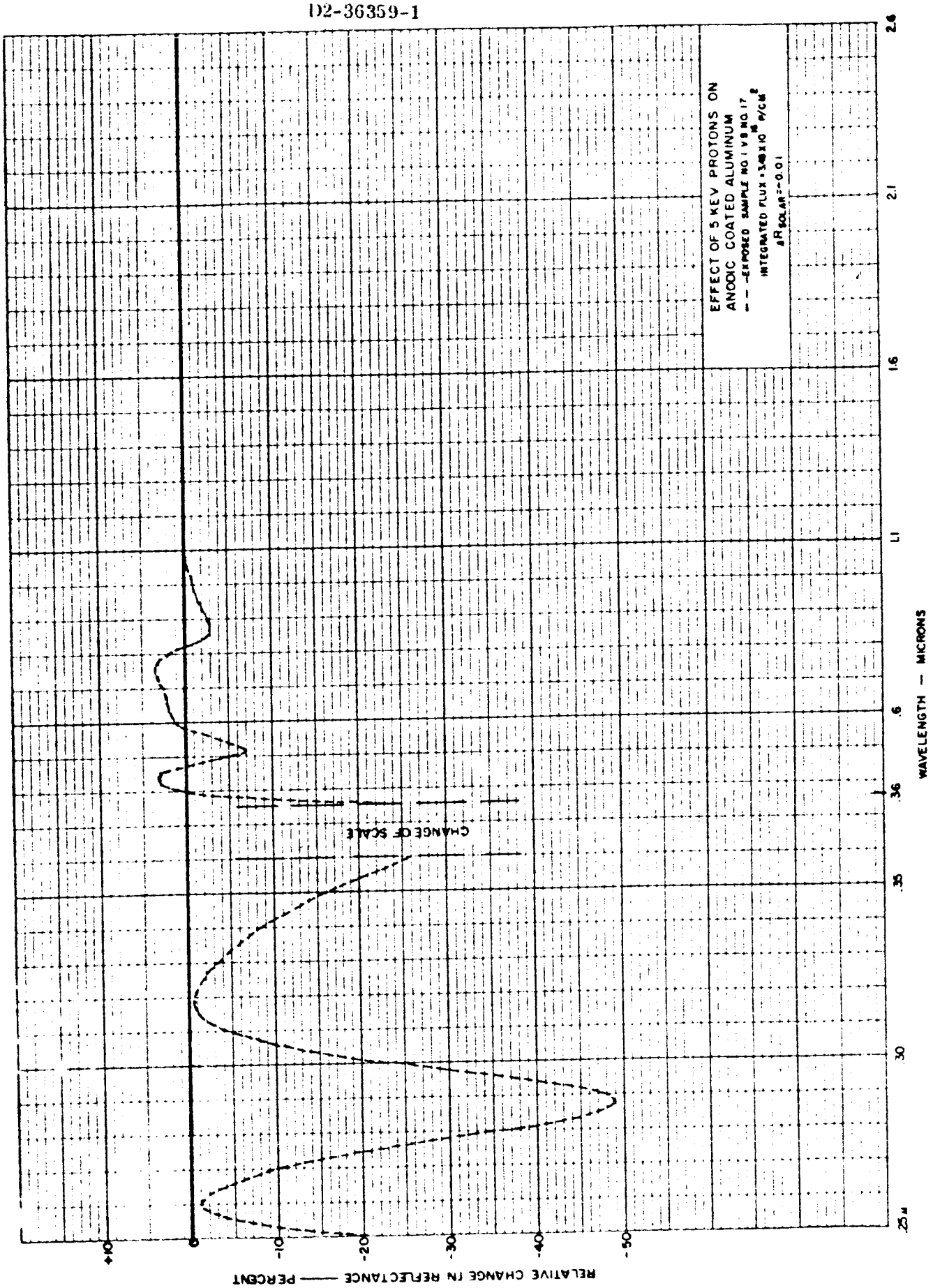

EFFECT OF 5 KEV PROTONS ON
ANODIC COATED ALUMINUM
-- EXPOSED SAMPLE NO. 1 VS NO. 17
INTEGRATED FLUX = 3.48 X 10^16 P/CM^2
ΔR SOLAR = 0.01
CHANGE OF SCALE
+10
0
-10
-20
-30
-40
-50
RELATIVE CHANGE IN REFLECTANCE —— PERCENT
.25
.30
.35
.36
.6
1.1
1.6
2.1
2.6
WAVELENGTH — MICRONS

FIGURE C18

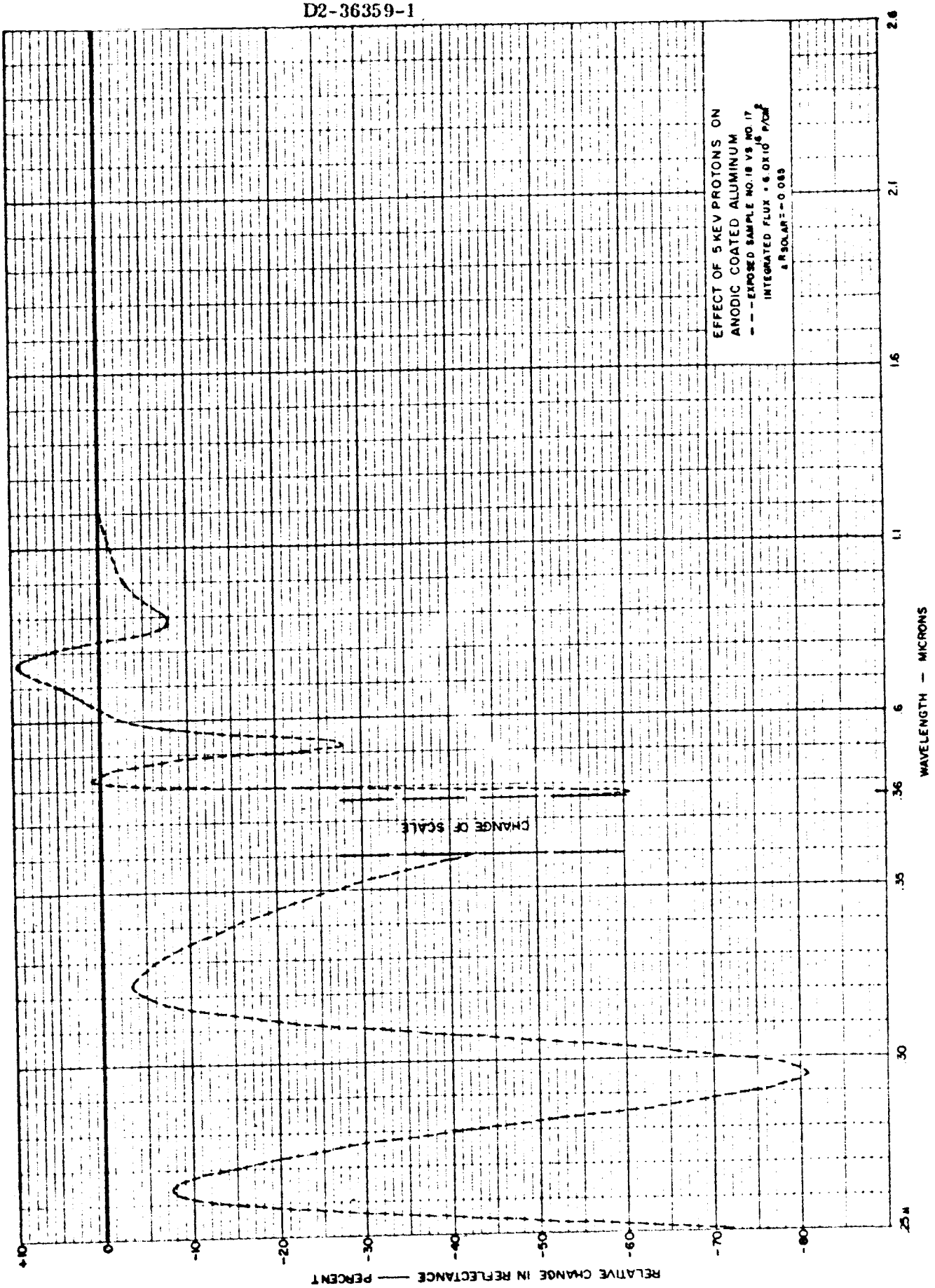

EFFECT OF 5 KEV PROTONS ON
ANODIC COATED ALUMINUM
- - - EXPOSED SAMPLE NO. 18 VS NO. 17
INTEGRATED FLUX = 6.0 X 10^15 P/CM^2
ΔR SOLAR = - 0.065
CHANGE OF SCALE
RELATIVE CHANGE IN REFLECTANCE —— PERCENT
+10
0
-10
-20
-30
-40
-50
-60
-70
-80
.25
.30
.35
.36
.6
1.1
1.6
2.1
2.6
WAVELENGTH — MICRONS

FIGURE C19

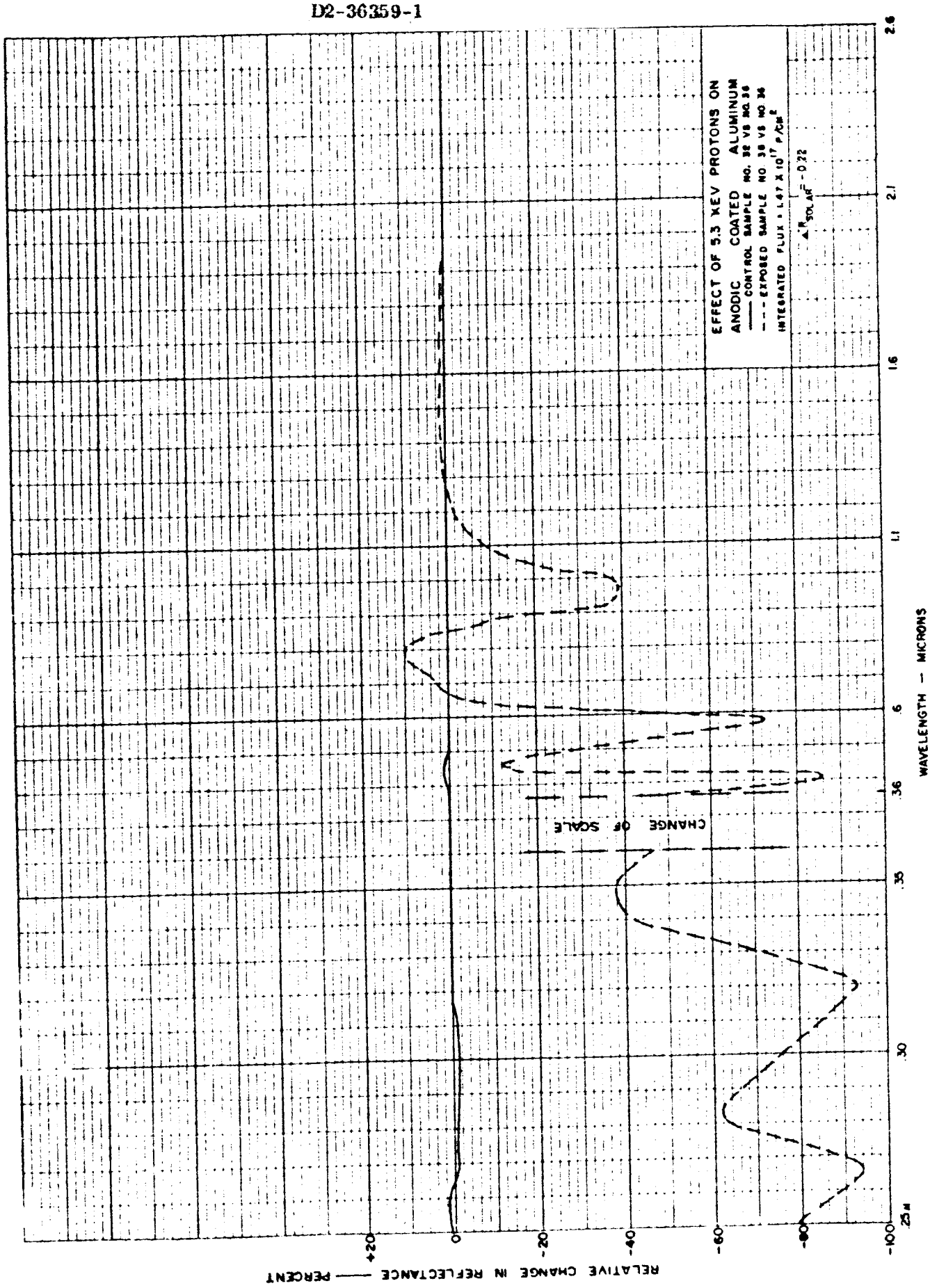

EFFECT OF 5.3 KEV PROTONS ON
ANODIC COATED ALUMINUM
—— CONTROL SAMPLE NO. 35 VS NO. 36
- - - EXPOSED SAMPLE NO. 35 VS NO. 36
INTEGRATED FLUX = 1.47 X 10^17 P/CM^2
ΔR SOLAR = 0.22
RELATIVE CHANGE IN REFLECTANCE —— PERCENT
+20
0
-20
-40
-60
-80
-100
CHANGE OF SCALE
.25μ
.30
.35
.36
.6
1.1
1.6
2.1
2.6
WAVELENGTH — MICRONS

FIGURE C 20

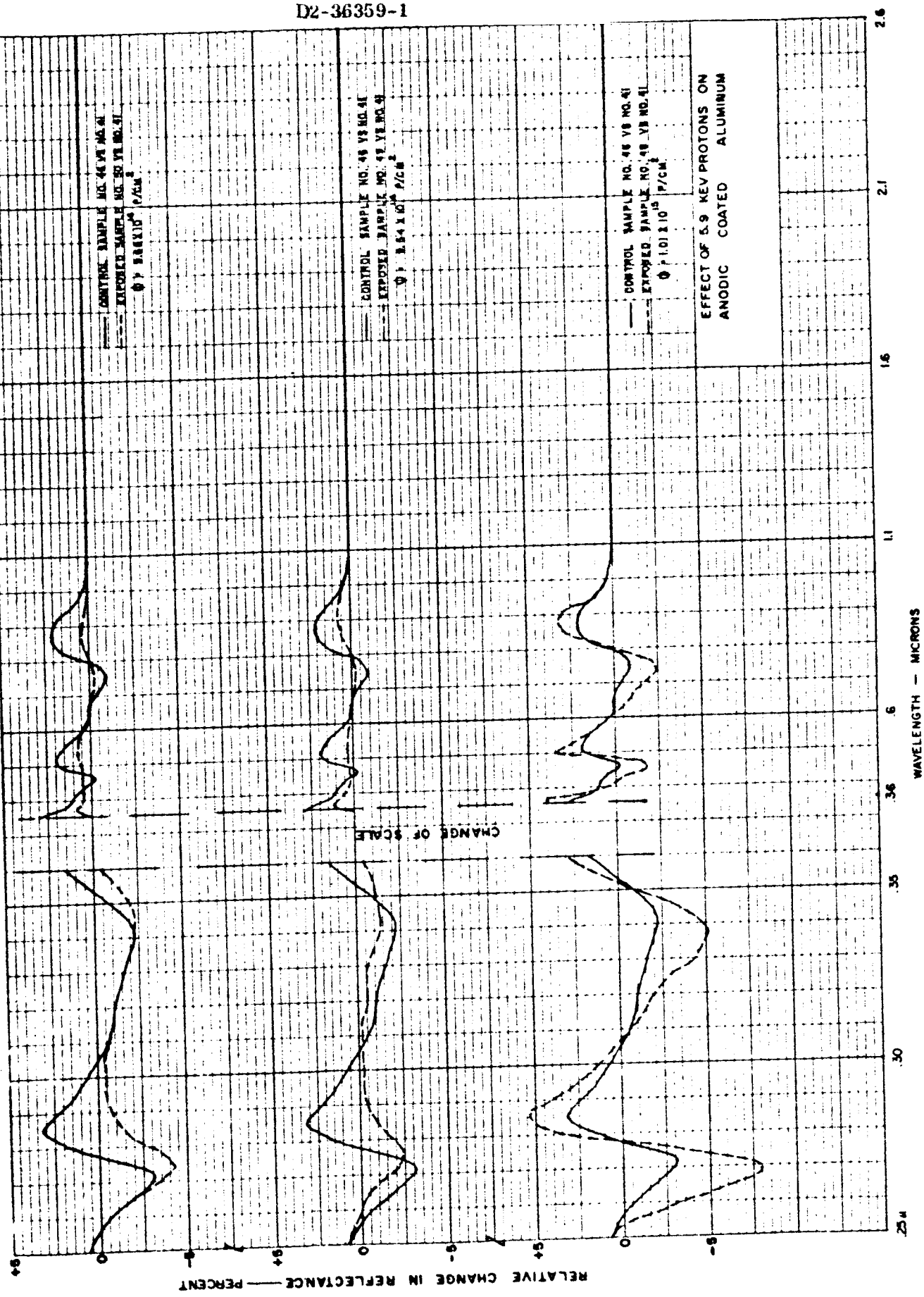

EFFECT OF 5.9 KEV PROTONS ON ANODIC COATED ALUMINUM
CONTROL SAMPLE NO. 46 VS NO. 41
EXPOSED SAMPLE NO. 46 VS NO. 41
Φ = 1.01 X 10^15 P/CM^2
CONTROL SAMPLE NO. 46 VS NO. 41
EXPOSED SAMPLE NO. 49 VS NO. 41
Φ = 1.64 X 10^14 P/CM^2
CONTROL SAMPLE NO. 46 VS NO. 41
EXPOSED SAMPLE NO. 50 VS NO. 41
Φ = 8.66 X 10^14 P/CM^2
RELATIVE CHANGE IN REFLECTANCE —— PERCENT
CHANGE OF SCALE
WAVELENGTH — MICRONS
+6
0
-6
2.6
2.1
1.6
1.1
.6
.36
.35
.30
.25 M

FIGURE C 21

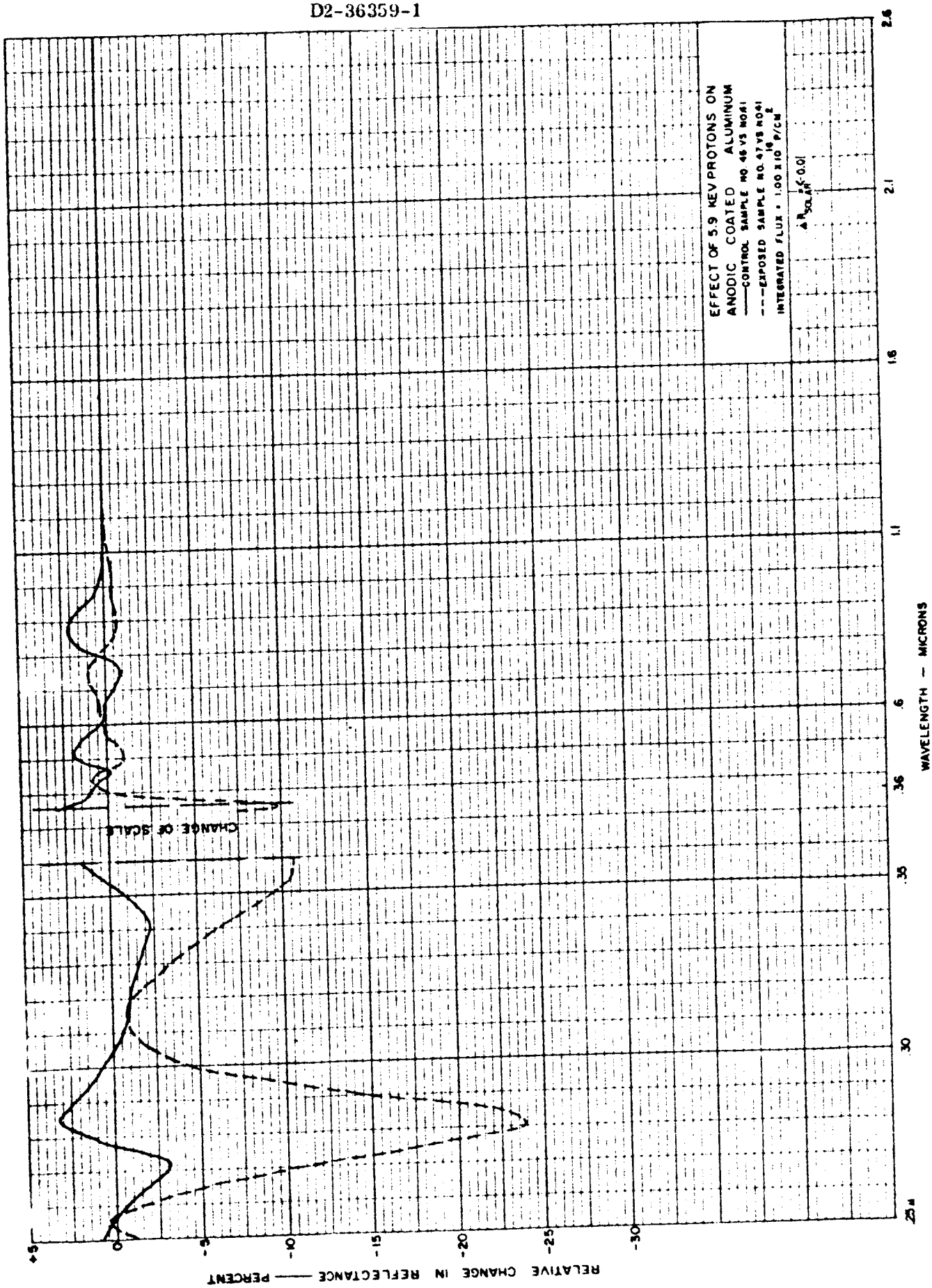

EFFECT OF 5.9 KEV PROTONS ON
ANODIC COATED ALUMINUM
——CONTROL SAMPLE NO 46 VS NO 41
- - -EXPOSED SAMPLE NO. 47 VS NO 41
INTEGRATED FLUX = 1.00 X 10^15 P/CM^2
ΔR_SOLAR ≤ 0.01
CHANGE OF SCALE
+5
0
-5
-10
-15
-20
-25
-30
RELATIVE CHANGE IN REFLECTANCE —— PERCENT
.25
.30
.35
.36
.6
1.1
1.6
2.1
2.6
WAVELENGTH — MICRONS

FIGURE C22

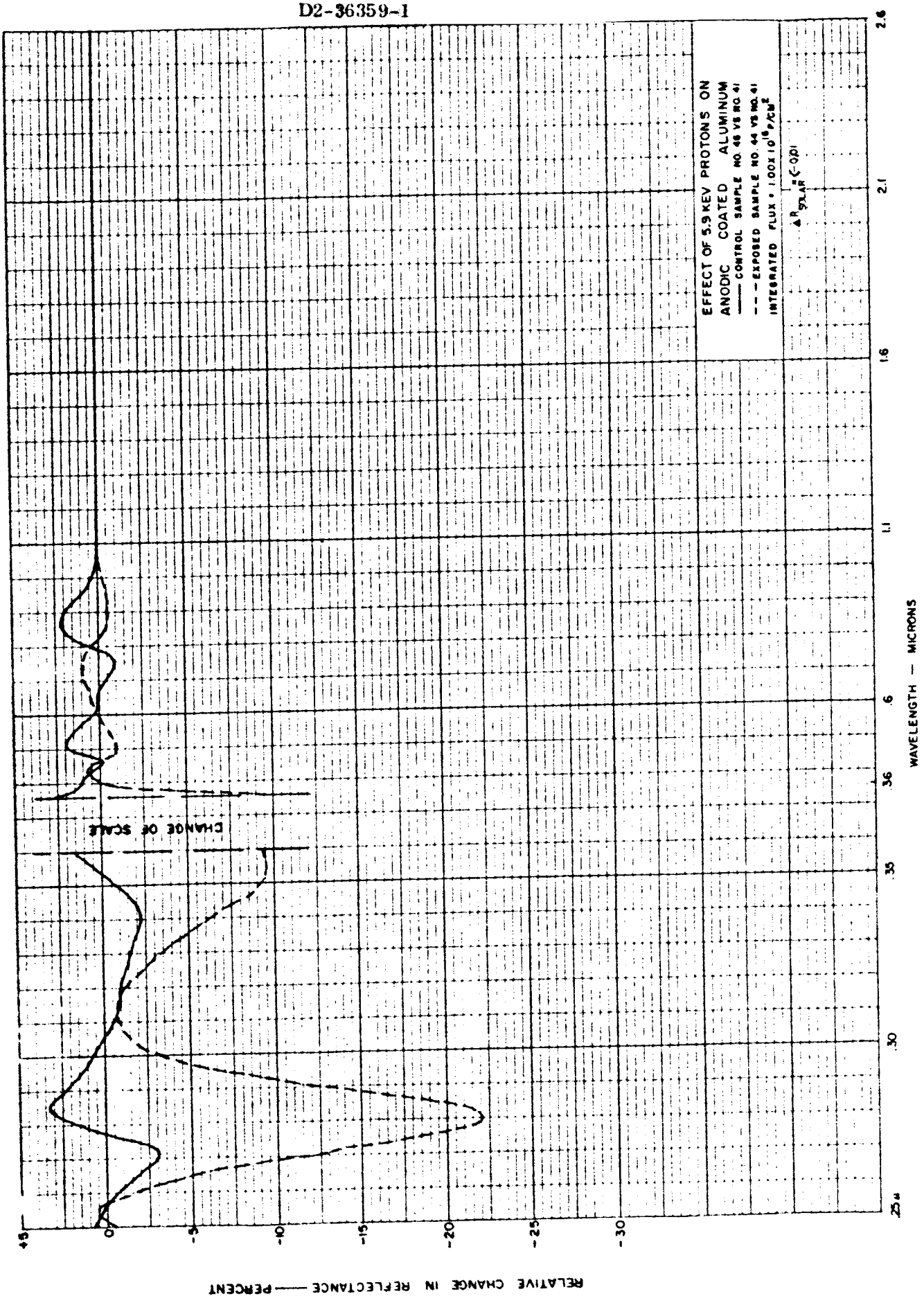

EFFECT OF 5.9 KEV PROTONS ON
ANODIC COATED ALUMINUM
—— CONTROL SAMPLE NO. 46 VS NO. 41
- - - EXPOSED SAMPLE NO. 44 VS NO. 41
INTEGRATED FLUX = 1.00 X 10^15 P/CM^2
ΔR_SOLAR = 0.021
CHANGE OF SCALE
+5
0
-5
-10
-15
-20
-25
-30
.25μ
.30
.35
.36
.6
1.1
1.6
2.1
2.6
WAVELENGTH — MICRONS
RELATIVE CHANGE IN REFLECTANCE —— PERCENT

FIGURE C23

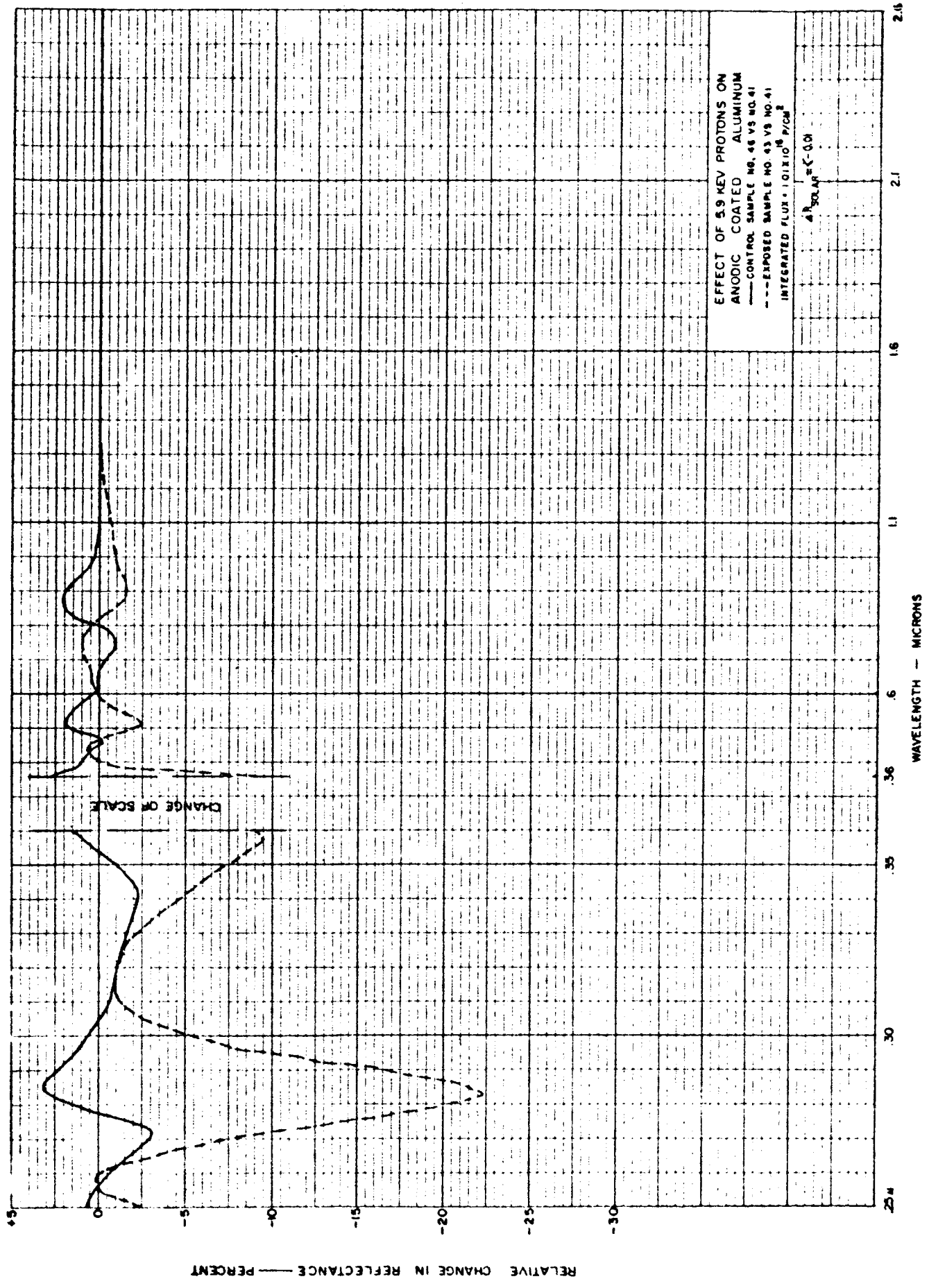

EFFECT OF 5.9 KEV PROTONS ON
ANODIC COATED ALUMINUM
—CONTROL SAMPLE NO. 46 VS NO. 41
---EXPOSED SAMPLE NO. 43 VS NO. 41
INTEGRATED FLUX = 1.01 X 10^16 P/CM^2
Δρ500 Å = < 0.01
CHANGE OF SCALE
+5
0
-5
-10
-15
-20
-25
-30
.25
.30
.35
.36
.6
1.1
1.6
2.1
2.6
WAVELENGTH — MICRONS
RELATIVE CHANGE IN REFLECTANCE —— PERCENT

FIGURE C24

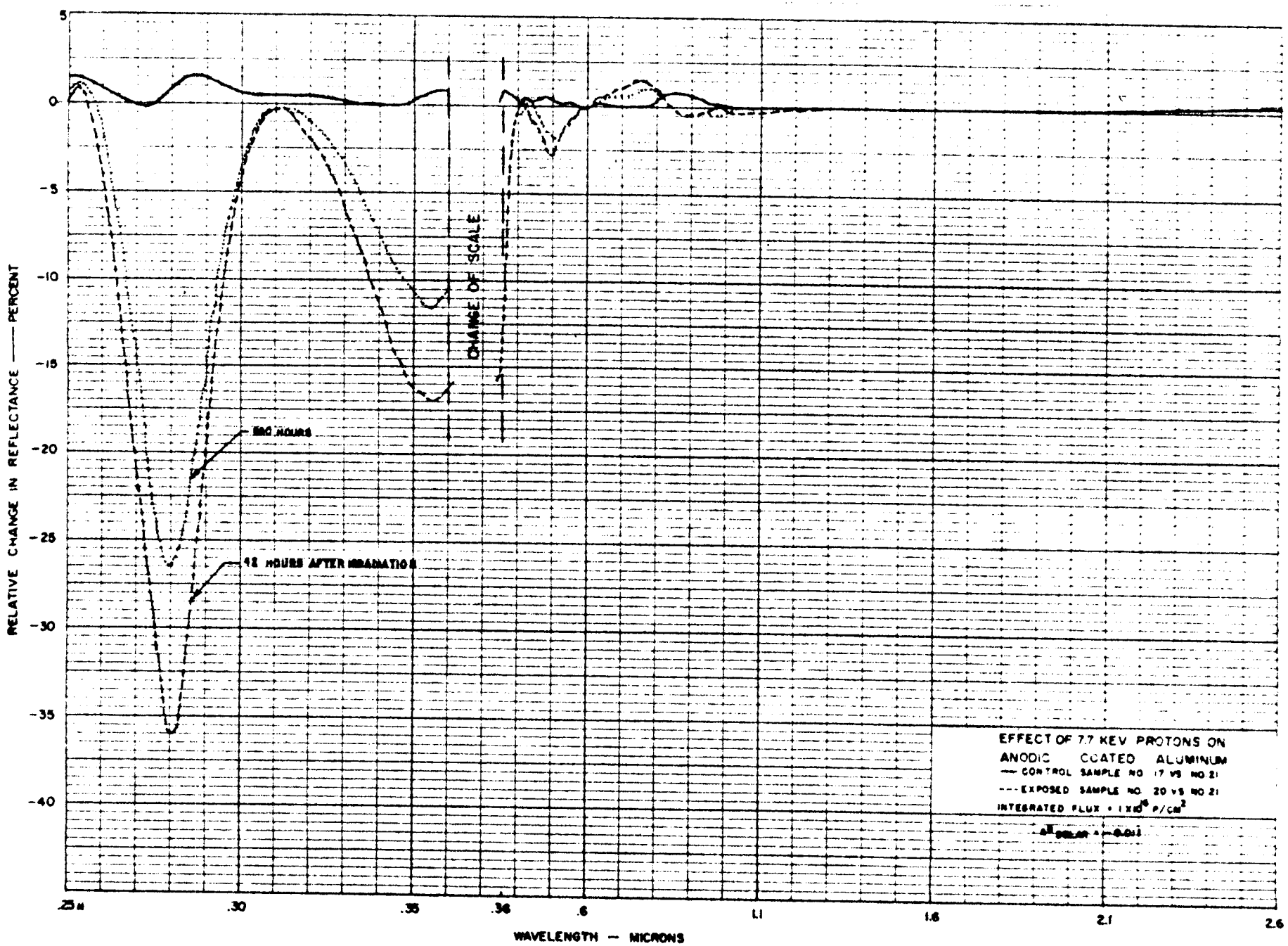


FIGURE G25
135

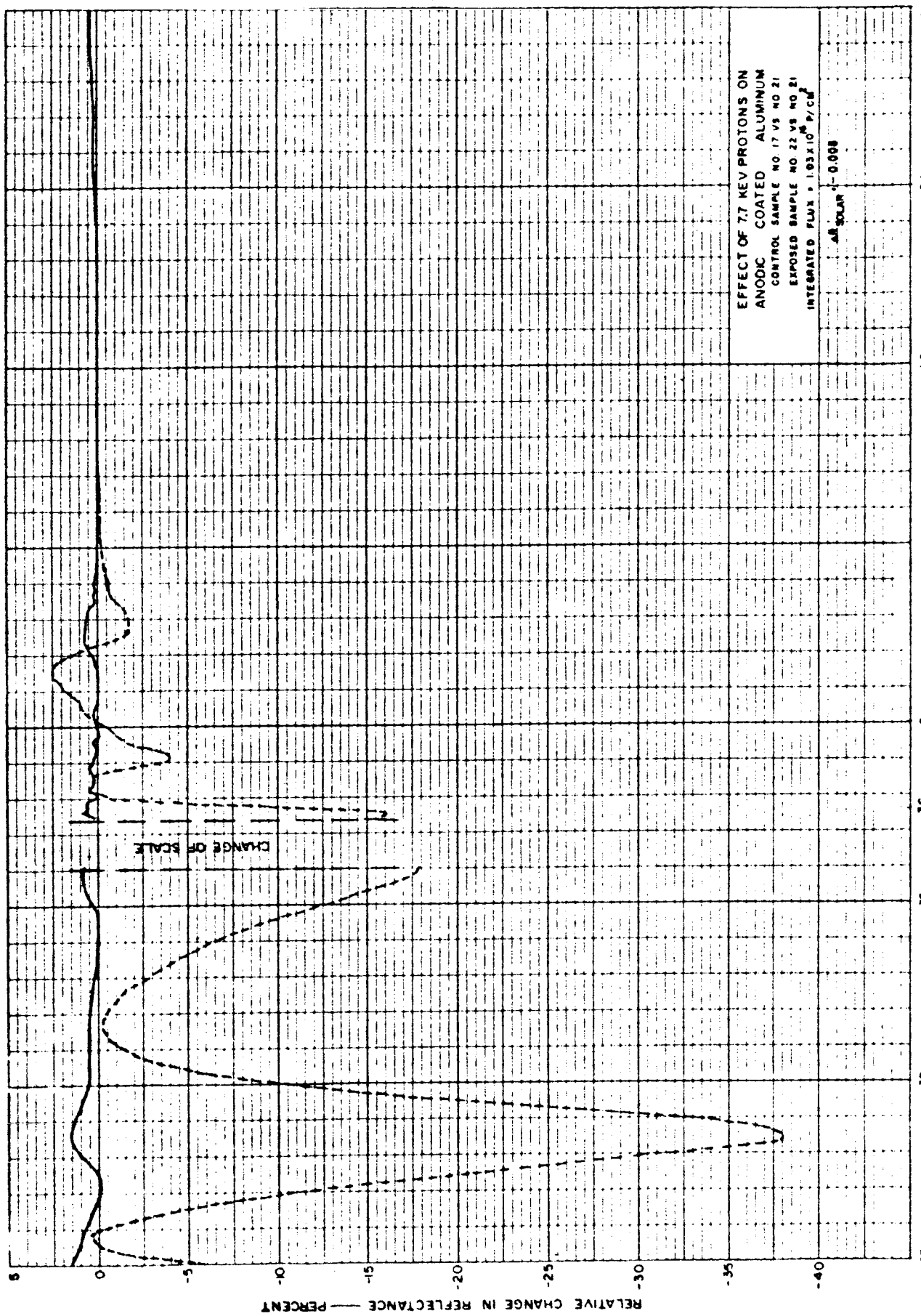

EFFECT OF 7.7 KEV PROTONS ON
ANODIC COATED ALUMINUM
CONTROL SAMPLE NO 17 VS NO 21
EXPOSED SAMPLE NO 22 VS NO 21
INTEGRATED FLUX = 1.03 x 10^16 P/CM^2
Δα SOLAR +/- 0.008
CHANGE OF SCALE
RELATIVE CHANGE IN REFLECTANCE — PERCENT
5
0
-5
-10
-15
-20
-25
-30
-35
-40
.25
.30
.35
.36
.6
1.1
1.6
2.1
2.6
WAVELENGTH — MICRONS

FIGURE C 26

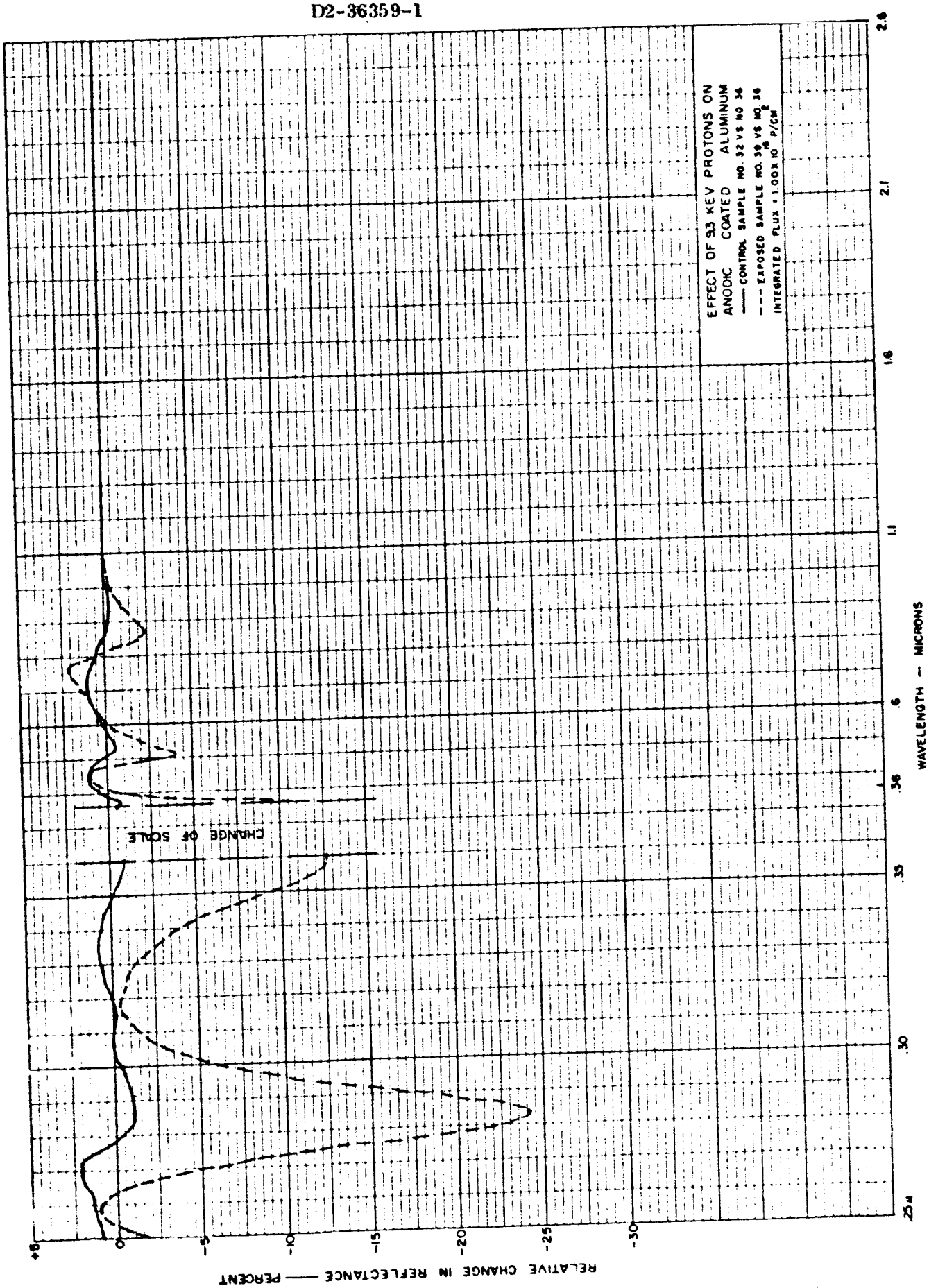

EFFECT OF 93 KEV PROTONS ON
ANODIC COATED ALUMINUM
—— CONTROL SAMPLE NO. 32 VS NO 34
- - - EXPOSED SAMPLE NO. 39 VS NO. 36
INTEGRATED FLUX = 1.00 X 10^14 P/CM^2
CHANGE OF SCALE
+5
0
-5
-10
-15
-20
-25
-30
RELATIVE CHANGE IN REFLECTANCE —— PERCENT
.25
.30
.35
.36
.6
1.1
1.6
2.1
2.6
WAVELENGTH — MICRONS

FIGURE C 27

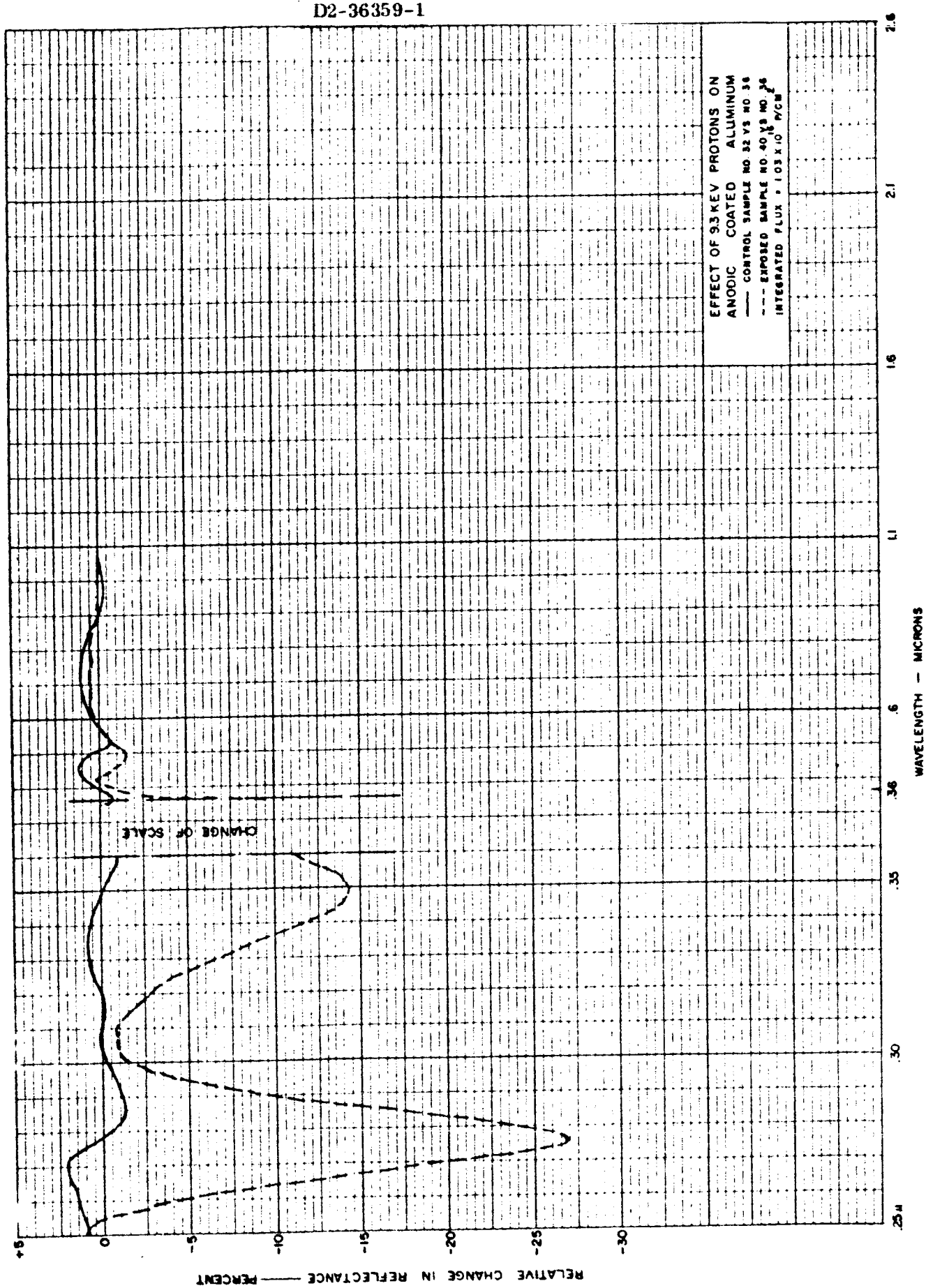

EFFECT OF 9.3 KEV PROTONS ON ANODIC COATED ALUMINUM
CONTROL SAMPLE NO 32 VS NO 36
EXPOSED SAMPLE NO. 40 VS NO. 36
INTEGRATED FLUX = 1.03 x 10^15 P/CM^2
CHANGE OF SCALE
RELATIVE CHANGE IN REFLECTANCE —— PERCENT
+5
0
-5
-10
-15
-20
-25
-30
.25μ
.30
.35
.36
.6
1.1
1.6
2.1
2.6
WAVELENGTH — MICRONS

FIGURE C28

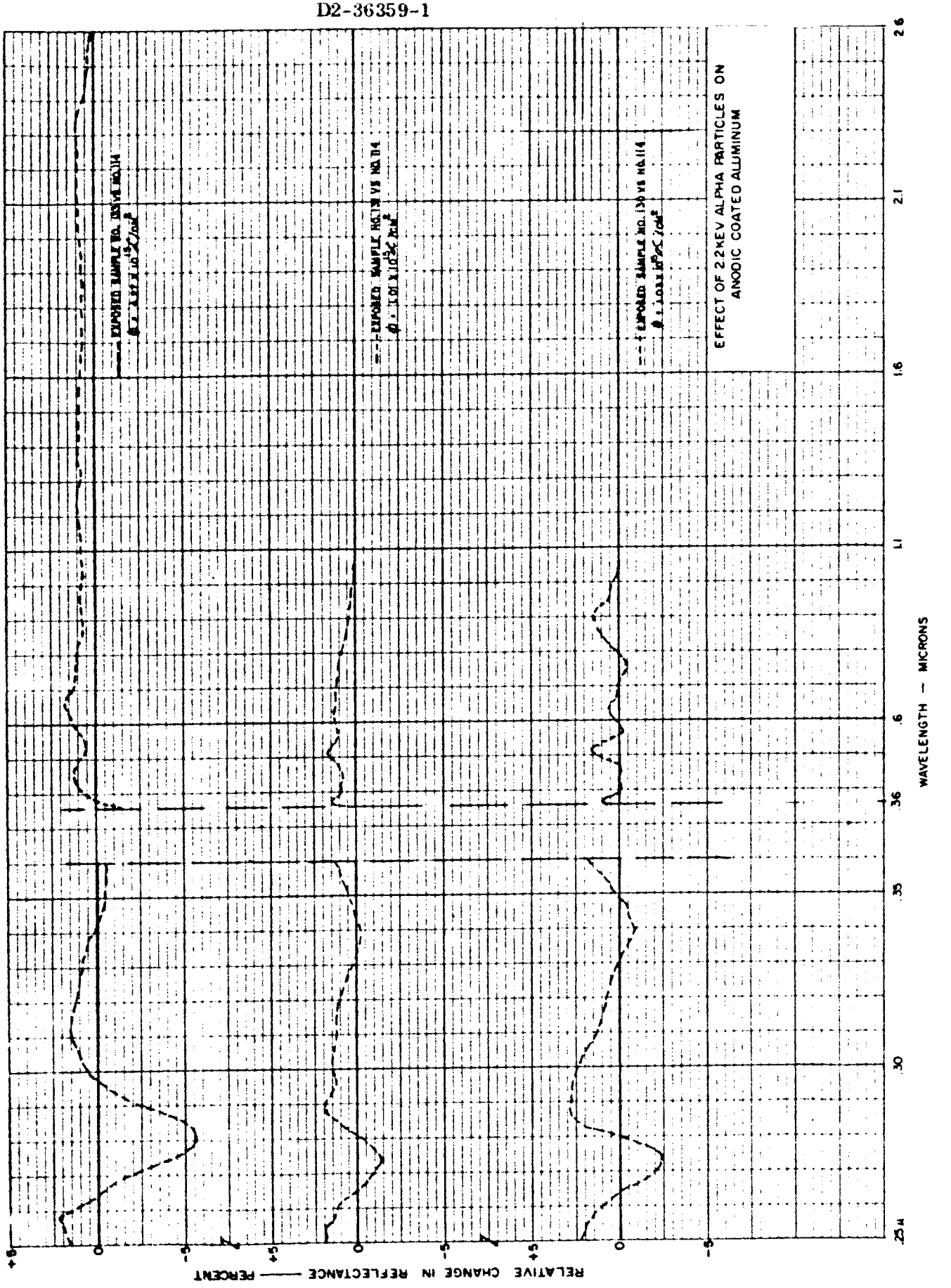

EFFECT OF 2.2 KEV ALPHA PARTICLES ON
ANODIC COATED ALUMINUM
EXPOSED SAMPLE NO. 134 VS NO. 114
EXPOSED SAMPLE NO. 113 VS NO. 114
EXPOSED SAMPLE NO. 130 VS NO. 114
RELATIVE CHANGE IN REFLECTANCE —— PERCENT
WAVELENGTH — MICRONS
+5
0
-5
.25μ
.30
.35
.36
.6
1.1
1.6
2.1
2.6

FIGURE C 29

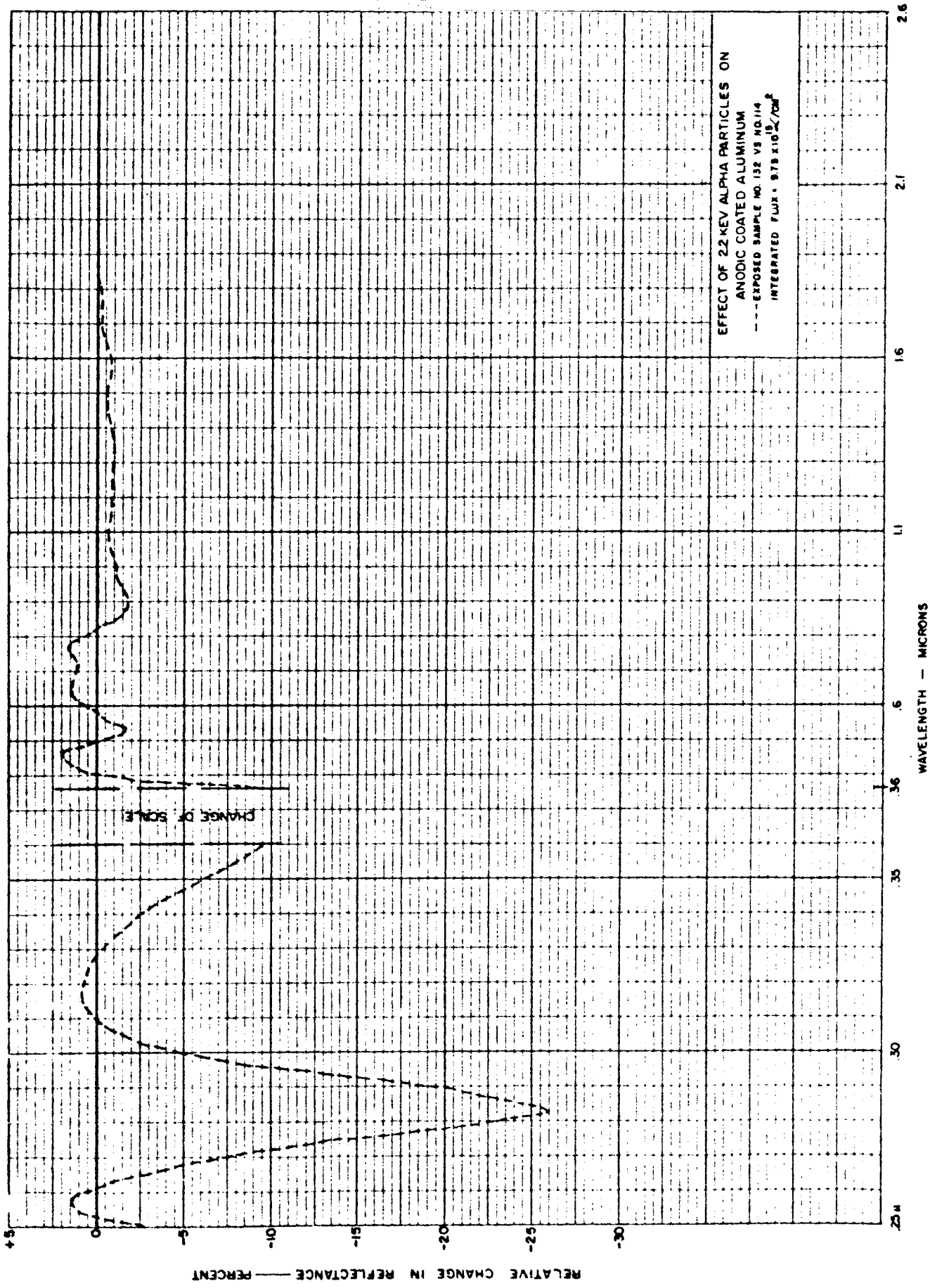

EFFECT OF 22 KEV ALPHA PARTICLES ON
ANODIC COATED ALUMINUM
---EXPOSED SAMPLE NO. 132 VS NO. 114
INTEGRATED FLUX = 9.78 x 10^15 p/cm^2
CHANGE OF SCALE
RELATIVE CHANGE IN REFLECTANCE —— PERCENT
+5
0
-5
-10
-15
-20
-25
-30
2.6
2.1
1.6
1.1
.6
.36
.35
.30
.25 μ
WAVELENGTH — MICRONS

FIGURE C 30

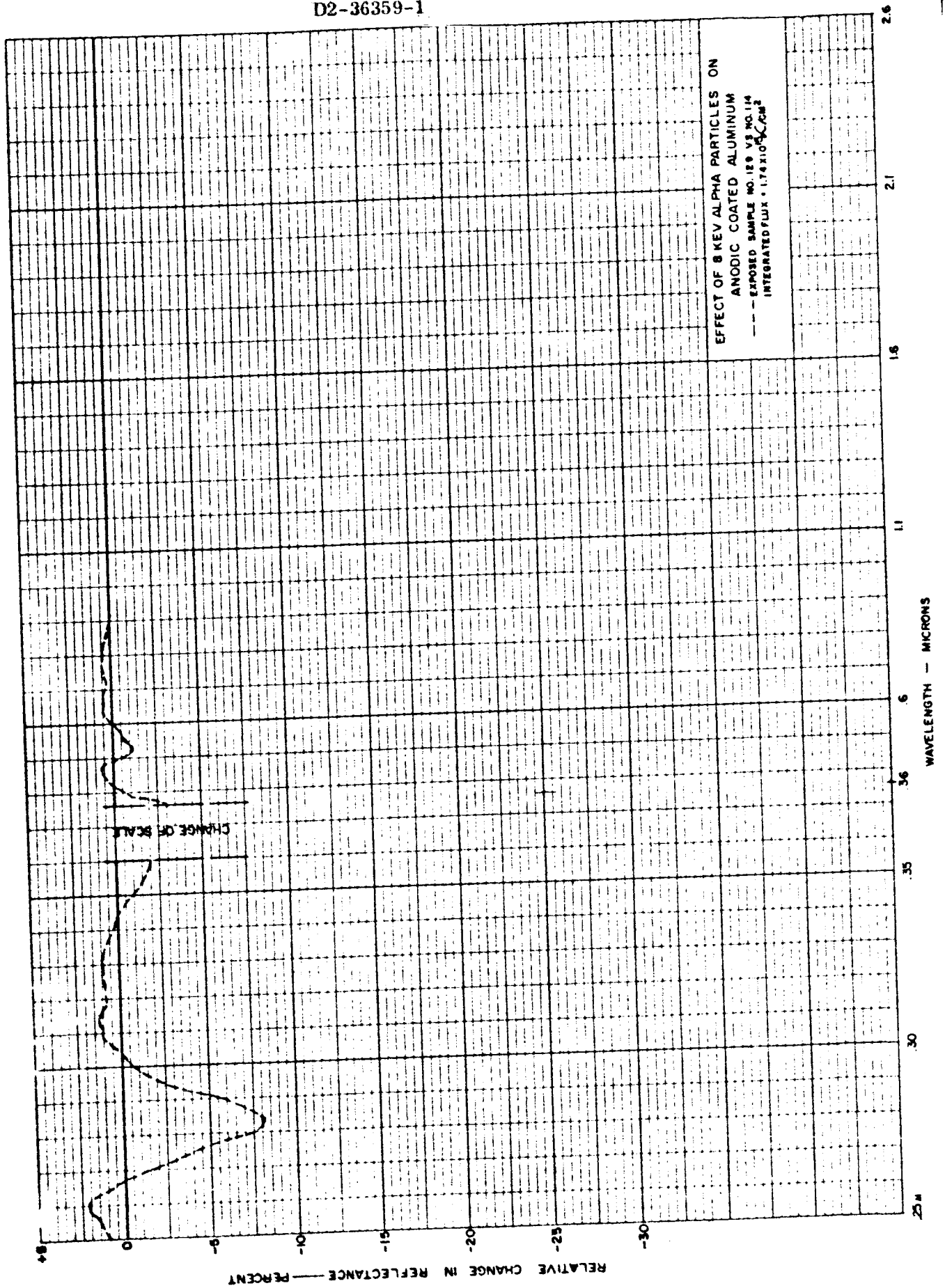

EFFECT OF 8 KEV ALPHA PARTICLES ON
ANODIC COATED ALUMINUM
EXPOSED SAMPLE NO. 129 VS NO. 114
INTEGRATED FLUX = 1.74 X 10^14 P/cm^2
CHANGE ON SCALE
RELATIVE CHANGE IN REFLECTANCE — PERCENT
+5
0
-5
-10
-15
-20
-25
-30
2.6
2.1
1.6
1.1
.6
.36
.35
.30
.25 μ
WAVELENGTH — MICRONS

FIGURE C 31

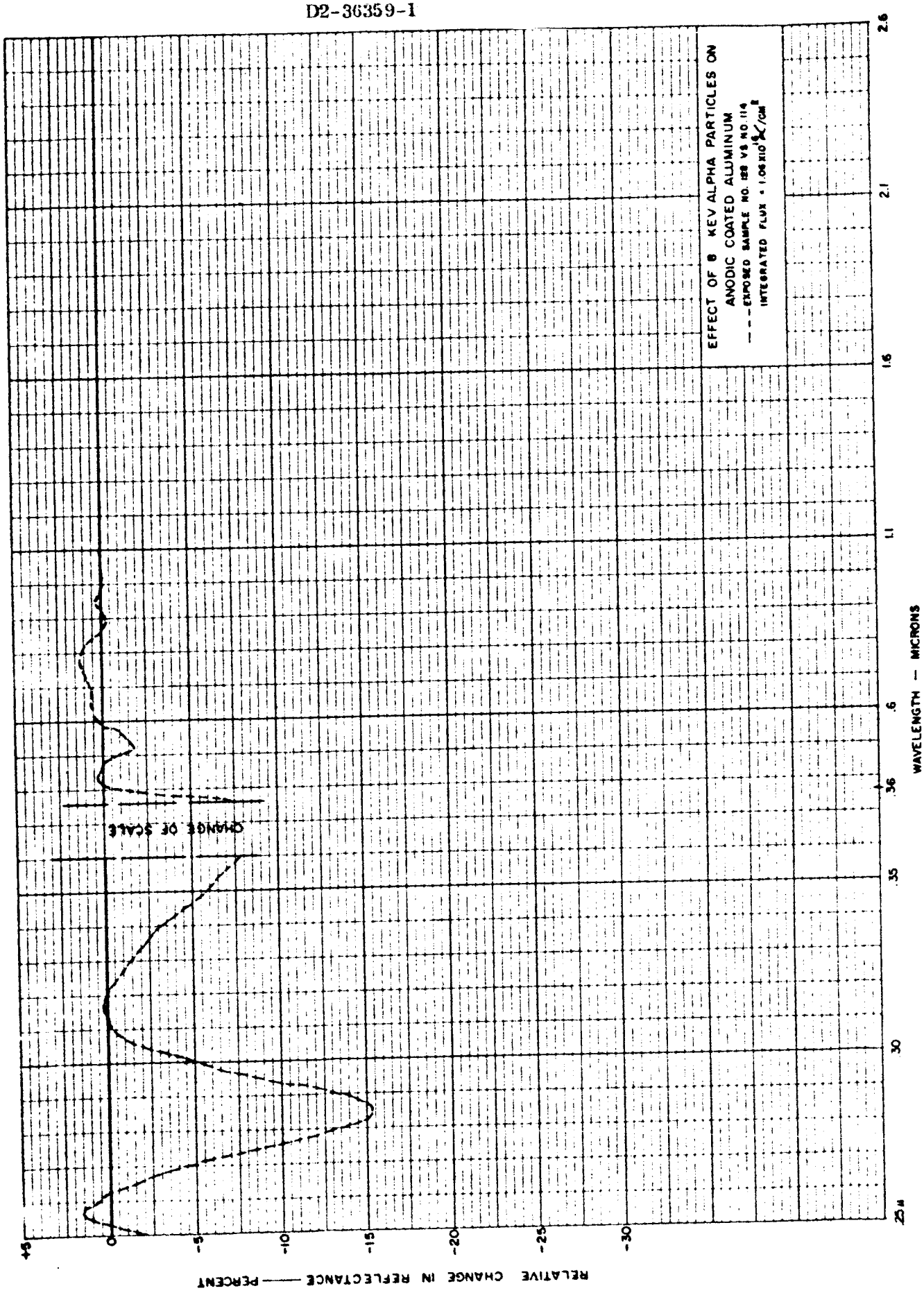

EFFECT OF 8 KEV ALPHA PARTICLES ON
ANODIC COATED ALUMINUM
---EXPOSED SAMPLE NO. 128 V8 NO. 114
INTEGRATED FLUX = 1.06 X10¹⁴ P/CM²
CHANGE OF SCALE
+5
0
-5
-10
-15
-20
-25
-30
RELATIVE CHANGE IN REFLECTANCE —— PERCENT
2.6
2.1
1.6
1.1
.6
.36
.35
.30
.25 μ
WAVELENGTH — MICRONS

FIGURE C32

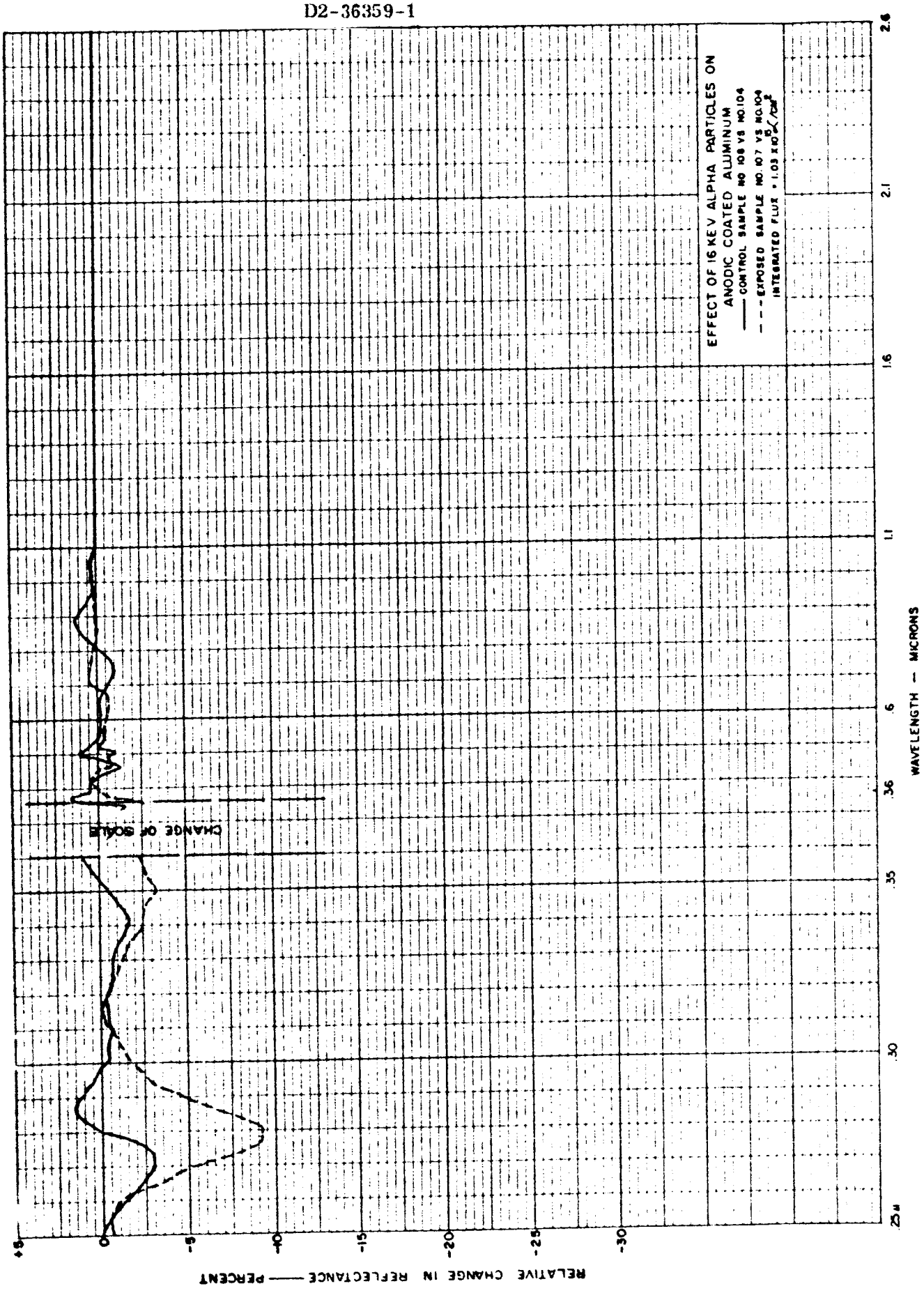

EFFECT OF 16 KEV ALPHA PARTICLES ON
ANODIC COATED ALUMINUM
—— CONTROL SAMPLE NO 108 VS NO.104
- - - EXPOSED SAMPLE NO. 107 VS NO.104
INTEGRATED FLUX = 1.03 X 10^15 P/cm^2
CHANGE OF SCALE
+5
0
-5
-10
-15
-20
-25
-30
RELATIVE CHANGE IN REFLECTANCE —— PERCENT
.25μ
.30
.35
.36
.6
1.1
1.6
2.1
2.6
WAVELENGTH — MICRONS

FIGURE C 33

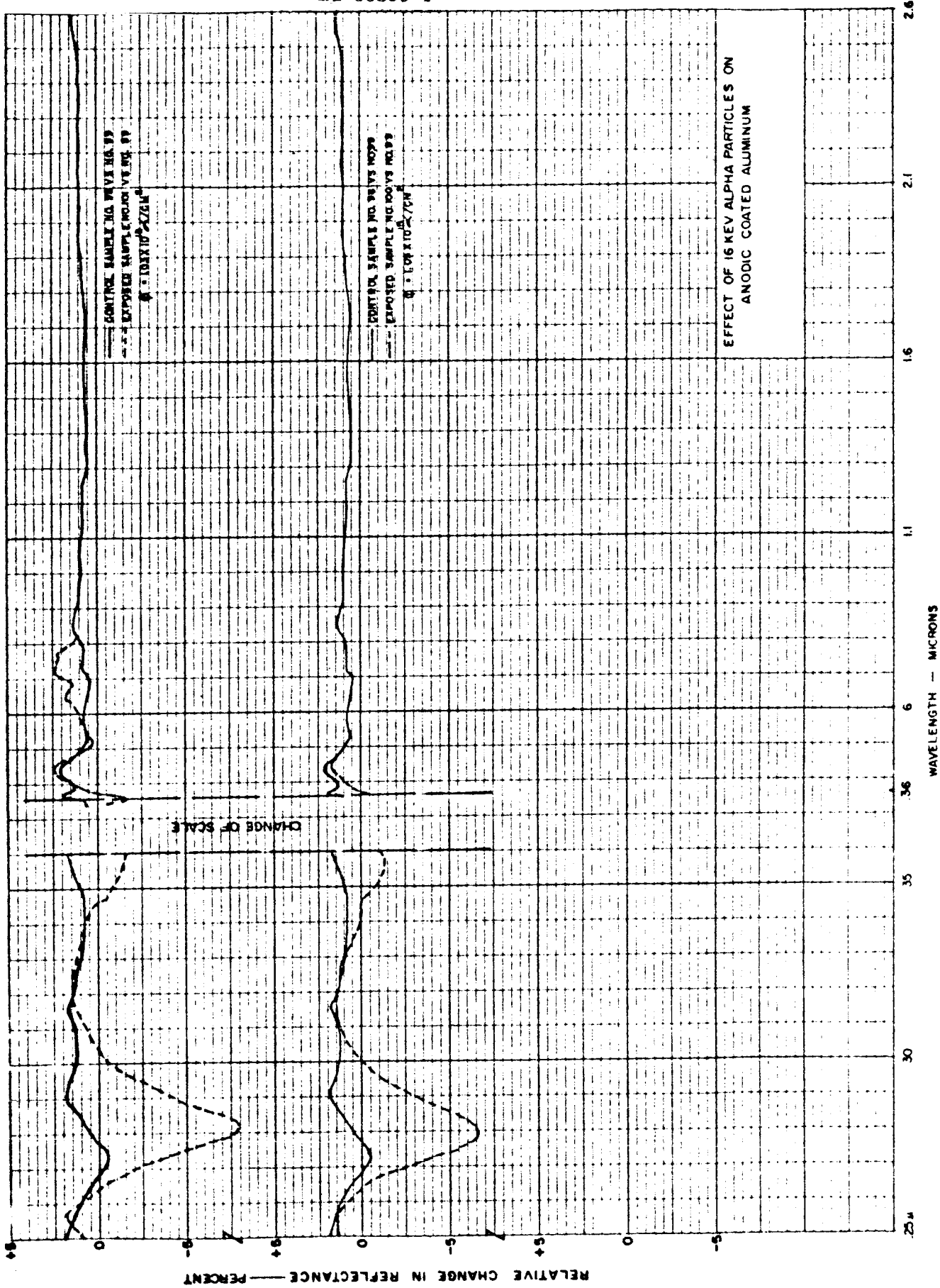


FIGURE C34
144

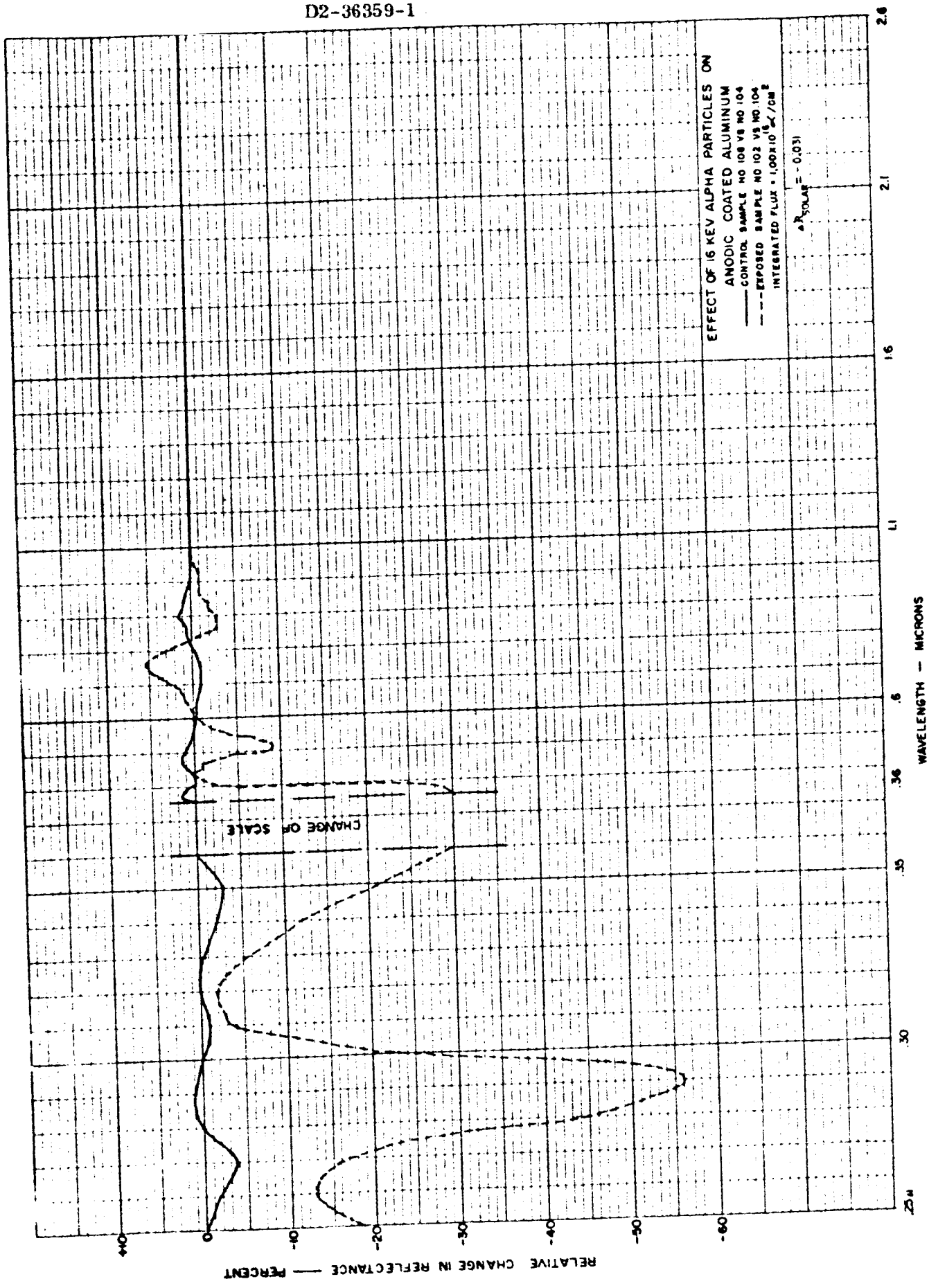

EFFECT OF 16 KEV ALPHA PARTICLES ON
ANODIC COATED ALUMINUM
CONTROL SAMPLE NO 108 VS NO 104
EXPOSED SAMPLE NO 102 VS NO 104
INTEGRATED FLUX = 1.000 X 10^16 ∝/CM^2
α_SOLAR = 0.031
CHANGE OF SCALE
RELATIVE CHANGE IN REFLECTANCE — PERCENT
+10
0
-10
-20
-30
-40
-50
-60
.25 μ
.30
.35
.36
.6
1.1
1.6
2.1
2.6
WAVELENGTH — MICRONS

FIGURE C 35

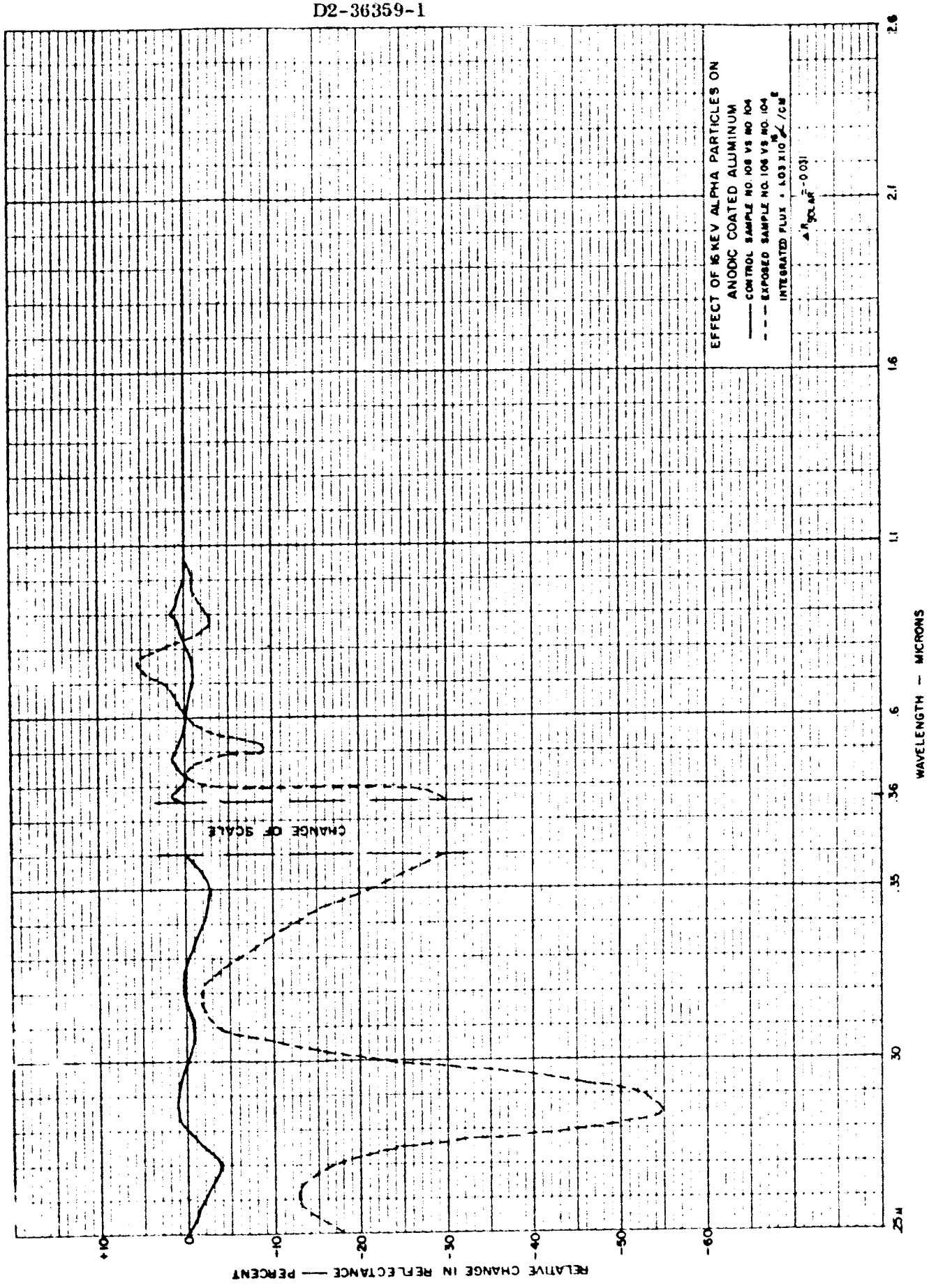

EFFECT OF 15 KEV ALPHA PARTICLES ON
ANODIC COATED ALUMINUM
—— CONTROL SAMPLE NO. 108 VS NO. 104
- - - EXPOSED SAMPLE NO. 106 VS NO. 104
INTEGRATED FLUX = 1.03 X 10^15 P/CM^2
Δ R_SOLAR = 0.031
CHANGE OF SCALE
+10
0
-10
-20
-30
-40
-50
-60
RELATIVE CHANGE IN REFLECTANCE —— PERCENT
2.6
2.1
1.6
1.1
.6
.36
.35
.30
.25 μ
WAVELENGTH — MICRONS

FIGURE C36

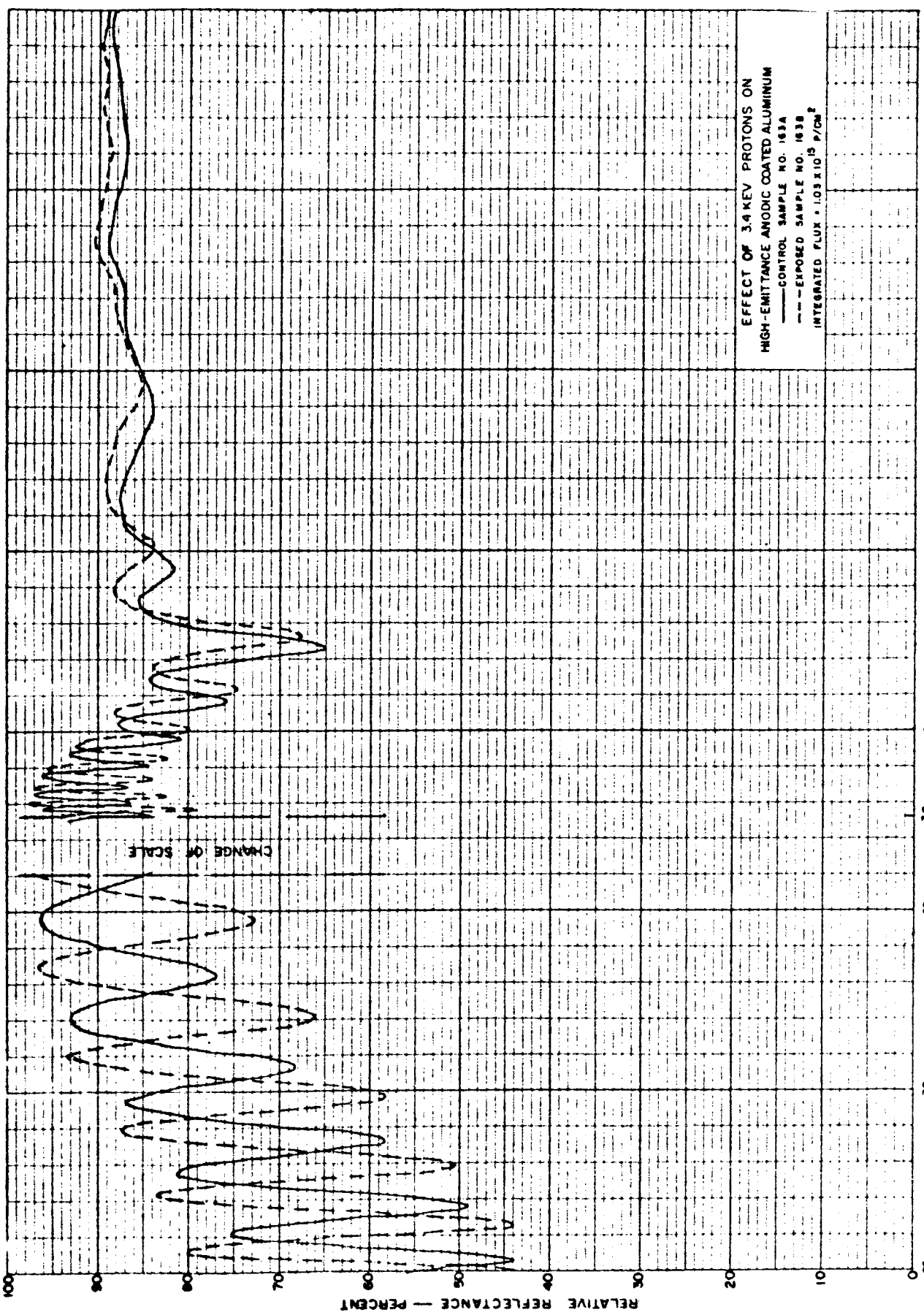

EFFECT OF 3.4 KEV PROTONS ON
HIGH-EMITTANCE ANODIC COATED ALUMINUM
——CONTROL SAMPLE NO. 163A
– – –EXPOSED SAMPLE NO. 163B
INTEGRATED FLUX = 1.03 X 10^15 P/CM^2
CHANGE OF SCALE
RELATIVE REFLECTANCE — PERCENT
WAVELENGTH — MICRONS

FIGURE 6 37

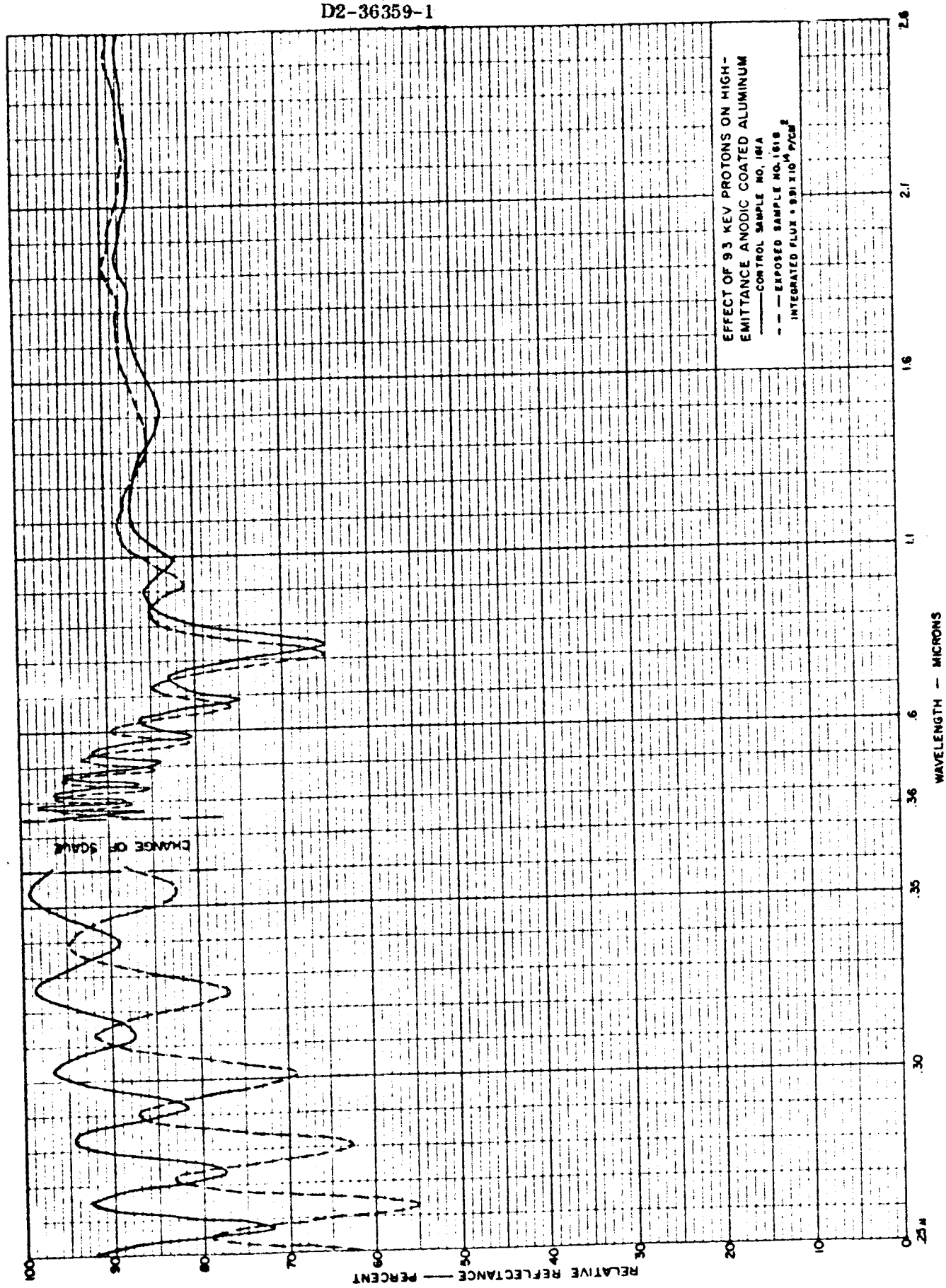

EFFECT OF 93 KEV PROTONS ON HIGH-EMITTANCE ANODIC COATED ALUMINUM
——CONTROL SAMPLE NO. 1614
– – – EXPOSED SAMPLE NO. 1615
INTEGRATED FLUX = 9.91 X 10^14 P/CM^2
CHANGE OF SCALE
RELATIVE REFLECTANCE —— PERCENT
WAVELENGTH — MICRONS

FIGURE C38

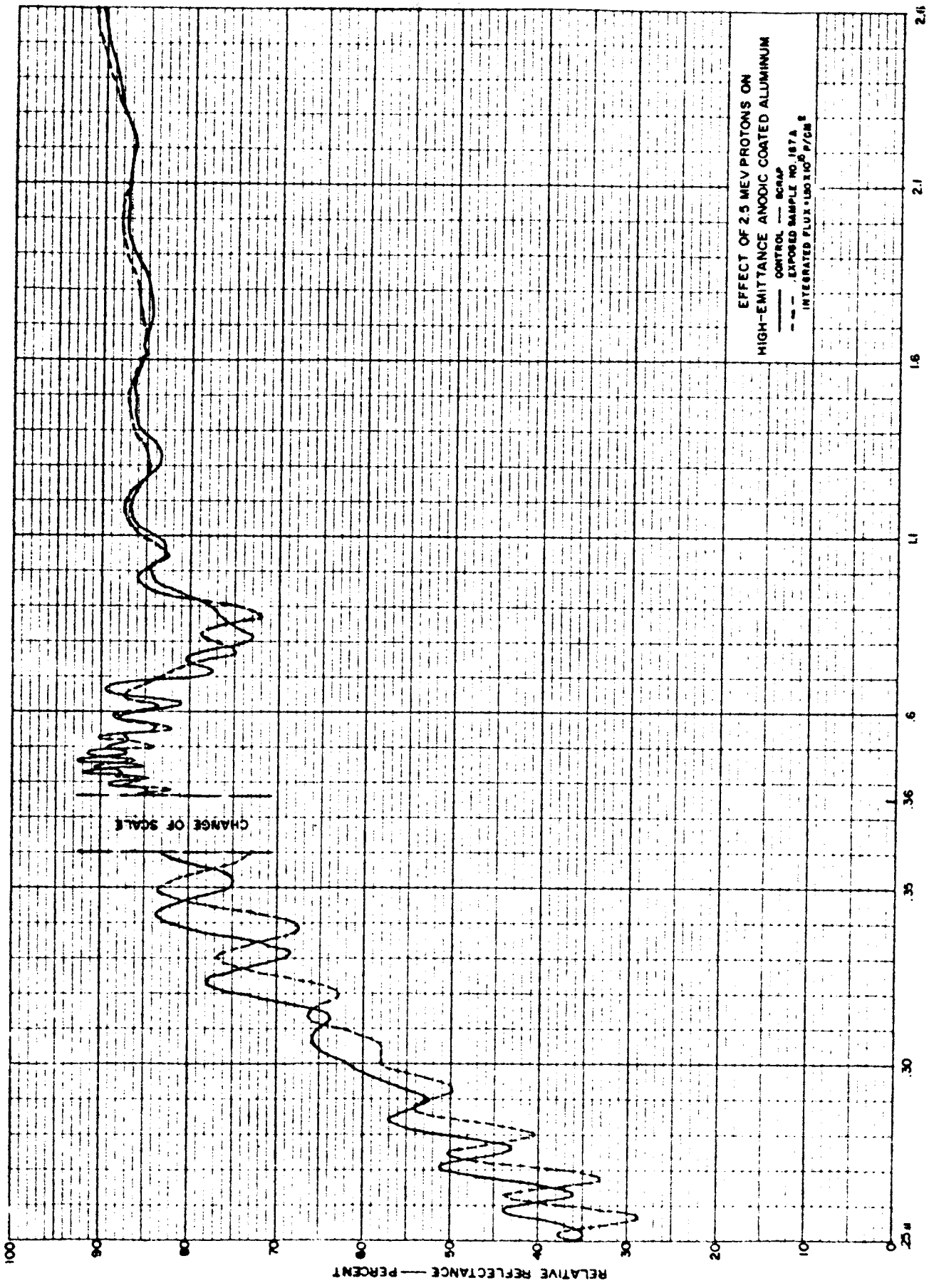

EFFECT OF 2.5 MEV PROTONS ON
HIGH-EMITTANCE ANODIC COATED ALUMINUM
—— CONTROL — SCRAP
– – – EXPOSED SAMPLE NO. 187A
INTEGRATED FLUX: 1.00 X 10^15 P/CM^2
CHANGE OF SCALE
RELATIVE REFLECTANCE — PERCENT
WAVELENGTH — MICRONS
100
90
80
70
60
50
40
30
20
10
0
.25 μ
.30
.35
.36
.6
1.1
1.6
2.1
2.6

FIGURE C39

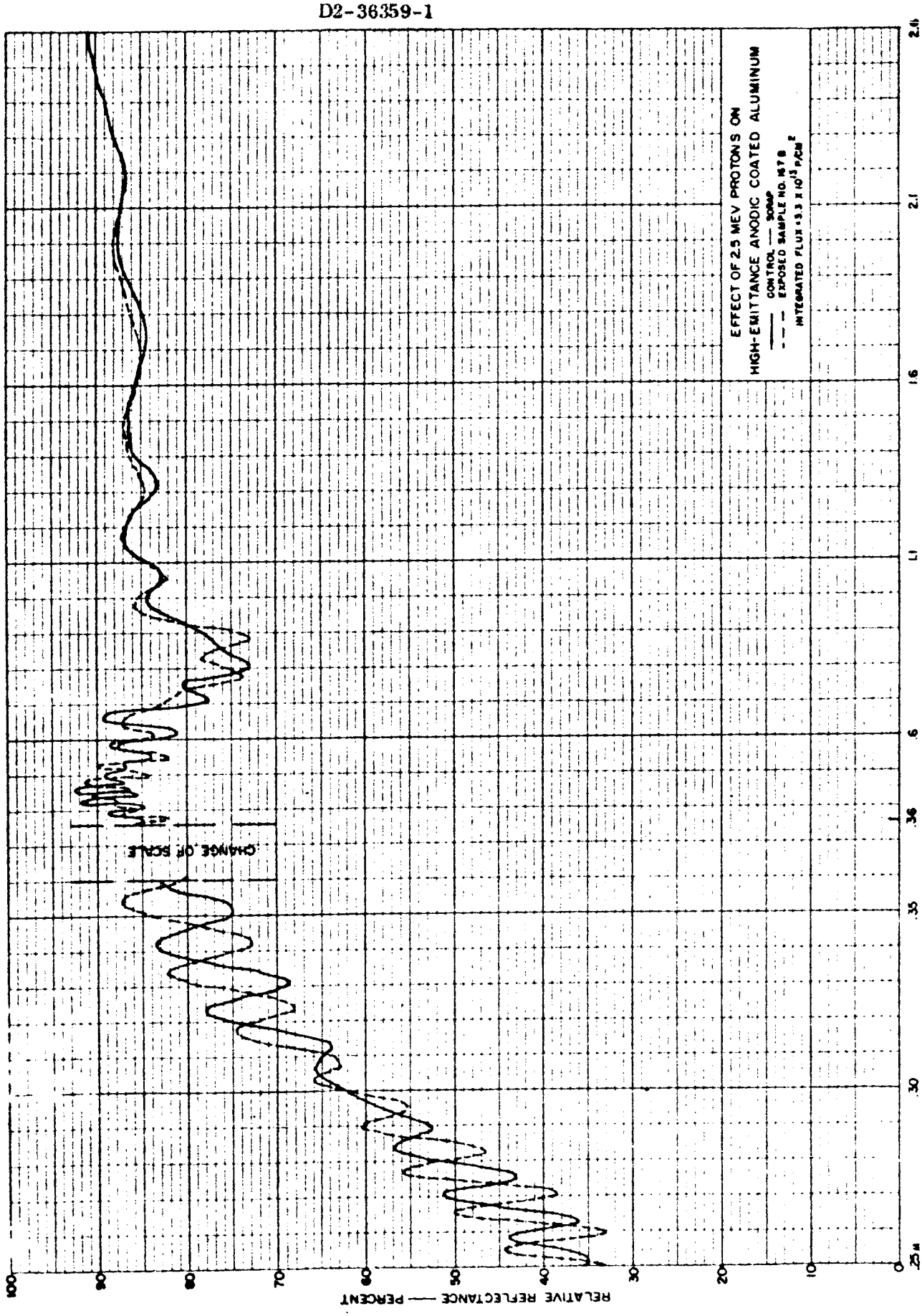

EFFECT OF 2.5 MEV PROTONS ON
HIGH-EMITTANCE ANODIC COATED ALUMINUM
—— CONTROL — SCRAP
- - - EXPOSED SAMPLE NO. 167 B
INTEGRATED FLUX = 9.3 X 10^13 P/CM^2
CHANGE OF SCALE
RELATIVE REFLECTANCE — PERCENT
WAVELENGTH — MICRONS

FIGURE C40

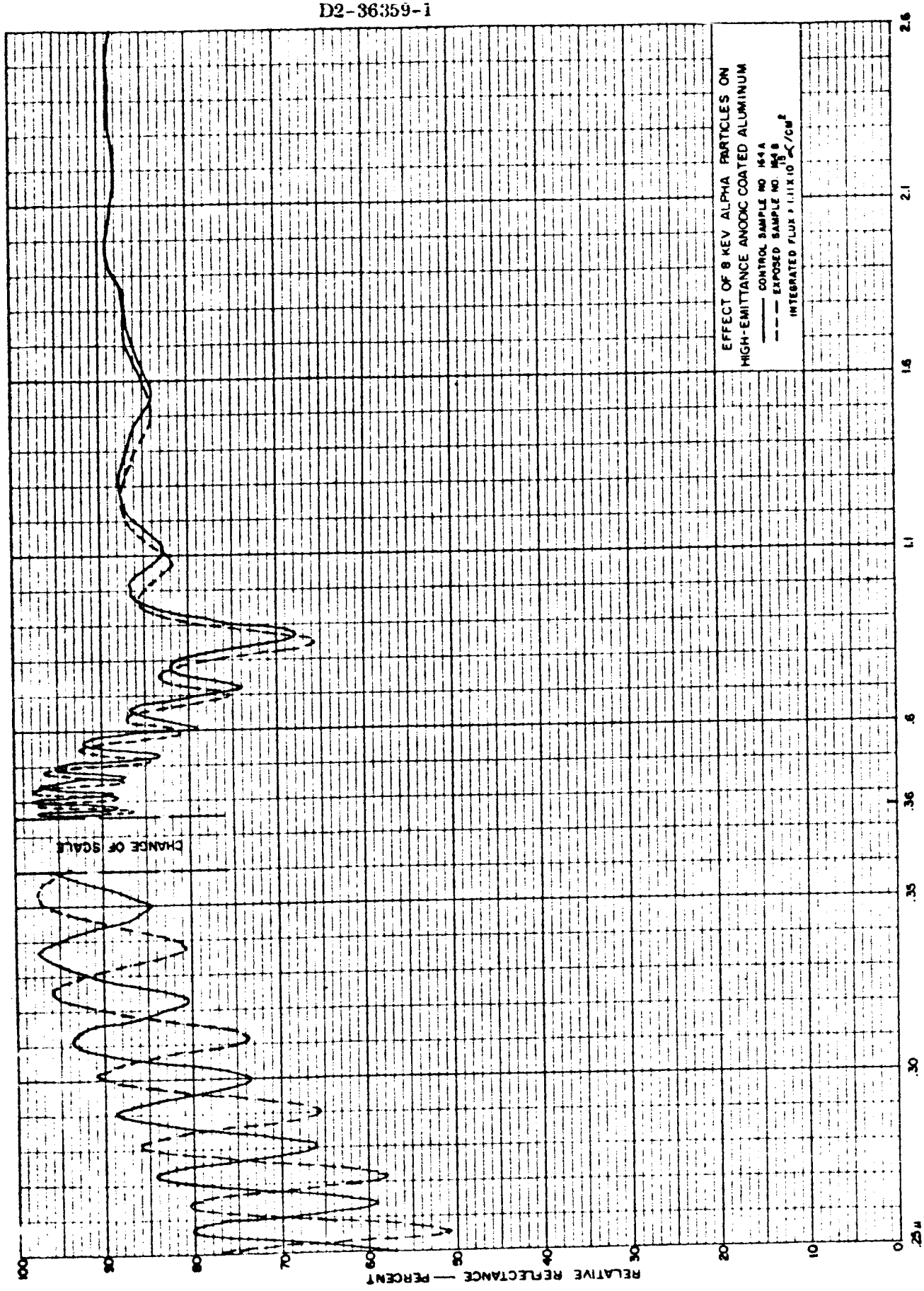

EFFECT OF 8 KEV ALPHA PARTICLES ON
HIGH-EMITTANCE ANODIC COATED ALUMINUM
CONTROL SAMPLE NO 164 A
EXPOSED SAMPLE NO 164 B
INTEGRATED FLUX = 1.11 X 10^15 ∝/cm²
CHANGE OF SCALE
RELATIVE REFLECTANCE — PERCENT
WAVELENGTH — MICRONS

FIGURE C 41

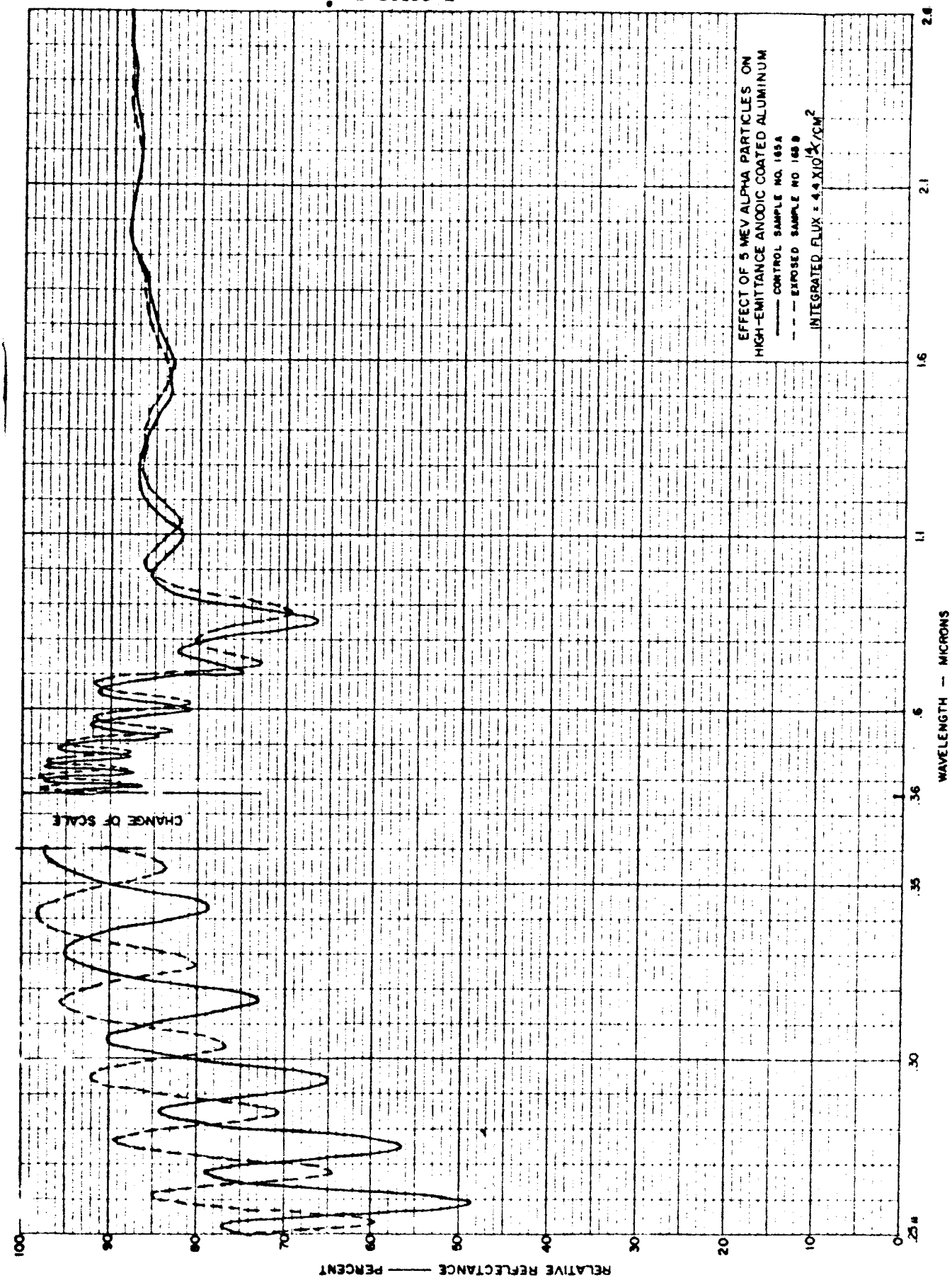

EFFECT OF 5 MEV ALPHA PARTICLES ON
HIGH-EMITTANCE ANODIC COATED ALUMINUM
—— CONTROL SAMPLE NO. 169A
- - - EXPOSED SAMPLE NO 168 B
INTEGRATED FLUX = 4.4 X 10^14 P/CM^2
CHANGE OF SCALE
RELATIVE REFLECTANCE —— PERCENT
WAVELENGTH — MICRONS
100
90
80
70
60
50
40
30
20
10
0
.25
.30
.35
.36
.6
1.1
1.6
2.1
2.6

FIGURE C 42

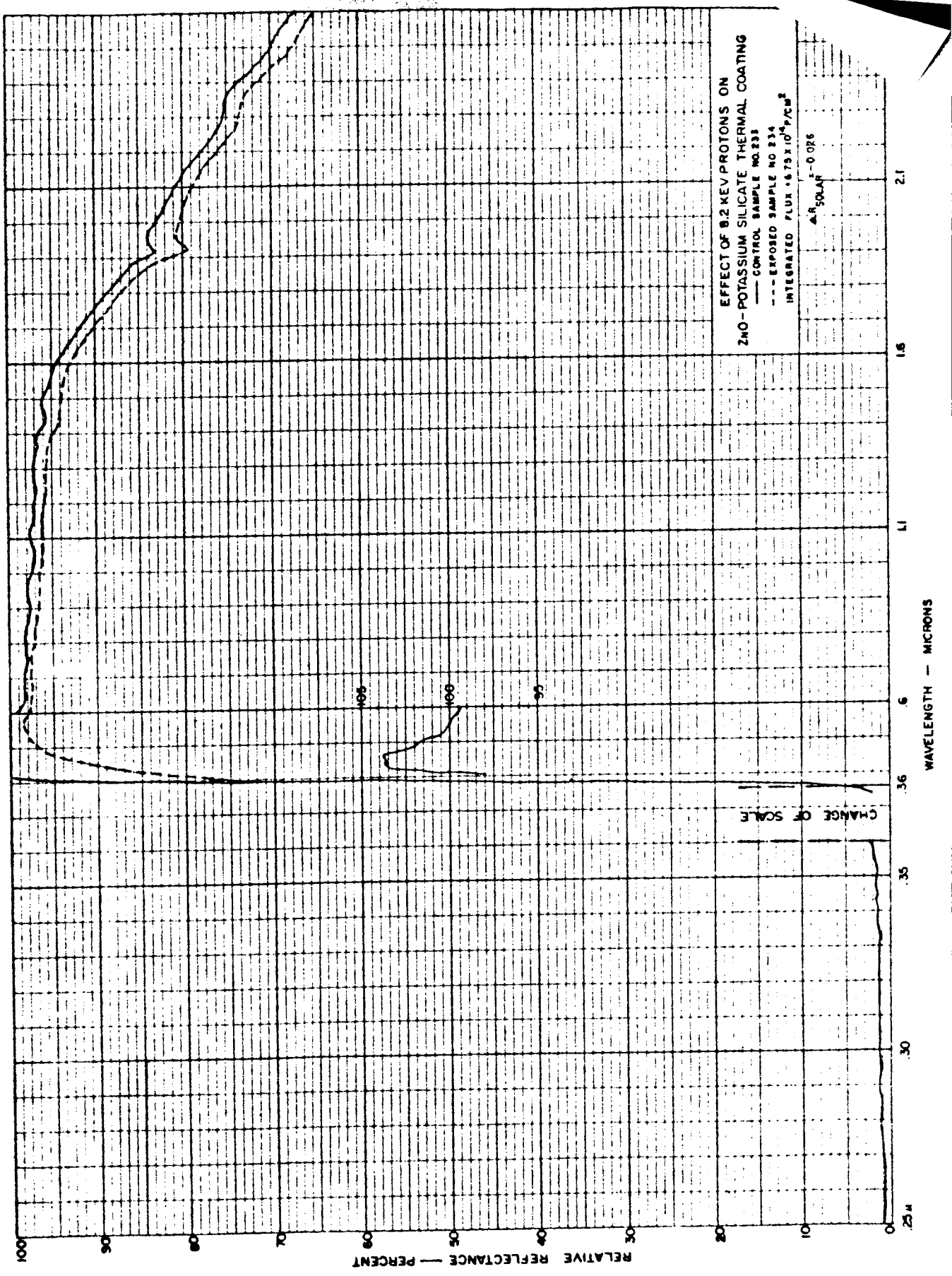

EFFECT OF 8.2 KEV PROTONS ON
ZnO-POTASSIUM SILICATE THERMAL COATING
—— CONTROL SAMPLE NO. 233
- - - EXPOSED SAMPLE NO 234
INTEGRATED FLUX 4.73 x 10^14 P/CM^2
ΔR SOLAR = 0.026
RELATIVE REFLECTANCE — PERCENT
WAVELENGTH — MICRONS
CHANGE OF SCALE
100
90
80
70
60
50
40
30
20
10
0
.25 μ
.30
.35
.36
.6
1.1
1.6
2.1

FIGURE C 43

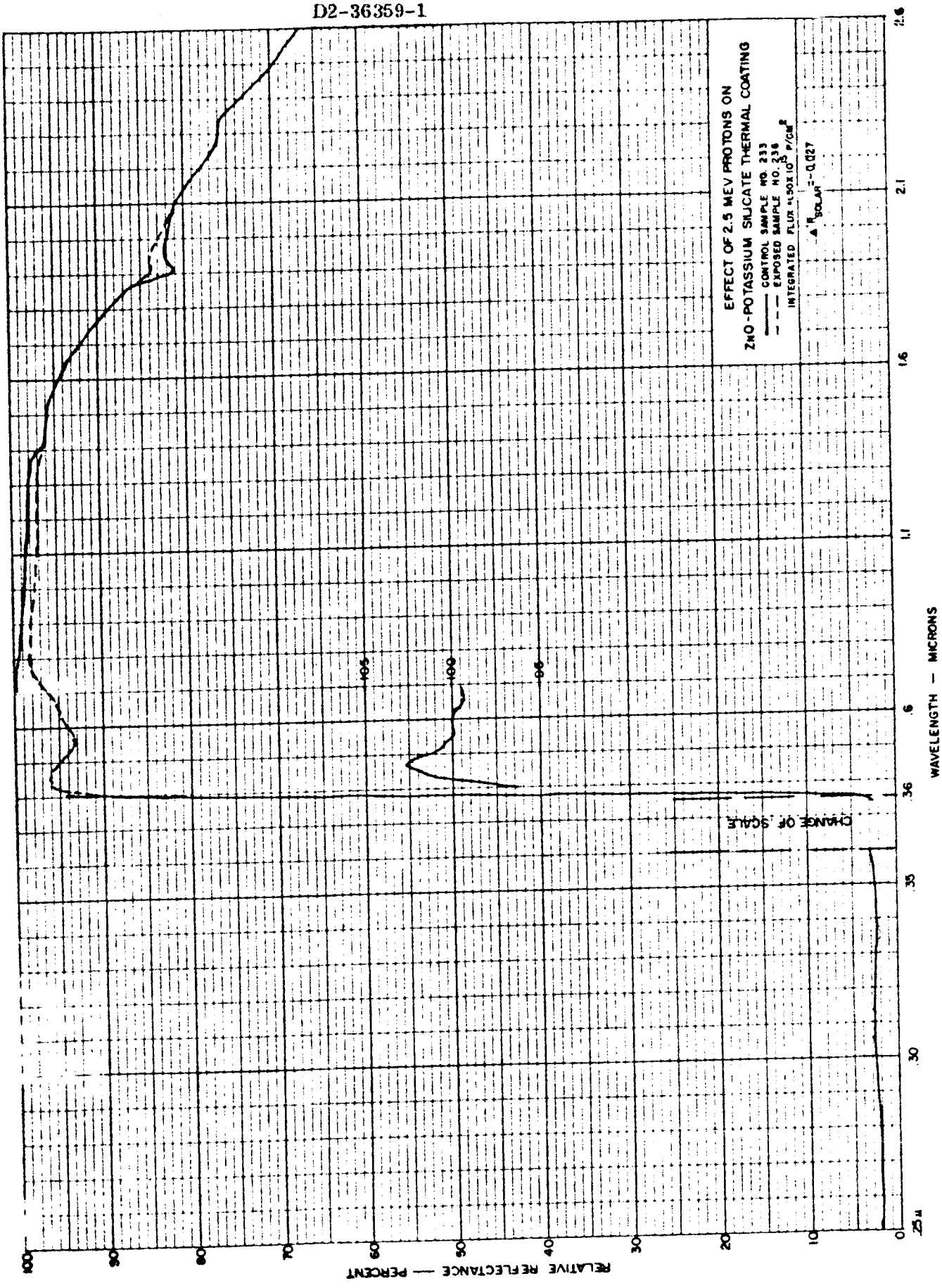

EFFECT OF 2.5 MEV PROTONS ON
ZnO-POTASSIUM SILICATE THERMAL COATING
—— CONTROL SAMPLE NO. 233
– – – EXPOSED SAMPLE NO. 236
INTEGRATED FLUX = 1.50 X 10^15 P/CM^2
Δα_SOLAR = 0.027
CHANGE OF SCALE
RELATIVE REFLECTANCE — PERCENT
WAVELENGTH — MICRONS

FIGURE C44

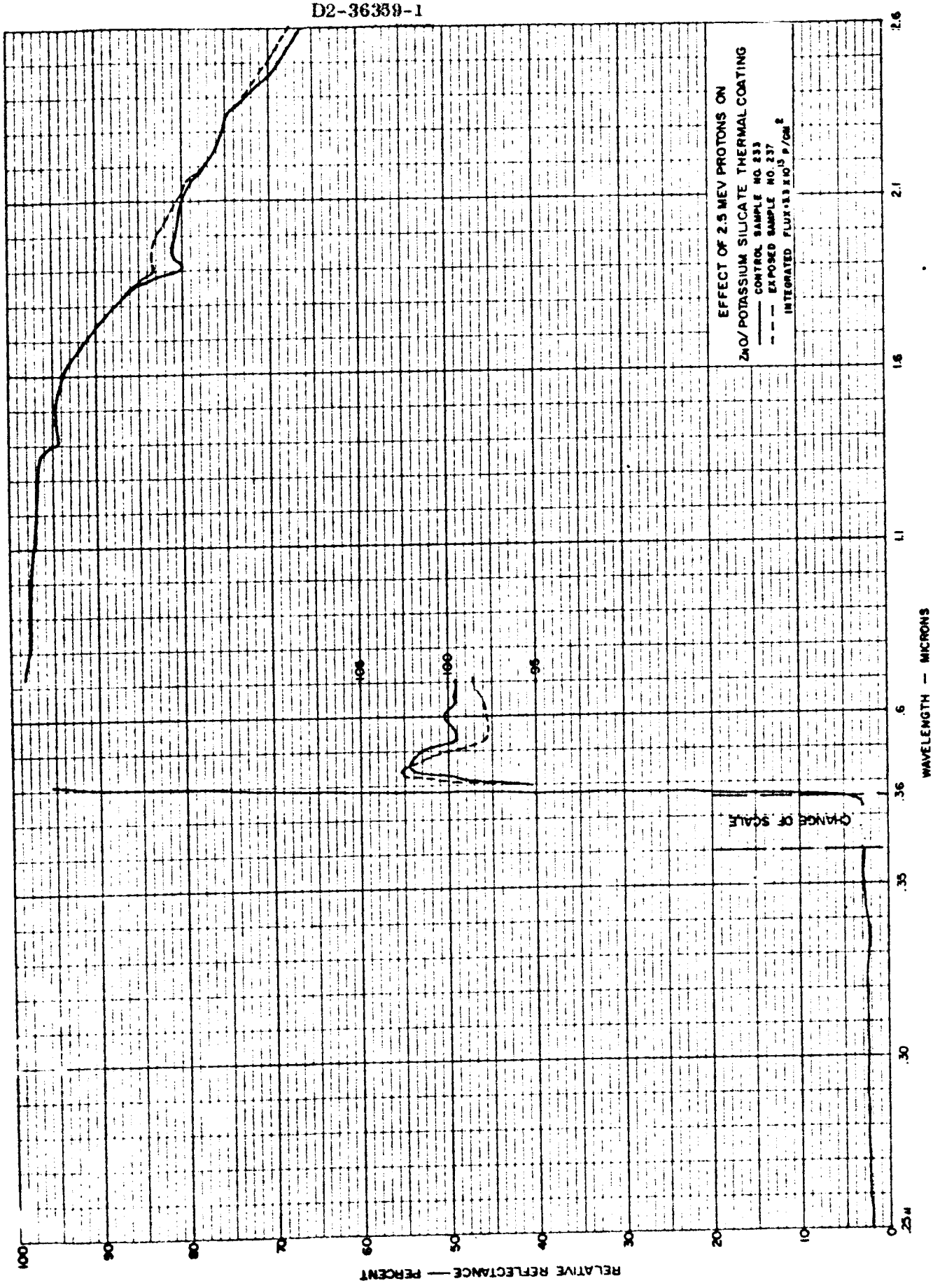

EFFECT OF 2.5 MEV PROTONS ON
ZnO/POTASSIUM SILICATE THERMAL COATING
—— CONTROL SAMPLE NO. 233
– – – EXPOSED SAMPLE NO. 237
INTEGRATED FLUX = 5.3 X 10^13 P/CM^2
CHANGE OF SCALE
RELATIVE REFLECTANCE — PERCENT
WAVELENGTH — MICRONS

FIGURE C45

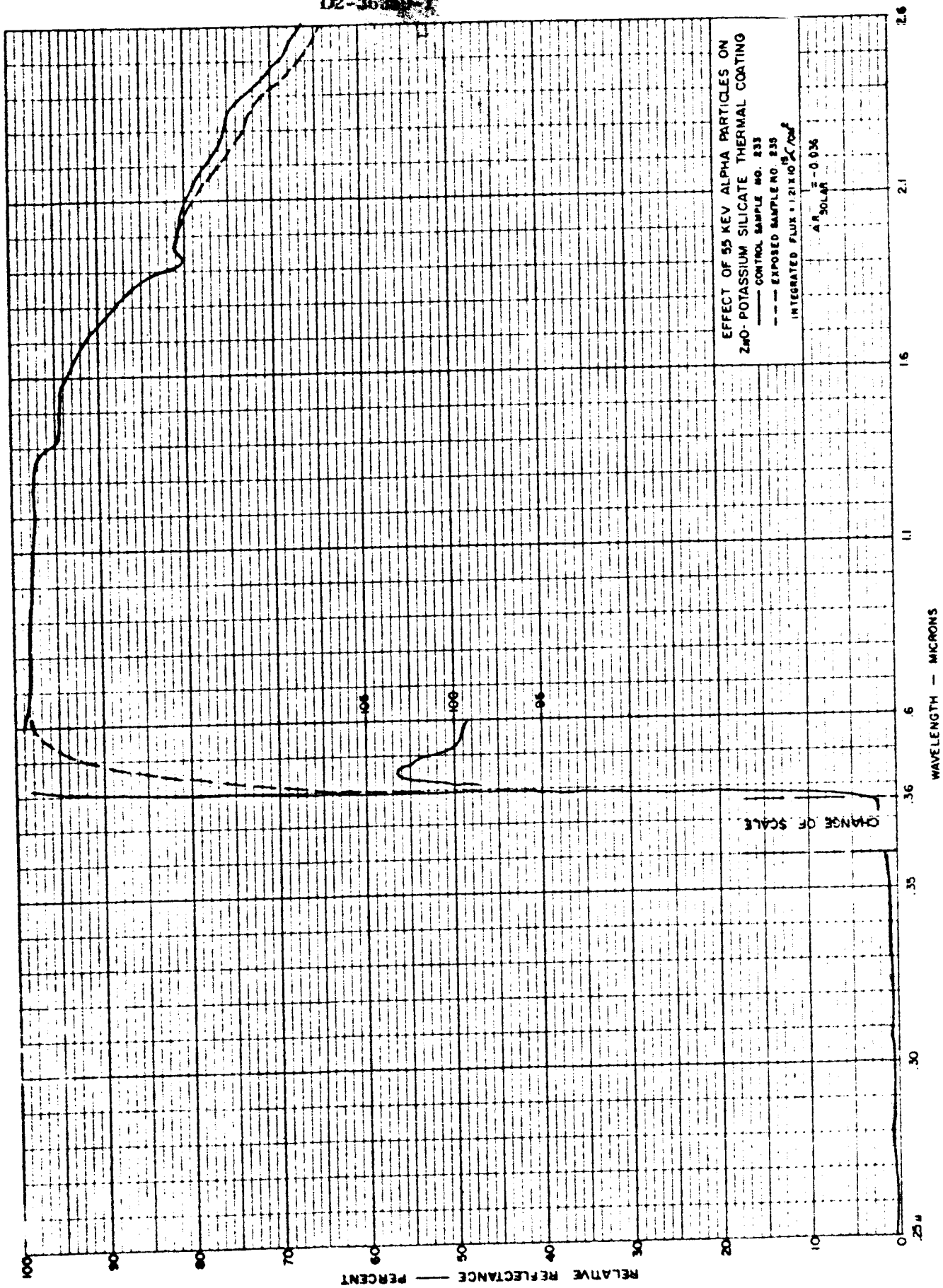


FIGURE C46
156

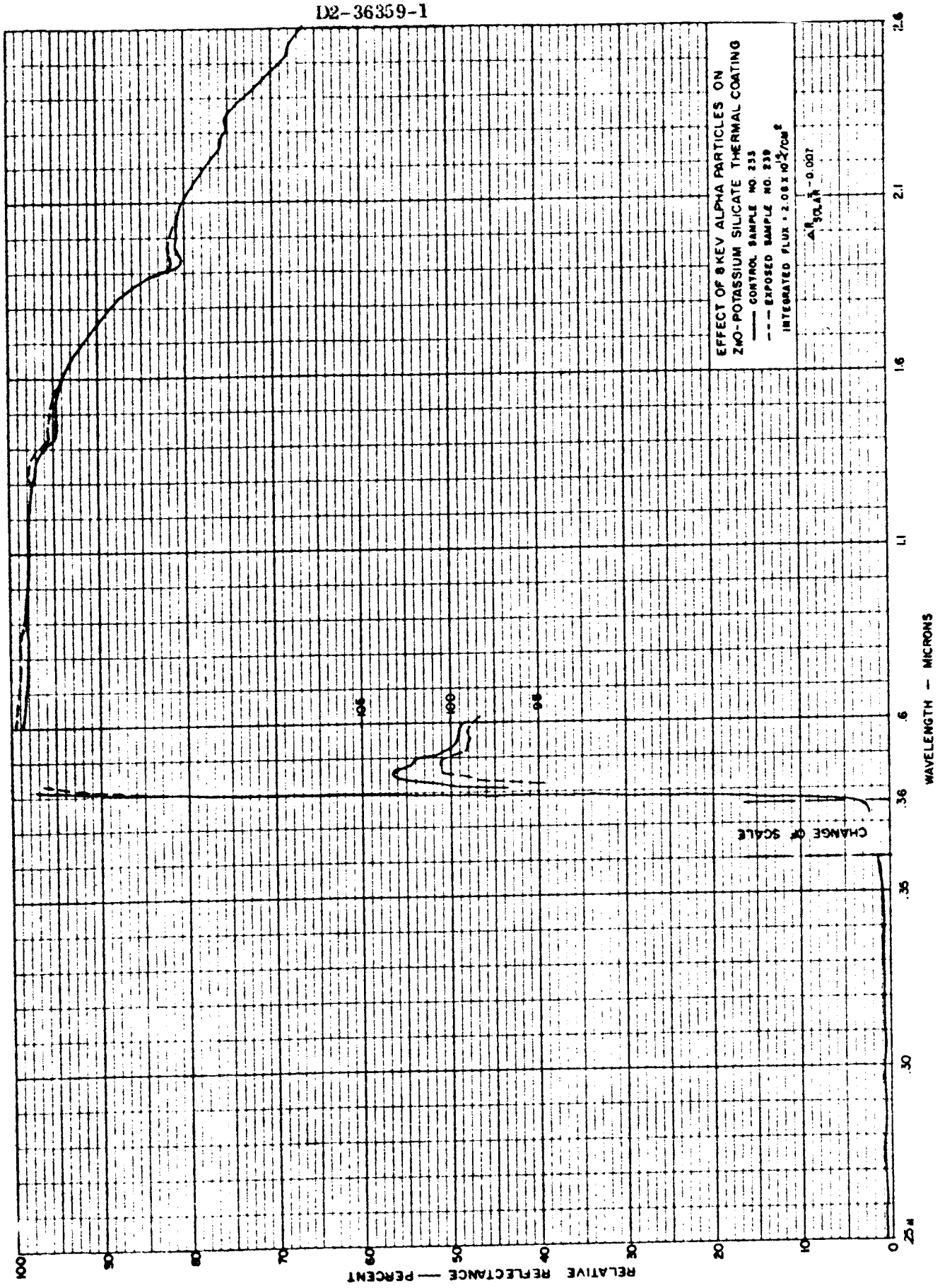

EFFECT OF 8 KEV ALPHA PARTICLES ON
ZnO-POTASSIUM SILICATE THERMAL COATING
—— CONTROL SAMPLE NO. 233
- - - EXPOSED SAMPLE NO. 239
INTEGRATED FLUX = 2.08 x 10¹⁴ P/cm²
Δα 300 Å = 0.007
CHANGE OF SCALE
RELATIVE REFLECTANCE — PERCENT
WAVELENGTH — MICRONS

FIGURE C47

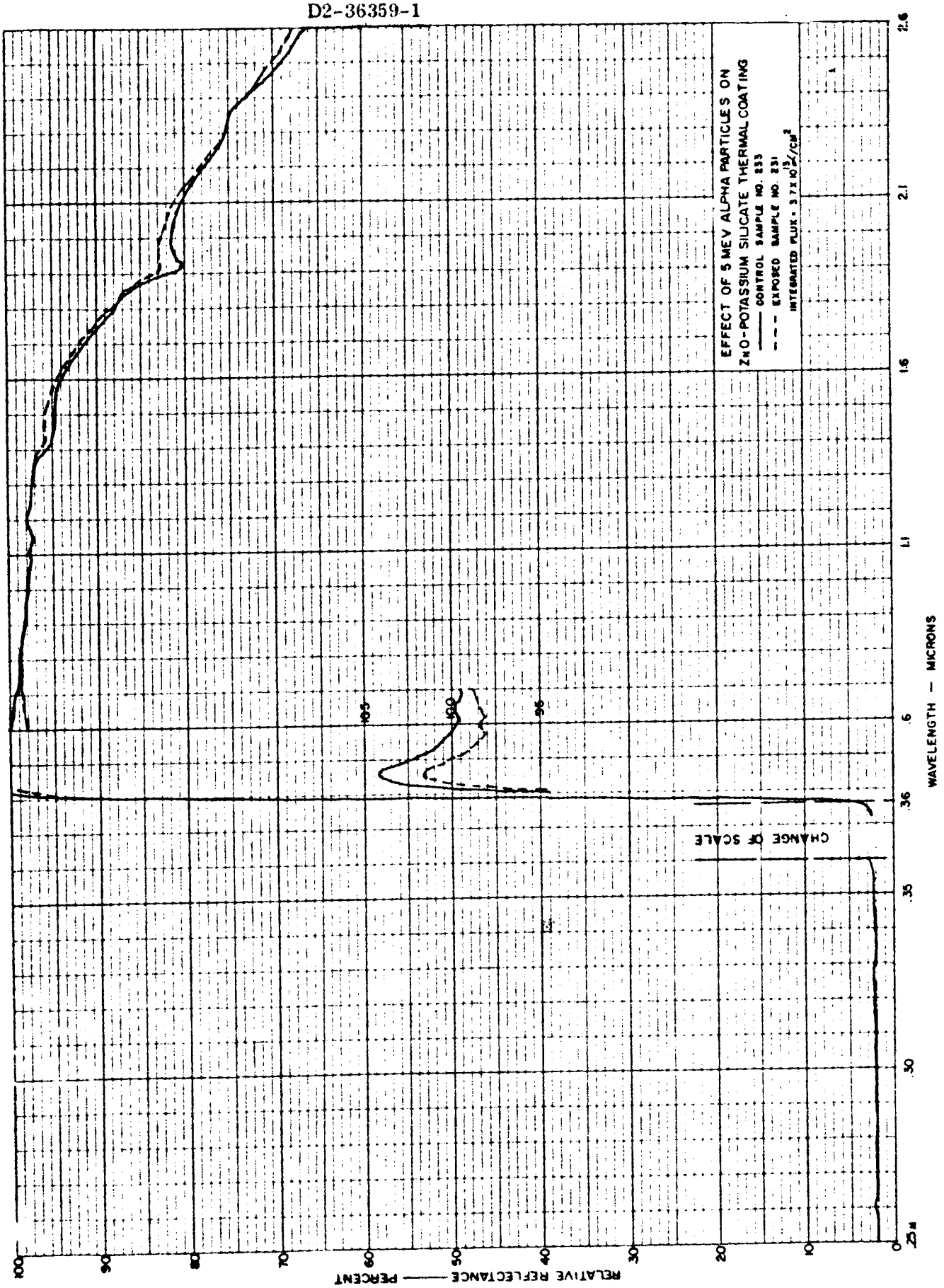

EFFECT OF 5 MEV ALPHA PARTICLES ON
ZnO-POTASSIUM SILICATE THERMAL COATING
—— CONTROL SAMPLE NO. 233
- - - EXPOSED SAMPLE NO. 231
INTEGRATED FLUX = 3.7 x 10^13 P/CM^2
CHANGE OF SCALE
RELATIVE REFLECTANCE —— PERCENT
WAVELENGTH — MICRONS

FIGURE C48

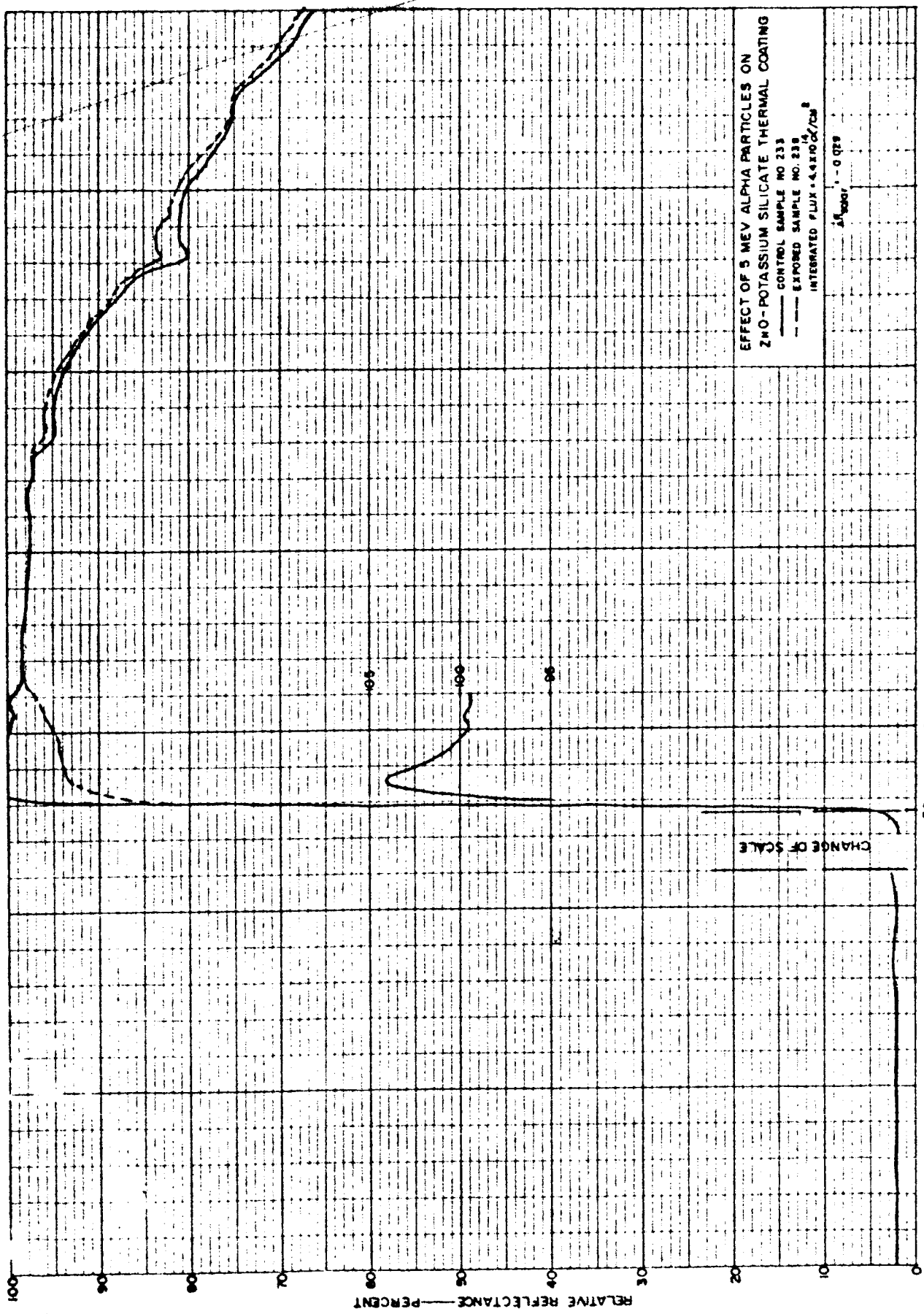

EFFECT OF 5 MEV ALPHA PARTICLES ON
ZnO-POTASSIUM SILICATE THERMAL COATING
CONTROL SAMPLE NO 233
EXPOSED SAMPLE NO. 238
INTEGRATED FLUX = 4.4 x 10^14 e/cm^2
Δα_solar = 0.079
CHANGE OF SCALE
RELATIVE REFLECTANCE — PERCENT
WAVELENGTH — MICRONS

FIGURE C49

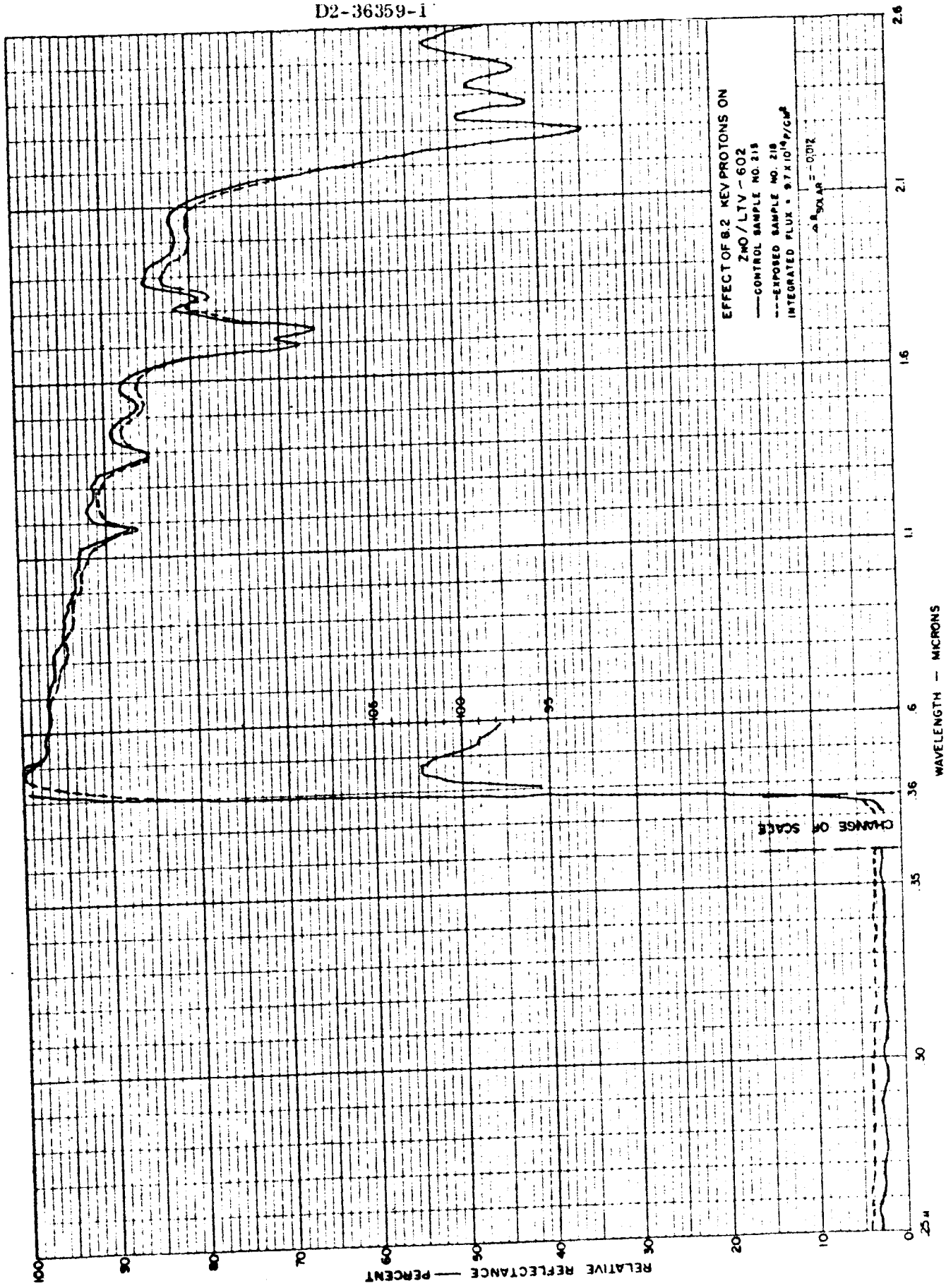

EFFECT OF 8.2 KEV PROTONS ON
ZnO/LTV-602
—CONTROL SAMPLE NO. 215
---EXPOSED SAMPLE NO. 218
INTEGRATED FLUX = 9.7 x 10^14 P/CM^2
α SOLAR = 0.212
CHANGE OF SCALE
RELATIVE REFLECTANCE — PERCENT
WAVELENGTH — MICRONS
100
90
80
70
60
50
40
30
20
10
0
2.6
2.1
1.6
1.1
.6
.36
.35
.30
.25 μ

FIGURE G50

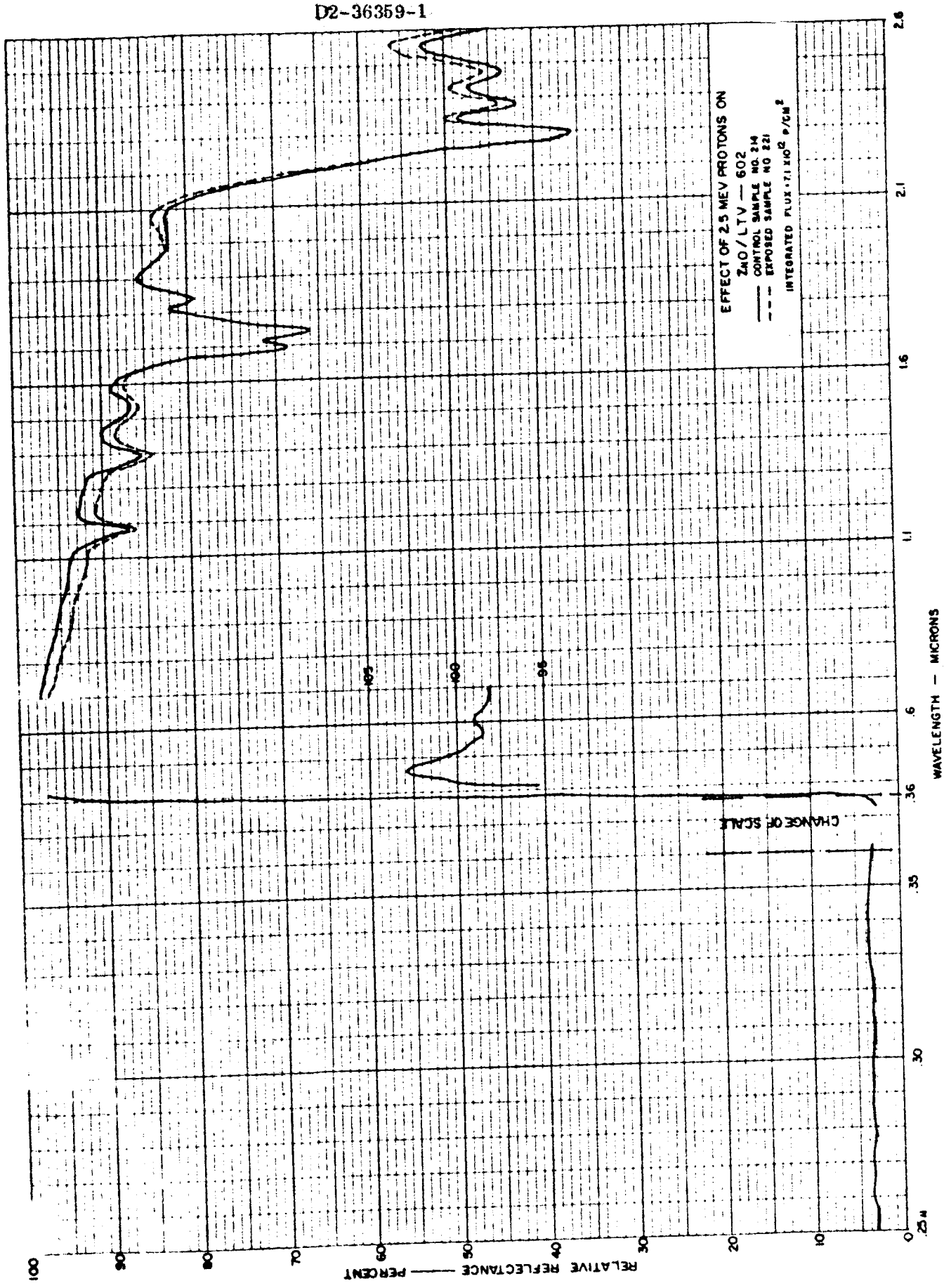

EFFECT OF 2.5 MEV PROTONS ON
ZnO / LTV — 602
CONTROL SAMPLE NO. 214
EXPOSED SAMPLE NO. 221
INTEGRATED FLUX = 7.1 X 10^12 P/CM^2
CHANGE OF SCALE
RELATIVE REFLECTANCE — PERCENT
WAVELENGTH — MICRONS

FIGURE C 51

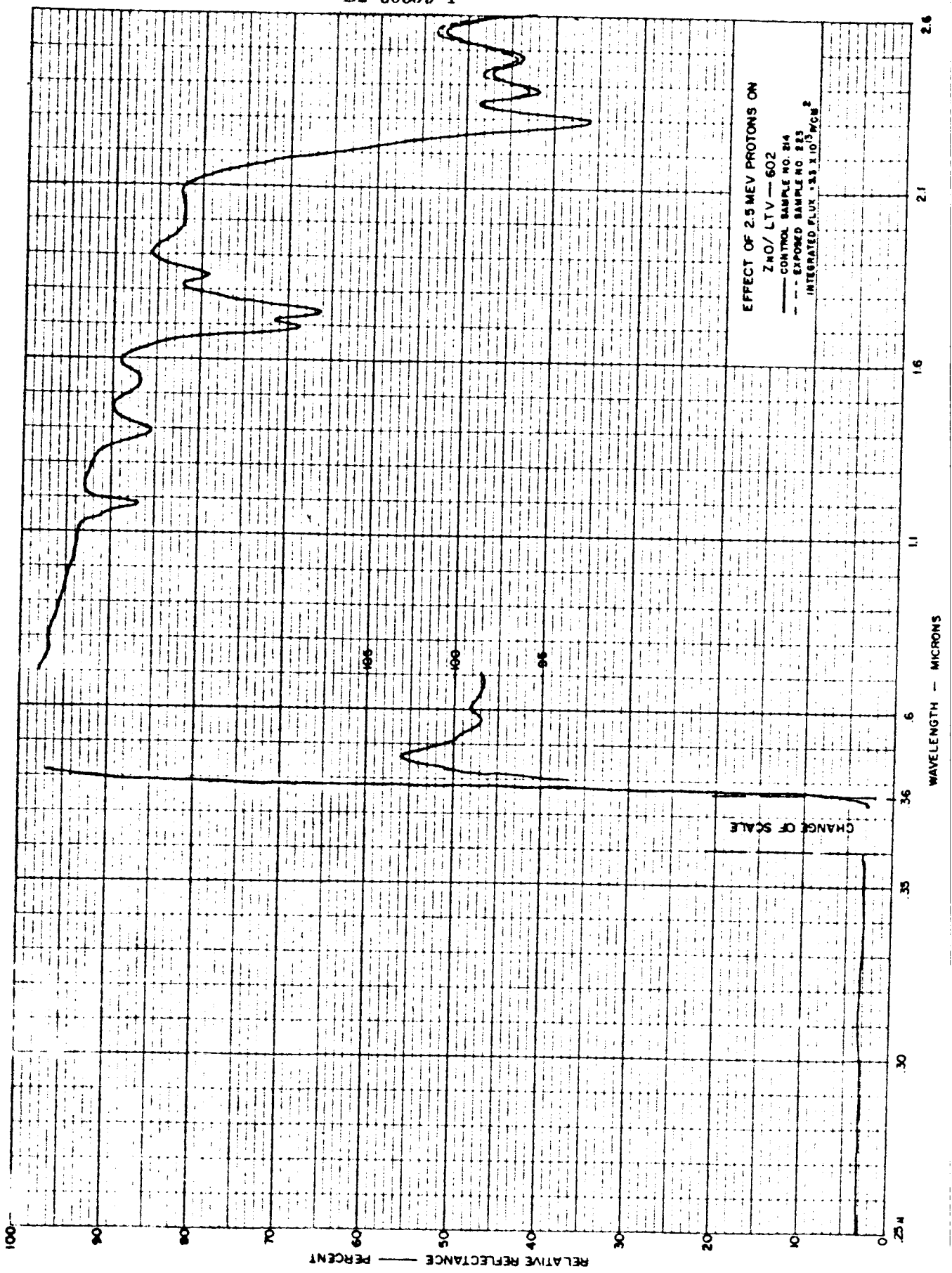

EFFECT OF 2.5 MEV PROTONS ON
ZnO/ LTV — 602
—— CONTROL SAMPLE NO. 214
– – – EXPOSED SAMPLE NO. 223
INTEGRATED FLUX = 3.5 X 10^15 P/CM^2
CHANGE OF SCALE
RELATIVE REFLECTANCE —— PERCENT
WAVELENGTH — MICRONS

FIGURE C 5 2

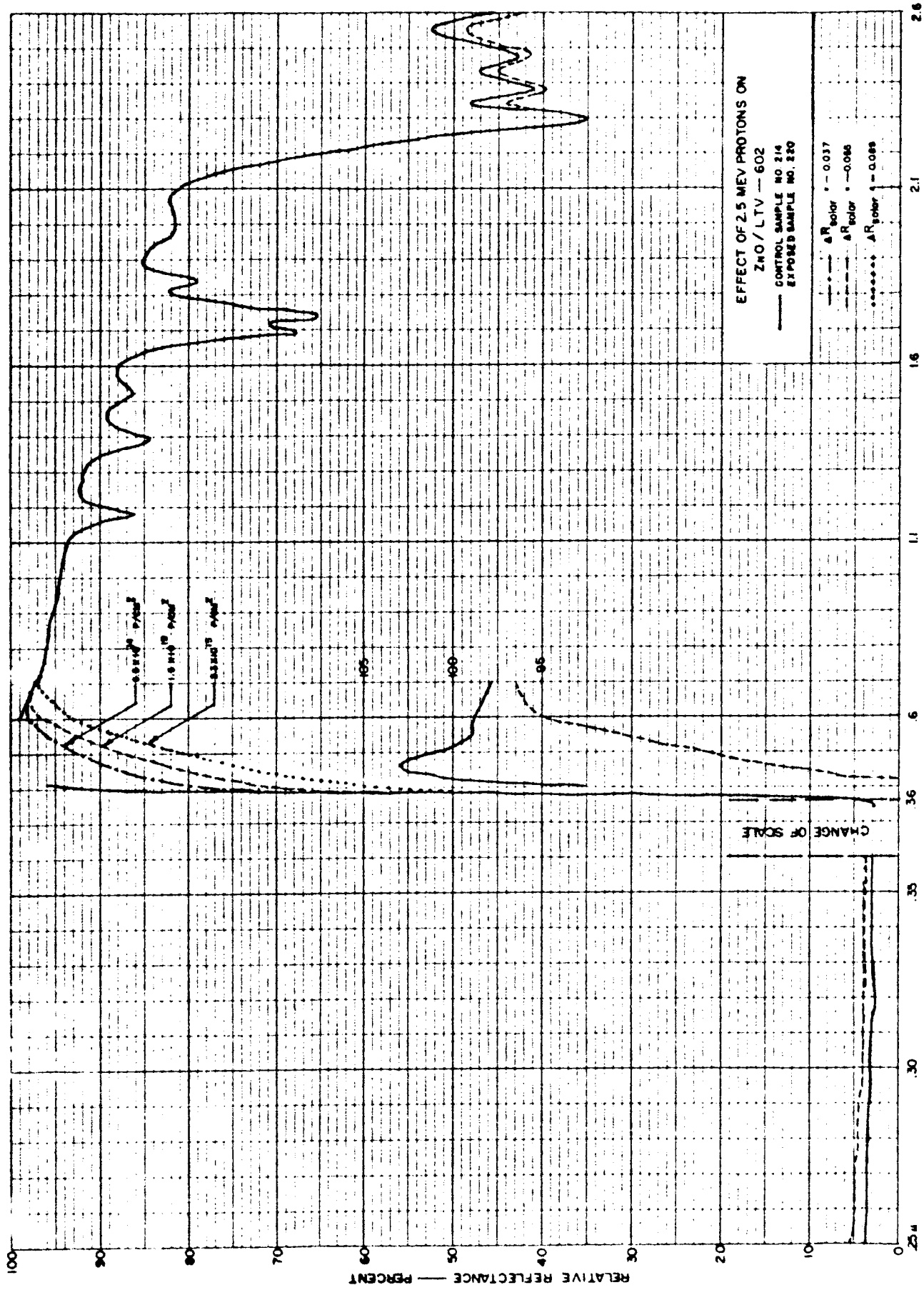

EFFECT OF 2.5 MEV PROTONS ON
ZnO / LTV — 602
CONTROL SAMPLE NO 214
EXPOSED SAMPLE NO. 220
ΔR_{solar} = -0.037
ΔR_{solar} = -0.065
ΔR_{solar} = -0.088
CHANGE OF SCALE
RELATIVE REFLECTANCE — PERCENT
WAVELENGTH — MICRONS

FIGURE 053

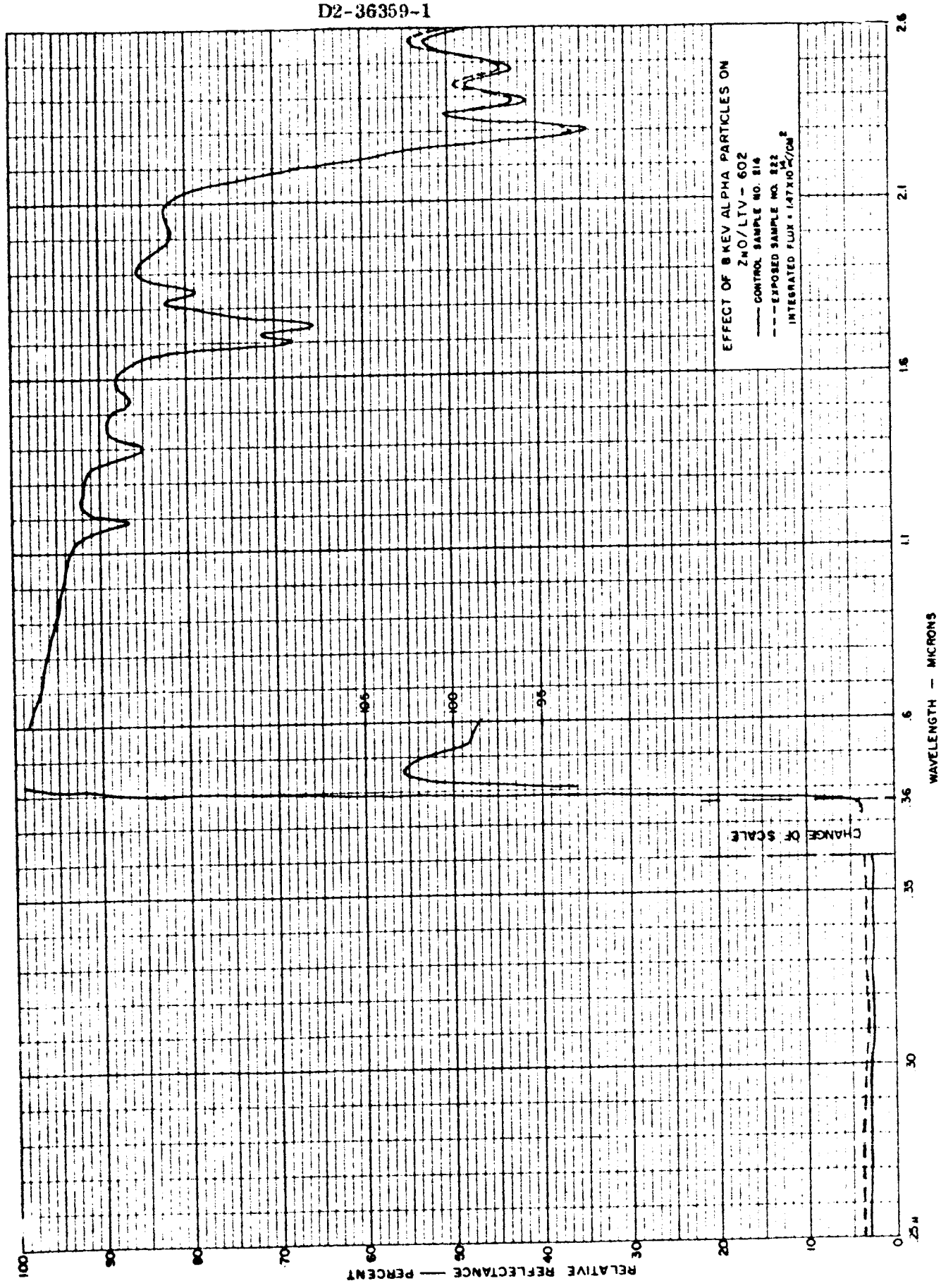

EFFECT OF 8 KEV ALPHA PARTICLES ON
ZnO/LTV - 602
—— CONTROL SAMPLE NO. 814
- - - EXPOSED SAMPLE NO. 822
INTEGRATED FLUX = 1.47 X 10^14 P/CM^2
CHANGE OF SCALE
RELATIVE REFLECTANCE — PERCENT
WAVELENGTH — MICRONS

FIGURE C 5 4

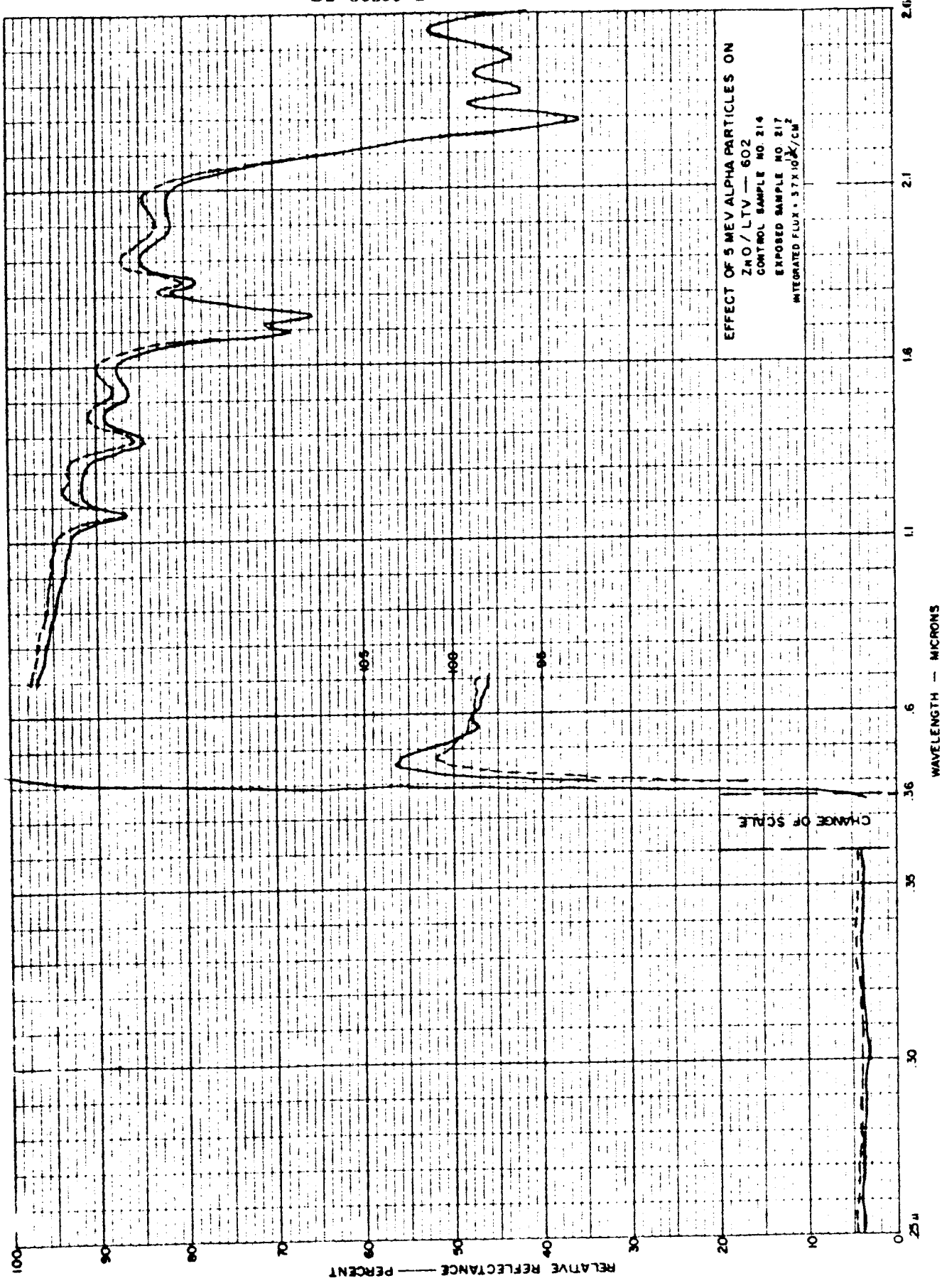

EFFECT OF 5 MEV ALPHA PARTICLES ON
ZnO / LTV — 602
CONTROL SAMPLE NO. 214
EXPOSED SAMPLE NO. 217
INTEGRATED FLUX = 3.7 X 10¹³ P/CM²
CHANGE OF SCALE
RELATIVE REFLECTANCE — PERCENT
WAVELENGTH — MICRONS

FIGURE C56

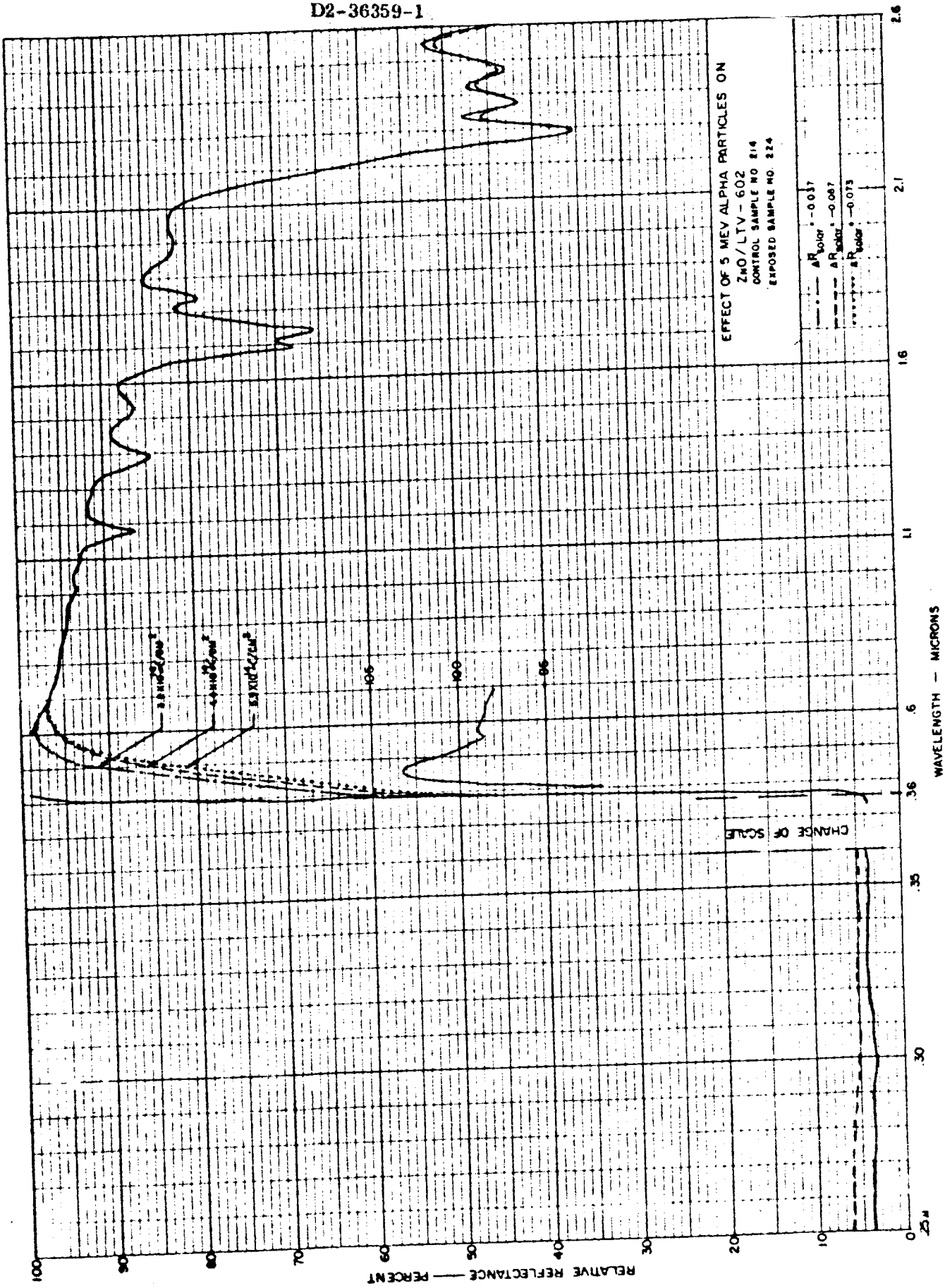

EFFECT OF 5 MEV ALPHA PARTICLES ON
ZnO/LTV-602
CONTROL SAMPLE NO 214
EXPOSED SAMPLE NO 224
ΔR_{color} = -0.037
ΔR_{color} = -0.067
ΔR_{color} = -0.073
CHANGE OF SCALE
RELATIVE REFLECTANCE —— PERCENT
WAVELENGTH — MICRONS

FIGURE C57

APPENDIX D - DETAILED DATA TABLE

APPENDIX D - TABLE OF TEST DATA

Sample Number	Type Material	Particle Type	Particle Energy	Integrated Flux	Solar Absorptance α	Solar Absorptance Δ α	Emittance
91	Low-Emittance Anodic Coatings	Proton	1.0 Kev	4.05×10^{15}		--	
61			1.0	8.00×10^{15}		--	
109			1.0	1.35×10^{16}		--	
56			3.4	1.00×10^{15}		~0.018	
57			3.4	1.05×10^{15}		<0.018	
58			3.4	2.18×10^{15}		<0.018	
55			3.4	1.00×10^{16}		0.018	
59			3.4	1.05×10^{16}		~0.018	
53			3.4	1.06×10^{16}		~0.018	
51			3.4	9.25×10^{16}	0.236	0.149	
34			4.7	1.065×10^{15}		--	
33			4.7	1.09×10^{15}		--	
35			4.7	1.19×10^{15}		--	
31			4.7	9.65×10^{15}		0.01	0.06
29			4.7	1.00×10^{16}	0.119	<0.01	
30			4.7	1.03×10^{16}		<0.01	0.06
1			5.0	3.48×10^{16}		0.01	
16			5.0	6.00×10^{16}		0.0648	
38			5.3	1.47×10^{17}		0.22	0.06
49			6.0	9.54×10^{14}		--	
50			6.0	9.68×10^{14}		--	
48			6.0	1.01×10^{15}		--	
44			6.0	1.00×10^{16}		0.0092	
47			6.0	1.00×10^{16}		0.0092	
43			6.0	1.01×10^{16}		<0.0092	
26			7.4	1.05×10^{15}		--	
24			7.7	1.00×10^{15}		--	

Sample Number	Type Material	Particle Type	Particle Energy	Integrated Flux	Solar Absorptance α	Solar Absorptance $\Delta\alpha$	Emittance
26	Low-Emittance	Proton	7.7 Kev	1.00×10^{15}		--	
20	Anodic Coatings		7.7	1.00×10^{16}	0.120	0.0112	
22			7.7	1.03×10^{16}		0.0083	
23			7.7	1.03×10^{16}		0.0079	
42			9.0	1.01×10^{17}		0.132	0.06
39			9.3	1.00×10^{16}		--	
40			9.3	1.03×10^{16}		--	
123			2.5	7.10×10^{12}		--	
124			2.5	7.10×10^{12}		--	
127			2.5	7.10×10^{12}		--	
116			2.5	3.30×10^{13}		--	
121			2.5	3.30×10^{13}		--	
122			2.5	3.30×10^{13}		--	
111			2.5	1.50×10^{15}		--	
113			2.5	1.50×10^{15}		--	
115		Proton	2.5 Mev	1.50×10^{15}		--	
131		Alpha	2.2 Kev	1.01×10^{15}		--	
130			2.2	1.03×10^{15}		--	
133			2.2	4.20×10^{15}		--	
132			2.2	9.75×10^{15}		--	
65			4.2	4.70×10^{14}		--	
69			4.2	4.92×10^{14}		--	
67			4.2	5.90×10^{14}		--	
72			4.5	5.00×10^{12}		--	
70			4.5	5.20×10^{13}		--	
71			4.5	5.20×10^{13}		--	
88			8.0	$< 1.33 \times 10^{14}$		--	
89			8.0	$< 1.33 \times 10^{14}$		--	
87			8.0	2.85×10^{14}		--	
90			8.0	No calc.		--	

Sample Number	Type Material	Particle Type	Particle Energy	Integrated Flux	Solar Absorptance α	Solar Absorptance Δ α	Emittance
92	Low-Emittance	Alpha	8.0 Kev	8.45×10^{14}		--	
93	Anodic Coatings		8.0	8.50×10^{14}		--	
94			8.0	9.60×10^{14}		--	
129			8.0	1.74×10^{15}		--	
128			8.0	1.06×10^{16}		--	
103			16.0	1.11×10^{14}		--	
97			16.0	1.15×10^{14}		--	
96			16.0	1.75×10^{14}		--	
101			16.0	1.03×10^{15}		--	
107			16.0	1.03×10^{15}		--	
100			16.0	1.05×10^{15}		--	
102			16.0	1.00×10^{16}		0.031	
106			16.0 Kev	1.03×10^{16}		0.031	
79			5.0 Mev	1.10×10^{13}		--	
84			5.0	1.10×10^{13}		--	
85			5.0	1.10×10^{13}		--	
74			5.0	3.70×10^{13}		--	
76			5.0	3.70×10^{13}		--	
75			5.0	3.70×10^{13}		--	
80			5.0	4.40×10^{14}		--	
82			5.0	4.40×10^{14}		--	
83		Alpha	5.0 Mev	4.40×10^{14}		--	
162B	High-Emittance	Proton	8.7 Kev	1.00×10^{16}		--	0.28
161B	Anodic Coatings		9.3 Kev	9.91×10^{14}		--	0.25
167B			2.5 Mev	3.30×10^{13}		--	
167A		Proton	2.5 Mev	1.50×10^{15}		--	
164B		Alpha	8.0 Kev	1.11×10^{15}		--	
165B		Alpha	5.0 Mev	4.40×10^{14}		--	
187	Chemically	Proton	8.2 Kev	4.60×10^{15}	0.171	--	0.078
189	Brightened		8.2 Kev	6.10×10^{15}		--	

Sample Number	Type Material	Particle Type	Particle Energy	Integrated Flux	Solar Absorptance α	Solar Absorptance Δ α	Emittance
196	Aluminum	Proton	2.5 Mev	7.10×10^{12}		--	
199		Proton	2.5 Mev	3.30×10^{13}		--	
194		Alpha	5.5 Kev	1.18×10^{15}		--	
195			8.0 Kev	1.38×10^{14}		--	
193			5.0 Mev	1.10×10^{13}		--	
192		Alpha	5.0 Mev	3.70×10^{13}		--	
178	Vapor-Deposited	Proton	7.4 Kev	1.00×10^{16}		0.0158	
179	Aluminum	Proton	8.0	8.90×10^{14}		--	0.05
185		Alpha	8.0	1.38×10^{14}		--	
174			8.0 Kev	1.04×10^{15}		--	
182			5.0 Mev	1.10×10^{13}		--	
181		Alpha	5.0 Mev	3.70×10^{13}		--	
232	Zinc Oxide/	Proton	7.7 Kev	1.00×10^{16}		0.1310	0.855
234	Potassium		8.2 Kev	6.75×10^{14}		0.0262	
237	Silicate		2.5 Mev	3.30×10^{13}		--	
236		Proton	2.5 Mev	1.50×10^{15}		0.027	
235		Alpha	5.5 Kev	1.21×10^{15}		0.0361	
239			8.0 Kev	2.08×10^{14}		0.007	
231			5.0 Mev	3.70×10^{13}		--	
238		Alpha	5.0 Mev	4.40×10^{14}		0.029	
218	Zinc Oxide/	Proton	8.2 Kev	9.70×10^{14}		0.0122	
216	LTV-602		8.2 Kev	6.10×10^{15}		0.0830	0.85
221			2.5 Mev	7.10×10^{12}		--	
223	Zinc Oxide/	Proton	2.5 Mev	3.30×10^{13}		--	
220	LTV-602	Proton	2.5 Mev	1.50×10^{15}		0.0558	
222		Alpha	8.0 Kev	1.47×10^{14}		--	
219			8.0 Kev	1.49×10^{15}		--	
217			5.0 Mev	3.70×10^{13}		--	
224		Alpha	5.0 Mev	4.40×10^{14}		0.051	

Sample Number	Type Material	Particle Type	Particle Energy	Integrated Flux	Solar Absorptance α	Solar Absorptance Δ α	Emittance
19				Control	0.21		
214				Control	0.181		0.89
175				Control			
233				Control	0.157		0.855
227				Control			0.855
196				Control			0.078
175				Control			0.05
183				Control			0.05
163A				Control			0.264
21				Control	0.12		
161A				Control			
162A				Control			
36				Control	0.12		
180				Control			